

Nirmal Mazumder ·
Gireesh Gangadharan ·
Yury V. Kistenev *Editors*

Advances in Brain Imaging Techniques



Springer

Advances in Brain Imaging Techniques

Nirmal Mazumder • Gireesh Gangadharan •
Yury V. Kistenev
Editors

Advances in Brain Imaging Techniques

 Springer

Editors

Nirmal Mazumder
Department of Biophysics, Manipal
School of Life Sciences
Manipal Academy of Higher Education
Manipal, Karnataka, India

Gireesh Gangadharan
Department of Cell and Molecular Biology,
Manipal School of Life Sciences
Manipal Academy of Higher Education
Manipal, Karnataka, India

Yury V. Kistenev
Tomsk State University
Tomsk, Russia

ISBN 978-981-19-1351-8

ISBN 978-981-19-1352-5 (eBook)

<https://doi.org/10.1007/978-981-19-1352-5>

© The Editor(s) (if applicable) and The Author(s), under exclusive license to Springer Nature Singapore Pte Ltd. 2022

This work is subject to copyright. All rights are solely and exclusively licensed by the Publisher, whether the whole or part of the material is concerned, specifically the rights of translation, reprinting, reuse of illustrations, recitation, broadcasting, reproduction on microfilms or in any other physical way, and transmission or information storage and retrieval, electronic adaptation, computer software, or by similar or dissimilar methodology now known or hereafter developed.

The use of general descriptive names, registered names, trademarks, service marks, etc. in this publication does not imply, even in the absence of a specific statement, that such names are exempt from the relevant protective laws and regulations and therefore free for general use.

The publisher, the authors and the editors are safe to assume that the advice and information in this book are believed to be true and accurate at the date of publication. Neither the publisher nor the authors or the editors give a warranty, expressed or implied, with respect to the material contained herein or for any errors or omissions that may have been made. The publisher remains neutral with regard to jurisdictional claims in published maps and institutional affiliations.

This Springer imprint is published by the registered company Springer Nature Singapore Pte Ltd.

The registered company address is: 152 Beach Road, #21-01/04 Gateway East, Singapore 189721, Singapore

Preface

Technical innovations in neuroimaging technology have allowed us to comprehend better the molecular mechanisms governing neurological diseases and fundamental responses in humans and animal model. It has led to the increasing popularity of neuroimaging approaches in clinical practice and fundamental research. This book *Advances in Brain Imaging Techniques* aims to provide a comprehensive picture of contemporary discoveries in brain imaging and their technological improvements to the structural, molecular, and functional knowledge of molecular systems linked with the nervous system of humans and other closely related animals. Advanced neuroimaging techniques offer a wide range of applications because they allow for a precise understanding of the pathomechanisms of brain illnesses, the development of the nervous system, and gain a better knowledge of the connectome in the brain and spinal cord. Such knowledge is beneficial for the diagnosis and effective treatment of physiological changes associated with many neurodegenerative diseases (ND). Optical microscopy technologies with subcellular resolution, endogenous contrast specificity, optical sectioning capabilities, high penetration depth, and spatiotemporal activity of neurons, among others, are employed as a potent tool for in vivo neuroimaging. Although multiple volumes have addressed various areas of neuroscience, brain mechanism, and brain biology, we are unaware of any volume that covers sophisticated neurological techniques, both optical and non-optical, in cognition and neurological illnesses. We believe this book will be particularly beneficial for the students and researchers interested in creating or implementing new neurological techniques to understand brain mechanisms better.

In *Advances in Brain Imaging Techniques*, we've gathered articles exploring the various exciting aspects of advanced microscopy techniques and their aspects in technology development as well as applications. Chapter 1 by Gladkova et al. discusses the applications of optical coherence tomography (OCT), a rapidly emerging imaging technique that allows real-time high-resolution imaging of tissues to detect brain gliomas and evaluate white matter state in the brain. It introduces the complexities and issues faced during brain tumor surgery and the potential application of OCT to overcome the said issues. Chapter 2 by Gagan and Mazumder explores the application of two-photon fluorescence lifetime imaging (TP-FLIM) for brain studies. Current neuroimaging techniques fall short of meeting the challenges offered by this complexly constructed organ in fully revealing a wide

range of neurological phenomena. This chapter examines the relevance of TP-FLIM of nicotinamide adenine dinucleotide (NADH), a ubiquitous endogenous fluorophore responsible for cellular autofluorescence, as an indication of cellular metabolic alterations associated with pathophysiological circumstances of diverse illnesses such as cancer. Neurodegenerative disorders, age-related and otherwise, are fast emerging as a major threat to the health of individuals. These disorders cannot be detected at early stages, making it difficult to be treated and controlled at later stages as the disease progresses. Chapter 3 by Kumari et al. discusses the application of Raman spectroscopy and microscopy techniques for the detection and early diagnosis of neurodegenerative disorders, thereby making it a potential diagnostic tool for similar diseases. The optical heterogeneity of brain tissues imposes a major limitation for its study and visualization, which can be minimized through the multiphoton fluorescence imaging technique. In Chap. 4, Bueno et al. touch the application of the multiphoton fluorescence process in combination with adaptive optics for imaging brain tissues using animal models such as a mouse, zebrafish, with special emphasis on the drosophila brain imaging. The myelin sheath is a component of the myelinated neurons. However, most of what we know about the myelin sheath, its structural organization, and function using transmission electron microscopy images. It provides much to be explored in the field to gain a comprehensive understanding of this important structure of the nervous system. Chapter 5 by Piazza and Hernandez discusses the latest imaging and spectroscopy techniques and also their application in myelin sheath studies. Visualizing the brain connectome would help us in understanding the wiring of the brain, which would further enhance our knowledge of neuronal pathways, and the onset and progress of various diseases associated with the brain and nervous system. In Chap. 6, Makkithaya et al. discuss “Brainbow,” a novel technique that was developed to effectively visualize the brain connectome through a combination of molecular biology and fluorescence microscopy. Photoacoustic imaging is a technique that is an amalgamation of two physical methods, viz., laser absorption spectroscopy and ultrasound imaging. This fast-emerging technique that finding its applications in many fields of biology. Chapter 7 by Sunder et al. iterates the principle and application of photoacoustic imaging to gain an insight into the in vivo brain activity, the peculiarities in the brain, and the current state in persisting brain disorders. Photodynamic therapy is a cutting-edge cancer treatment option, which has been used mostly to treat brain cancer. However, recent research on the reactive oxygen species, particularly singlet oxygen has revealed more prospects for the application of photodynamic therapy. Chapter 8 by Telenova et al. discusses the principle and applications of photodynamic therapy in neurobiology for the treatment of diseases and disorders associated with the brain. Magnetic resonance imaging (MRI) is a technique that is extensively used to generate high-resolution images of the brain. This noninvasive technique that allows the structural and functional evaluation of the brain. Chapter 9 by Kaur et al. discusses the application of other advanced techniques such as diffusion-weighted imaging, MR perfusion, and MR spectroscopy, with MRI to evaluate the brain’s cytoarchitecture. Indirect cancer imaging methods are based on the regulation of molecular indicators in tissue that are linked to cancer-specific changes from

proteomic, genomic, and metabolomic perspectives. Chapter 10 by Peng et al. provides an overview of current strategies for indirect cancer imaging using neurodegenerative disorders molecular markers control by various molecular spectroscopy and imaging methods. Purohit and Roy, in Chap. 11, discuss the various multimodal MRI strategies that enable us to monitor the progression of neurodegenerative diseases and disorders. Machine learning is commonly employed in visual data imaging analysis, identification, and classification. Chapter 12 by Kistenev and Vrazhnov provides an overview of the subject. It illustrates the application of machine learning to diagnose brain disorders using MRI and optical imaging modalities. The nervous system, our body's command center, plays a critical role in regulating and managing numerous physiological operations. However, the precise neuronal or cellular processes that control these functions remain unknown. It is vital to identify them to comprehend the functional consequences of neuronal circuits and their participation in various neurological illnesses. Smaller animal models, like *Drosophila*, provide a wealth of genetic data for dissecting brain circuitry. It aids in comprehending some neural circuits and their control in various brain activities. Chapter 13 by Mugudthi et al. discusses the techniques employed for the brain mapping of *Drosophila melanogaster*, and its implications for mapping the human brain. Alzheimer's disease (AD) is a progressive and irreversible neurological ailment in which memory and cognitive skills and the ability to complete even simple activities, deteriorate with time. Although AD is primarily a memory problem, people with the disease also exhibit various behavioral and psychological symptoms of dementia. It is crucial to study the small animal models to gain a comprehensive understanding of the manifestation and progression of AD. Chapter 14 by Bettagere et al. focuses on the behavioral phenotypes of AD seen in rodents. It illustrates the various behavioral tests employed to detect the non-cognitive symptoms of AD in rodent models.

We appreciate the authors' contributions to this book, as well as their prompt answers to the reviewers' remarks. We are grateful to the reviewers for devoting their time to providing insightful recommendations and comments on the chapters. We also acknowledge our colleagues who helped us with this volume's suggestions. Selvakumar Rajendran and Bhavik Sawhney (Springer Nature Publishing) deserve special thanks for their contributions to the book. More importantly, we wish our readers a pleasant and productive browsing experience.

Manipal, Karnataka, India
Manipal, Karnataka, India
Tomsk, Russia

Nirmal Mazumder
Gireesh Gangadharan
Yury V. Kistenev

Contents

1	Optical Coherence Tomography in Brain Gliomas Detection and Peritumoral White Matter State Evaluation	1
	N. D. Gladkova, K. A. Achkasova, K. S. Yashin, E. B. Kiseleva, A. A. Moiseev, E. L. Bederina, S. S. Kuznetsov, I. A. Medyanik, L. Ya. Kravets, G. V. Gelikonov, and P. A. Shilyagin	
2	Two Photon Fluorescence Lifetime Imaging of Reduced Nicotinamide Adenine Dinucleotide in Brain Research	23
	Gagan Raju and Nirmal Mazumder	
3	Types of Raman Scattering Techniques for Neurodegenerative Diseases	39
	Sparsha Kumari, Apoorva Bettagere Shivakumar, Sonam Fathima Mehak, Nirmal Mazumder, Gireesh Gangadharan, and Vikram G. Pillai	
4	<i>Drosophila</i> Brain Advanced Multiphoton Imaging	59
	Juan M. Bueno, Yu-Shuo Liao, Francisco J. Ávila, Shiu-Feng Cheng, and Shi-Wei Chu	
5	Myelin Imaging	81
	Valeria Piazza and Victor H. Hernandez	
6	Brainbow: Principle, Technique, and Applications	95
	Kausalya Neelavara Makkithaya, Saina Rath, Sathya Sandilya Garemillla, Sai Sowmya, S. Keerthana, and Nirmal Mazumder	
7	Photoacoustic Imaging of Brain	109
	Mridula Sunder, Nirmal Mazumder, Yury V. Kistenev, and Denis A. Vrazhnov	
8	Photodynamic Therapy of Brain Diseases	125
	Valeria V. Telnova, Alexander I. Dubrovsky, Andrey V. Terskov, Anna S. Tsven, Oxana V. Semyachkina-Glushkovskaya, and Valery V. Tuchin	

9	Advanced Magnetic Resonance Imaging (MRI) of Brain	147
	Navdeep Kaur, Soumya Swaroop Sahoo, and Shailendra Singh Rana	
10	Indirect Imaging	163
	Yan Peng, Chenjun Shi, Yury V. Kistenev, Denis A. Vrazhnov, and Olga P. Cherkasova	
11	Multimodal Noninvasive Imaging Strategies for Clinically Monitoring Degenerative Disorders of the Brain	183
	Pratik Purohit and Prasun K. Roy	
12	Machine Learning Approach in Brain Imaging	203
	Yury V. Kistenev and Denis A. Vrazhnov	
13	Transgenic Brain Mapping Techniques in <i>Drosophila melanogaster</i>	231
	Deepa Mugudthi Venugopal, Raifa Abdul Aziz, and Shamprasad Varija Raghu	
14	Behavioural Phenotyping to Study Cognitive and Non-cognitive Symptoms in the Rodent Model of Alzheimer’s Disease	243
	Apoorva Bettagere Shivakumar, Sonam Fathima Mehak, Sparsha Kumari, Vikyath Saraf, and Gireesh Gangadharan	

About the Editors

Nirmal Mazumder is an Assistant Professor at the Department of Biophysics, Manipal School of Life Sciences, Manipal Academy of Higher Education (MAHE), Manipal, Karnataka, India. He obtained his Ph.D. in 2013 from National Yang Ming Chiao Tung University, Taipei, Taiwan. From 2013 to 2016, he worked as a postdoctoral fellow at the University of Virginia, the USA, and the Italian Institute of Technology, Genoa, Italy. He has been developing nonlinear optical microscopes, including two-photon fluorescence, second harmonic generation, coherent anti-Stokes Raman scattering for various biomedical applications. He has more than 10 years of teaching experience in biophysics, biophotonics, photonics, physics, and bioinformatics. He has published more than 50 research articles in the peer-reviewed international journals and is a member of several national and international scientific societies and organizations including, the Optical Society (OSA) (Senior member), SPIE—the International Society for Optical Engineering (Senior member), Society of Biological Chemists (I) (Life Member), Environmental Mutagen Society of India (Life Member).

Gireesh Gangadharan is an Assistant Professor in the Department of Cell and Molecular Biology at Manipal School of Life Sciences, Manipal Academy of Higher Education (MAHE), Manipal, Karnataka, India. He is the recipient of Ramalingaswami Fellowship, a prestigious fellowship from the Department of Biotechnology, Government of India. Dr. Gangadharan received his Ph.D. in Neuroscience from Cochin University of Science and Technology (CUSAT), India. Subsequently, he did postdoctoral training at the Korea Institute of Science and Technology (KIST) and the Institute for Basic Science (IBS), South Korea, where he has made many critical findings on the neural mechanisms of behaviors at the integrated levels from genes to systems. His research interest is to understand the neural mechanism of animal behaviors such as exploration, anxiety, and memory. He is trying to understand how different brain circuits are controlling diverse behaviors, with emphasis on the network interaction between different brain regions.

Yury V. Kistenev is a Professor at the Tomsk State University (TSU), Russia. He received his Ph.D. in optics in 1987; doctoral in physics and mathematics in 1997. He is the author of more than 150 research articles and has written two book chapters. His current research interests include laser molecular imaging, laser spectroscopy, and machine learning.



Optical Coherence Tomography in Brain Gliomas Detection and Peritumoral White Matter State Evaluation

1

N. D. Gladkova, K. A. Achkasova, K. S. Yashin, E. B. Kiseleva, A. A. Moiseev, E. L. Bederina, S. S. Kuznetsov, I. A. Medyanik, L. Ya. Kravets, G. V. Gelikonov, and P. A. Shilyagin

Abstract

Optical coherence tomography (OCT) is a rapidly emerging visualization method providing real-time detailed information about the biological tissues structure without any contrast agents based on the backscattered light detection. In this chapter, we discuss the perspectives of application of OCT in brain glioma surgery. The reader can get acquainted with the problems arising in brain tumor surgery and the possibility of using OCT to solve them. The information about the types of OCT data collected in neurosurgery, approaches for their assessment as well as main features of OCT signal representative for different brain tissue types are presented in the chapter. In addition to the perspectives of using OCT for differentiating tumor and healthy brain tissues, we also demonstrate the possibility of using this technology to evaluate morphological features of white matter in the perifocal area of the tumor and talk about the prospects of using machine learning and artificial intelligence for classifying OCT images.

N. D. Gladkova (✉) · K. A. Achkasova · E. B. Kiseleva
Institute of Experimental Oncology and Biomedical Technologies, Privolzhsky Research Medical University, Nizhny Novgorod, Russia

K. S. Yashin · I. A. Medyanik · L. Y. Kravets
Department of Neurosurgery, Privolzhsky Research Medical University, Nizhny Novgorod, Russia

A. A. Moiseev · G. V. Gelikonov · P. A. Shilyagin
Institute of Applied Physics of the Russian Academy of Sciences, Nizhny Novgorod, Russia

E. L. Bederina · S. S. Kuznetsov
Department of Pathology, Privolzhsky Research Medical University, Nizhny Novgorod, Russia

Keywords

Optical coherence tomography · Attenuation coefficient · Brain · Glioma · Machine learning

1.1 Introduction

Malignant glial tumors represent the group of the widespread primary brain tumors and amount up to 63% of all astrocytic neoplasms [1]. The key feature of gliomas is their infiltrative growth into surrounding brain tissues, especially white matter, causing difficulties in tumor/non-tumorous tissues differentiating. This group of tumors is characterized by morphological and molecular heterogeneity, which is important to take into account for defining the medical prognosis in such patients. It is customary to divide astrocytic tumors into two groups based on the degree of invasion and the growth rate. The first group represents slow-growing tumors including pilocytic astrocytoma (Grade I) and diffuse astrocytoma (Grade II). Fast-growing tumors form the second group that includes anaplastic astrocytoma (Grade III) and glioblastoma (Grade IV) [2]. The attribution of tumor to the certain group is reflected in the patient's life expectancy. Thus, in the case of high-grade gliomas (Grade III–IV) the average life expectancy is 25 months for anaplastic astrocytoma and 14 months for glioblastoma [1]. If the low-grade glial tumors are concerned, the life expectancy varies from 61.1 to 90 months according to different studies [3]; however, it is necessary to take into account the possibility of malignant transformation that appears in approximately 45% of cases [4, 5].

Treatment of brain gliomas usually includes several stages, while the resection of the neoplasm plays an important role for achieving the positive outcome. First of all, it allows decreasing the level of intracranial pressure and the degree of neurological deficit due to removal of volume of tumorous tissue, stabilizing the patient's state. Moreover, it offers the possibility to establish the tumor phenotype that is essential for choosing the treatment strategy. The necessity for high-quality resection of gliomas is emphasized in a number of studies demonstrating a significant correlation between the volume of tumor tissue removed and the life expectancy of patients [6–10], especially when the low-grade astrocytomas are concerned as it allows reducing the risk of malignant transformation [3].

As it was already mentioned, the key prognostic factor for patients in glioma surgery is high-quality resection of brain neoplasm, that is, maximum removal of the tumorous tissue accompanied with minimum risk of functionally significant regions lesions [11–13]. However, the implementation of this task is associated with a number of difficulties, due to the impossibility of maximum removal of the tumor using a white-light microscope [8, 9, 14], which emphasizes the importance of developing additional methods for intraoperative differentiation of tumor and normal tissues.

Currently, intraoperative differentiation of brain tissues is performed using a number of approaches:

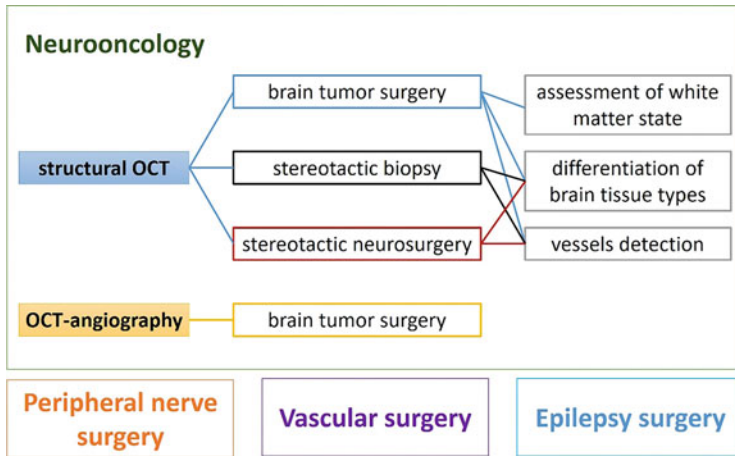


Fig. 1.1 Implementation of OCT in neurosurgery

- registration of tissue metabolism (fluorescence diagnostics, laser spectroscopy),
- administration of contrast agents and registration of their accumulation in the bloodstream of the tumor,
- registration of tissue density (ultrasound investigation).

The most effective intraoperative diagnostic methods during resection of brain neoplasms are intraoperative magnetic resonance imaging (iMRI) and fluorescence. However, these methods have several limitations. That way, a number of studies emphasize the low sensitivity of fluorescence for low-grade gliomas [15, 16]. The point is the subjectivity of assessment of fluorescence intensity performed by neurosurgeon what may cause preservation of tumor regions characterized by low fluorescence [17]. When iMRI is concerned, it is necessary to mention such limitations as high cost, impossibility of integration with a microscope, the need to use special surgical instruments and long learning curve [18].

The absence of an “ideal” intraoperative imaging technique contributes to continue the search for other effective methods, where optical coherence tomography (OCT) can be emphasized. This method is characterized by a number of significant advantages, including high resolution and no need to use contrast agents. Currently, intraoperative OCT imaging in neurosurgery is available in the form of a special microscope module [19, 20] or through usage of various optical probes [21, 22]. In addition, it is necessary to highlight the multimodality of OCT (polarization sensitivity, angiography, and elastography) and the possibility of using the method to solve several groups of problems in neurosurgery (Fig. 1.1).

Currently, OCT allows solving several problems in the field of neurooncology: (1) express biopsy and identification of the boundaries of tumor growth; (2) express biopsy and vessel identification during stereotactic biopsy. Moreover, OCT may be used for assessing the white matter damage in the perifocal area of the tumor. In

addition, the use of OCT for visualization of the nervous tissue is not limited to the tasks of neurooncology. For example, this technology can be successfully used to study the structural characteristics of peripheral nerves [23, 24]; however, the issues of application of OCT in vascular and functional neurosurgery have been underexplored.

1.2 Visual and Quantitative Evaluation of OCT Data Obtained in Brain Tumors

Usually, the obtained initial OCT images are characterized by insufficient clarity and ease of presentation of the information received, in particular, for people without experience in “reading” images, which leads to the need for further processing. Accordingly, initially OCT data is obtained as structural and angiographic pictures (Fig. 1.2a); further, their quantitative evaluation can be performed based on estimation of distributions of optical coefficients values (Fig. 1.2b). Visual representation of the results of quantitative assessment is usually carried out by using en-face color-coded maps (Fig. 1.2c).

Analysis of 2D structural images is a conventional method for OCT signal analysis. The first works demonstrating the promise of using this method for visualizing tumorous and non-tumorous brain tissues were published in the late 90s to early 2000s [25–27]. While the OCT technology developed, the two-dimensional images quality improved, as well as the resolution did, which made it possible to identify small structural details and determine the features of the OCT signal characteristic of a particular type of tissue. For example, if differentiation between tumor and normal white matter is concerned, OCT showed a high sensitivity (82–85%) and specificity (92–94%) [21].

Undoubtedly, the use of the visual method for the analysis of OCT images has a number of advantages and disadvantages. The main advantages of this approach include high speed of image acquisition, the possibility of quick interpretation by a surgeon, and the availability of use in the operating room both using an optical probe or as part of an operating microscope module [19, 21]. However, this method also has a number of limitations, including a relatively low contrast of OCT images, subjectivity of the surgeon’s assessment due to the need to master the technique of “reading” OCT images, passing the corresponding learning curve, as well as low diagnostic accuracy relative to other approaches.

Among the structural images that can be obtained by the OCT method, an important place is occupied by images of the microvasculature which is widely used in fundamental research in the field of oncology and neuroscience [28–31]. At the same time, the ability to visualize the microvasculature may be in demand in the surgical treatment of brain tumors.

Quantitative assessment of OCT data is considered more objective in comparison with visual evaluation of images and is performed by **optical coefficients estimation**. The most widespread optical coefficient being used for OCT data analysis is the attenuation coefficient [19, 32, 33], while if the device has functional extensions

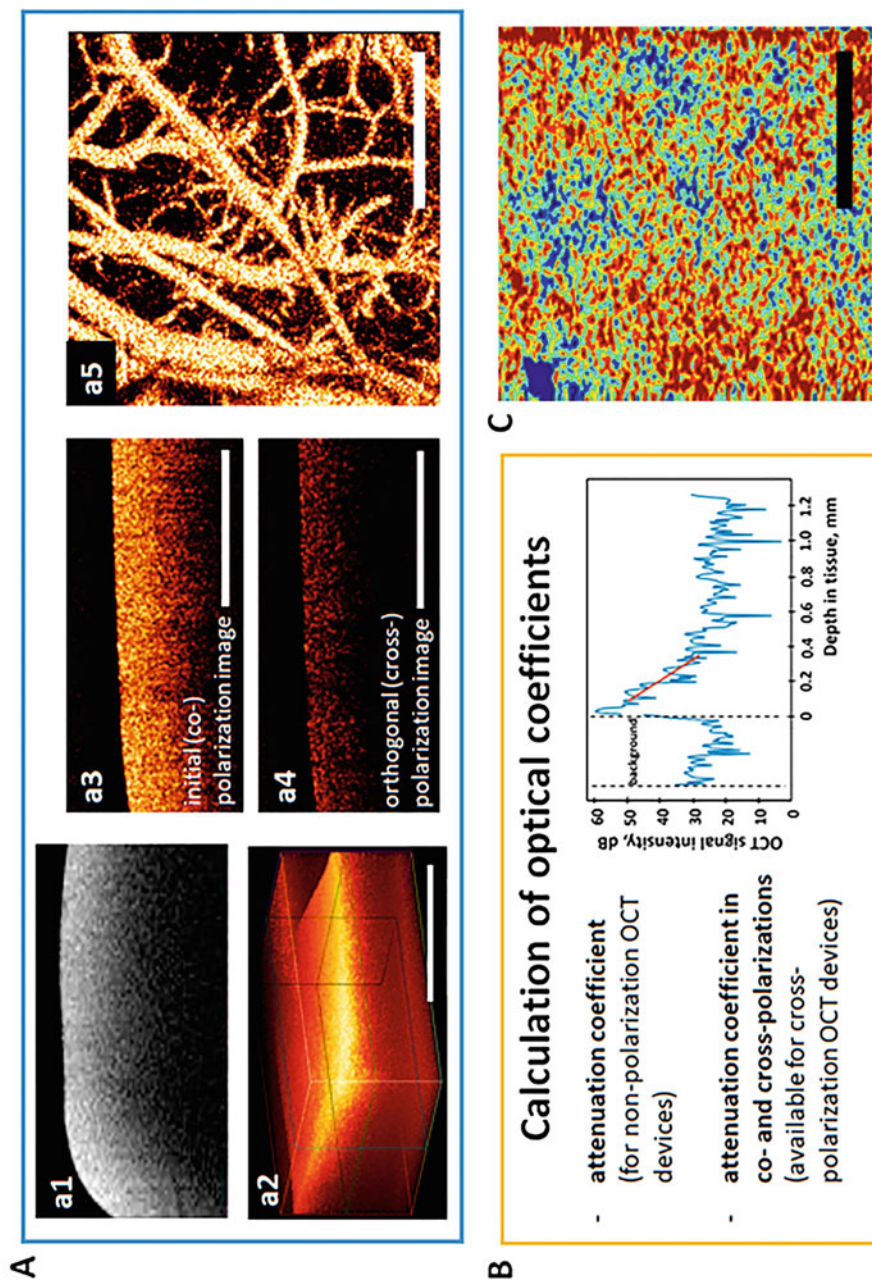


Fig. 1.2 Types of OCT data obtained in brain tumors: (a) initially obtained OCT data. a1—a4—structural OCT images; a1—2D image obtained with non-polarization OCT device, a2—3D OCT image, a3, a4—2D images in co- and cross-polarization obtained with cross-polarization OCT device, a5—2D

(e.g., polarization mode), it is possible to calculate other coefficients depending on the signal processing methods [34]. The use of threshold values of optical coefficients can increase the diagnostic accuracy of OCT for differentiation of the tumor and white matter up to 100% [32, 34]. Despite the high accuracy and objectivity of the approach, its use in the operating room looks unpromising due to the impossibility of assessing the homogeneity of the received signal and the unusual decision-making based on the “number” for the practicing surgeon.

The most illustrative and easy-to-understand way of presenting information is the construction of color-coded maps based on the distribution of optical coefficient values over the OCT image. This method allows combining the advantages of visual and quantitative approaches to image analysis: the convenience of assessing the resulting contrast image directly during the operation and the accuracy of the quantitative approach [32, 34].

Separately, it is necessary to mention angiographic images, which can be used to study the microvasculature of the cerebral cortex and various tumors. The use of this modality can be both fundamental in the study of pathological changes that occur in tumor tissue and applied. In particular, obtaining angiographic images can be used during tumor removal, since a number of studies have established significant differences in the microvasculature of these tissues [28, 35].

1.3 OCT Images of White Matter, Cortex, and Brain Tumors

To be able to use OCT in surgery of glial brain tumors or as a method of optical biopsy, differences in the optical signal from the main types of tissues: cortex, white matter, and tumor should be described. This is performed mostly using the example of cross-polarization images obtained by our group in several experiments [21, 28, 34]. At the same time, the features that are described for images in co-polarization are representative for traditional structural OCT images obtained in OCT devices that do not have polarization sensitivity.

Tumor tissue is characterized by low-intense and slowly attenuating OCT signal due to its heterogeneous structure and high cellular density (Fig. 1.3, a1–3, b1–3). It is important to distinguish between tumor tissue with and without areas of necrosis since the presence of necrosis significantly enhances the OCT signal. Tumor tissue without the areas of necrosis and hemorrhage is characterized by a low-intensity homogeneous OCT signal both in intensity and in the attenuation depth. At the same

Fig. 1.2 (continued) OCT angiographic picture; (b) quantitative analysis through calculation of optical coefficients; (c) construction of color-coded optical maps based on distribution of optical coefficients values. Scale bar—1 mm. (Adapted from: Giese et al. 2006, SPIE Digital Library (licensed under the Creative Commons Attribution 4.0 International License); Yashin et al. 2019, Nature Research (licensed under the Creative Commons Attribution 4.0 International License))

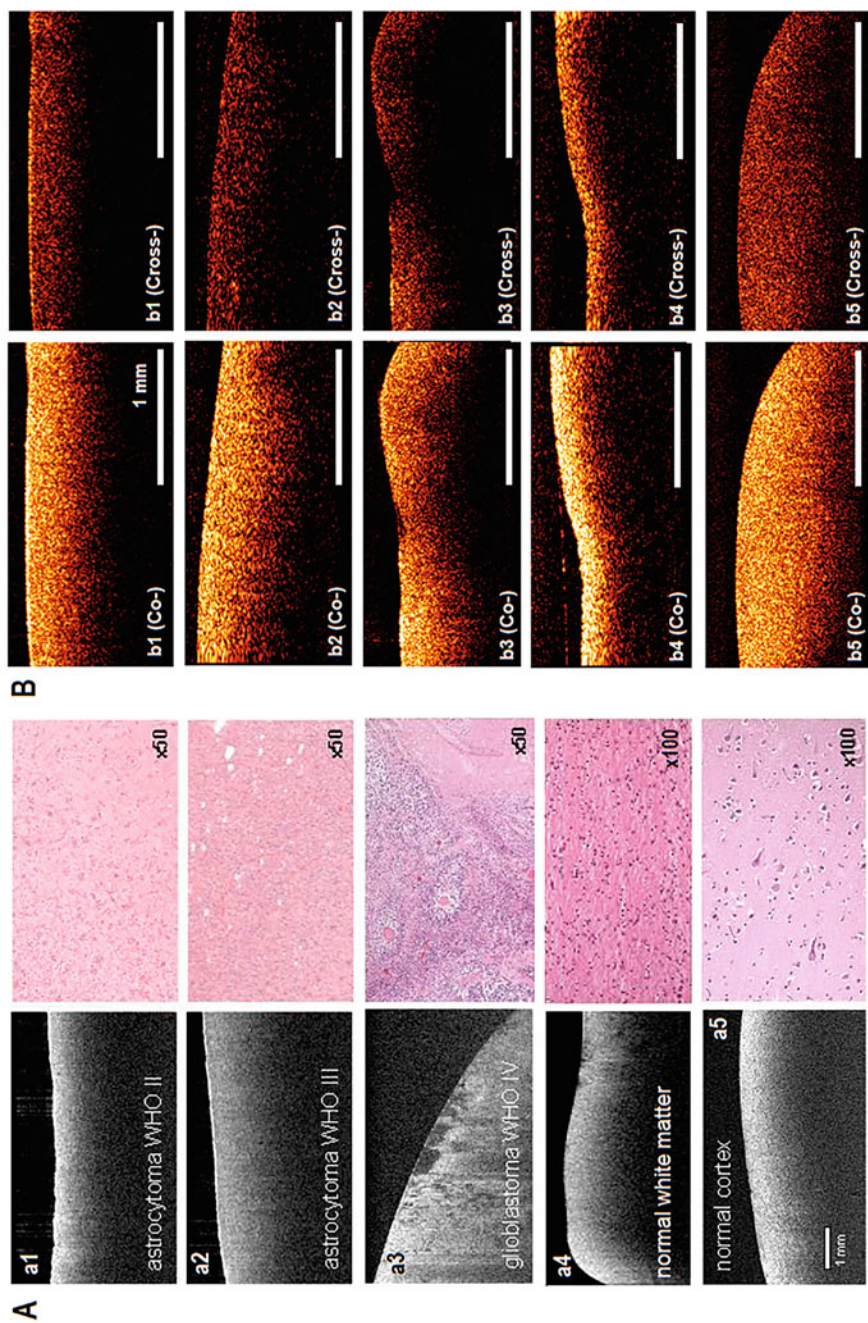


Fig. 1.3 Histology and ex vivo OCT images obtained with non-polarization OCT device (a) and cross-polarization OCT device (b) of astrocytoma Grade II (a1, b1), astrocytoma Grade III (a2, b2), glioblastoma Grade IV (a3, b3), normal white matter (a4, b4), and cortex (a5, b5). (Figure (a) is adapted from Giese et al. 2006, SPIE Digital Library (licensed under the Creative Commons Attribution 4.0 International License); Figure (b) is adapted with permission from Yashin et al. 2019, Frontiers Media SA)

time, the values of the attenuation coefficient are low, which is clearly visualized on optical maps, where the tumor tissue is characterized by color palette from azure to dark blue (Fig. 1.4, a1, a2, b1, b2). The presence of areas of necrosis increases the values of the attenuation coefficient. In such cases, the acquired OCT signal is inhomogeneous, both in intensity and in the attenuation depth, and areas that differ in color palette from a tumor without necrosis appear on the optical maps (Fig. 1.4, c1, c2). In addition, OCT allows the identification of a number of structural elements (e.g., microcysts), which can be used to differentiate various types of tumors (including low and high grade) (Fig. 1.3, a3).

White matter in OCT images is represented by a strip of a homogeneous intense signal on the tissue surface with its uniform attenuation with depth both in co- (Fig. 1.3, a4, b4) and cross-polarization (Fig. 1.3, b4). The results of the quantitative processing of the OCT signal demonstrate high values of the attenuation coefficient, which is reflected on the optical maps (Fig. 1.4, d1, d2) where the white matter is represented by completely different color palette in comparison with tumor. These features of the OCT signal are connected to the morphological characteristics of the white matter, namely, the presence of a large number of nerve fibers covered with the myelin sheath. Myelin is a set of layers of cell membranes of oligodendrocytes with high scattering properties. Moreover, myelin, apparently, is capable of changing the polarization properties of the probe radiation, and therefore is clearly visualized in cross-polarization.

The cortex in in vivo OCT images, in comparison with the white matter, has a less intense, heterogeneously and slowly attenuating OCT signal with the presence of a specific vertical striation, which disappears in ex vivo images (Fig. 1.3, a5, b5). The low intensity of the OCT signal in this situation is explained by the morphological features of cortical area. Thus, gray matter includes neurons, glial cells, neuropil (axons, dendrites, glial processes); the myelin fibers presented here do not have the dense packing observed in the white matter. The optical maps are characterized by the predominance of the same colors as for the tumor (Fig. 1.4, e1, e2). In this regard, despite the presence of certain OCT criteria for differential diagnosis, the difference between the cortex and the tumor can cause difficulties.

1.4 Identification of Tissue Type in Brain Gliomas Using OCT

1.4.1 Differentiation of Tumor and White Matter

As it was mentioned above, the differentiation of tumor tissue from normal white matter plays an extremely important role for the implementation of high-quality tumor resection, in particular, ensuring maximum removal of the tumor mass and avoiding complications associated with damage to the pathways. For the possibility of using OCT in clinical practice in order to solve this problem, it is necessary to establish distinct criteria for OCT images specific for a particular type of tissue.

Criteria for white matter and tumor differentiation based on visual assessment of two-dimensional OCT images were proposed in [21]. As a result of the study, the

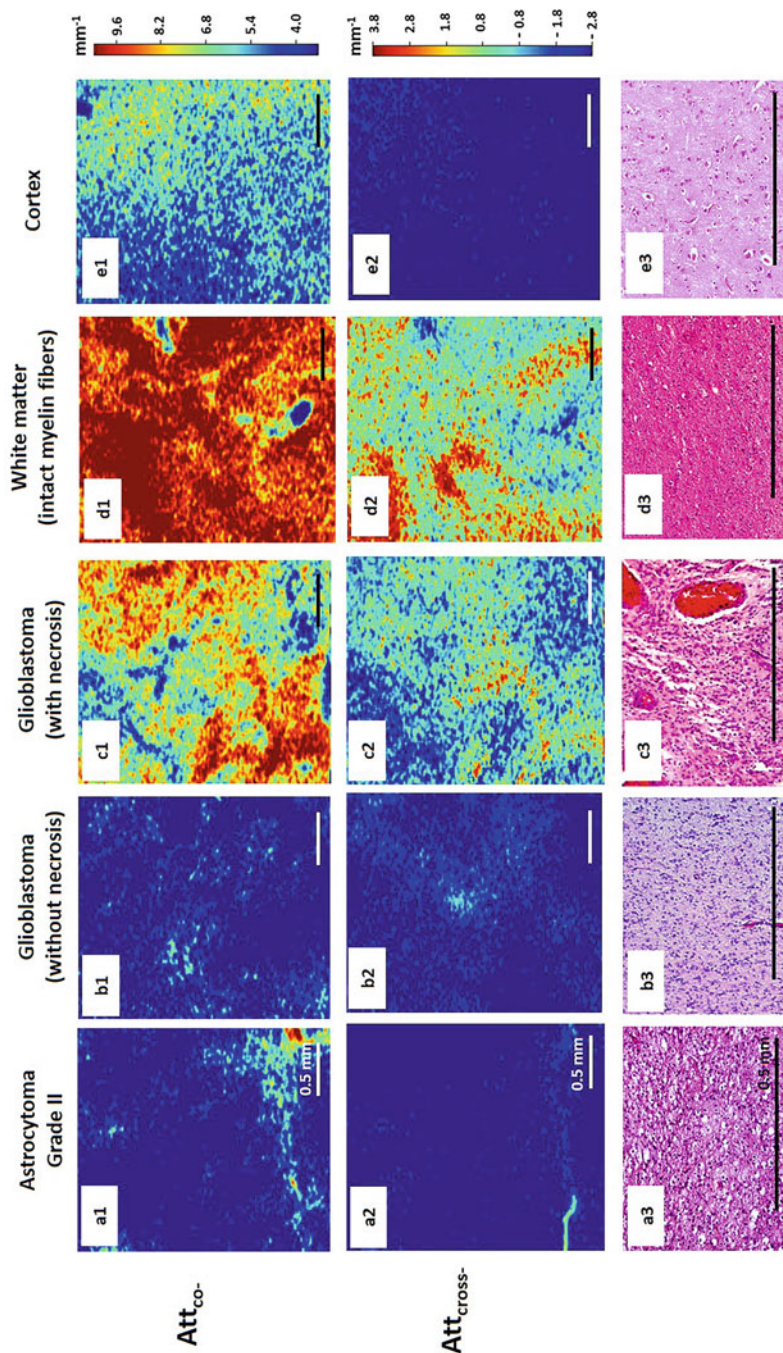


Fig. 1.4 Color-coded maps and corresponding histology of tumorous and normal brain tissues. Based on attenuation coefficient in co-polarization (a1–e1) and attenuation coefficient in cross-polarization (a2–e2) coefficients, en-face color-coded maps of astrocytoma Grade II (a1, a2), glioblastoma Grade IV with necrosis (b1, b2) and without necrosis (c1, c2), white matter (d1, d2), and cortex (e1, e2), corresponding to histology in HE (a3–e3) staining. (Adapted from Yashin et al. 2019, Nature Research (licensed under the Creative Commons Attribution 4.0 International License))

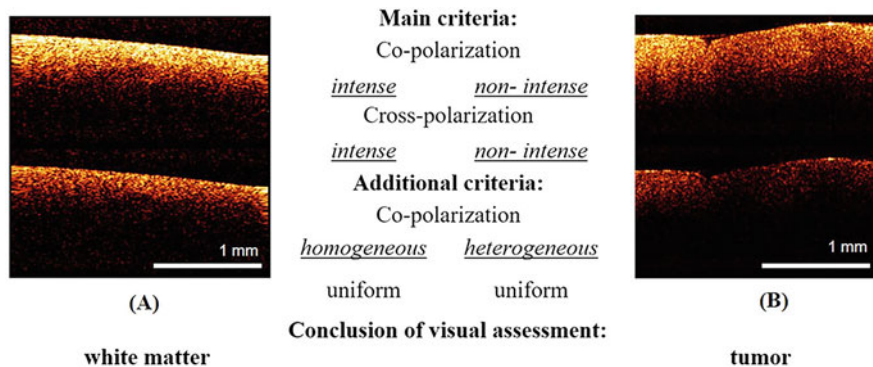


Fig. 1.5 Examples of images from the training set for the second test: (a)—white matter, (b)—tumor. The responder identifies tissue type using main criteria: white matter is characterized by high intense signal in co- and cross-polarization unlike low intensity signal of tumorous tissue. In the doubtful case, the additional criteria can be used. (Adapted with permission from Yashin et al. 2019, Frontiers Media SA)

criteria that are most important for the qualitative differentiation of various types of tumors and normal white matter were established. In this case, as the main criterion it was proposed to use the intensity of the OCT signal in both polarizations, while the homogeneity of the signal and the uniformity of signal attenuation along the lower boundary in the co-polarization were established as additional criteria (Fig. 1.5).

The use of optical coefficients makes it possible to achieve higher OCT diagnostic accuracy in the differentiation of tumors and white matter in comparison with qualitative processing of OCT images. Moreover, as it was mentioned above, color-coded maps allow better delineation between these tissue types due to more contrast and easy-to-read images. The use of the attenuation coefficient to differentiate between tumor tissue and normal white matter was first demonstrated by Kut et al. [32]. They obtained the values of the attenuation coefficient for a number of normal and tumor brain tissues: for normal white matter— $6.2 \pm 0.8 \text{ mm}^{-1}$; for high malignancy gliomas core— $3.9 \pm 1.6 \text{ mm}^{-1}$; in the infiltration zone— $7.1 \pm 1.0 \text{ mm}^{-1}$; for low malignancy gliomas core— $4.0 \pm 1.4 \text{ mm}^{-1}$; and in the infiltration zone— $2.7 \pm 1.0 \text{ mm}^{-1}$. At the same time, a threshold value of this coefficient of 5.5 mm^{-1} was proposed, where high values of specificity and sensitivity were obtained (100% and 92% for high-grade patients, 80% and 100% for low-grade patients, respectively). Color-coded maps, built based on the distribution of coefficient values, made it possible to visualize the areas of white matter, the tumor, and the border zone.

However, the values of the attenuation coefficients may vary in different studies, which, apparently, is due to the features of the OCT device used. Thus, in the study [34], the values of the attenuation coefficient for the brain tissue were obtained, which differ from those presented in the work of Kut et al. (Table 1.1). The proposed threshold values for tumor/white matter differentiation in this study were higher than in the study by Kut et al. (8.2 mm^{-1} for patients of all grades and 6.1 mm^{-1}

Table 1.1 Optical coefficients difference between tumorous and non-tumorous tissue types

		Coefficient Me [<i>Q</i> 1; <i>Q</i> 3] ^a	<i>p</i> (versus white matter) ^b	<i>p</i> (versus cortex) ^b
	Attenuation mm ⁻¹			
Normal tissue	White matter (<i>n</i> = 16)	8.5 [8.2; 9.3]	–	<0.0001
	Cortex (<i>n</i> = 16)	5.0 [3.2; 5.5]	<0.0001	–
Tumor subtype 1 (T1) without necrotic areas	Astrocytoma Grade I–III (<i>n</i> = 28)	3.0 [2.6; 3.5]	<0.0001	<0.0001
	Glioblastoma Grade IV without necrotic areas (<i>n</i> = 16)	3.15 [2.6; 4.2]	<0.0001	0.015
Tumor subtype 2 (T2) with necrotic areas	Glioblastoma Grade IV with necrotic areas (<i>n</i> = 28)	6.3 [5.4; 6.8]	<0.0001	<0.001
	Necrosis (<i>n</i> = 19)	7.5 [5.3; 7.7]	<0.001	<0.0001

Adapted from Yashin et al. (2019), Nature Research

^a Me [*Q*1; *Q*3]: Me—median; [*Q*1; *Q*3]—25th and 75th percentiles values, respectively

^b *U*-test Mann-Whitney

specifically for low-grade patients); however, sensitivity and specificity values are also reached almost 100% (sensitivity/specificity: 95.6%/81.3% for all grades and sensitivity/specificity: 100%/100%, respectively, for low-grade).

Thus, the use of this approach for the white matter/tumor delineation must necessarily pay attention to the features of the OCT device. Nevertheless, the first works that show the possibility of using this method in vivo in the operating room are published [36], which indicates the need to continue research in this area. Almasian et al. [36] extracted the attenuation coefficient from both glioma tissue and normal parenchyma of the brain during usual procedure of tumor resection and obtained the results that were in the range of previously reported values indicating the feasibility of this approach in brain gliomas surgery.

It is worth mentioning that OCT differentiation of the tumor and white matter can cause difficulties in the presence of areas of necrosis in the tumor structure, which is characterized by high scattering and therefore leads to a decrease in the diagnostic accuracy of the method (Table 1.1). Foci of necrosis can be found during removal of glioblastoma in its central region as a result of bipolar coagulation as well as during re-resection after radiation therapy. At the same time, the damage to myelinated fibers or edema may cause the decrease in the white matter scattering properties [37]. Such changes are characteristic of the peritumoral area of malignant astrocytomas.

Thus, OCT has a number of limitations, which, however, can be overcome with the combined use of methods of intraoperative diagnostics and assessment of the location of the tumor relative to functionally significant areas of the brain and its presumptive nature according to MRI data. Accordingly, the reduced diagnostic value of OCT will be observed in the following cases: (1) resection of glioblastoma with significant edema in the peritumoral zone; (2) resection of continued tumor

growth after combined treatment. As in the case of fluorescence diagnostics, severe bleeding in the area of the removed tumor leads to a significant decrease in the information content of OCT [19]. During OCT scanning, blood and bipolar coagulation areas should be removed from the scanned area.

Taking into account the possible variability of the obtained OCT images of the white matter, depending on the degree of destruction or the severity of edema, along with the use of the described criteria, it is advisable to collect OCT images of the white matter in the control area (no doubt) and then compare the received OCT images with it. In some cases, with a large spread of the tumor or in the case of continued growth of the formation after combined treatment, such an image is difficult to obtain. In this case, the previously indicated criteria can be used.

1.4.2 Differentiation of Tumor and Gray Matter

Currently, it is not possible to formulate clear criteria for the differentiation of the tumor and the cortex by analogy with the existing criteria for white matter. *Ex vivo* analysis of OCT images from the cortex and the tumor does not allow distinguishing significant differences between them both in visual assessment and using optical coefficients with building optical maps (Figs. 1.3 and 1.4).

At the same time, *in vivo* OCT images of the cerebral cortex, in addition to the inhomogeneous slowly attenuating signal, have a vertical striation due to the presence of blood vessels. These signs can be considered specific to the normal cortex. In the case of microstructural changes in the cortex (e.g., gliosis or post-radiation changes), the obtained OCT signal changes: in co-polarization it becomes heterogeneous with the presence of areas of higher intensity, “vascular shadows” disappear, and in cross-polarization, it becomes heterogeneous with the presence of areas of high-intensity signal.

The tactics of OCT scanning to determine the border of tumor growth on the cortex depends on the presence of visible invasion of the cortex by the tumor: (1) if it is present, scanning is performed from the tumor towards the visually unchanged cortex until an OCT signal characteristic of the normal cortex appears; (2) in the case of its absence—OCT examination is carried out from the area of tumor invasion of the cortex according to the data of preoperative MRI and the corresponding data of neuronavigation.

1.5 OCT for Stereotactic Biopsy

Despite the fact that stereotactic biopsy is a standard method in the diagnosis of glial brain tumors and intracerebral lymphomas, during the procedure it is possible to obtain diagnostically uninformative samples (which amount can reach up to 24% in the series described [38–40]). In this case, it becomes necessary to carry out a second operation. An increase in the accuracy of the procedure is currently achieved by obtaining a series of biopsies (thereby increasing the number of samples) [41, 42]

and conducting an intraoperative express biopsy by a pathologist [40, 41, 43]. However, the described techniques have a number of significant disadvantages: (1) intraoperative histopathological examination increases the time of the procedure, requires additional financial costs and is not always available in the clinic [40, 44, 45]; (2) obtaining a series of biopsies increases the risk of intracerebral hemorrhage, which is observed in 0.3–59.8% of cases [39, 46, 47] and is associated with a high incidence of complications (0–16.1%) [40, 41, 48, 49] and deaths (3.9%) [39, 40, 48, 49].

Both of these problems—visualization of blood vessels in the biopsy area and differentiation of tissue type—can be solved by OCT. Express optical biopsy performed by OCT will escape the necessity to carry out intraoperative histopathological examination of tissue and reduce the risk of development of intracerebral hemorrhages. Thus, OCT can increase the accuracy and safety of stereotaxic biopsy; minimize the risks of developing neurological deficit and death in the postoperative period.

The OCT probe can be integrated into a standard biopsy needle (Fig. 1.6a, d, f) to solve a number of problems: monitoring the movement of the needle towards the target (Fig. 1.6a), detecting blood vessels in order to prevent bleeding (Fig. 1.6a–c), as well as performing direct analysis of the tissue in the biopsy area (Fig. 1.6g, h).

A similar probe was proposed by a team of scientists led by Professor Robert McLaughlin from The University of Adelaide (Australia) [50–53]. However, the authors consider the use of OCT only to detect vessels in the area of sampling (Fig. 1.6a).

1.6 Determination of Myelination State of White Matter by OCT

The invasive nature of the growth of glial tumors is manifested in the penetration of tumor cells into the surrounding tissue along the pathways (tracts) of the white matter, meninges, and blood vessels [54, 55]. When a tumor develops and grows near the nerve tracts, edema, displacement of myelin fibers and their destruction are observed [56], which leads to functional disorders and, ultimately, to the non-viability of this white matter area. Accordingly, in order to perform a better tumor resection, it is necessary to remove the damaged non-viable white matter infiltrated by tumor cells without harming healthy pathways.

The only method of intravital assessment of the structure of the pathways is currently diffusion tensor MRI (DT-MRI). This technology makes it possible to quantitatively and qualitatively assess the direction of diffusion of water molecules in the human brain by calculating the fractional anisotropy coefficient and the average diffusion coefficient, as well as to perform three-dimensional reconstruction of commissural, associative, and projection pathways [57, 58]. DT-MRI is used in the preoperative period for planning the surgery and can be used during surgery for neuronavigation. However, this method has a number of limitations, such as insufficient resolution and the impossibility of assessing the state of the white matter in a

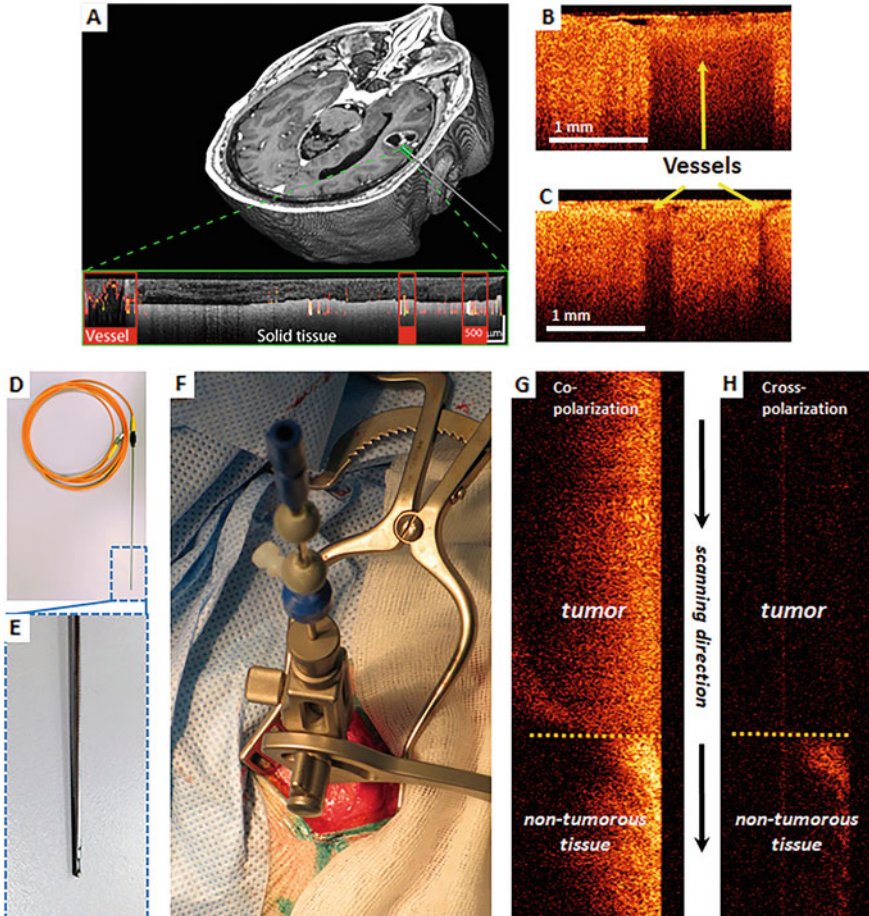


Fig. 1.6 The OCT probes integrated into a standard biopsy needle (**a**, **d**, **e**, **f**) that may be used for brain vessels identification (**a–c**) or direct analysis of the tissue in the biopsy area (**g**, **h**). (Figure **a**) is adapted from Ramakonar et al. 2018, American Association for the Advancement of Science (licensed under the Creative Commons Attribution 4.0 International License)

specific area of interest to the neurosurgeon since due to changes in intracranial pressure during tumor resection, brain structures can be displaced. Thus, it is necessary to develop a method for intraoperative visualization of the white matter to be able to assess its state in real time.

The white matter of the brain has a multicomponent structure, the main elements of which (about 60%) are nerve fibers [59, 60]. Most of the nerve fibers (70–95% of all fibers) are myelinated [61], which means that they are covered with a specific myelin sheath, which increases the speed of nerve impulse conduction [62]. Myelin is a two-layer membrane structure formed by the process of an oligodendrocyte that

is repeatedly wounded around the axonal process of a neuron. This sheath is characterized by a relatively low water content (about 40%), being rich in lipids and proteins [63]. In studies of the attenuation of the OCT signal in brain tissues, it was found that the degree of signal attenuation is characterized by inverse correlation with the water content, while structures with a lower water content are characterized by a rapid signal attenuation in OCT images [37, 64]. Thus, taking into account all of the above, it can be assumed that the main structural component that affects the attenuation of the OCT signal is the myelin sheath. Accordingly, based on the recorded changes in the features of the OCT signal, it is possible to assess the preservation of myelinated fibers, as well as their arrangement in the region of interest.

As mentioned above, structural OCT images from intact white matter in both polarizations are characterized by the presence of a uniform high-intensity signal rapidly attenuating in depth (Fig. 1.7, 1b, 1c). When the state of myelination of fibers changes due to their destruction in the peritumoral zone (Fig. 1.7, 2b, 2c), the

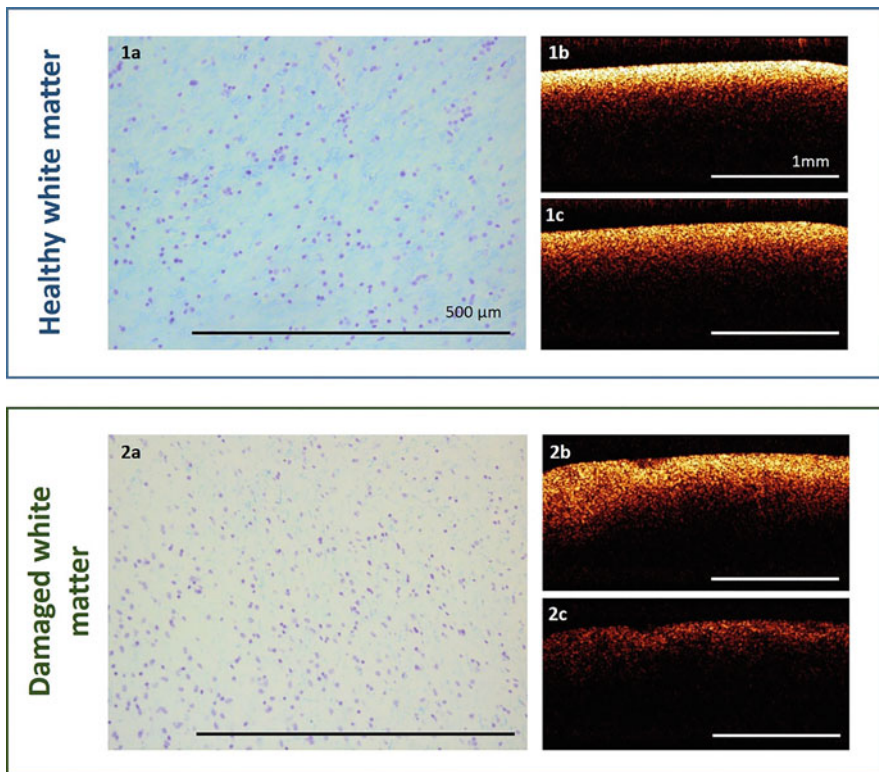


Fig. 1.7 Structural OCT images of white matter in co- (1b, 2b) and cross-polarizations (1c, 2c) with the corresponding histology in Luxol fast blue with cresyl violet (1a, 2a). Healthy white matter is represented by a narrow strip of uniform high-intensity signal rapidly attenuating with depth. Damaged white matter in the peritumoral area is characterized by severe destruction of myelin fibers that causes low intensity of OCT signal in both polarizations, its heterogeneity and non-uniformity of attenuation

features of the received OCT signal change significantly. At the same time, there is a decrease in the signal intensity in both polarizations, its heterogeneity and non-uniformity of attenuation in depth. Thus, in terms of visual characteristics, structural OCT images of damaged white matter are similar to images obtained from tumor tissue.

However, as mentioned above, visual assessment of OCT data is subjective and depends on the existing experience of “reading” two-dimensional OCT images. A more objective assessment of the degree of myelination of white matter fibers can be performed by calculating a number of optical coefficients based on three-dimensional OCT data. The use of quantitative processing of OCT images demonstrates a statistically significant difference between intact and damaged peritumoral white matter in the values of the signal attenuation coefficient in co- and cross-polarizations ($p > 0.0001$), while the presence of damaged myelin fibers manifests itself in a decrease in the values of these coefficients. The building of optical maps based on the calculation of optical coefficients also allows noticing a significant difference in images obtained from damaged and intact white matter (Fig. 1.8).

1.7 Artificial Intelligence and Machine Learning Application for OCT Images Classification

Recently, the use of machine learning and artificial intelligence methods has been actively developing for the classification of the received OCT images in order to obtain objective information about the type of tissue in the studied area in real time. Since research in this area is still at an early stage, there is a need for works demonstrating the methodological part of the selection of the necessary images, their histological verification and quantitative processing [65], for further software training. These works play an important role, demonstrating the possibility of using the classifier algorithm directly during the operation.

With regard to visualization of brain tissue, works that demonstrate the methodological part of a set of images, their processing and histological assessment [65] for subsequent use in training the classifier algorithm have been published, which can subsequently be used for navigation directly during tumor resection.

Juarez-Chambi et al. in 2019 [22] published the work where they demonstrated the application of artificial intelligence for automatic in situ detection of glioma infiltration in real time. At the same time, a fundamentally different approach was demonstrated, based not on the attenuation coefficient estimation, which requires a high resolution of the OCT device and the use of calibration procedures, but on a modeling approach to parametrize the information encoded in the shape of each depth-dependent OCT intensity signal. This algorithm allowed precise differentiation of tissue heavily infiltrated with tumor cells with high sensitivity (>90%) and specificity (>82%). At the same time, the user is presented with a three-dimensional color-coded map of the region of interest, which allows real-time neurosurgical guidance.

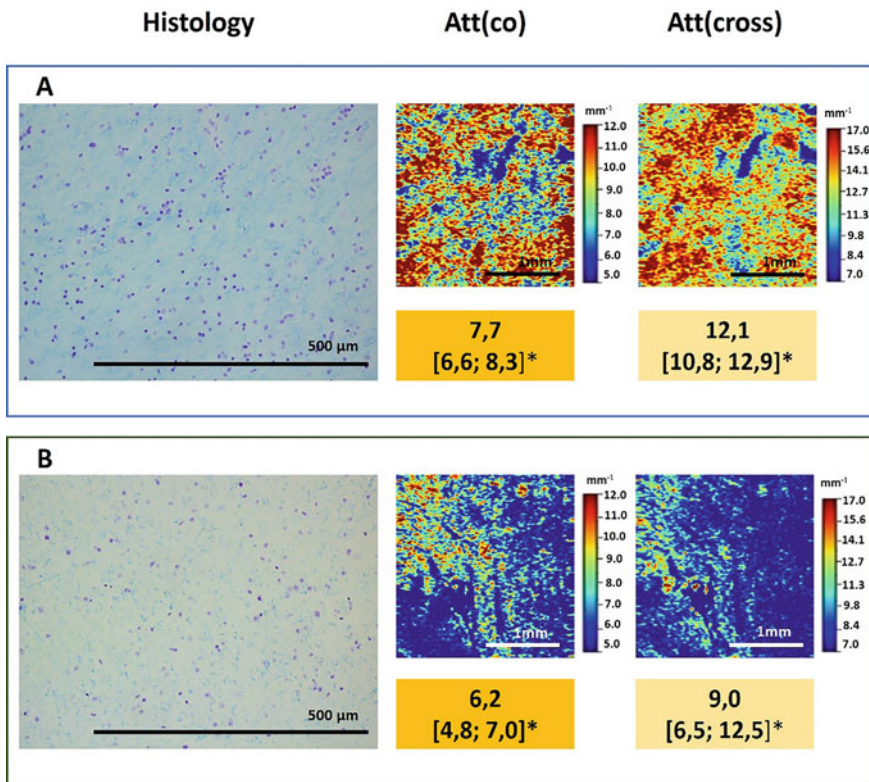


Fig. 1.8 En-face color-coded maps and values for attenuation coefficient in co-polarization (Att (co)), attenuation coefficient in cross-polarization (Att(cross)) for healthy (a) and damaged (b) white matter. *Me [Q1; Q3]: Me—median value; Q1 and Q3 are the values of the 25th and 75th percentile of the distribution

In addition, promising results have been shown in the application of machine learning to differentiate tumor and necrosis from normal brain tissue [66]. In this study, B-scan analysis was applied using principal component analysis (PCA) and support vector machines (SVM), with the diagnostic accuracy of this method being 95.75% and 99.10% for differentiating tumor and normal brain tissue and necrosis and brain tissue, respectively.

1.8 Conclusions

OCT allows multimodal assessment of brain tissue; however, of the currently available functional extensions, the modes of polarization-sensitive (and cross-polarization) OCT and OCT angiography are the best studied. This method has demonstrated high diagnostic accuracy for tumor and white matter differentiation

using the criteria for visual assessment of OCT images and using methods of quantitative analysis of OCT data.

OCT allows solving several problems simultaneously (determining the type of tissue and the presence of a blood vessel in the scanned area) and can be used in various neurosurgical procedures (removing a tumor or performing a stereotactic biopsy).

The introduction into clinical practice of the latest modifications of OCT with the creation of software with automatic determination of optical coefficients will significantly improve tissue visualization and make it possible to differentiate the tumor and white matter using quantitative criteria. In addition, the ability to visualize the microvasculature will make it possible to assess the degree of microvascular proliferation, which may indirectly indicate the degree of tumor malignancy.

For the widespread introduction of OCT into neurosurgical practice, it is necessary to conduct additional studies in order to determine algorithms for verifying the boundaries of tumor growth with the simultaneous use of OCT and existing methods of intraoperative diagnostics (fluorescence diagnostics, neuronavigation, ultrasound). It is also necessary to conduct translational studies to identify the possibilities of other OCT modalities in the field of neurosurgery.

Acknowledgments The development of an approach for quantitative assessment of CP OCT data was supported by the Russian Foundation for Basic Research, grant No. 18-29-01049_mk.

References

1. Crocetti E, Trama A, Stiller C et al (2012) Epidemiology of glial and non-glial brain tumours in Europe. *Eur J Cancer* 48(10):1532–1542. <https://doi.org/10.1016/j.ejca.2011.12.013>
2. Louis DN, Perry A, Reifenberger G et al (2016) The 2016 World Health Organization classification of tumors of the central nervous system: a summary. *Acta Neuropathol* 131(6):803–820. <https://doi.org/10.1007/s00401-016-1545-1>
3. Hervey-Jumper SL, Berger MS (2016) Maximizing safe resection of low- and high-grade glioma. *J Neuro-Oncol* 130(2):269–282. <https://doi.org/10.1007/s11060-016-2110-4>
4. Smith JS, Chang EF, Lamborn KR et al (2008) Role of extent of resection in the long-term outcome of low-grade hemispheric gliomas. *J Clin Oncol* 26(8):1338–1345. <https://doi.org/10.1200/JCO.2007.13.9337>
5. Snyder LA, Wolf AB, Oppenlander ME et al (2014) The impact of extent of resection on malignant transformation of pure oligodendrogliomas. *J Neurosurg* 120(2):309–314. <https://doi.org/10.3171/2013.10.JNS13368>
6. Sanai N, Berger MS (2008) Glioma extent of resection and its impact on patient outcome. *Neurosurgery* 62(4):753–764; discussion 264–266. <https://doi.org/10.1227/01.neu.0000318159.21731.cf>
7. Sanai N, Polley MY, McDermott MW et al (2011) An extent of resection threshold for newly diagnosed glioblastomas. *J Neurosurg* 115(1):3–8. <https://doi.org/10.3171/2011.2.jns10998>
8. Stummer W, Reulen HJ, Meinel T et al (2008) Extent of resection and survival in glioblastoma multiforme: identification of and adjustment for bias. *Neurosurgery* 62(3):564–576; discussion 564–576. <https://doi.org/10.1227/01.neu.0000317304.31579.17>
9. McGirt MJ, Chaichana KL, Gathinji M et al (2009) Independent association of extent of resection with survival in patients with malignant brain astrocytoma. *J Neurosurg* 110(1):156–162. <https://doi.org/10.3171/2008.4.17536>

10. Kuhnt D, Becker A, Ganslandt O et al (2011) Correlation of the extent of tumor volume resection and patient survival in surgery of glioblastoma multiforme with high-field intraoperative MRI guidance. *Neuro-Oncology* 13(12):1339–1348. <https://doi.org/10.1093/neuonc/nor133>
11. Almeida JP, Chaichana KL, Rincon-Torroella J et al (2014) The value of extent of resection of glioblastomas: clinical evidence and current approach. *Curr Neurol Neurosci Rep* 15(2):517. <https://doi.org/10.1007/s11910-014-0517-x>
12. Anton K, Baehring JM, Mayer T (2012) Glioblastoma multiforme: overview of current treatment and future perspectives. *Hematol Oncol Clin North Am* 26(4):825–853. <https://doi.org/10.1016/j.hoc.2012.04.006>
13. Wolbers JG (2014) Novel strategies in glioblastoma surgery aim at safe, supra-maximum resection in conjunction with local therapies. *Chin J Cancer* 33(1):8–15. <https://doi.org/10.5732/cjc.013.10219>
14. Colditz MJ, Jeffree RL (2012) Aminolevulinic acid (ALA)-protoporphyrin IX fluorescence guided tumour resection. Part 1: clinical, radiological and pathological studies. *J Clin Neurosci* 19(11):1471–1474. <https://doi.org/10.1016/j.jocn.2012.03.009>
15. Diez Valle R, Tejada Solis S, Idoate Gastarena MA et al (2011) Surgery guided by 5-aminolevulinic fluorescence in glioblastoma: volumetric analysis of extent of resection in single-center experience. *J Neuro-Oncol* 102(1):105–113. <https://doi.org/10.1007/s11060-010-0296-4>
16. Roberts DW, Valdés PA, Harris BT et al (2011) Coregistered fluorescence-enhanced tumor resection of malignant glioma: relationships between delta-aminolevulinic acid-induced protoporphyrin IX fluorescence, magnetic resonance imaging enhancement, and neuropathological parameters. Clinical article. *J Neurosurg* 114(3):595–603. <https://doi.org/10.3171/2010.2.JNS091322>
17. Valdes PA, Kim A, Brantsch M et al (2011) Delta-aminolevulinic acid-induced protoporphyrin IX concentration correlates with histopathologic markers of malignancy in human gliomas: the need for quantitative fluorescence-guided resection to identify regions of increasing malignancy. *Neuro-Oncology* 13(8):846–856. <https://doi.org/10.1093/neuonc/nor086>
18. Raheja A, Tandon V, Suri A et al (2015) Initial experience of using high field strength intraoperative MRI for neurosurgical procedures. *J Clin Neurosci* 22(8):1326–1331. <https://doi.org/10.1016/j.jocn.2015.02.027>
19. Bohringer HJ, Lankenau E, Stellmacher F et al (2009) Imaging of human brain tumor tissue by near-infrared laser coherence tomography. *Acta Neurochir (Wien)* 151(5):507–517; discussion 517. <https://doi.org/10.1007/s00701-009-0248-y>
20. Hartmann K, Stein KP, Neyazi B et al (2021) Optical coherence tomography of cranial dura mater: microstructural visualization in vivo. *Clin Neurol Neurosurg* 200:106370. <https://doi.org/10.1016/j.clineuro.2020.106370>
21. Yashin KS, Kiseleva EB, Gubarkova EV et al (2019) Cross-polarization optical coherence tomography for brain tumor imaging. *Front Oncol* 9:201. <https://doi.org/10.3389/fonc.2019.00201>
22. Juarez-Chambi RM, Kut C, Rico-Jimenez JJ et al (2019) AI-assisted in situ detection of human glioma infiltration using a novel computational method for optical coherence tomography. *Clin Cancer Res* 25(21):6329–6338. <https://doi.org/10.1158/1078-0432.CCR-19-0854>
23. Henry FP, Wang Y, Rodriguez CLR et al (2015) In vivo optical microscopy of peripheral nerve myelination with polarization sensitive-optical coherence tomography. *J Biomed Opt* 20(4):046002. <https://doi.org/10.1117/1.JBO.20.4.046002>
24. Yoon Y, Jeon SH, Park YH et al (2016) Visualization of prostatic nerves by polarization-sensitive optical coherence tomography. *Biomed Opt Express* 7(9):3170–3183. <https://doi.org/10.1364/BOE.7.003170>
25. Boppart SA, Brezinski ME, Pitris C et al (1998) Optical coherence tomography for neurosurgical imaging of human intracortical melanoma. *Neurosurgery* 43(4):834–841. <https://doi.org/10.1097/00006123-199810000-00068>

26. Bizheva K, Unterhuber A, Hermann B et al (2005) Imaging ex vivo healthy and pathological human brain tissue with ultra-high-resolution optical coherence tomography. *J Biomed Opt* 10(1):11006. <https://doi.org/10.1117/1.1851513>
27. Giese A, Böhringer HJ, Leppert J et al (2006) Non-invasive intraoperative optical coherence tomography of the resection cavity during surgery of intrinsic brain tumors. In: *Proceedings of SPIE*, vol 6078, Photonic therapeutics and diagnostics II, p 60782Z. <https://doi.org/10.1117/12.674436>
28. Yashin KS, Kiseleva EB, Gubarkova EV et al (2017) Multimodal optical coherence tomography for in vivo imaging of brain tissue structure and microvascular network at glioblastoma. In: *Proceedings of SPIE*, vol 10050, Clinical and translational neurophotonics, p 100500Z. <https://doi.org/10.1117/12.2252286>
29. Leitgeb RA, Werkmeister RM, Blatter C et al (2014) Doppler optical coherence tomography. *Prog Retin Eye Res* 41(100):26–43. <https://doi.org/10.1016/j.preteyeres.2014.03.004>
30. Park K, You J, Du C et al (2015) Cranial window implantation on mouse cortex to study microvascular change induced by cocaine. *Quant Imaging Med Surg* 5(1):97–107. <https://doi.org/10.3978/j.issn.2223-4292.2014.11.31>
31. Zhang K, Huang Y, Pradilla G et al (2011) Real-time intraoperative full-range complex FD-OCT guided cerebral blood vessel identification and brain tumor resection in neurosurgery. In: *Proceedings of SPIE*, vol 7883, Photonic therapeutics and diagnostics VII, p 78833Y. <https://doi.org/10.1117/12.874190>
32. Kut C, Chaichana KL, Xi J et al (2015) Detection of human brain cancer infiltration ex vivo and in vivo using quantitative optical coherence tomography. *Sci Transl Med* 7(292):292ra100. <https://doi.org/10.1126/scitranslmed.3010611>
33. Yuan W, Kut C, Liang W et al (2017) Robust and fast characterization of OCT-based optical attenuation using a novel frequency-domain algorithm for brain cancer detection. *Sci Rep* 7: 44909. <https://doi.org/10.1038/srep44909>
34. Yashin KS, Kiseleva EB, Moiseev AA et al (2019) Quantitative nontumorous and tumorous human brain tissue assessment using microstructural co- and cross-polarized optical coherence tomography. *Sci Rep* 9:2024. <https://doi.org/10.1038/s41598-019-38493-y>
35. You J, Pan C, Park K et al (2020) In vivo detection of tumor boundary using ultrahigh-resolution optical coherence angiography and fluorescence imaging. *J Biophotonics* 13(3): e201960091. <https://doi.org/10.1002/jbio.201960091>
36. Almasian M, Wilk LS, Bloemen PR et al (2019) Pilot feasibility study of in vivo intraoperative quantitative optical coherence tomography of human brain tissue during glioma resection. *J Biophotonics* 12(10):e201900037. <https://doi.org/10.1002/jbio.201900037>
37. Rodriguez CL, Szu JI, Eberle MM et al (2014) Decreased light attenuation in cerebral cortex during cerebral edema detected using optical coherence tomography. *Neurophotonics* 1(2): 025004. <https://doi.org/10.1117/1.NPh.1.2.025004>
38. Zoeller GK, Benveniste RJ, Landy H et al (2009) Outcomes and management strategies after nondiagnostic stereotactic biopsies of brain lesions. *Stereotact Funct Neurosurg* 87(3):174–181. <https://doi.org/10.1159/000222661>
39. Dammers R, Haitzma IK, Schouten JW et al (2008) Safety and efficacy of frameless and frame-based intracranial biopsy techniques. *Acta Neurochir (Wien)* 150(1):23–29. <https://doi.org/10.1007/s00701-007-1473-x>
40. Dammers R, Schouten JW, Haitzma IK et al (2010) Towards improving the safety and diagnostic yield of stereotactic biopsy in a single centre. *Acta Neurochir (Wien)* 152(11): 1915–1921. <https://doi.org/10.1007/s00701-010-0752-0>
41. Tilgner J, Herr M, Ostertag C et al (2005) Validation of intraoperative diagnoses using smear preparations from stereotactic brain biopsies: intraoperative versus final diagnosis—influence of clinical factors. *Neurosurgery* 56(2):257–265; discussion 257–265. <https://doi.org/10.1227/01.neu.0000148899.39020.87>
42. Woodworth G, McGirt M, Samdani A et al (2005) Accuracy of frameless and frame-based image-guided stereotactic brain biopsy in the diagnosis of glioma: comparison of biopsy and

- open resection specimen. *Neurol Res* 27(4):358–362. <https://doi.org/10.1179/016164105X40057>
43. Heper AO, Erden E, Savas A et al (2005) An analysis of stereotactic biopsy of brain tumors and nonneoplastic lesions: a prospective clinicopathologic study. *Surg Neurol* 64(Suppl 2):S82–S88. <https://doi.org/10.1016/j.surmeu.2005.07.055>
 44. Gralla J, Nimsky C, Buchfelder M et al (2003) Frameless stereotactic brain biopsy procedures using the Stealth Station: indications, accuracy and results. *Zentralbl Neurochir* 64(4):166–170. <https://doi.org/10.1055/s-2003-44620>
 45. Shooman D, Belli A, Grundy PL (2010) Image-guided frameless stereotactic biopsy without intraoperative neuropathologic examination. *J Neurosurg* 113(2):170–178. <https://doi.org/10.3171/2009.12.JNS09573>
 46. Grossman R, Sadetzki S, Spiegelmann R et al (2005) Haemorrhagic complications and the incidence of asymptomatic bleeding associated with stereotactic brain biopsies. *Acta Neurochir (Wien)* 147(6):627–631; discussion 631. <https://doi.org/10.1007/s00701-005-0495-5>
 47. Field M, Witham TF, Flickinger JC et al (2001) Comprehensive assessment of hemorrhage risks and outcomes after stereotactic brain biopsy. *J Neurosurg* 94(4):545–551. <https://doi.org/10.3171/jns.2001.94.4.0545>
 48. Dorward NL, Paleologos TS, Alberti O et al (2002) The advantages of frameless stereotactic biopsy over frame-based biopsy. *Br J Neurosurg* 16(2):110–118. <https://doi.org/10.1080/02688690220131705>
 49. Lunsford LD, Niranjana A, Khan AA et al (2008) Establishing a benchmark for complications using frame-based stereotactic surgery. *Stereotact Funct Neurosurg* 86(5):278–287. <https://doi.org/10.1159/000147636>
 50. Lorensen D, Yang X, Kirk RW et al (2011) Ultrathin side-viewing needle probe for optical coherence tomography. *Opt Lett* 36(19):3894–3896. <https://doi.org/10.1364/OL.36.003894>
 51. Scolari L, Lorensen D, McLaughlin RA et al (2012) High-sensitivity anastigmatic imaging needle for optical coherence tomography. *Opt Lett* 37(24):5247–5249. <https://doi.org/10.1364/OL.37.005247>
 52. McLaughlin RA, Quirk BC, Curatolo A et al (2012) Imaging of breast cancer with optical coherence tomography needle probes: feasibility and initial results. *IEEE J Sel Top Quant Electron* 18(3):1184–1191. <https://doi.org/10.1109/JSTQE.2011.2166757>
 53. Ramakonar H, Quirk BC, Kirk RW et al (2018) Intraoperative detection of blood vessels with an imaging needle during neurosurgery in humans. *Sci Adv* 4(12):eaav4992. <https://doi.org/10.1126/sciadv.aav4992>
 54. Cuddapah VA, Robel S, Watkins S et al (2014) A neurocentric perspective on glioma invasion. *Nat Rev Neurosci* 15(7):455–465. <https://doi.org/10.1038/nrn3765>
 55. Preusser M, Haberler C, Hainfellner JA (2006) Malignant glioma: neuropathology and neurobiology. *Wien Med Wochenschr* 156(11–12):332–337. <https://doi.org/10.1007/s10354-006-0304-7>
 56. Witwer BP, Mofhtakhar R, Hasan KM et al (2002) Diffusion-tensor imaging of white matter tracts in patients with cerebral neoplasm. *J Neurosurg* 97(3):568–575. <https://doi.org/10.3171/jns.2002.97.3.0568>
 57. Potapov AA, Goryainov SA, Zhukov VY et al (2014) The long-associative pathway of the white matter: modern view from the perspective of neuroscience. *Zh Vopr Neirokhir Im N N Burdenko* 78(5):66–77; discussion 77
 58. Mori S, Frederiksen K, van Zijl PCM et al (2002) Brain white matter anatomy of tumor patients evaluated with diffusion tensor imaging. *Ann Neurol* 51(3):377–380. <https://doi.org/10.1002/ana.10137>
 59. Mottershead J, Schmierer K, Clemence M et al (2003) High field MRI correlates of myelin content and axonal density in multiple sclerosis. *J Neurol* 250(11):1293–1301. <https://doi.org/10.1007/s00415-003-0192-3>

60. Stikov N, Campbell JSW, Stroh T et al (2015) Quantitative analysis of the myelin g-ratio from electron microscopy images of the macaque corpus callosum. *Data Brief* 4:368–373. <https://doi.org/10.1016/j.dib.2015.05.019>
61. Liewald D, Miller R, Logothetis N et al (2014) Distribution of axon diameters in cortical white matter: an electron-microscopic study on three human brains and a macaque. *Biol Cybern* 108(5):541–557. <https://doi.org/10.1007/s00422-014-0626-2>
62. Trapp BD, Kidd GJ (2004) Structure of the myelinated axon. In: Lazarini RA, Griffin JW, Lassmann H, Nave KA, Miller RH, Trapp BD (eds) *Myelin biology and disorders*. Elsevier, Amsterdam, pp 3–27
63. Morrell P, Quarles RH (1999) Myelin formation, structure and biochemistry. In: Siegel GJ, Agranoff BW, Alber RW, Risher SK, Uhler MD (eds) *Basic neurochemistry*, 6th edn. Raven Press, New York, pp 70–93
64. Kiseleva EB, Yashin KS, Moiseev AA et al (2017) Cross-polarization optical coherent tomography in comparative in vivo and ex vivo studies of optical properties of normal and tumorous brain tissues. *Sovrem Tehnol Med* 9(4):177–185. <https://doi.org/10.17691/stm2017.9.4.22>
65. Strenge P, Lange B, Grill C et al (2020) Segmented OCT data set for depth resolved brain tumor detection validated by histological analysis. In: *Proceedings of SPIE*, vol 11228, Optical coherence tomography and coherence domain optical methods in biomedicine XXIV, p 112282O. <https://doi.org/10.1117/12.2545659>
66. Möller J, Bartsch A, Lenz M et al (2021) Applying machine learning to optical coherence tomography images for automated tissue classification in brain metastases. *Int J Comput Assist Radiol Surg* 16(9):1517–1526. <https://doi.org/10.1007/s11548-021-02412-2>



Two Photon Fluorescence Lifetime Imaging of Reduced Nicotinamide Adenine Dinucleotide in Brain Research

2

Gagan Raju and Nirmal Mazumder

Abstract

Current understanding of the structure and functions of the brain is inadequate to explain the complex neurobiological phenomenon associated with the pathophysiology of an organism. Hence, there is a scope for better understanding of the morpho-functional features of the brain. On this note, present-day conventional neuroimaging techniques fail to meet the challenges posed by this complex structured organ to completely unveil the wide array of neurological phenomenon. To make this possible, a novel imaging technique established by combining principles of both two photon excitation and fluorescence lifetime imaging into one system is called two photon fluorescence lifetime imaging microscopy (TP-FLIM). This imaging modality has always been the choice of technique in neurobiology research, as this avenue demands high spatial ($\sim 1 \mu\text{m}$) and temporal resolution (less than milliseconds). Here, the chapter mainly spotlights on the importance of TP-FLIM of nicotinamide adenine dinucleotide (NADH), a ubiquitous endogenous fluorophore responsible for cellular autofluorescence, and its significance as an indicator of cellular metabolic changes associated with pathophysiological conditions of various disorders. A brief information about the instrumentation of TP-FLIM and fluorescence lifetime measurement methods such as frequency domain and time domain are discussed. NAD^+ biogenesis pathway along with its reduced counterpart NADH's autofluorescence property has been illustrated. Chapter also highlights the application of this technique in cancer diagnosis and in understanding the pathophysiology of neurodegenerative diseases.

G. Raju · N. Mazumder (✉)

Department of Biophysics, Manipal School of Life Sciences, Manipal Academy of Higher Education, Manipal, Karnataka, India

Keywords

Two photon excitation · Fluorescence lifetime imaging microscopy · Reduced nicotinamide adenine dinucleotide · Autofluorescence · Time-correlated single photon counting · Cellular metabolism

2.1 Introduction

The brain is regarded as the most complex organ of any biological system, and it has been quite a challenging task to completely study brain morphology owing to the complex neuronal network between billions of neurons. As we fail to understand this complexity it gets, even more, worse in case of studying brain disorders due to a lack of reliable imaging techniques. Even though many techniques such as single photon emission computed tomography (SPECT), functional magnetic resonance imaging (fMRI), positron emission tomography (PET), and computerized tomography (CT) were developed to diagnose brain disorders, none of them potentially proved to be efficient [1, 2]. Therefore, it is need of the hour to develop one such reliable imaging modality with greater imaging depth, higher spatial and temporal resolution. Lifetime-based modalities have been established for deep tissue imaging only after the advent of two photon fluorescence (TPF) microscopy. Two photon absorption is an aberrant phenomenon in which two photons should interact with the molecule almost at the same time, means anything less than 10^{-18} s will favour the two photon excitation [2]. The advantages of using these mode-locked ultrashort laser pulses that keep the average peak power low, in such a way it compresses the laser power into small time packets so that photon density is high at a given time point. In parallel, usage of objective lens with high numerical aperture (NA) concentrates the light in a diffraction limited focal volume [3]. Cumulatively pulsed lasers and high NA objective lens is crucial in creating the high photon flux at a small focal volume. The reason behind the success of this technique lies in how efficiently one can produce non-linear excitation to make this possible ultrashort laser sources in combination with efficient scanning system is must.

Over the past three decades, fluorescence lifetime imaging microscopy (FLIM) stood out as the most promising technique since it is sensitive to changes in tissue microenvironment also independent of the concentration of fluorophore [4]. Fluorescence lifetime is the average time that any fluorophore spends in its excited state before coming back to the ground state by emitting a photon [5, 6]. This feature is a unique characteristic of endogenous fluorophores, which can be a precise reporter of minute changes in tissue microvasculature [7–10]. As the lifetime of any fluorophore is sensitive towards the microenvironment, it will be easy to analyse the physical status of fluorescent molecules, whether it exists in the free or bound state. Henceforth, this property allows researchers to study tissues and cells in greater details. In recent times, FLIM has exploited to study varied interactions between proteins as well [11, 12].

Every biological system has myriad endogenous fluorophores, which fluoresce without the aid of any external probes. These fluorophores transition to a higher energy excited state by absorbing the light of a suitable wavelength and emitting a photon of energy lower than absorbed; this phenomenon is exhibited by intracellular fluorophores termed as autofluorescence [13]. Metabolically active coenzymes such as nicotinamide adenine dinucleotide (NADH) and flavin adenine dinucleotide (FAD) fluoresce by absorbing a photon of suitable wavelength; nowadays studies are focused on using these endogenous fluorophores for non-invasive, label-free intravital imaging to monitor rate of cellular energy metabolism and physiological status of the organisms [14, 15]. Technical advancements and commercial availability of ultrafast lasers, fast electronics, and highly sensitive detectors made it possible for the amalgamation of TPF microscopy with FLIM, resulting in emergence of a novel optical imaging technique, which works on the principle of non-linear excitation of fluorophores called two photon fluorescence lifetime microscopy (TP-FLIM) [16]. In the grounds of neurobiology, TP-FLIM has advanced diagnostics approaches in various neurodegenerative diseases. Furthermore, current understanding of the complex morphology and pathophysiology of the brain has improved significantly, allowing researchers to pinpoint the exact mechanism underlying the illness. [14, 17, 18]. Moreover, the technique possibly sheds light on finding novel treatment strategies for many disease conditions associated with neurology [19]. Whereas this ideal bio-imaging approach has gained popularity because of its outstanding intravital imaging potential, where it can efficiently produce images at hundreds of micrometre depth into subcortical layers of the brain [8].

2.2 Instrumentation

Way back in 1931, Maria Goppert-Mayer predicted the phenomenon of two photon absorption [20]. The milestone invention from Denk et al. has revolutionized across scientific and biomedical optical imaging field with exceptional research finding about the two photon excitation process that paves the way for establishment of TPF microscopy. Study proved the feasibility of TPF microscopy by using sub-picosecond pulse mode-locked lasers, which can generate ultrafast light pulses [21]. Primary requisition of TPF microscopy is to generate high density photon flux to the specimen to guarantee efficient absorption, and it is made possible by using femtosecond pulsed laser excitation. Soon after, they successfully implemented two photon excitation phenomenon to microscopy by integrating the advanced laser scanning microscope with ultrashort pulsed laser (mode-locked laser). As this specific type of laser produces pulses of near-infrared (NIR) light, having wavelength around 720 nm, it generates high peak power with a pulse repetition rate of 80 MHz which is sufficient for two photon excitation with average power less than 25 mW, inducing very minimal photodamage to the living tissue [22] (as shown in Fig. 2.1). This non-linear interactions are generated by high photon fluxes of about 10^{20} – 10^{30} /($\text{cm}^2 \text{ s}$) and delivering these high photon flux continuously without

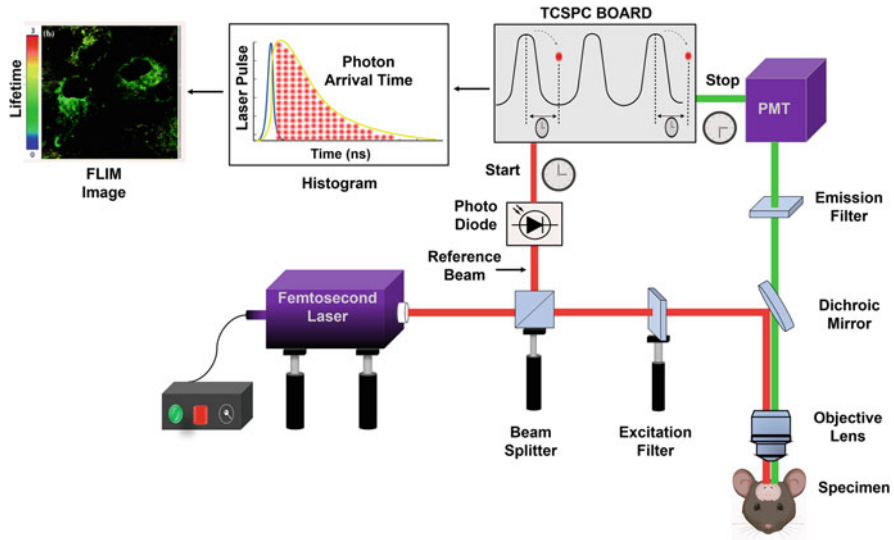


Fig. 2.1 Schematic representation of TP-FLIM setup

vaporizing it to the specimen was the major obstacle in making two photon microscopy feasible for in vivo imaging [3, 23].

Generally, there are three key components of TPF microscope: an ultrafast light source, scanning microscope, and a detection system. Modern technology has made it possible that lasers and detectors are commercially available; however, one can also build customized TPF microscopes using above-mentioned components or even the existing confocal microscopes can also be modified. For TP-FLIM measurement, ultrashort pulsed laser with high repetition rate up to 80 MHz is required, as it quantifies the fluorescence decay rate of a fluorophore on the timescale of sub-nanoseconds to hundreds of nanoseconds [24]. Image acquisition is possible only if fast electronics are working in tandem with efficient photon detectors. Inclusion of scan lens and tube lens will be significant as it expands the beam [25]. Addition of short pass filters and dichroic mirror, guides the reflected excitation beam to objective lens [26]. The autofluorescence signal from the tissue specimen is collected by the same objective lens, which then passes through the dichroic mirror and emission filter before being recorded by the PMT. Usually, additional barrier filters are used to weaken the signals to a greater extent. The fluorescence signals are detected by photodetectors of the microscope. Some of the conventionally used photodetectors are photomultiplier tube (PMT), charge-coupled device (CCD) cameras, and avalanche photodiodes. However, PMT is most preferred because it is relatively efficient and more sensitive in comparison with its peers [27].

2.2.1 Fluorescence Lifetime Measurement

Ever since FLIM measurement found its way into optical imaging techniques, series of experiments were carried out in combination with widefield microscopes, confocal microscopes, and TPF microscopes. There are two dedicated detection methods available exclusively to measure the fluorescence lifetime: frequency domain and time domain [28]. In frequency domain detection method, specimens or samples are excited to higher energy state with the aid of pulsed or modulated light. The fluorescence signals from the sample will be of reduced modulation degree and phase shift in comparison with that of excitation. These values are calculated and used to draw the fluorescence decay profile. The changes associated with phase shift and modulation degree are bound by fluorescence lifetime (τ) and frequency of modulation (ω) [29, 30]. Hence, fluorescence lifetime can be calculated by means of either the phase shift or modulation degree [31]. Frequency domain has some disadvantages while imaging in vivo since fluorescence signal from the endogenous fluorophores are usually weak. Time domain detection method works by recording the fluorescence signal and reconstruct the decay curve. Lifetime of a respective fluorophore can be measured by fitting the decay curve using single or multi-exponential function [32]. The methods for determining fluorescence lifetime can be divided into two categories from the standpoint of electronics: analogue techniques and digital (photon counting) techniques [33–35]. Photon-counting techniques, consider the fluorescence signal to be a random sequence of single photon pulses. A histogram of the time intervals between the emission signals and the excitation laser pulses is plotted by recording the number of photon pulses arriving at a series of time channels. This histogram depicts the fluorescence decay. To detect intensity in time domain, photon-counting techniques record the density of photon pulses rather than their amplitude. As a result, accuracy of photon-counting techniques raises without the interference of noise gain or electronic gain, which ultimately results in a superior signal-to-noise ratio over analogue techniques [31]. Time-correlated single photon counting (TCSPC) is a widespread photon-counting technique that offers lifetime measurement at high time resolution and wide dynamic range, which makes the modality popular for microscopy and spectroscopy applications [34, 35]. It is effective for analysing low-intensity signals with a high repetition rate, like two photon excitation fluorescence of biological tissues. It is specifically tailored for detecting endogenous autofluorescence with short fluorescence lifetimes. Rapid technical advancements guided the development of TCSPC into a single board integrated with all the components essential for recording the fluorescence signals and obtaining fluorescence decay profile either through single or multidimensional techniques [31]. With all the advanced features, TCSPC has turned out to be a cutting-edge tool studying complex neurobiological phenomena [29, 36].

2.3 NADH Biogenesis

William Young and Sir Arthur Harden were the pioneers to illustrate NADH autofluorescence during 1906 while working on alcoholic fermentation observed something unusual and depicted as “conferment” [37]. Almost after three decades, a German scientist, Otto Heinrich Warburg came up with the fact that the nicotinamide part of NADH is acting as the site of oxidation and reduction reactions [38]. Later in 1950, tri- and diphosphopyridine nucleotide structure was elucidated by Kornberg and Pricer [39]. The structure of NADH is having two ribose molecules attached by phosphate group, whereas one is linked with adenine group and the other is connected to nicotinamide group. NADH, a pyridine nucleotide, acts as an electron donor in cellular metabolic pathway [40]. Majority of the dehydrogenases donates hydrogen and electrons to NAD^+ for producing NADH. Glycolysis results in synthesis of two NADH, whereas the Krebs cycle yields six such molecules and these electrons are carried to mitochondrial inner membrane to participate in electron transport chain which finally fields ATP via oxidative phosphorylation [41]. Complete understanding of the structure and function of NADH and its ability to monitor the changes associated with cellular metabolism of the organism has gained the attention of a wide array of researchers. Every living organism synthesizes the NAD^+ by two means: de novo and salvage pathway. Dietary tryptophan acts as a starting material for NAD^+ biosynthesis through de novo pathway, whereas nicotinic acid, nicotinamide, and nicotine riboside are the starting materials for the same through salvage pathway [42].

2.3.1 NADH Biosynthesis Pathway

As already stated, aromatic amino acid tryptophan is the raw material, which yields NAD in eight-step de novo pathway [43, 44]. In first step, conversion of tryptophan to *N*-formyl kynurenine is facilitated by either of the two key enzymes: tryptophan 2,3-dioxygenase and indoleamine 2,3-dioxygenase [45]. In next stages, after four consecutive enzymatic reactions 2-amino 3-carboxymunic acid semialdehyde (ACMS) will be formed. Formation of unstable ACMS is regarded as branching point of this pathway as it leads the pathway into two lineages, one heads towards the formation of CO_2 , H_2O , and ATP on complete oxidation of ACMS into α -amino- β -muconate- ϵ -semialdehyde (AMS), another lineage leads to form quinolinic acid, precursor of NAD^+ through spontaneous cyclization of ACMS. In subsequent stage, as the quinolinic acid gets converted into nicotinic acid mononucleotide (NAMN) by quinolinic acid phosphoribosyl transferase (QPRT) [46]. Next, pathway is connected with Preiss-Handler pathway and proceeds further to sequentially yield nicotinic acid adenine dinucleotide (NAAD) and NAD^+ catalysed by the action of nicotinamide mononucleotide adenylyl transferases (NMNAT 1) and NAD synthase, respectively [47] (as shown in Fig. 2.2).

In salvage pathway, mainly three precursors from which NAD^+ will be biosynthesized and they are: nicotinic acid, nicotinamide, and nicotinic riboside.

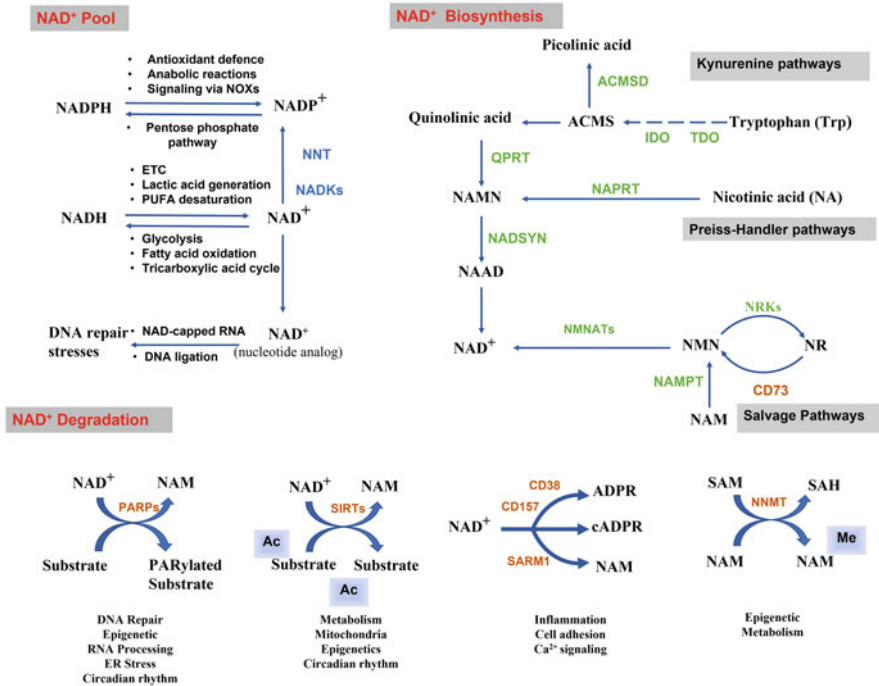


Fig. 2.2 Overview of NAD⁺ biosynthesis via kynurenine, salvage, and Preiss-Handler pathways represents NAD⁺ metabolism and its physiological function. (Figure is adopted with permission from Ref. [48])

Firstly, catalytic conversion of nicotinic acid along with alpha-D-5-phosphoribosyl-1-pyrophosphate (PRPP) to nicotinic acid mononucleotide (NAMN) by nicotinic acid phosphoribosyl transferase (NAPRT). Further subsequent catalytic activities of nicotinamide mononucleotide adenylyl transferases (NMNAT) and nicotinic acid synthase (NADS) yields NAD⁺. In second pathway, enzyme nicotinamide phosphoribosyl transferase (NAMPT) converts nicotinamide into nicotinamide mononucleotide (NMN) by adding PRPP, further nicotinamide mononucleotide adenylyl transferase (NMNAT) ultimately gives rise to NAD⁺ by acting on NMN [49]. Once NR crosses the membrane, it's got phosphorylated by nicotinamide riboside kinases (NMRK) 1 and 2, resulting in the formation of NMN, which finally got fused with ATP by the activity of NMNAT to arrive at NAD. NAD⁺-dependent enzymes such as sirtuins, NAD⁺ glycohydrolases, and PARPs have their own significant roles in age-related pathologies and neurodegeneration [50]. Even there are scientific evidence suggesting that elevating the expression levels of NAD⁺-dependent histone deacetylases will eventually result in increased lifespan of an individual [51].

2.4 NADH Autofluorescence and Lifetime

Biological system has many endogenous fluorophores which are collectively accountable for tissues exhibiting fluorescence properties [52]. This naturally occurring phenomenon, where light-tissue interactions eventually result in emitting fluorescence is called autofluorescence. Several endogenous fluorophores are present in living system namely, flavins, NAD(P)H, cytokeratin, collagen/elastin, porphyrin derivatives, etc. [53]. The intricate association of intrinsic fluorophores with morpho-functional status of the biological systems, influencing fluorescence signals, stand out as an effective tool for monitoring biological substrate condition. Both NADH and NADPH have identical autofluorescence hence, combined fluorescence signal of NADH and NADPH is denoted as NAD(P)H [54, 55].

Existence of life is unimaginable without the presence of NADH; it plays a crucial role in the cellular metabolism of various living systems starting from microorganisms to humans. NAD is not only involved in energy production as a coenzyme for most of the actively participating enzymes of cellular metabolism but also serves as a co-substrate to enzymes such as sirtuins, poly (ADP-ribosyl) polymerases, mono (ADP-ribosyl) transferases, and CD38 [48]. The reduced form (NADH) is exhibiting autofluorescence, however, not the oxidized one (NAD⁺), single photon excitation and emission peaks of NADH are around 340 and 470 nm, respectively [4, 56]. Fluorophore has its signature lifetime, which is the average time duration the molecule spends in excited state before emitting the photon [57]. As this intrinsic autofluorescence signals emitted by the biological system refers to the alterations in physiology during diseased state of the organisms, this will be the effective tool in portraying morpho-functional status of the organism based on variations in lifetime of a fluorophore. NADH exists in two forms, one is free form and other is bound form. Whereas the free state is indicated by lifetime around 0.4–0.8 ns conversely, 1–5 ns lifetime suggests that NADH is in bound state with proteins or enzymes [58–60]. The lifetime information obtained is significant enough to predict the location to which the fluorophore is confined, for example in case of NADH, free forms indicate that the fluorescence signals are from the cytoplasmic region of the cell; on the contrary, the longer lifetime fractions of NADH are from mitochondrial region, where these coenzymes actively take part in oxidative phosphorylation as an electron carrier. Owing to its intricate association with cellular metabolism, this has been used for real-time assessment of changes associated with the metabolism under any pathophysiological conditions [59, 61, 62].

2.5 Applications

Changes associated with the cellular metabolism during oncogenesis is one of the hallmarks of cancer. As NADH is the key coenzymes actively involved in cellular metabolism, it can be used to monitor the changes in real time. It is well-known fact that the metabolic changes are altered during the progression of glioma, so to analyse

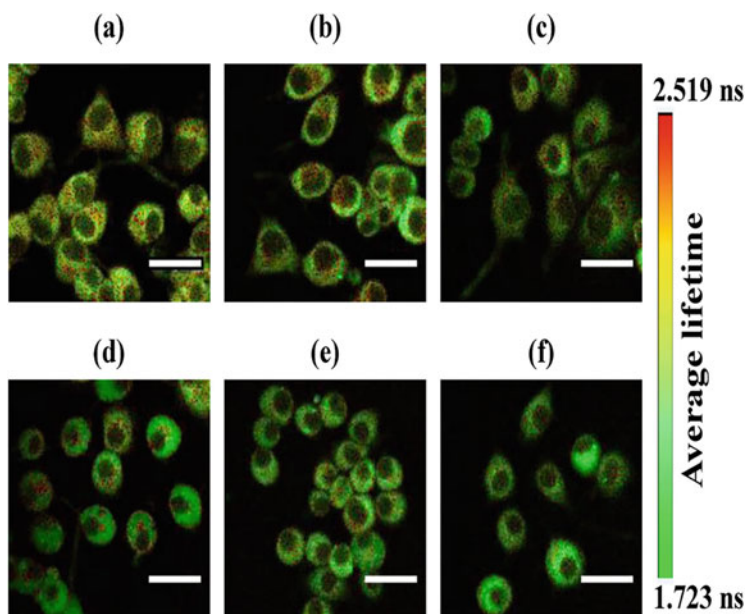


Fig. 2.3 Micrographs show average lifetime of NADH of PC12 cells using pseudo colour mapping that were (a) differentiated and untreated; and cells treated with (b) 50, (c) 100, (d) 250, (e) 500, (f) 1000 μM of MPP^+ . Colour bar represents the range of average fluorescence lifetime. (Figure reproduced from Ref. [66] with kind permission from Springer Nature)

this metabolic activity certain parameters such as optical redox ratio, fluorescence intensity of NADH and FAD were employed [15]. Parkinson's disease (PD) is the most prevalent age-associated neurodegenerative disease, globally more than 10 million people living with PD [63]. A characterizing pathological condition associated with PD is the loss of dopaminergic neurons in the region of substantia nigra of the brain, which plays a central role in maintaining the body movements in more coordinated and controlled manner [64, 65]. Chakraborty et al. worked on functional mapping of cellular energetics in 1-methyl-4-phenylpyridinium (MPP^+) treated PD cell model with the aid of 2P-FLIM of intracellular endogenous fluorophores, NADH and FAD. Cellular model of PD is developed by nerve growth factor (NGF)-induced PC12 cells on treating with MPP^+ , which significantly mimics pathological conditions associated with PD. Fluorescence lifetime images are instrumental in validating the effects of MPP^+ on PC12 cells, as the average lifetime of free NADH (τ_1) decreased from 0.52 ns (control) to 0.45 ns on treatment with 1000 μM MPP^+ (as shown in Fig. 2.3). The ratio of relative contributions of free and protein-bound NADH significantly increased from 1 to 1.56 ns upon treatment implies the redox variation brought about by the neurotoxin MPP^+ . Similar changes are seen with FAD; however, the differences in FAD lifetime distribution among the PD-induced cells were smaller when compared with that of NADH. Lower metabolic activity of treated PC12 cells were inferred by the increase and decrease in ratio

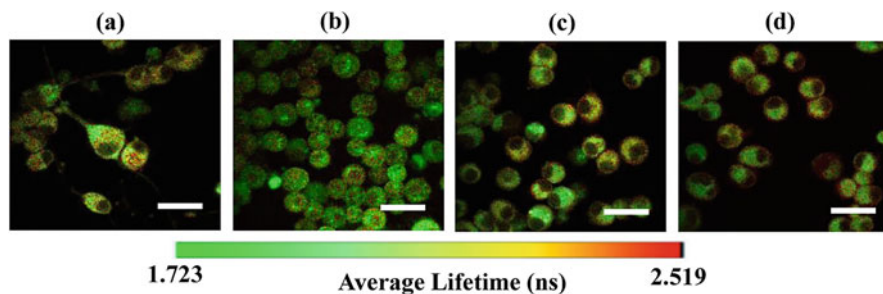


Fig. 2.4 Shows average NADH FLIM images of PC12 cells after various chemical treatment. (a) Control cells, (b) cells treated only with 1 mM MPP⁺, (c) cells treated with combination of 1 mM MPP⁺ and 10 μM curcumin, and (d) combination of 1 mM MPP⁺ and 10 μM cyclocurcumin. Colour bar represents the range of average fluorescence lifetime. (Figure reproduced from Ref. [68] with kind permission from Springer Nature)

of relative contribution of free to protein-bound NADH and FAD, respectively [66]. Hence, NADH FLIM turns out to be a tool of choice for assessment of PD progression.

TP-FLIM has been used for studying inhibitory effects of phytochemicals namely, curcumin and cyclocurcumin on neurotoxicity in MPP⁺-induced PD-like cell model. MPP⁺, a potent neurotoxin used to induce disease-like state in cell, which can cross BBB (blood–brain barrier) and get congregated in mitochondria resulting impaired cellular respiration [67]. Assessment of inhibitory effects of curcumin and cyclocurcumin on neurotoxicity was done using MTT assay, ROS level, and 2P-FLIM of intracellular NADH. Primarily, untreated neuronal-like PC12 cells are tested with varying concentrations (0.01, 0.1, 1, and 10 μM) of curcumin and cyclocurcumin separately to verify whether these phytochemicals possess phyto-toxic effects, as expected there were no significant changes in the cell viability. Average lifetime value of free (τ_1) NADH reduced from 0.52 ns (control) to 0.28 ns upon treatment with 1 mM MPP⁺ and in case of protein-bound NADH lifetime values was decreased to 1.4 ns from 2 ns (control). Subsequent treatment of PC12 cells with 10 μM curcumin and 10 μM cyclocurcumin has increased the lifetime values to 0.32 and 0.48 ns, respectively, in case of τ_1 . The same treatment resulted in the increased τ_2 values 1.6–2.25 ns in comparison with MPP⁺ treatment (as shown in Fig. 2.4). Positive outcome has also been recorded in case of reactive oxygen species (ROS) measurements for the same plant-derived compounds. Cells tend to aggregate due to toxicity induced by MPP⁺ when compared to uniformly distributed normal PC12 cells. Ratio of relative lifetime components (a_1/a_2) value changes from 1 to 3.4 ns after MPP⁺ treatment alone, and this ratio is analogous to the NADH/NAD⁺ ratio, which can be a potential metabolic maker to decipher the cellular metabolic changes [68].

Alzheimer's disease (AD) is one among the most prevalent neurodegenerative diseases haunting mankind at the later stages of life [69]. Regarded as the most common cause of dementia, accounting for about 60–80% of cases. Gomez et al.

studied the alterations in cerebral energy metabolism associated with AD using TP-FLIM of endogenous NADH in mouse model. According to the findings, in vivo quantification of intrinsic autofluorescence signals are useful for identifying changes brought by residence of A β plaques in mitochondrial cellular metabolism and lipofuscin accumulation. The research outcome evaluates A β -associated discrepancies in ROS congregation and plaque formation non-invasively. Metabolic function is clearly affected in areas near plaques; however, it is ambiguous whether changes in mitochondrial function and ROS formation are entirely due to amyloid β [70, 71]. Norambuena and his colleagues used TP-FLIM of endogenous fluorophore NADH to show that accumulation of amyloid β oligomers eventually leads to disruption of lysosome to mitochondria signalling pathway [72, 73]. Study unveils that insulin and amino acids activate mTORC1, which in turn regulate mitochondrial DNA synthesis in nerve cells thus play a key role in stimulating the activity of mitochondria. Results were evident in portrayal of the fact that intrinsic fluorescence of NADH is co-localized specifically with mitochondria, and there is a significant increase in the fluorescence lifetime from 0.3–0.8 to 1–6.5 ns after binding with enzymes, which depicts increased production of energy by NADH. Lifetime images also signify the enzyme-bound fraction of NADH ($a_2\%$) in mouse cortical neurons, and human neurons were 63% and 67%, respectively, during starved condition. Same fractions change to 59% and 64%, respectively, after supplementing with amino acids and 59% and 64% upon insulin supplement. Spectrally inseparable NADH and NADPH were discriminated by fluorescence lifetime to know their relative contributions to overall measured lifetimes before and after the stimulation, which were 63% and 37%, respectively. Study concludes that it is lysosomal mTORC1, not the mitochondrial mTORC1, that regulates nutrient-mediated mitochondrial activity [73].

A-synuclein (α S) aggregates, varied dopamine homeostasis, and rampant death of dopaminergic neurons are hallmarks of PD [74], which is an age-associated, multifactorial disease. Currently, over 10 million people living with PD worldwide; men are more prone to this disease than females. Hence, the need of the hour is to study the exact role of aggregation products of α S and their toxicity inducing mechanisms. Plotegher et al. showed that NADH fluorescence lifetime can be effectively used as an endogenous reporter of protein aggregation or cellular oxidative stress, by demonstrating the α -synuclein aggregation in HEK293 (human embryonic kidney) cell models. Fluorescence lifetime and phasor plot histograms were constructed for HEK293 cells transfected with empty vector, overexpressed α S, and preformed α S fibrils. Phasor approach has been implemented to FLIM to measure free-to-bound NADH ratio in accordance with α S overexpression and aggregation in HEK293 cells, also location-specific relative contributions of free and bound fractions of NADH. NADH lifetime images clearly suggest the overexpression of α S by increased protein-bound fraction of NADH (as shown in Fig. 2.5). α S oligomerization and mitochondrial damage is indicated by decreased ratio of relative lifetime components (NADH:NAD⁺) HEK293- α S overexpression and HEK293 cells with seed shows some red or orange spots, signifies higher bound fractions of NADH and decreased free: bound NADH ratio in comparison with that of control (HEK293 cells

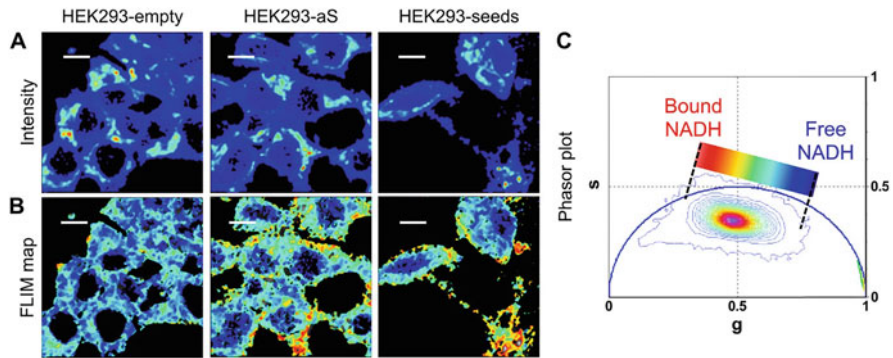


Fig. 2.5 (a) Fluorescence intensity images of human embryonic kidney 293 cells transfected with empty vector (left panel), α S (middle panel) α S with seeding (right panel). (b) Fluorescence lifetime images corresponding to the same region of interest of (a). (c) Shows the phasor plot histogram represents lifetime distribution of every pixel in all six images. (Figure reproduced from Ref. [75] with kind permission from Wiley Publications)

transfected with empty vector). The outcome indicates that the severe damage caused to mitochondria by α S oligomers accumulation, elevates the oxidative stress in HEK293- α S, which leads to the fluctuation in free to bound NADH ratio.[75].

2.6 Conclusion

Over the past two decades, TP-FLIM has established as one of the most sophisticated optical imaging modality for intravital imaging by surpassing all disadvantages such as photodamage, and light scattering while imaging *in vivo*. Deep tissue imaging demands high temporal and spatial resolution to visualize the minute changes of tissue microenvironment. The recent advancements in the field of neuroimaging have made it feasible to assemble laser scanning microscopy, optic fibres, and fast electronics like PMT detectors together to image even a single neuronal cell non-invasively with enhanced depth penetration, reduced photo damage. Major challenges posed while imaging brain, the most dynamic and complex organ of living system got answered by fluorescence lifetime imaging of endogenous fluorophore, NADH. Fluorescence lifetime values of free NADH (τ_1) and protein-bound NADH (τ_2) increase and the ratio of relative lifetime components (NADH: NAD⁺ or a_1/a_2) will decrease significantly, in case of altered cellular metabolism during various pathological conditions such as cancer and neurodegenerative diseases. Based on the lifetime measurement, Plotegher et al. [75] proved α S overexpression induces PD. Norambuena et al. [73] illustrated the cross link that exists between the mitochondrial dysfunction and AD. In this way, TP-FLIM has strengthened our basic understandings of neurobiological phenomenon and in the near future it will be the gold standards for analysing cellular metabolic changes in relevance with the various pathophysiological condition. Commercial availability of

lasers and high throughput signal detectors that have encouraged research community to image intact brain tissue in their natural habitat reveal more information which eventually ease the elucidation of structural and behavioural dynamicity of the brain.

Acknowledgements We acknowledge the Indian Council of Medical Research (ICMR), Government of India, India, for financial support (Grant Nos. ICMR/ITR/Ad-hoc/43/2020-21, ID No. 2020-3286, File no.ICMR 5/3/8/60/2020-ITR). We thank Manipal School of Life Sciences, Manipal Academy of Higher Education (MAHE), Manipal, India, for providing the infrastructure and facilities.

References

1. Ntziachristos V (2010) Going deeper than microscopy: the optical imaging frontier in biology. *Nat Methods* 7(8):603–614
2. De Graaf RA, Chowdhury GM, Brown PB, Rothman DL, Behar KL (2009) In situ 3D magnetic resonance metabolic imaging of microwave-irradiated rodent brain: a new tool for metabolomics research. *J Neurochem* 109(2):494–501
3. Periasamy A, Mazumder N, Sun Y, Christopher KG, Day RN (2015) FRET microscopy: basics, issues and advantages of FLIM-FRET imaging. In: *Advanced time-correlated single photon counting applications*. Springer, Cham, pp 249–276
4. Lakowicz JR (ed) (2013) *Principles of fluorescence spectroscopy*. Springer Science & Business Media, New York
5. Hercules DM (1966) *Fluorescence and phosphorescence analysis*. Interscience Publishers, New York
6. Clegg RM (2010) Fluorescence lifetime-resolved imaging: what, why, how—a prologue. In: *FLIM microscopy in biology and medicine*. CRC Press, London, pp 3–34
7. Wallrabe H, Periasamy A (2005) Imaging protein molecules using FRET and FLIM microscopy. *Curr Opin Biotechnol* 16(1):19–27
8. Kobat D, Horton NG, Xu C (2011) In vivo two-photon microscopy to 1.6-mm depth in mouse cortex. *J Biomed Opt* 16(10):106014
9. Helmchen F, Denk W (2005) Deep tissue two-photon microscopy. *Nat Methods* 2(12):932–940
10. Kurtz R, Fricke M, Kalb J, Tinnefeld P, Sauer M (2006) Application of multiline two-photon microscopy to functional in vivo imaging. *J Neurosci Methods* 151(2):276–286
11. Elangovan M, Day RN, Periasamy A (2002) Nanosecond fluorescence resonance energy transfer-fluorescence lifetime imaging microscopy to localize the protein interactions in a single living cell. *J Microsc* 205(1):3–14
12. Datta R, Gillette A, Stefely M, Skala MC (2021) Recent innovations in fluorescence lifetime imaging microscopy for biology and medicine. *J Biomed Opt* 26(7):070603
13. Monici M (2005) Cell and tissue autofluorescence research and diagnostic applications. *Biotechnol Annu Rev* 11:227–256
14. Yaseen MA, Sakadžić S, Wu W, Becker W, Kasischke KA, Boas DA (2013) In vivo imaging of cerebral energy metabolism with two-photon fluorescence lifetime microscopy of NADH. *Biomed Opt Express* 4(2):307–321
15. Sorrells JE, Martin EM, Aksamitiene E, Mukherjee P, Alex A, Chaney EJ et al (2021) Label-free characterization of single extracellular vesicles using two-photon fluorescence lifetime imaging microscopy of NAD (P) H. *Sci Rep* 11(1):1–12
16. Boyd RW (2020) *Nonlinear optics*. Academic Press, London
17. Baackai BJ, Skoch J, Hickey GA, Allen R, Hyman BT (2003) Fluorescence resonance energy transfer determinations using multiphoton fluorescence lifetime imaging microscopy to characterize amyloid-beta plaques. *J Biomed Opt* 8(3):368–375

18. Mazumder N, Lyn RK, Singaravelu R, Ridsdale A, Moffatt DJ, Hu CW et al (2013) Fluorescence lifetime imaging of alterations to cellular metabolism by domain 2 of the hepatitis C virus core protein. *PLoS One* 8(6):e66738
19. Nyström S, Bäck M, Nilsson KPR, Hammarström P (2017) Imaging amyloid tissues stained with luminescent conjugated oligothiophenes by hyperspectral confocal microscopy and fluorescence lifetime imaging. *J Vis Exp* 128:56279
20. Göppert-Mayer M (1931) Über elementarakte mit zwei quantensprüngen. *Ann Phys* 401(3): 273–294
21. Denk W, Strickler JH, Webb WW (1990) Two-photon laser scanning fluorescence microscopy. *Science* 248(4951):73–76
22. König K, So PTC, Mantulin WW, Gratton E (1997) Cellular response to near-infrared femto-second laser pulses in two-photon microscopes. *Opt Lett* 22(2):135–136
23. Zhuo GY, Spandana KU, Sindhoora KM, Kistenev YV, Kao FJ, Nikolaev VV et al (2021) Label-free multimodal nonlinear optical microscopy for biomedical applications. *J Appl Phys* 129(21):214901
24. Datta R, Heaster TM, Sharick JT, Gillette AA, Skala MC (2020) Fluorescence lifetime imaging microscopy: fundamentals and advances in instrumentation, analysis, and applications. *J Biomed Opt* 25(7):071203
25. Müller M, Schmidt J, Mironov SL, Richter DW (2003) Construction and performance of a custom-built two-photon laser scanning system. *J Phys D Appl Phys* 36(14):1747
26. Wolf DE (2007) Fundamentals of fluorescence and fluorescence microscopy. *Methods Cell Biol* 81:63–91
27. Yotter RA, Wilson DM (2003) A review of photodetectors for sensing light-emitting reporters in biological systems. *IEEE Sensors J* 3(3):288–303
28. Royant A, Carpentier P, Ohana J, McGeehan J, Paetzold B, Noirclerc-Savoie M et al (2007) Advances in spectroscopic methods for biological crystals. 1. Fluorescence lifetime measurements. *J Appl Crystallogr* 40(6):1105–1112
29. Marcu L (2012) Fluorescence lifetime techniques in medical applications. *Ann Biomed Eng* 40(2):304–331
30. Seah LK, Wang P, Murukeshan VM, Chao ZX (2006) Application of fluorescence lifetime imaging (FLIM) in latent finger mark detection. *Forensic Sci Int* 160(2–3):109–114
31. Masters BR, So P (eds) (2008) *Handbook of biomedical nonlinear optical microscopy*. Oxford University Press, New York
32. Yasuda R (2012) Imaging intracellular signaling using two-photon fluorescent lifetime imaging microscopy. *Cold Spring Harbor Protocols* 2012(11):1121–1128
33. Böhmer M, Wahl M, Rahn HJ, Erdmann R, Enderlein J (2002) Time-resolved fluorescence correlation spectroscopy. *Chem Phys Lett* 353(5–6):439–445
34. Becker W (2005) *Advanced time-correlated single photon counting techniques*, vol 81. Springer Science & Business Media, Berlin
35. So PT, Dong CY, Masters BR, Berland KM (2000) Two-photon excitation fluorescence microscopy. *Annu Rev Biomed Eng* 2(1):399–429
36. Niesner R, Gericke KH (2008) Fluorescence lifetime imaging in biosciences: technologies and applications. *Front Phys China* 3(1):88–104
37. Harden A, Young WJ (1906) The alcoholic ferment of yeast-juice. Part II—The conferment of yeast-juice. *Proc R Soc Lond B Containing Papers Biol Charact* (1905–1934) 78:6
38. Warburg O, Christian WJBZ (1936) Pyridin, the hydrogen-transferring component of the fermentation enzymes (pyridine nucleotide). *Biochemische Zeitschrift* 287(291):291–328
39. Kornberg A, Pricer WE Jr (1950) On the structure of triphosphopyridine nucleotide. *J Biol Chem* 186(2):557–567
40. Blacker TS, Duchon MR (2016) Investigating mitochondrial redox state using NADH and NADPH autofluorescence. *Free Radic Biol Med* 100:53–65
41. Ramsay RR (2019) Electron carriers and energy conservation in mitochondrial respiration. *ChemTexts* 5(2):1–14

42. Ghosh S, George S, Roy U, Ramachandran D, Kolthur-Seetharam U (2010) NAD: a master regulator of transcription. *Biochim Biophys Acta* 1799(10–12):681–693
43. Bender DA (1983) Biochemistry of tryptophan in health and disease. *Mol Asp Med* 6(2): 101–197
44. Magni G, Orsomando G, Raffelli N, Ruggieri S (2008) Enzymology of mammalian NAD metabolism in health and disease. *Front Biosci* 13:6135–6154
45. Badawy AA (2017) Kynurenine pathway of tryptophan metabolism: regulatory and functional aspects. *Int J Tryptophan Res* 10:1178646917691938
46. Demarest TG, Babbar M, Okur MN, Dan X, Croteau DL, Fakouri NB et al (2019) NAD+ metabolism in aging and cancer. *Annu Rev Cancer Biol* 3:105–130
47. Dölle C, Hvidsten Skoge R, VanLinden MR, Ziegler M (2013) NAD biosynthesis in humans—enzymes, metabolites and therapeutic aspects. *Curr Top Med Chem* 13(23):2907–2917
48. Xie N, Zhang L, Gao W, Huang C, Huber PE, Zhou X et al (2020) NAD+ metabolism: pathophysiological mechanisms and therapeutic potential. *Signal Transduct Target Ther* 5(1): 1–37
49. Chiarugi A, Dölle C, Felici R, Ziegler M (2012) The NAD metabolome—a key determinant of cancer cell biology. *Nat Rev Cancer* 12(11):741–752
50. Ma Y, Chen H, He X, Nie H, Hong Y, Sheng C et al (2012) NAD+ metabolism and NAD+-dependent enzymes: promising therapeutic targets for neurological diseases. *Curr Drug Targets* 13(2):222–229
51. Tannous C, Booz GW, Altara R, Muhieddine DH, Mericskay M, Refaat MM, Zoueini FA (2021) Nicotinamide adenine dinucleotide: biosynthesis, consumption and therapeutic role in cardiac diseases. *Acta Physiol* 231(3):e13551
52. Berezin MY, Achilefu S (2010) Fluorescence lifetime measurements and biological imaging. *Chem Rev* 110(5):2641–2684
53. Croce AC, Bottiroli G (2014) Autofluorescence spectroscopy and imaging: a tool for biomedical research and diagnosis. *Eur J Histochem* 58(4):2461
54. Rocheleau JV, Head WS, Piston DW (2004) Quantitative NAD (P) H/flavoprotein autofluorescence imaging reveals metabolic mechanisms of pancreatic islet pyruvate response. *J Biol Chem* 279(30):31780–31787
55. Klingenberg M, Bucher T (1960) Biological oxidations. *Annu Rev Biochem* 29(1):669–708
56. Scott TG, Spencer RD, Leonard NJ, Weber G (1970) Synthetic spectroscopic models related to coenzymes and base pairs. V. Emission properties of NADH. Studies of fluorescence lifetimes and quantum efficiencies of NADH, AcPyADH, reduced acetylpyridine adenine dinucleotide and simplified synthetic models. *J Am Chem Soc* 92(3):687–695
57. Lakowicz JR, Szmacinski H, Nowaczyk K, Berndt KW, Johnson M (1992) Fluorescence lifetime imaging. *Anal Biochem* 202(2):316–330
58. Ramanujam N (2000) Fluorescence spectroscopy of neoplastic and non-neoplastic tissues. *Neoplasia* 2(1–2):89–117
59. Yu Q, Heikal AA (2009) Two-photon autofluorescence dynamics imaging reveals sensitivity of intracellular NADH concentration and conformation to cell physiology at the single-cell level. *J Photochem Photobiol B Biol* 95(1):46–57
60. Sharick JT, Favreau PF, Gillette AA, Sdao SM, Merrins MJ, Skala MC (2018) Protein-bound NAD (P) H lifetime is sensitive to multiple fates of glucose carbon. *Sci Rep* 8(1):1–13
61. Chance B, Cohen P, Jobsis F, Schoener B (1962) Intracellular oxidation-reduction states in vivo: the microfluorometry of pyridine nucleotide gives a continuous measurement of the oxidation state. *Science* 137(3529):499–508
62. Mayevsky A, Chance B (1982) Intracellular oxidation-reduction state measured in situ by a multichannel fiber-optic surface fluorometer. *Science* 217(4559):537–540
63. Marras C, Beck JC, Bower JH, Roberts E, Ritz B, Ross GW et al (2018) Prevalence of Parkinson’s disease across North America. *NPJ Parkinson’s Dis* 4(1):1–7
64. Dauer W, Przedborski S (2003) Parkinson’s disease: mechanisms and models. *Neuron* 39(6): 889–909

65. Lang AE, Lozano AM (1998) Parkinson's disease. *N Engl J Med* 339(15):1044–1053
66. Chakraborty S, Nian FS, Tsai JW, Karmenyan A, Chiou A (2016) Quantification of the metabolic state in cell-model of Parkinson's disease by fluorescence lifetime imaging microscopy. *Sci Rep* 6(1):1–9
67. Przedborski S, Tieu K, Perier C, Vila M (2004) MPTP as a mitochondrial neurotoxic model of Parkinson's disease. *J Bioenerg Biomembr* 36(4):375–379
68. Chakraborty S, Karmenyan A, Tsai JW, Chiou A (2017) Inhibitory effects of curcumin and cyclocurcumin in 1-methyl-4-phenylpyridinium (MPP+) induced neurotoxicity in differentiated PC12 cells. *Sci Rep* 7(1):1–9
69. Farrer LA, Cupples LA, Haines JL, Hyman B, Kukull WA, Mayeux R et al (1997) Effects of age, sex, and ethnicity on the association between apolipoprotein E genotype and Alzheimer disease: a meta-analysis. *JAMA* 278(16):1349–1356
70. Gómez CA, Fu B, Sakadžić S, Yaseen MA (2018) Cerebral metabolism in a mouse model of Alzheimer's disease characterized by two-photon fluorescence lifetime microscopy of intrinsic NADH. *Neurophotonics* 5(4):045008
71. Gómez-Virgilio L, Luarte A, Ponce DP, Bruna BA, Behrens MI (2021) Analyzing olfactory neuron precursors non-invasively isolated through NADH FLIM as a potential tool to study oxidative stress in Alzheimer's disease. *Int J Mol Sci* 22(12):6311
72. Deus CM, Yambire KF, Oliveira PJ, Raimundo N (2020) Mitochondria–lysosome crosstalk: from physiology to neurodegeneration. *Trends Mol Med* 26(1):71–88
73. Norambuena A, Wallrabe H, Cao R, Wang DB, Silva A, Svindrych Z et al (2018) A novel lysosome-to-mitochondria signaling pathway disrupted by amyloid- β oligomers. *EMBO J* 37(22):e100241
74. Fasano M, Lopiano L (2008) A-synuclein and Parkinson's disease: a proteomic view. *Expert Rev Proteomics* 5(2):239–248
75. Plotegher N, Stringari C, Jahid S, Veronesi M, Giroto S, Gratton E, Bubacco L (2015) NADH fluorescence lifetime is an endogenous reporter of α -synuclein aggregation in live cells. *FASEB J* 29(6):2484–2494



Types of Raman Scattering Techniques for Neurodegenerative Diseases

3

Sparsha Kumari, Apoorva Bettagere Shivakumar, Sonam Fathima Mehak, Nirmal Mazumder, Gireesh Gangadharan, and Vikram G. Pillai

Abstract

As human life expectancy has increased, age-related neurodegenerative disorders (NDs) are emerging as one of the greatest health and social threats of the twenty-first century. Most NDs manifest clinical symptoms at an advanced stage after the disease onset, making it difficult to detect before irreversible degenerative alterations in the brain occur. As a result, understanding the neural mechanisms and early detection of ND are crucial for enhancing human health and quality of life. Raman spectroscopy and microscopy techniques allow for label-free, video-rate data acquisition without any sample preparation, making them a viable tool for disease detection early on. Raman-based approaches can be employed in vivo for early diagnosis of NDs as they are noninvasive. They require simple instrumentation and enable non-destructive sample analysis, which makes them useful for real-time diagnosis. Here, we outline the various Raman spectroscopic and microscopic techniques with a special focus on their application as a diagnostic tool for neurodegenerative diseases.

S. Kumari · A. B. Shivakumar · S. F. Mehak · G. Gangadharan
Department of Cell and Molecular Biology, Manipal School of Life Sciences, Manipal Academy of Higher Education, Manipal, Karnataka, India

N. Mazumder
Department of Biophysics, Manipal School of Life Sciences, Manipal Academy of Higher Education, Manipal, Karnataka, India

V. G. Pillai (✉)
Department of Biophysics, Institute of Medical Sciences, Banaras Hindu University, Varanasi, Uttar Pradesh, India
e-mail: vgpillai@bhu.ac.in

Keywords

Neurodegenerative diseases · Raman spectroscopy · Coherent anti-Stokes Raman scattering · Stimulated Raman scattering · Hyperspectral Raman imaging

3.1 Introduction

The increasing prevalence of ND is partly due to the improved public health and extension of life span [1–3]. The increase in older population and the socio-economic constraints caused by ND makes the development of better diagnostic and therapeutic strategies necessary [2]. Accurate and early diagnosis of NDs like Alzheimer's disease (AD) is extremely important for early treatment before irreversible damage to the pathological processes occurs [4, 5]. Currently, the lack of complete understanding of the pathogenesis underlining many ND limits the development of effective diagnostic techniques and treatment [2, 6]. Also, the clinical symptoms of most of the ND appear years or decades after the early stage making early detection and treatment challenging [2]. Histological examination of the brain tissue conducted exclusively at the autopsy is the only possible confirmation of NDs [5–7]. Past research shows that ND spreads in a structured manner across the brain and accumulates in a prion-like form and is known to originate by the aggregation of specific types of proteins. Several neurodegenerative diseases like AD, Parkinson's disease (PD), dementia with Lewy bodies (DLB), and multiple system atrophy (MSA) are closely linked to accumulation of protein particles such as prion protein (PrP), amyloid β (A- β) peptides, α -synuclein (α Syn), and tau. It has been demonstrated that the injection of misfolded, aggregated neurodegeneration-related proteins in asymptomatic animals caused the induction and spreading of prion-like mechanisms within the brain [8, 9]. A better understanding of these diseases is possible through elucidating their structure-function roles and/or analyzing their pathological and physiological changes [2]. ND can also be diagnosed and treated by understanding the nanomolar concentration changes in neurotransmitter levels in the various regions of the brain [5, 7, 10, 11]. Effective diagnosis can be performed by developing a rapid and sensitive sensor for the detection of neurotransmitter levels in vivo through the skull [7, 12].

Imaging techniques like magnetic resonance imaging (MRI), perfusion imaging, diffusion tensor imaging, and permeability imaging are advanced techniques that can be used for diffusion diagnosis of the masses present in the brain, but as they are not definitive enough in many cases they cannot be used for pathologic tissue diagnosis [13]. Optical techniques can be effectively utilized to visualize and understand the molecular composition and interactions [14–18]. Techniques like second harmonic generation (SHG), optical coherence tomography (OCT), two-photon excited fluorescence (TPEF), infrared microscopy (IR), third-harmonic generation (THG), and confocal reflection (CR) imaging are label-free and considered reliable imaging tools for neurological research [17, 19, 20]. Though SHG, OCT, THG, and CR show morphological features, they are incapable of differential diagnosis as they do not

show chemical contrast [17, 21]. On the other hand, IR microscopy provides chemical contrast by probing molecular vibrations, but due to the long-wavelength of infrared light, they have low spatial resolution and show strong water absorption in biological specimens [14, 17, 22, 23]. Infrared spectroscopic methods like Fourier transform infrared (FT-IR) spectroscopy are utilized to classify the AD brain tissues [6, 24]. Since infrared penetration depth in tissue is small, infrared spectroscopy is not used for the *in vivo* diagnosis of AD [6]. Fluorescence imaging dominates high-resolution optical microscopy as it shows high sensitivity and generates large signals by a sizable collection of fluorophores, but since it has a limited number of intrinsic fluorophores it cannot be used for chemical selectivity [14, 15, 21]. Although extrinsic fluorophores can be used to provide specific probes, they often give rise to unwanted perturbations and their use for *in vivo* applications is limited due to the need for tissue-specific labeling [14]. Photoacoustic imaging and confocal fluorescence microscopy, on the other hand, offer high sensitivity, specificity, and speed, but they depend upon the specific absorption of dyes. The use of dyes can be toxic or can cause uneven distribution among cells or tissues [17].

Spectroscopic and microscopic techniques based on the principle of Raman scattering can be used for *in vivo* probing of biomolecules (i.e., proteins, carbohydrates, lipids, nucleic acids) in complex matrices without sample preparation [17, 25]. Raman scattered photons excited by a laser can be spatially correlated to obtain images of biomolecular distributions [15]. Raman scattering effect was discovered in 1928 and was first reported by the Indian physicist Chandrasekhara Venkata Raman [6, 26, 27]. In the past few decades, it has become a promising tool for clinical and laboratory uses owing to the advances in spontaneous and nonlinear Raman techniques [15]. The inelastic scattering of monochromatic laser radiation is the physical mechanism behind Raman scattering. The intensity of the weak Raman signals from biomolecules can be improved by using intense excitation lasers and sensitive detection schemes. When combined with complementary techniques like rapid scanning microscopes they improve clinical diagnosis, by collecting images at video rates, and when coupled with other multiphoton techniques the chemical contrast is improved [17]. In recent years, Raman-based sensors are used to detect and monitor demyelination, traumatic brain injuries (TBI), brain tumors, neurological diseases like amyotrophic lateral sclerosis (ALS), etc. and hence serve as a potential diagnostic tool for ND [25]. Table 3.1 summarizes the Raman fingerprint of various molecules that are used in the diagnosis of ND.

Here, we discuss the various types of Raman spectroscopic and microscopic techniques along with their applications in ND research, especially for investigating the functional groups associated with ND.

Table 3.1 Assignment of Raman fingerprint for molecules involved in neurodegenerative diseases

Raman shift (cm ⁻¹)	Assignment	References
607, 700, 1440, 1674	C ₂₇ H ₄₆ O, cholesterol (lipid)	Czamara et al. (2015) [28], Krafft et al. (2016) [17]
622, 1004, 1030, 1159, 1208, 1607	C ₉ H ₁₁ NO ₂ , phenylalanine (protein)	Krafft et al. (2016) [17], Rzhetskii (2019) [29]
644, 830, 855, 1175, 1612	C ₉ H ₁₁ NO ₃ , tyrosine (protein)	Krafft et al. (2016) [17], Fonseca et al. (2019) [30]
667, 757, 780, 1277	C ₅ H ₆ N ₂ O ₂ , thymine (nucleic acids)	Krafft et al. (2016) [17]
680, 1490, 1580	C ₅ H ₅ N ₅ O, guanine (nucleic acids)	Krafft et al. (2016) [17]
716, 875	N(CH ₃) ₃ (lipid)	Czamara et al. (2015) [28], Krafft et al. (2016) [17]
727, 1490, 1580	C ₅ H ₅ N ₅ , adenine (nucleic acids)	Krafft et al. (2016) [17]
757, 1159, 1340, 1555, 1617	C ₁₁ H ₁₂ N ₂ O ₂ , tryptophan (protein)	Thomas (1999) [31], Krafft et al. (2016) [17]
785	PO ₄ ³⁻ , symmetric phosphodiester stretch (nucleic acids)	Figueroa et al. (2018) [18]
815	O–P–O stretching (phosphate)	Guo et al. (2019) [32]
898, 935	Peptide C–C _α (protein)	Krafft et al. (2016) [17]
1084	Skeletal C–C vibrations (lipid)	Czamara et al. (2015) [28], Figueroa et al. (2018) [18]
1100	Nucleic acids	Figueroa et al. (2018) [18]
1154	C–C stretching (lipid)	Czamara et al. (2015) [28], Guo et al. (2019) [32]
1422	CH ₂ (nucleic acid)	Krafft et al. (2016) [17]
1452	CH ₂ bending (δCH ₂) vibration modes	Fonseca et al. (2019) [30]
1658	Amide I (protein)	Krafft et al. (2016) [17], Fonseca et al. (2019) [30]
1660	C=C (lipid)	Czamara et al. (2015) [28], Krafft et al. (2016) [17]
1740	C=O (lipid)	Czamara et al. (2015) [28], Krafft et al. (2016) [17]
2845	CH ₂ symmetric stretch vibrations (lipids)	Bégin et al. (2014) [33], Czamara et al. (2015) [28]
2877	CH ₂ antisymmetric stretching vibrations (lipids)	Czamara et al. (2015) [28], Fonseca et al. (2019) [30]
2930	CH ₃ symmetric stretching (lipids)	Czamara et al. (2015) [28], Fonseca et al. (2019) [30]
2935	CH-stretch (proteins)	Michael et al. (2014) [34]
3015	Stretching mode of =C–H (lipids)	Freudiger et al. (2008) [21], Czamara et al. (2015) [28]
3390	H ₂ O	Michael et al. (2014) [34]

3.2 Raman Techniques

3.2.1 Raman Spectroscopy

Raman spectroscopy being a sensitive and label-free optical micro-spectroscopic method, provides unique, specific fingerprint-like spectral information about the structure and composition of macromolecules [4, 7, 35–38]. Raman spectroscopy involves the sensitive and precise acquirement of spatially resolved and frequency-resolved scattering of light that enables identification of the functional groups of macromolecules which have indistinguishable structural features [36]. Raman spectroscopy does not use any external labels and hence is non-destructive to living organisms [2, 17, 39, 40]. Owing to its simple instrumentation and capacity to reveal molecular information, Raman spectroscopy is capable of being used for the in situ evaluation of living tissues (as shown in Fig. 3.1a) [6, 12, 35, 38, 41]. Raman spectroscopy provides the spectral fingerprint corresponding to the molecular and biochemical composition of the biological sample. These spectral fingerprints are obtained when light causes temporary changes in the bond's polarizability and results in the change of the vibrational frequency, which in turn results in a Raman spectrum [35, 38]. It measures the inelastic light scattering by the intrinsic molecular vibrations in the sample and can provide an accurate in vivo diagnosis of the diseases [6, 38]. Optical fibers can collect and deliver light rapidly and can be incorporated into cannulas, needles, endoscopes, and catheters facilitating the use of Raman spectroscopy in vivo (as shown in Fig. 3.2a, b) [6, 29].

Raman spectroscopy is widely being researched for medical diagnostics applications that use bio-fluids, cell, and tissue samples, and has gained much interest as a biological sensing technique [4, 7, 12, 38]. It has been shown that Raman spectroscopy can potentially be used as a selective diagnostic instrument for AD detection and differentiation, and it successfully differentiates between the brain tissues of healthy and AD patients [4, 6]. It has been demonstrated that using the hollow-core photonic crystal fiber along with the Raman spectroscopy setup can provide sharp and intense Raman signals of the major biomarker of AD, amyloid β (1–42) peptide ($A\beta_{42}$), thus enabling the development of a sensitive detection tool for the early diagnosis of AD [42]. Similar to infrared spectroscopy, Raman spectroscopy gives details regarding the molecular vibrations, and also the near-IR light which is used for the Raman excitation has a larger tissue penetration depth, i.e., of the order of a few centimeters [6]. Hence, near-infrared Raman spectroscopy promises to be used as an effective diagnostic technique to detect AD in vivo [4, 38]. The major drawback of Raman spectroscopy is the inherently weak signals obtained, limiting its use for clinical diagnosis [7, 11, 38]. However, surface-enhanced Raman spectroscopy (SERS) overcome this problem and produce stronger signals by using the optical properties of metal nanoparticles [7, 10, 38].

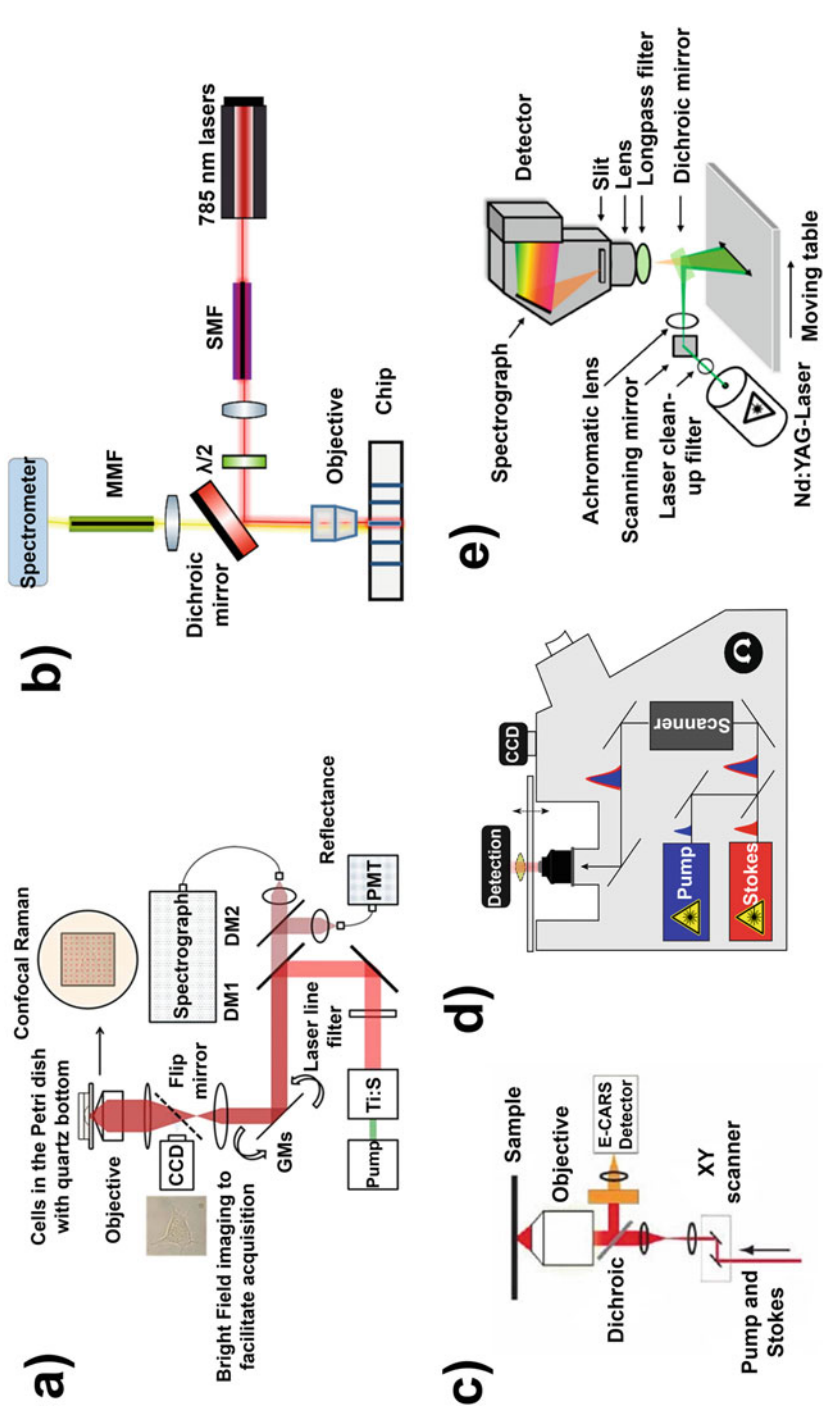


Fig. 3.1 (a) Setup for Raman spectroscopic system (Reprinted with permission from Singh et al. [37]). (b) Schematic of the setup for SERS (Reprinted with permission from Turk et al. [43]). (c) Schematic of the CARS microscope (Reprinted with permission from Evans et al. [13]). (d) Experimental setup of SRS microscopy (Reprinted with permission from Goltreich et al. [44]). (e) Schematic of the hyperspectral Raman imaging system (Reprinted with permission from Gruber et al. [45])

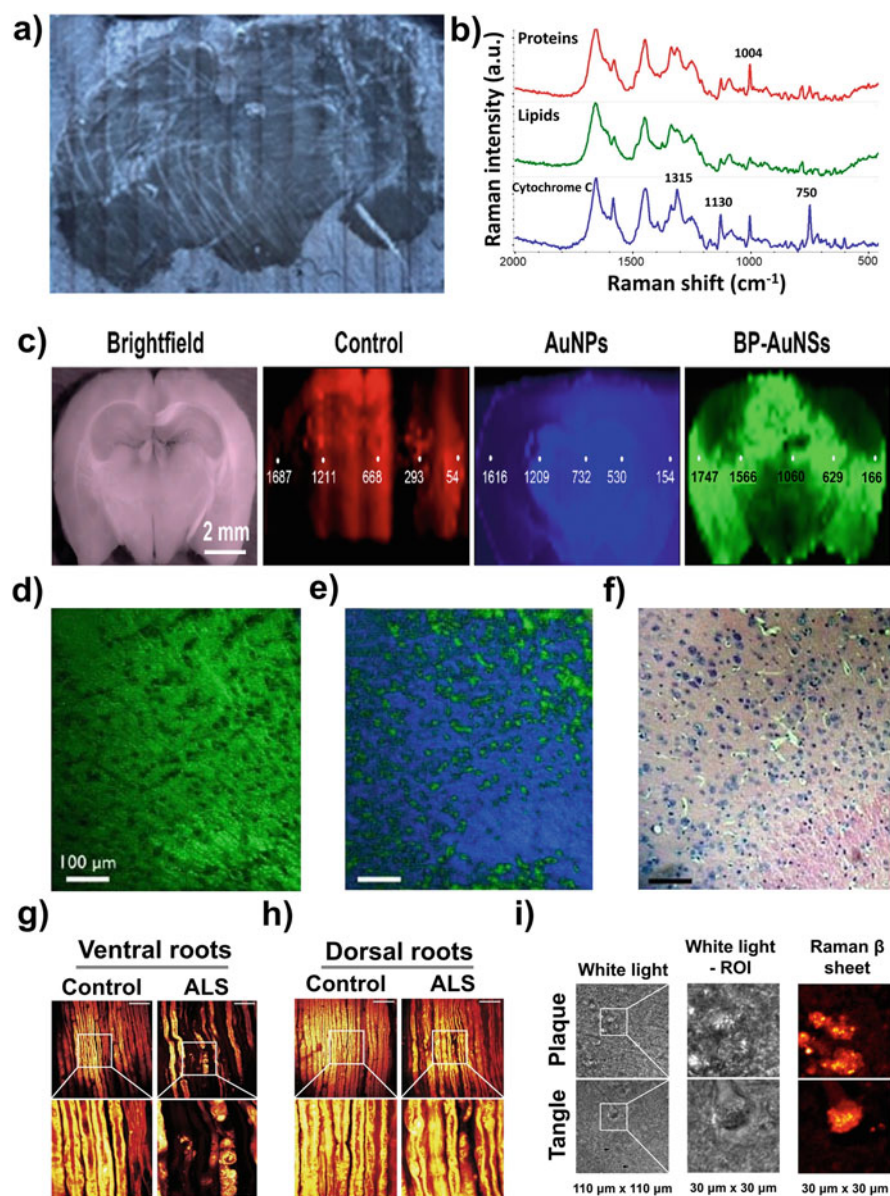


Fig. 3.2 Raman image of a mouse brain tissue section: (a) “mosaic” optical image captured with 20 \times objective lens; (b) the “fingerprint” region for live HEK cells with the marked peaks at 1004 cm^{-1} assigned to phenylalanine (Phe) typical for proteins, and the resonantly enhanced peaks at 1315, 1130, and 750 cm^{-1} in the cytochrome C (Reprinted with permission from Rzhetskii [29]). (c) Full-scale label-free SERS imaging of mouse brain section using gold nanoparticles (AuNPs) and black phosphorus-gold nano-sheets (BP-AuNSs) (Reprinted with permission from Guo et al. [32]). CARS image of the brain with chemical selectivity. (d) Positive lipid contrast image of CARS microscopy at 2845 cm^{-1} . (e) Negative lipid contrast image of CARS microscopy at 2955 cm^{-1} showing the cell bodies with positive contrast. (f) Corresponding H&E image (Reprinted with permission from Evans et al. [13]). SRS imaging identified lipid ovoid deposition

3.2.2 Surface-Enhanced Raman Spectroscopy (SERS)

Nano-metals such as gold nanoparticles interact with the incident light and enhance the Raman signal in SERS [10, 12, 38, 46]. The enhancing effect is locally confined to the molecules close to the gold nanoparticles and the SERS spectrum obtained reflects majorly the contribution from these molecules (as shown in Fig. 3.1b) [12, 38, 43]. SERS-based sensors have proven to be an excellent candidate for the rapid detection of biological molecules and monitoring the neurotransmitters associated with neurological disease using metal nanoparticles (as shown in Fig. 3.2c) [7, 11, 12, 47, 48]. Detection of neurotransmitters is necessary for the early diagnosis of neurodegenerative diseases. Recent studies have demonstrated that when SERS is combined with spatially offset Raman spectroscopy (SORS), it can be used for the sensitive and selective detection of neurotransmitters from within the skull [5, 11].

Patients suffering from Parkinson's disease (PD) lose more than 80% of their dopamine-producing cells [5, 10, 12, 46, 49, 50]. SERS has been used as a high throughput screening tool to detect the concentration of dopamine in the various brain regions using bio-barcode assay such as DNA barcodes, and thus differentiate between a healthy brain and a brain affected by PD [5, 10, 12]. SERS using gold nanoparticles are shown to be a reliable technique for investigating the effect of toxins on dopaminergic neurons in mice which in turn allows for the detection of PD [10]. It has also been found that SERS can be used in the prevention and detection of neurological diseases that involve abnormal changes in dopamine levels [50]. Huntington's disease (HD), another commonly found neurological disease can be studied in both pre-manifest and manifest stages owing to its genetic basis. The unavailability of easily accessible biomarkers that can track the progression of the disease hinders the early diagnosis and treatment of HD [38, 47]. Analysis of SERS spectra of the serum of HD patients showed substantial relationship with disease progression [38, 46, 50]. SERS reveals that the serum molecules related to protein misfolding and nucleotide catabolism are responsible for the advancement of HD from the pre-manifest stage [38]. SERS is used for many in vivo and in vitro biological applications but the metallic nanoparticles used for enhancing the sensitivity can be toxic to the physiological environment [25, 51]. Silver nanoparticles used on rats have been shown to alter the neurotransmitters and amino acids [25, 48]. Thus, limiting the application of SERS for in vivo diagnosis [25].

Fig. 3.2 (continued) in human ALS patient samples. (g) SRS imaging of ventral root nerve fibers from human ALS patients versus controls. Scale bar, 50 μ m. (h) SRS imaging of dorsal root nerve fibers from human ALS patients versus controls. Scale bar, 50 μ m (Reprinted with permission from Tian et al. [69]). (i) Hyperspectral Raman image of neuritic plaque (upper row) and neurofibrillary tangle (lower row). White light image with the square indicating the Raman scan region of interest (ROI) and Raman intensity image for β -sheets distribution (Reprinted with permission from Michael et al. [36])

3.2.3 Spontaneous Raman Microscopy

Spontaneous Raman scattering is an inelastic scattering of light and is becoming widely popular in biomedical applications [15, 17, 52, 53]. When implemented as a microscopic technique, Raman scattering gives images of molecular species at a submicrometer resolution [17, 18]. Spontaneous Raman microscopy involves the measurement of Raman spectra that is reflected by the molecular vibrations of intrinsic molecules. Raman microscopy gives details of the molecular species and structures in the tissues and cells through the molecular vibrations with a high spatial resolution [54, 55]. Raman microscopy is being used for biomedical applications since 1979 and also for imaging cytopathology and histopathology [15, 17]. In the past few decades, Raman microscopy is widely used in biomedical applications involving both *in vitro* and *in vivo* imaging [15]. High-resolution Raman microscopy can be used for imaging biological samples with a confocal microscope, but it is necessary to use high laser powers as the Raman signal is intrinsically weak [22]. Spontaneous Raman microscopy has shorter excitation wavelengths and thus offers high spatial resolution [21]. It serves as a powerful biomedical diagnostic tool and is used in applications like observing the distribution of biomolecules in the cells and tissues, studying drug delivery, analyzing cancer biopsies and other tissues [15, 17, 52, 53]. The data obtained from spontaneous Raman microscopy allows for the distinction of malignant and normal cells and tissues, thus making it useful for medical diagnostics [53]. Recent developments in spontaneous Raman microscopy has shown to be capable of imaging amyloid plaques and neurofibrillary tangles, thus being a promising tool in AD diagnosis [56].

Though spontaneous Raman microscopy is useful for the study of biological samples, it cannot be used for high-speed imaging as it has an extremely small cross-section [17, 18, 53]. Spontaneous Raman imaging cannot be effectively used for real-time vibrational imaging of living cells and organisms as they have low signal levels. To overcome this, coherent Raman scattering microscopy techniques have been developed that offer higher sensitivity and better video-rate imaging [17, 18, 53, 57].

3.2.4 Coherent Anti-Stokes Raman Scattering (CARS) Microscopy

Nonlinear coherent microscopy has growing attention in recent times as it enables three-dimensional imaging of microscopic objects present inside the living cells and tissues [58]. Techniques that enhance the Raman signals by using nonlinear optics to stimulate vibrations are called coherent Raman scattering techniques. There are two major forms of coherent Raman scattering, coherent anti-Stokes Raman scattering (CARS), and stimulated Raman scattering (SRS). CARS and SRS make use of multiple lasers of different wavelengths to excite the sample [2, 58, 59]. CARS is a third-order nonlinear optical method used for studying biological systems (as shown in Fig. 3.1c) [14, 33, 57, 60–62]. It is a chemical contrast method, i.e., the energy difference of two excited photons is the same as the energy of one of the

vibrational modes of the target system [57, 63]. A third photon investigates these coherently exciting vibration modes and then the system comes back to the ground state by emitting the CARS photons [63]. It provides real-time feedback about the tissue state, which in turn helps to differentiate between healthy and diseased tissue samples [13, 33, 60]. CARS microscopy is a highly responsive tool for vibrational imaging and micro-spectroscopy and requires moderate power for excitation which is bearable by most of the biological samples [21, 22, 64]. Hence, it is capable of in situ detection of NDs without causing any photo-damage [13, 65]. CARS microscopy technique has been used to monitor demyelination and neurodegeneration with high spatial resolution and signal-to-noise ratio. This was attained by recording the CH₂ vibration of myelin lipids in the live brain tissue of animals. In addition, the critical role of microglia in chronic inflammatory neurodegeneration has also been confirmed using CARS microscopy techniques (as shown in Fig. 3.2d–f) [13, 66].

AD involves lipidomic changes that may play a role in the disease progression [2]. The lipids linked to amyloid plaque present in the human AD prefrontal cortex samples can be imaged using CARS microscopy [2, 14]. The CARS intensity ratio of symmetric to asymmetric stretching vibrations gives the lipid fluidity [2]. PD is characterized by the presence of Lewy bodies whose chief constituent is α -synuclein which plays a significant role in the formation of Lewy neuritis (Lewy pathologies) [65]. The lack of complete study of the nature of these Lewy bodies necessitates the requirement of methods to draw conclusions about the pathogenesis and progression of PD [67]. CARS microscopy allows the identification of the lipids and proteins in the brain cells and provides information about their chemical composition [40, 68]. CARS signal of neurons from non-neurological samples showed lower lipid and protein levels compared to the surrounding tissues and the Lewy bodies show higher lipid and protein levels when analyzed through CARS microscopy. Thus, CARS microscopy is considered a reliable method for the early detection of PD [68]. CARS provides a higher sensitivity when compared to spontaneous Raman microscopy, but the non-resonant background present in the signal causes difficulties while interpreting the image and it also limits the detection sensitivity [21, 22, 64]. The dispersive CARS line shapes along with coherent image artifacts caused by the interference of the resonant and non-resonant CARS signals is a difficulty that arises from CARS microscopy and is inherently avoided in SRS microscopy [58, 64].

3.2.5 Stimulated Raman Scattering (SRS) Microscopy

SRS is a powerful non-destructive third-order nonlinear optical process similar to and developed as an alternative to CARS (as shown in Fig. 3.1d) [18, 56, 60, 61, 70]. SRS provides background-free chemical image contrasts as compared to CARS measurement that can be readily interpreted [58]. Unlike CARS, SRS intrinsically eliminates the non-resonant background contributions like that from water and does not display spectral distortion that limits the sensitivity. It also provides images that are free from the auto-fluorescence signal from the sample [2, 18, 58, 60, 61, 64,

71]. It provides faster imaging speeds with background-free chemical contrast images and directly detects the energy exchange that occurs between the chemical bonds and has a strictly linear relationship with molecular concentration, which facilitates quantitative image analysis [2, 18, 60, 61, 71]. SRS images on biological samples are based on the intrinsic components such as DNA, lipids, and proteins and are measured by the change in Stoke and pump intensities [56, 60, 70]. The difference between normal and misfolded proteins can be obtained through the SRS spectral shift, and this can be used for the detection of NDs [56]. Valuable details about the activity of the drugs in the complicated disease prototypes can be obtained by integrating biological imaging into the initial phases of the process of drug discovery. SRS shows faster acquisition speeds with high resolution and sensitivity while imaging cells and tissues [53, 60].

SRS is used in various biomedical applications including imaging brain tissues based on lipid contrast. CH_2 stretching vibration of lipids in the brain tissue, where axons are surrounded with myelin sheath that is rich in lipid content produces a strong stimulated Raman loss (SRL) signal [21]. SRS microscopy provides unbiased precise information about the disease onset and progression of ALS [64]. SRS microscopy has been used to investigate peripheral nerve degeneration in mice with ALS as well as human postmortem tissue. It has been reported that peripheral nerve degeneration is found to be among the first detectable pathological defects in mouse models of ALS when imaged using SRS. The peripheral nerves are distinguished by the presence of myelin sheath with high lipid content which makes it possible for SRS to identify them through intrinsic molecular vibration obtained from the lipid molecules (as shown in Fig. 3.2g, h) [69].

3.2.6 Hyperspectral Raman Imaging

Hyperspectral Raman imaging is a label-free technique that combines spatial and spectral data, in which vibrational frequency, object length, and width are examined with great detail (as shown in Fig. 3.1e) [45, 72]. Hyperspectral refers to obtaining spectral information at every pixel of the scan region and hyperspectral Raman microscopic imaging can be used to instantaneously acquire either an extensive spectral interval or the complete Raman spectrum at every image pixel [36, 73]. Raman techniques like Raman spectroscopy, SERS, CARS, and SRS are being used for hyperspectral imaging [36, 74, 75]. The hyperspectral Raman images can be obtained by illuminating the object with a point-focused laser beam and shifting the object under a static optical path [72]. The image can be acquired with a point-focused laser beam to attain one pixel at a time or with a line-focused beam to obtain one line at a time [72, 73]. Spectrum is attained from every point illuminated by the line to form the complete spectrum. After every movement of the object by a positioning stage beneath the line, a new spectrum is obtained. The spectrograph slit functions as a spatial filter and the total stage translation distance governs the observed object width. The observed object length is governed by the illumination line size, number of detector pixels illuminated, and the transfer optics [72]. This

technique does not require staining and can be performed on cryo-sections of unfixed brain tissue. This drastically decreases the time consumed for the pathological diagnosis of neurodegenerative diseases like AD [36].

The amyloid plaques in the human brain can be optically imaged using the hyperspectral Raman technique [30]. Neuritic plaques and neurofibrillary tangles are significant morphological conditions for the detection of AD. Hyperspectral Raman imaging along with hierarchical cluster analysis can be used for the detection of neuritic plaques and neurofibrillary tangles in label-free slices of human AD brain tissue (as shown in Fig. 3.2i). Tissue components including lipids, β -sheets, water, and proteins can be distinguished and quantified simultaneously using hyperspectral Raman imaging. The Raman fingerprint of plaques and tangles vary from the neighboring tissues. Lesions in pathological tissues distinguished by the storage of macromolecules with distinct molecular features can be identified using Hyperspectral Raman imaging [36].

3.3 Conclusions

Raman-based approaches have proven to be extremely beneficial in biomedical diagnosis, particularly in the detection of NDs, which has been a growing concern in the modern world. Raman spectroscopy has a high chemical specificity; however, inherently weak signals are obtained which open up possibilities of using an alternative method including SERS. Effective microscopy techniques are required to distinguish between healthy and diseased cells or tissues. Raman-based microscopy techniques like CARS microscopy, SRS microscopy, and hyperspectral Raman imaging provide precise data along with stain-free imaging. Table 3.2 shows a comparison of the various Raman techniques. Raman spectroscopic techniques use auto-fluorescence from the samples to obtain images. Hence, the quality of the obtained images depends on the nature of the sample. In vivo diagnosis using Raman techniques can potentially damage the sample due to long laser exposure that depends on the excitation wavelengths. As a result, in vivo measurements must be investigated using lower energy excitation wavelengths, which results in longer integration times due to the weak effect. By decreasing the excitation power and using setups with water immersion objectives, the damages to the samples can be prevented. However, in vivo Raman spectroscopic techniques are currently only employed in animal models; in humans, they are limited to ophthalmology, a thin layer of skin, or in combination with endoscopy. When compared to many other techniques, Raman-based techniques can provide high quality spectral information regarding the pathology and disease progression of NDs if methods to implement them under in vivo conditions in humans are improved.

Table 3.2 Comparison of various Raman spectroscopic and microscopic techniques

Technique	Principle and resolution	Advantages	Limitations	Applications	References
<i>Spectroscopy</i>					
Raman spectroscopy	Inelastic scattering of photons when light is incident on a sample. Spectral resolution: 7–10 cm^{-1}	High chemical specificity, sensitive, non-destructive, simple instrumentation, and label-free	Weak signals	Probing biochemical changes in tissues in situ	Hanlon et al. (2000) [6], Huefner et al. (2020) [38], Ramirez-Elias et al. (2018) [41]
SERS	Localized surface Plasmon resonance (LSPR) Spectral resolution: 200 nm—XY plane, 500 nm—YZ plane	Sensitive, rapid, label-free, and has multiplexing capabilities	Metallic nanoparticles used can be toxic to the physiological environment	Detection of neurotransmitters	An et al. (2015) [10], Moody and Sharma (2018) [7], Payne et al. (2020) [25]
<i>Microscopy</i>					
Spontaneous Raman microscopy	When a laser is incident at the pump frequency, it scatters inelastically to produce Raman signals at Stokes and anti-Stokes frequencies. Spectral resolution: 7 cm^{-1}	Label-free chemical contrast and real-time imaging	Extremely small cross-section	Monitoring biomolecule concentrations within cells, studying drug delivery, and tissue	Antonio and Schultz (2014) [15], Yu et al. (2014) [50], Krafft et al. (2016) [17]
CARS microscopy	When the difference in pump and Stokes frequencies correspond to a molecule's vibrational frequency, CARS is produced Spectral resolution: 0.3 μm -lateral plane, 1.5 μm -axial direction	High sensitivity and video-rate imaging	Non-resonant background	Chemical and morphological information from biological samples	Evans et al. (2005) [14], 2007 [13], Antonio and Schultz, 2014 [15], Yu et al. (2014) [76]

(continued)

Table 3.2 (continued)

Technique	Principle and resolution	Advantages	Limitations	Applications	References
SRS microscopy	Energy exchange between pump and Stokes beams creates loss and gain of intensities of these beams, respectively. These gain and loss signals are used to differentiate the target molecules. Spectral resolution: $\sim 25 \text{ cm}^{-1}$	The non-resonant background is not present	Less intense compared to CARS	For imaging the amyloid plaques in AD	Ji et al. (2013) [77], Tipping et al. (2016) [53], Figueroa et al. (2018) [18]
Hyperspectral Raman imaging	Merger of spatial and spectral data. Spectral resolution: $\sim 10 \text{ cm}^{-1}$	Facilitates visualization of the spread of different chemical components in the sample	Complex instrumentation	Evaluation of tissue components (i.e., proteins, lipids, water, β -sheets)	Lohumi et al. (2017) [78], Michael et al. (2017) [36], Figueroa et al. (2018) [18]

Acknowledgments This work was supported by Science and Engineering Research Board (SERB), Government of India (No. CRG/2020/004205) and Ramalingaswami Re-entry Fellowship, Department of Biotechnology, Government of India (No. BT/RLF/Re-entry/49/2018) to GG. SFM was supported by Dr. TMA Pai Ph.D. scholarship, Manipal Academy of Higher Education, Manipal, India. ABS was supported by Innovation in Science Pursuit for Inspired Research (INSPIRE) fellowship, Department of Science and Technology, Government of India (IF190783). The authors thank Manipal School of Life Sciences, Manipal Academy of Higher Education (MAHE), Manipal for the infrastructure and support.

Conflict of Interest The authors declare no conflict of interest.

Author Contributions V.G.P. and G.G. conceptualized the manuscript. All authors contributed to the literature search, writing and editing of the manuscript. All authors read and approved this manuscript.

Consent for Publication The authors affirm that necessary permissions were obtained for the publication of images in the figures.

References

1. Heemels M-T (2016) Neurodegenerative diseases. *Nature* 539(7628):179
2. Devitt G, Howard K, Mudher A, Mahajan S (2018) Raman spectroscopy: an emerging tool in neurodegenerative disease research and diagnosis. *ACS Chem Neurosci* 9(3):404–420
3. Kandlur A, Satyamoorthy K, Gangadharan G (2020) Oxidative stress in cognitive and epigenetic aging: a retrospective glance. *Front Mol Neurosci* 13:41
4. Ryzhikova E, Kazakov O, Halamkova L, Celmins D, Malone P, Molho E et al (2015) Raman spectroscopy of blood serum for Alzheimer’s disease diagnostics: specificity relative to other types of dementia. *J Biophotonics* 8(7):584–596
5. Moody AS, Payne TD, Barth BA, Sharma B (2020) Surface-enhanced spatially-offset Raman spectroscopy (SESORS) for detection of neurochemicals through the skull at physiologically relevant concentrations. *Analyst* 145(5):1885–1893
6. Hanlon EB, Manoharan R, Koo T-W, Shafer KE, Motz JT, Fitzmaurice M et al (2000) Prospects for in vivo Raman spectroscopy. *Phys Med Biol* 45(2):R1–R59
7. Moody AS, Sharma B (2018) Multi-metal, multi-wavelength surface-enhanced Raman spectroscopy detection of neurotransmitters. *ACS Chem Neurosci* 9(6):1380–1387
8. Villar-Piqué A, Schmitz M, Candelise N, Ventura S, Llorens F, Zerr I (2018) Molecular and clinical aspects of protein aggregation assays in neurodegenerative diseases. *Mol Neurobiol* 55(9):7588–7605
9. Gómez-Benito M, Granado N, García-Sanz P, Michel A, Dumoulin M, Moratalla R (2020) Modeling Parkinson’s disease with the alpha-synuclein protein. *Front Pharmacol* 11:356
10. An JH, Choi D-K, Lee K-J, Choi J-W (2015) Surface-enhanced Raman spectroscopy detection of dopamine by DNA targeting amplification assay in Parkinson’s model. *Biosens Bioelectron* 67:739–746
11. Moody AS, Baghernejad PC, Webb KR, Sharma B (2017) Surface enhanced spatially offset Raman spectroscopy detection of neurochemicals through the skull. *Anal Chem* 89(11):5688–5692
12. Moore TJ, Moody AS, Payne TD, Sarabia GM, Daniel AR, Sharma B (2018) In vitro and in vivo SERS biosensing for disease diagnosis. *Biosensors* 8(2):46
13. Evans CL, Xu X, Kesari S, Xie XS, Wong STC, Young GS (2007) Chemically-selective imaging of brain structures with CARS microscopy. *Opt Express* 15(19):12076–12087

14. Evans CL, Potma EO, Puoris'haag M, Côté D, Lin CP, Xie XS (2005) Chemical imaging of tissue in vivo with video-rate coherent anti-Stokes Raman scattering microscopy. *Proc Natl Acad Sci USA* 102(46):16807–16812
15. Antonio KA, Schultz ZD (2014) Advances in biomedical Raman microscopy. *Anal Chem* 86(1):30–46
16. Periasamy A, Mazumder N, Sun Y, Christopher KG, Day RN (2015) FRET microscopy: basics, issues and advantages of FLIM-FRET imaging. In: Becker W (ed) *Advanced time-correlated single photon counting applications* [internet]. Springer series in chemical physics. Springer International Publishing, Cham, pp 249–276. https://doi.org/10.1007/978-3-319-14929-5_7
17. Krafft C, Schie IW, Meyer T, Schmitt M, Popp J (2016) Developments in spontaneous and coherent Raman scattering microscopic imaging for biomedical applications. *Chem Soc Rev* 45(7):1819–1849
18. Figueroa B, Fu W, Nguyen T, Shin K, Manifold B, Wise F et al (2018) Broadband hyperspectral stimulated Raman scattering microscopy with a parabolic fiber amplifier source. *Biomed Opt Express* 9(12):6116–6131
19. Mazumder N, Qiu J, Foreman MR, Romero CM, Hu C-W, Tsai H-R et al (2012) Polarization-resolved second harmonic generation microscopy with a four-channel Stokes-polarimeter. *Opt Express* 20(13):14090–14099
20. Kao F-J, Deka G, Mazumder N (2015) Cellular autofluorescence detection through FLIM/FRET microscopy. In: Lee C-C (ed) *The current trends of optics and photonics* [internet]. Topics in applied physics. Springer, Dordrecht, pp 471–482. https://doi.org/10.1007/978-94-017-9392-6_26
21. Freudiger CW, Min W, Saar BG, Lu S, Holtom GR, He C et al (2008) Label-free biomedical imaging with high sensitivity by stimulated Raman scattering microscopy. *Science* 322(5909):1857–1861
22. Zumbusch A, Holtom GR, Xie XS (1999) Three-dimensional vibrational imaging by coherent anti-Stokes Raman scattering. *Phys Rev Lett* 82(20):4142–4145
23. Downes A, Elfick A (2010) Raman spectroscopy and related techniques in biomedicine. *Sensors* 10(3):1871–1889
24. Choo L-P, Mansfield JR, Pizzi N, Somorjai RL, Jackson M, Halliday WC et al (1995) Infrared spectra of human central nervous system tissue: diagnosis of Alzheimer's disease by multivariate analyses. *Biospectroscopy* 1(2):141–148
25. Payne TD, Moody AS, Wood AL, Pimiento PA, Elliott JC, Sharma B (2020) Raman spectroscopy and neuroscience: from fundamental understanding to disease diagnostics and imaging. *Analyst* 145(10):3461–3480
26. Raman CV, Krishnan KS (1928) A new type of secondary radiation. *Nature* 121(3048):501–502
27. Singh RCV (2002) Raman and the discovery of the Raman effect. *Phys Perspect* 4(4):399–420
28. Czamara K, Majzner K, Pacia MZ, Kochan K, Kaczor A, Baranska M (2015) Raman spectroscopy of lipids: a review. *J Raman Spectrosc* 46(1):4–20
29. Rzhetskii A (2019) The recent advances in Raman microscopy and imaging techniques for biosensors. *Biosensors* 9(1):25
30. Fonseca EA, Lafetá L, Cunha R, Miranda H, Campos J, Medeiros HG et al (2019) A fingerprint of amyloid plaques in a bitransgenic animal model of Alzheimer's disease obtained by statistical unmixing analysis of hyperspectral Raman data. *Analyst* 144(23):7049–7056
31. Thomas GJ (1999) Raman spectroscopy of protein and nucleic acid assemblies. *Annu Rev Biophys Biomol Struct* 28(1):1–27
32. Guo T, Ding F, Li D, Zhang W, Cao L, Liu Z (2019) Full-scale label-free surface-enhanced Raman scattering analysis of mouse brain using a black phosphorus-based two-dimensional nanoprobe. *Appl Sci* 9(3):398
33. Bégin S, Dupont-Therrien O, Bélanger E, Daradich A, Laffray S, De Koninck Y et al (2014) Automated method for the segmentation and morphometry of nerve fibers in large-scale CARS images of spinal cord tissue. *Biomed Opt Express* 5(12):4145–4161

34. Michael R, Otto C, Lenferink A, Gelpi E, Montenegro GA, Rosandić J et al (2014) Absence of amyloid-beta in lenses of Alzheimer patients: a confocal Raman microspectroscopic study. *Exp Eye Res* 119:44–53
35. Broadbent B, Tseng J, Kast R, Noh T, Brusatori M, Kalkanis SN et al (2016) Shining light on neurosurgery diagnostics using Raman spectroscopy. *J Neuro-Oncol* 130(1):1–9
36. Michael R, Lenferink A, Vrensen GFJM, Gelpi E, Barraquer RI, Otto C (2017) Hyperspectral Raman imaging of neuritic plaques and neurofibrillary tangles in brain tissue from Alzheimer's disease patients. *Sci Rep* 7(1):15603
37. Singh SP, Kang S, Kang JW, So PTC, Dasari RR, Yaqoob Z et al (2017) Label-free characterization of ultra violet-radiation-induced changes in skin fibroblasts with Raman spectroscopy and quantitative phase microscopy. *Sci Rep* 7(1):10829
38. Huefner A, Kuan W-L, Mason SL, Mahajan S, Barker RA (2020) Serum Raman spectroscopy as a diagnostic tool in patients with Huntington's disease. *Chem Sci* 11(2):525–533
39. Ember KJI, Hoeve MA, McAughtrie SL, Bergholt MS, Dwyer BJ, Stevens MM et al (2017) Raman spectroscopy and regenerative medicine: a review. *NPJ Regen Med* 2(1):1–10
40. Kajimoto S, Takeuchi M, Nakabayashi T (2017) Raman imaging microscopy for quantitative analysis of biological samples. In: Dmitriev RI (ed) *Multi-parametric live cell microscopy of 3D tissue models* [internet], *Advances in experimental medicine and biology*. Springer International Publishing, Cham, pp 163–172. https://doi.org/10.1007/978-3-319-67358-5_12
41. Ramirez-Elias MG, Gonzalez F (2018) Raman spectroscopy for in vivo medical diagnosis. *IntechOpen*, London, pp 293–312
42. Eravuchira PJ, Banchelli M, D'Andrea C, Angelis MD, Matteini P, Gannot I (2020) Hollow core photonic crystal fiber-assisted Raman spectroscopy as a tool for the detection of Alzheimer's disease biomarkers. *J Biomed Opt* 25(7):077001
43. Turk N, Raza A, Wuytens P, Demol H, Van Daele M, Detavernier C et al (2019) Comparison of free-space and waveguide-based SERS platforms. *Nanomaterials* 9(10):1401
44. Golreihani A, Steuwe C, Woelders L, Deprez A, Fujita Y, Vellekoop J et al (2018) Improving preservation state assessment of carbonate microfossils in paleontological research using label-free stimulated Raman imaging. *PLoS One* 13(7):e0199695
45. Gruber F, Wollmann P, Grählert W, Kaskel S (2018) Hyperspectral imaging using laser excitation for fast Raman and fluorescence hyperspectral imaging for sorting and quality control applications. *J Imaging* 4(10):110
46. Hussein MA, El-Said WA, Abu-Zied BM, Choi J-W (2020) Nanosheet composed of gold nanoparticle/graphene/epoxy resin based on ultrasonic fabrication for flexible dopamine biosensor using surface-enhanced Raman spectroscopy. *Nano Converg* 7(1):15
47. Paulsen JS, Langbehn DR, Stout JC, Aylward E, Ross CA, Nance M et al (2008) Detection of Huntington's disease decades before diagnosis: the predict-HD study. *J Neurol Neurosurg Psychiatry* 79(8):874–880
48. Ahmed MM, Hussein MMA (2017) Neurotoxic effects of silver nanoparticles and the protective role of rutin. *Biomed Pharmacother* 90:731–739
49. Schapira AHV (2002) Neuroprotection and dopamine agonists. *Neurology* 58(4 Suppl 1):S9–S18
50. Yu X, He X, Yang T, Zhao L, Chen Q, Zhang S et al (2018) Sensitive determination of dopamine levels via surface-enhanced Raman scattering of Ag nanoparticle dimers. *Int J Nanomed* 13:2337–2347
51. Teleanu DM, Chircov C, Grumezescu AM, Volceanov A, Teleanu RI (2018) Impact of nanoparticles on brain health: an up to date overview. *J Clin Med* 7(12):490
52. Minamikawa T, Harada Y, Takamatsu T (2015) Ex vivo peripheral nerve detection of rats by spontaneous Raman spectroscopy. *Sci Rep* 5(1):17165
53. Tipping WJ, Lee M, Serrels A, Brunton VG, Hulme AN (2016) Stimulated Raman scattering microscopy: an emerging tool for drug discovery. *Chem Soc Rev* 45(8):2075–2089
54. Durrant B, Trappett M, Shipp D, Nottingher I (2019) Recent developments in spontaneous Raman imaging of living biological cells. *Curr Opin Chem Biol* 51:138–145

55. Eberhardt K, Stiebing C, Matthäus C, Schmitt M, Popp J (2015) Advantages and limitations of Raman spectroscopy for molecular diagnostics: an update. *Expert Rev Mol Diagn* 15(6): 773–787
56. Ji M, Arbel M, Zhang L, Freudiger CW, Hou SS, Lin D et al (2018) Label-free imaging of amyloid plaques in Alzheimer's disease with stimulated Raman scattering microscopy. *Sci Adv* 4(11):eaat7715
57. Tu H, Boppart SA (2014) Coherent anti-Stokes Raman scattering microscopy: overcoming technical barriers for clinical translation. *J Biophotonics* 7(1–2):9–22
58. Nandakumar P, Kovalev A, Volkmer A (2009) Vibrational imaging based on stimulated Raman scattering microscopy. *N J Phys* 11(3):033026
59. Ozaki Y (1988) Medical application of Raman spectroscopy. *Appl Spectrosc Rev* 24(3–4): 259–312
60. Folic A, Min W, Wang MC (2011) Label-free imaging of lipid dynamics using coherent anti-Stokes Raman scattering (CARS) and stimulated Raman scattering (SRS) microscopy. *Curr Opin Genet Dev* 21(5):585–590
61. Krafft C, Dietzek B, Popp J, Schmitt M (2012) Raman and coherent anti-Stokes Raman scattering microspectroscopy for biomedical applications. *J Biomed Opt* 17(4):040801
62. Mazumder N, Lyn RK, Singaravelu R, Ridsdale A, Moffatt DJ, Hu C-W et al (2013) Fluorescence lifetime imaging of alterations to cellular metabolism by domain 2 of the hepatitis C virus core protein. *PLoS One* 8(6):e66738
63. Canta A, Chiorazzi A, Carozzi VA, Meregalli C, Oggioni N, Bossi M et al (2016) Age-related changes in the function and structure of the peripheral sensory pathway in mice. *Neurobiol Aging* 45:136–148
64. Ozeki Y, Dake F, Kajiyama S, Fukui K, Itoh K (2009) Analysis and experimental assessment of the sensitivity of stimulated Raman scattering microscopy. *Opt Express* 17(5):3651–3658
65. Goedert M, Spillantini MG, Del Tredici K, Braak H (2013) 100 years of Lewy pathology. *Nat Rev Neurol* 9(1):13–24
66. Imitola J, Rasmussen S, Liu Y, Chitnis T, Khoury S, Côté D et al (2011) Multimodal coherent anti-Stokes Raman scattering microscopy reveals microglia-associated myelin and axonal dysfunction in multiple sclerosis-like lesions in mice. *J Biomed Opt* 16(2):021109
67. Wakabayashi K, Tanji K, Odagiri S, Miki Y, Mori F, Takahashi H (2013) The Lewy body in Parkinson's disease and related neurodegenerative disorders. *Mol Neurobiol* 47(2):495–508
68. Shahmoradian SH, Lewis AJ, Genoud C, Hench J, Moors TE, Navarro PP et al (2019) Lewy pathology in Parkinson's disease consists of crowded organelles and lipid membranes. *Nat Neurosci* 22(7):1099–1109
69. Tian F, Yang W, Mordes DA, Wang J-Y, Salameh JS, Mok J et al (2016) Monitoring peripheral nerve degeneration in ALS by label-free stimulated Raman scattering imaging. *Nat Commun* 7(1):13283
70. Ji M, Lewis S, Camelo-Piragua S, Ramkisson SH, Snuderl M, Venetti S et al (2015) Detection of human brain tumor infiltration with quantitative stimulated Raman scattering microscopy. *Sci Transl Med* 7(309):309ra163
71. Pointer KB, Zhang RR, Kuo JS, Dempsey RJ (2014) Detecting brain tumor with Raman scattering microscopy. *Neurosurgery* 74(2):N12–N14
72. Jestel NL, Shaver JM, Morris MD (1998) Hyperspectral Raman line imaging of an aluminosilicate glass. *Appl Spectrosc* 52(1):64–69
73. Christensen KA, Morris MD (1998) Hyperspectral Raman microscopic imaging using Powell lens line illumination. *Appl Spectrosc* 52(9):1145–1147
74. Napoli CD, Pope I, Masia F, Watson P, Langbein W, Borri P (2014) Hyperspectral and differential CARS microscopy for quantitative chemical imaging in human adipocytes. *Biomed Opt Express* 5(5):1378–1390

75. Masia F, Karuna A, Borri P, Langbein W (2015) Hyperspectral image analysis for CARS, SRS, and Raman data. *J Raman Spectrosc* 46(8):727–734
76. Yu Y, Ramachandran PV, Wang MC (2014) Shedding new light on lipid functions with CARS and SRS microscopy. *Biochim Biophys Acta Mol Cell Biol Lipids* 1841(8):1120–1129
77. Ji M, Orringer DA, Freudiger CW, Ramkissoon S, Liu X, Lau D et al (2013) Rapid, label-free detection of brain tumors with stimulated Raman scattering microscopy. *Sci Transl Med* 5(201): 201ra119
78. Lohumi S, Kim MS, Qin J, Cho B-K (2017) Raman imaging from microscopy to macroscopy: quality and safety control of biological materials. *TrAC Trends Anal Chem* 93:183–198



Drosophila Brain Advanced Multiphoton Imaging

4

Juan M. Bueno, Yu-Shuo Liao, Francisco J. Ávila, Shiu-Feng Cheng, and Shi-Wei Chu

Abstract

Multiphoton fluorescence microscopy is being widely used in neuroscience. The optical heterogeneity of brain tissues imposes a major limitation that can be minimized by means of this imaging technique, often in combination with adaptive optics approaches. Animal models such as mouse, zebrafish, and *Drosophila* are employed to study both brain structure and functional aspects. This chapter presents a review on the different adaptive optics multiphoton devices used to enhance the visualization of ex vivo/in vivo brain tissues, with a special interest in *Drosophila*. Moreover, some new results on this topic are also introduced and discussed.

Keywords

Multiphoton microscopy · Adaptive optics · *Drosophila* brain

J. M. Bueno (✉)

Laboratorio de Óptica, Universidad de Murcia, Murcia, Spain

e-mail: bueno@um.es

Y.-S. Liao · S.-F. Cheng

Department of Physics and Molecular Imaging Center, National Taiwan University, Taipei, Taiwan

F. J. Ávila

Departamento de Física Aplicada, Universidad de Zaragoza, Zaragoza, Spain

S.-W. Chu

Department of Physics and Molecular Imaging Center, National Taiwan University, Taipei, Taiwan

Brain Research Center, National Tsing Hua University, Hsinchu, Taiwan

© The Author(s), under exclusive license to Springer Nature Singapore Pte Ltd. 2022

59

N. Mazumder et al. (eds.), *Advances in Brain Imaging Techniques*,

https://doi.org/10.1007/978-981-19-1352-5_4

4.1 Introduction: *Drosophila* as an Animal Model for Brain Analysis

Since 1910, Thomas Hunt Morgan started using *Drosophila* to study heredity and confirmed the chromosome theory of inheritance [1], this animal model became widely used. There are eight Nobel prizes awarded to researchers involved in *Drosophila* studies [2]. In the field of neuroscience, *Drosophila* exhibits several particular advantages, making it a model system of choice [3]. In the following sections, we briefly introduce its advantages, in particular for brain imaging.

First, the brain of *Drosophila* is not only complicated enough [4] but small enough (about $700 \times 300 \times 300 \mu\text{m}^3$ as estimated by Zheng et al. [5]) thus able to be completely mapped by optical microscopy with sub-cellular resolution. Second, its complete genome sequence was unraveled in 2000 [6]. It is estimated that about 60% of genes are conserved between *Drosophila* and the human genome [7] and 75% of human diseases have homologs in *Drosophila* [8]. As an example, Alzheimer's disease and Parkinson's disease models have been found in *Drosophila* [9, 10]. The similarity to humans and much-simplified structure makes *Drosophila* an ideal model organism for whole-brain analysis.

In 2011, the combination of these two advantages led to a “common standardized framework to produce a virtual fly brain” (Fig. 4.1) [11]. The open database FlyCircuit was constructed [12]. This contained 16,000 single neurons with detailed morphology through high-resolution confocal microscopy and optical clearing. The number of neurons now in the database is about 50,000 (FlyCircuit 1.3) and will soon expand to 90,000. Except for simple model animals like *C. elegans*, whose 302 neurons are all identified, *Drosophila* is the only model animal having more than half of the total neurons in the brain (135,000) structurally and genetically registered, with more than 10,000 drivers. The nearly whole-brain structure and genetic database is the third advantage, offering a comprehensive connectivity map.

Fourth, *Drosophila* is the only model animal that has whole-brain electron microscopy data with 8-nm 3D resolution [5]. Extensive efforts of automatic image segmentation and recognition are ongoing [13], pushing forward establishing the first whole-brain structural connectome with resolution better than synapses.

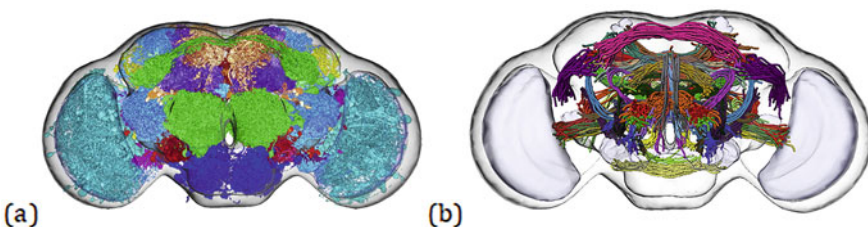


Fig. 4.1 A standardized framework of a virtual *Drosophila* brain. (a) Distribution of 41 putative local processing units (LPUs), which are the main hubs for signal recognition and management. (b) 58 interregional fiber bundles that are the major pathway of signal propagation and exchange. (Adapted with permission from Chiang et al. [11] © Elsevier)

However, the high-resolution structural connectomes, based on either light or electron microscopy, are not adequate to understand the brain. Like a computer, a functional brain should be composed of both hardware and software. Structural mapping provides hardware composition, but software, which may be defined as “the rule and operating information used by the brain,” requires the study of emergent properties of the pan-neuron/synapse functional connectivity across the whole-brain [14]. The advantages of small brain size and the unique single-neuron genetic database, together with the rapidly developing fluorescent proteins and optogenetic tools, make *Drosophila* a unique model animal that nearly any specific neuron in the whole-brain could be precisely labeled and manipulated. For example, various genetically encoded indicators, including calcium, voltage, pH, neurotransmitter, have been utilized in *Drosophila* [15], providing the potential to construct functional connectomics maps via watching neurons in action across the whole-brain.

4.2 Functional Multiphoton Microscopy of the *Drosophila* Brain

When considering an imaging technique, there are typically four important parameters to consider: contrast, resolution, penetration depth, and speed. A recent review provides a detailed overview of multiphoton (MP) advantages in neuroscience [14]. Here we focus on recent developments of MP microscopy techniques to probe neural activities in *Drosophila* with genetically encoded fluorescent indicators, which give functional contrast. The resolution of MP microscopy is typically a sub-micrometer, which is more than adequate to capture cellular dynamics. One of the main advantages of MP microscopy is its intrinsic optical sectioning and improved penetration depth due to nonlinear and long-wavelength excitations, respectively. *Drosophila* seems to be the best model animal to achieve whole-brain in vivo imaging at cellular resolution with MP microscopy; nevertheless, this has not been demonstrated in adult *Drosophila* until recently. The underlying mechanism from the aberration of the trachea in this insect brain is introduced below.

The fourth parameter to take into account while MP imaging is speed. A strategy to boost MP imaging speed up to a millisecond scale will also be discussed in Sect. 4.2.2. As described in Sect. 4.2.3, the combination of precise optogenetic stimulation and high-speed MP volumetric microscopy demonstrate functional connectomics establishment in the visual circuit of *Drosophila*.

4.2.1 Depth

The most common approach nowadays is to optically clear the sample to enhance imaging depth in a biological structure [16]. Nevertheless, most of the clearing reagents are not compatible with in vivo observations. Therefore, to achieve in vivo functional imaging, the strong scattering/aberration of the brain is the main

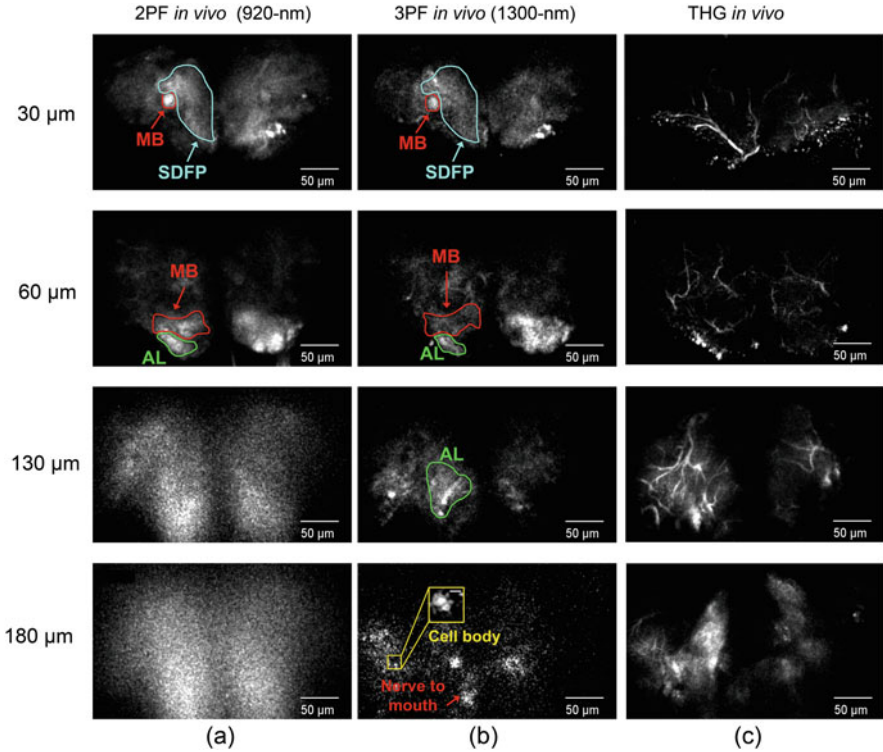


Fig. 4.2 Penetration comparison of two-photon, three-photon, and THG microscopies in a living *Drosophila* brain. The advantage of the higher order optical nonlinear excitations in this type of tissue can be qualitatively observed. (a) Two-photon excited GFP with 920-nm laser wavelength. The fluorescence images become blurred at $>100\text{-}\mu\text{m}$ depth. (b) Three-photon excited GFP with the 1300-nm laser wavelength, showing clear images all the way to the bottom of the brain. (c) THG contrast reveals the distribution of the trachea across the whole-brain. (Figures have been reprinted with permission from Hsu et al. [18] © The Optical Society)

bottleneck. In a living, uncleared mouse brain, MP microscopy can easily penetrate over $500\text{ }\mu\text{m}$ [17]. Since the thickness of a *Drosophila* brain is about $300\text{ }\mu\text{m}$, this should be straightforward to map the whole-brain. However, it has been found by these authors that in a living *Drosophila* brain, MP imaging reaches only about $100\text{ }\mu\text{m}$ (Fig. 4.2a), and no literature shows deeper penetration.

To understand this limited MP imaging depth, the signal attenuation coefficient in different treated *Drosophila* brain samples (i.e., in vivo and degas) was quantified [18]. Apart from the scattering effects from neuron tissues, the densely distributed and branched tracheal system caused strong aberration and scattering (mainly due to the refractive index difference between air and tissue interface).

To reduce these effects, one plausible solution is to use long-wavelength excitation. It has been shown that scattering and aberration attenuate fluorescence signals with λ^{-2} and $\lambda^{-0.9}$ dependencies, respectively [18]. High order nonlinear excitations

are required when using 1300 nm, together with the mature genetically labeled green fluorescent proteins (GFP). Panels in Fig. 4.2b show that the enhancement in penetration depth using three-photon excitation reaches the bottom of a living *Drosophila* brain. In addition, Fig. 4.2c presents that third-harmonic generation (THG), a complementary contrast of the three-photon excitation process, reveals the trachea distribution within the *Drosophila* brain.

4.2.2 High-Speed Volumetric Imaging

With adequate imaging depth, whole-brain observation in *Drosophila* becomes feasible. However, to study the emergent properties of a brain, it is necessary to capture high-speed neural connection dynamics. The observables of brain function include voltage changes during neuron firing action potentials and subsequent calcium concentration variations. The voltage signal transduction is on the scale of milliseconds, while calcium dynamics is sub-second level. In addition, the neuronal connection inside a brain is three-dimensional, thus to capture these signals, not only high-speed acquisition but also volumetric imaging are required. A representative technique is light-sheet microscopy, which achieves 200 volumes/s and relies on wide-field thin-layer excitation combined with wide-field detection [19]. Nevertheless, in a scattering tissue such as the *Drosophila* brain, its wide-field detection degrades rapidly with imaging depth. As mentioned in the previous section, MP imaging alleviates the depth issue, but is typically much slower. The state-of-the-art MP microscopy reaches 3000 frames/s [20], via multifocal scanning, although it is two-dimensional imaging. By combining axial extension techniques such as Bessel beam volumetric MP microscopy reaches a 50 Hz imaging rate in the mouse brain [21]. Nevertheless, the Bessel beam approach integrates the axial signals together in one projection, thus losing the optical sectioning capability and being restricted to sparsely labeled samples.

An interesting technical advance is to use high-speed axial scan devices [22] to enable fast volumetric imaging in the living brain. One of the fastest z-scan devices is the tunable acoustic gradient-index (TAG) lens [23]. The TAG lens is inertia-free and provides axial scan at 100 kHz to MHz rate, enabling the 200 volume/s light-sheet microscopy that we mentioned above. It has also been integrated with two-photon microscopy [24], achieving a 10-Hz volumetric imaging rate with full 3D resolution.

High-speed volumetric MP images have been obtained by introducing a TAG lens as an axial extension in a 2D MP high-speed scanning system [25]. Figure 4.3a compares images acquired with conventional MP microscopy (left) and a TAG-lens-based volumetric system (right). The former acquires only one optical section of a *Drosophila* brain, while the latter collects the same *XY* field-of-view within the same acquisition time (~ 0.5 s), but an *XYZ* volume of $320 \times 180 \times 120 \mu\text{m}^3$. Note that the 120 μm depth is the limit of MP microscopy penetration in the *Drosophila* brain (see Sect. 4.2.1).

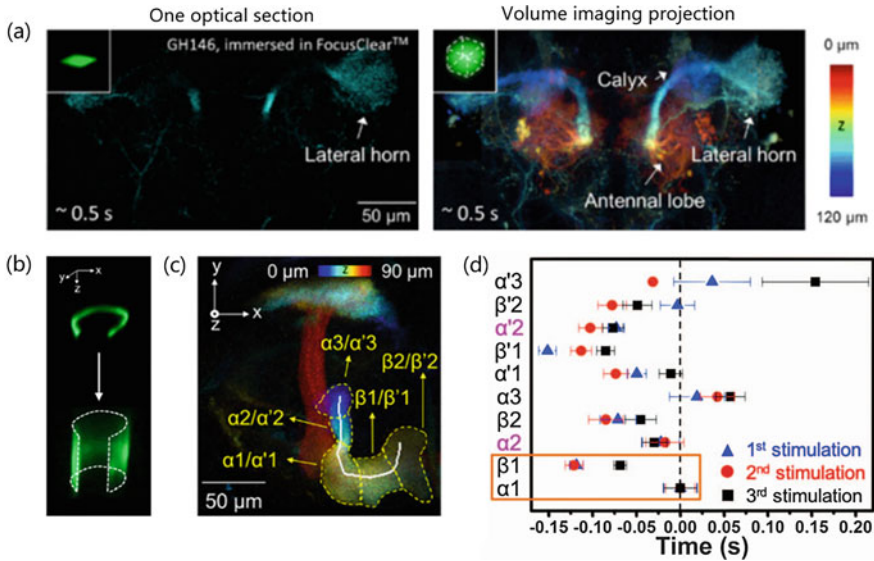


Fig. 4.3 High-speed volumetric imaging of the *Drosophila* brain. (a) The olfactory circuit of *Drosophila*: conventional MP imaging takes 0.5 s for an optical section and the whole 3D structure of the circuit acquired using the same acquisition time (right). (b) The curve on top is the laser line scanning trajectory. By applying a TAG lens as an axial extension, the ribbon scanning of the bottom is obtained. (c) The MB and its subunits. The slash indicates two laterally overlapped subunits that are axially separated. The white curve on the image is the trajectory of the ribbon scan on the X - Y view. (d) The response time of each subunit after receiving an olfactory stimulus. ((a, b) Reproduced with permission from AAPPS Bulletin. (c, d) Reprinted with permission from Hsu et al. [25] © The Optical Society)

To further push temporal resolution down to millisecond scale, a ribbon scan mode has been proposed combining an XY line scan and a TAG lens (Fig. 4.3b) [25]. This high-speed ribbon scanning technique has been used to explore the mushroom body (MB), which is the olfactory learning and memory central processing unit of *Drosophila*. Figure 4.3c presents an example of the structure of a GCaMP-labeled MB. The subunits of MB ($\alpha 1/\alpha'1$, $\alpha 2/\alpha'2$, $\alpha 3/\alpha'3$, $\alpha 1/\alpha'1$, $\alpha 2/\alpha'2$) are marked, whose colors represent their locations at different depths. Anatomically, upstream neural signals should start from $\alpha 1$, then propagate to $\alpha 3$ and $\alpha 2$. The ribbon scan technique overcomes the limitation of conventional 2D planar microscopy, achieving functional imaging of these subunits simultaneously. The solid white line in Fig. 4.3c shows the location of our ribbon scan, which intersects with all these subunits in 3D. Figure 4.3d shows the subunit response time after an olfactory stimulus. Surprisingly, the result indicates that the neuronal firing of $\alpha 1$ is not the earliest event, contradicting the anatomical prediction. This result indicates that it might be risky to understand the brain function only by structural imaging and points out the importance of functional imaging.

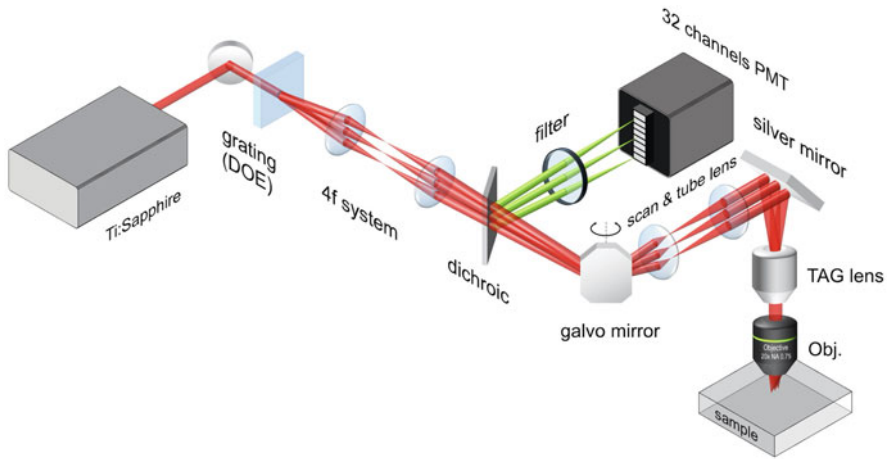


Fig. 4.4 32 Channel volumetric imaging MP microscope. The three key components are the grating, the galvo mirror and the TAG lens. The former splits the laser into 32 beams, the galvo mirror enables the system to scan in 2D plane and the TAG lens converts the 2D scanning system into a volumetric one. For more details, see Tsai et al. [26]

The high-speed ribbon scanning technique was extended to 32 parallel ribbon scans to improve the full volumetric imaging rate. This provided an imaged larger region using the same exposure time [26]. The updated setup is depicted in Fig. 4.4. A grating converts a single beam into 32 beamlets, and a galvo mirror scans 32 beam spots into 32 lines. The TAG lens subsequently extends the 32 lines into 32 ribbons in the XZ plane. MP signals from these 32 ribbons are simultaneously collected by a 32-channel PMT. Combined with a $20\times$ objective, this system achieves $800(x) \times 200(y) \times 360(z) \mu\text{m}^3$ volume imaging within millisecond temporal resolution. This imaging rate and volume are enough to capture action potential dynamics in both a living mouse brain slice and across the whole *Drosophila* brain.

4.2.3 Functional Connectome

In addition to the capability of high-speed observation, to fully understand the neuronal interactions in a brain, it is necessary to perturb the system via precise stimulation. With the aid of optogenetic tools, a 3D all-optical physiology (AOP) platform to study the anterior visual pathway (AVP) of *Drosophila* has been recently developed [27]. Figure 4.5a shows the schematic design of the experimental system, which contains a red beam for multipoint stimulation and an MP beam for volumetric imaging. Figure 4.5b presents the concept of the connectome study of the AVP. A single-photon point focus is used to precisely stimulate part of the upstream neurons Intermediate-Lateral Anterior Optical Tubercle (AOTUil) that express CsChrimson

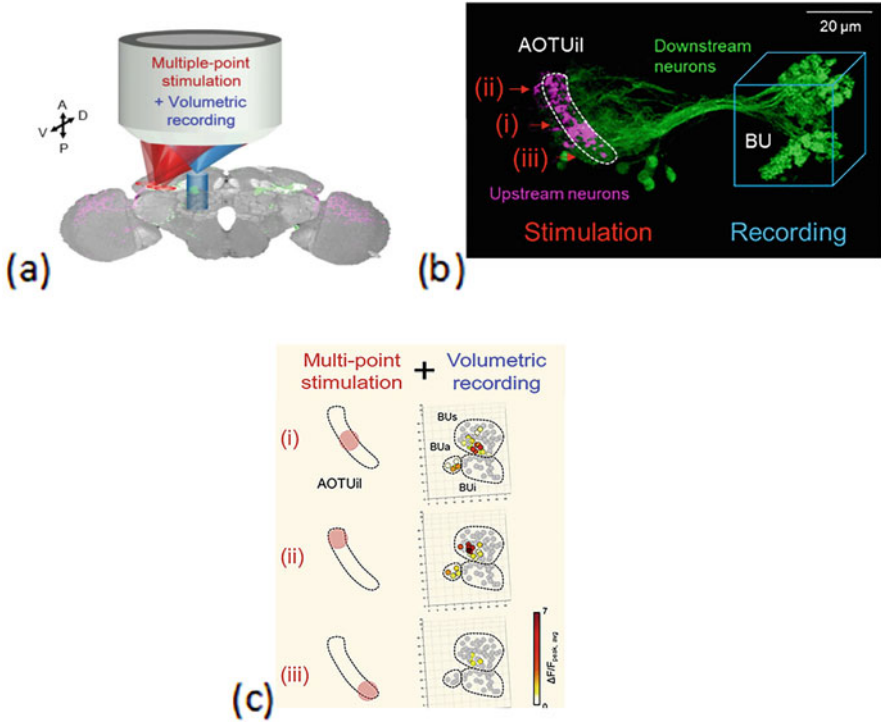


Fig. 4.5 (a) Illustration of the 3D AOP platform (Reproduced from Huang et al. [27]). (b) Structure of the AOTUil (upstream) and the BU (downstream) where red arrows indicate the stimulation points and the blue cubic represents the recording area (Reproduced from Lee [28]). (c) Stimulation on a different part of the AOTUil and functional response in the BU. The response of the stimulation is color-coded based on their response intensity (Reproduced with permission from Huang et al. [27] © Elsevier)

(purple color in Fig. 4.5b). Simultaneously, the MP TAG lens system achieves high-speed volumetric recording of downstream neurons. The dendritic output of the downstream neuron is a bulb (BU), which is a 3D structure that is composed of ~80 microglomeruli, each one 2 μm in diameter. Here BU is labeled with GCaMP6f (green color in Fig. 4.5b) such that we can record the calcium dynamics. Conventional 2D microscopy is not able to capture the response of all 3D-distributed 80 microglomeruli simultaneously, so volumetric imaging is necessary to unravel the functional coding. The result is given in Fig. 4.5c highlights the functional connectome mapping between AOTUil sub-compartments and BU microglomeruli. The connection between AOTUil and BUs or BUa has been separately reported in anatomical literature. Here we demonstrate that functionally, AOTUil directly links to BUs and BUa simultaneously, manifesting again the necessity of functional volumetric imaging.

4.3 Adaptive Optics Multiphoton Microscopy for 3D Imaging Improvement

MP microscopy is an imaging tool capable of imaging through scattering and opaque tissues [29]. Despite the fact that it is widely regarded as an effective tool for deep tissue imaging, its inherent confocality might be seriously affected as depth location increases (Fig. 4.6). In addition, scattering and optical aberrations created by the tissue reduce MP efficiency, which leads to poor MP image quality [30].

Although the laser beam and the optics might present some aberrations in an MP microscope, the most important contribution comes from the specimen itself. Then, deep imaging within a sample, in particular the brain, is challenging because this type of tissue presents random variations in the refractive index. Like many others, this inhomogeneity causes wavefront distortions, which turn the ideal focal spot of the microscope objective (i.e., diffraction-limited) into a distorted one (Fig. 4.7).

To mitigate such effects, the easier solution is to boost the incident power of the pulsed laser beam used as an illumination source. However, this increases the risk of tissue photodamage. An alternative is the use of adaptive optics (AO). Although originally used in Astronomy [31] since Neil et al. [32] combined AO correction and MP imaging for the first time, many authors have reported different, interesting, and useful results. The procedure is based on modifying the wavefront of the excitation beam to compensate for tissue-induced aberrations and recover diffraction-limited conditions. Nowadays, this is the most common solution to enable deep MP imaging within thick biological specimens, both *ex vivo* and *in vivo*.

Depending on how AO is implemented into the MP microscope, the approach is usually classified into direct and indirect. The former requires a sensor to measure the wavefront aberration (typically a Hartmann-Shack), and an adaptive element (either a deformable mirror or a spatial-light modulator) for correction [33–35]. On the other hand, indirect AO (non-direct or sensor-less) only involves the adaptive

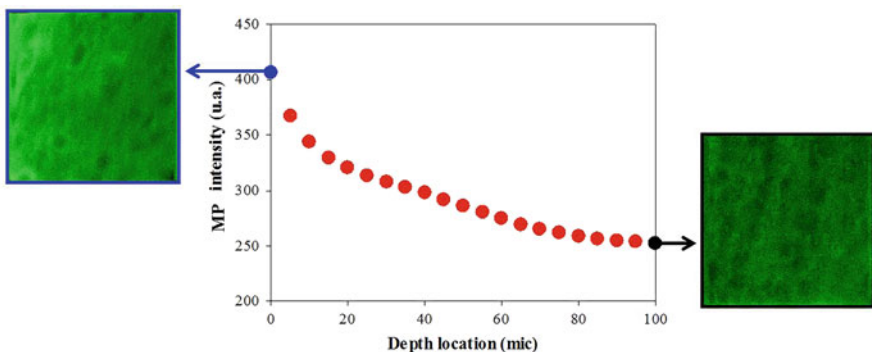


Fig. 4.6 MP intensity decreases as a function of depth in a cleared mouse brain. For this particular sample, the decrease at 100 μm was 38%. The reduction in contrast and resolution of MP images can be easily observed. Images were recorded at Laboratorio de Óptica, Universidad de Murcia, Spain. The sample was gently donated by Dr. Marta Agudo, Universidad de Murcia, Spain

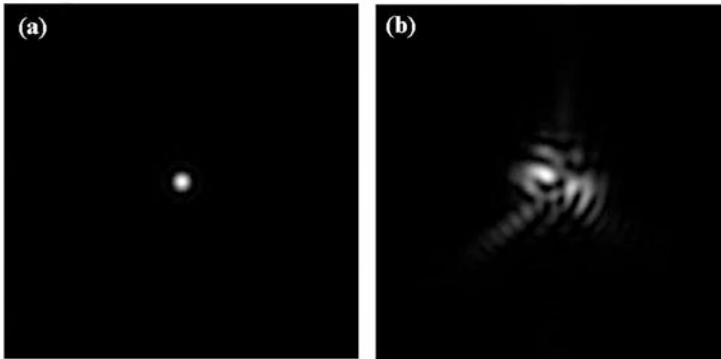


Fig. 4.7 Example of two focal spots (i.e., Point Spread Functions, PSFs) where the negative effects of the wavefront distortion are easily observed. (a) Diffraction-limited; (b) affected by aberrations

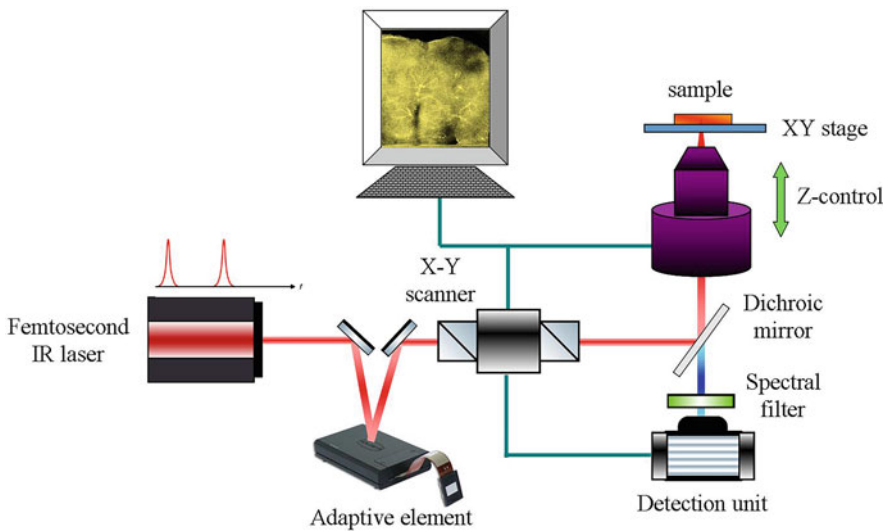


Fig. 4.8 Schematic of an AO-MP microscope. The most important components are shown

element. Figure 4.8 shows a simplified diagram of a typical AO-MP microscope. The incoming wavefront is changed to improve the image according to a pre-defined metric using different optimization algorithms (hill-climbing, genetic, stochastic, etc.) [36–38]. Since these algorithms modify the different Zernike modes of the wavefront, this is called modal wavefront sensor-less method. Another non-direct approach, known as pupil segmentation, allows for the correction of the local wavefront across different pupil subregions [39].

When the sample to be imaged is highly scattering, AO imaging is complicated since Zernike modes might be insufficient to describe the wavefront distortions [40]. To overcome this, an iterative MP adaptive compensation technique

(IMPACT) has been reported [41]. The essence of this wavefront engineering technique is to split the segments of the deformable mirror and run parallel phase modulation with each pixel at a unique frequency. The authors obtained super penetration and acquired clear MP images from deeper locations within the samples with reduced excitation laser power.

As most biological tissues, mammalian and *Drosophila* brains are not transparent and present major challenges when imaged through MP microscopy. In spite of this, to the best of our knowledge, Girkin and co-workers [42] reported the first AO-MP images of the rat brain tissue in 2007. Since then, significant research efforts have been devoted to developing AO-MP microscopes to image brain structures of animal models at different depth locations (both *ex vivo* and *in vivo*), using either direct or indirect AO procedures. As important as morphological imaging, AO correction also enhances contrast and increases the brightness of functional images [43].

In direct AO schemes, the light used by the sensor must come from a “guide star” within the sample (i.e., a point-like fluorescent source). This seems to be challenging for non-transparent specimens since the amount of ballistic light reaching the sensor might not be enough for an accurate assessment of the wavefront. Despite this, Tao et al. [44] applied this technique to a fixed brain tissue slice where a dendrite and a cell body of a neuron labeled with yellow fluorescent protein were tested as guide stars. Although they only reported confocal imaging, the corrected images showed signal increased ($3\times$) and contrast improvement at depths of 70 μm . On the opposite, Wang et al. [45, 46] combined a direct AO approach and a descanned laser-induced guided start to acquire MP images of large volumes ($>240\ \mu\text{m}$ per side) of the (transparent) brain of a living zebrafish embryo at a 14-ms update rate. In particular, a membrane-labeled subset of neurons was readily observable via MP imaging. The same method was extended to the (non-transparent) *in vivo* mouse brain, which strongly scatters visible light [47]. An exogenous dye was injected into the mouse cortex to generate the guide star signal. The method enabled MP imaging in the anesthetized animal to determine spine geometry functional imaging at $\sim 600\ \mu\text{m}$ below the pia mater. This imaging depth within the mouse brain was over-passed by Liu et al. [48] using awake mice. They combined direct AO and a guide star from MP excitation of cyanine5.5-conjugated dextran within microvessels. MP images from up to 800 μm below the pia in the parietal cortex of the awake mouse were acquired. In particular, MP images of the cortex microvasculature, dendritic spines, and thalamocortical axons were reported.

Although direct AO approaches have been shown to be robust and efficient, a number of indirect AO procedures have been used to enhance MP imaging of deep brain features and structures. Among the different indirect schemes, pupil segmentation seems to be the most useful in MP neuro-imaging. This is a zonal-based method where a spatial-light modulator divided into sub-areas is used. Although the optical aberrations varied across the sample and increased in magnitude with depth, Ji et al. [39] reported results on fixed mouse cortical slices illustrating the ability of this AO technique to improve signal and resolution to depths of 400 μm . The procedure was later applied with success in the living mouse cortex [45, 46]. The correction of aberrations yields enhanced MP images down to 450 μm over fields of

view of hundreds of μm . Moreover, a five-fold signal improvement for small neuronal structures as well as an increment in signal-to-noise ratio during functional Ca^{2+} imaging in single neurons. Submicrometer-sized spines deep within the mouse brain were resolved through AO pupil segmentation combined with frequency multiplexing. The correction was able to improve functional and structural imaging of fine neuronal processes over a large volume [43, 45, 46]. Pupil segmentation and MP comprehensive imaging have also been successful in characterizing the orientation tuning properties of thalamic boutons in the primary visual cortex of awake mice [49].

Although many experiments reported improved MP images based on two-photon excitation, three-photon microscopy also allowed deeper imaging in the *in vivo* mouse brain [50]. The use of a 1675-nm laser beam, a deformable mirror, and an iterative wavefront optimization (i.e., a sensor-less modal approach) were able to provide *in vivo* three-photon imaging of neurons and vasculature (at 780- μm and 1-mm depth, respectively) [51]. More recently, combining a pupil-segmentation-based AO module into a two- and three-photon fluorescence microscope has been reported to achieve drastic improvements in image quality. Synaptic structures in the mouse brain's deep cortical and sub-cortical areas have been resolved, along with somatosensory-evoked calcium responses in the mouse spinal cord at unprecedented depths *in vivo*.

IMPACT has been shown to extend the penetration depth within the brain with reduced photo damage, through aberration compensation and random scattering suppression (i.e., full correction). In fixed mouse brain samples, an intensity enhancement of $20\times$ was obtained at 400- μm depth, which provided high-quality three-dimensional images [41]. The benefit of using IMPACT has also been demonstrated in awake mice [52]. MP images of *in vivo* neurons imaging of the mouse cortex located at $\sim 660\ \mu\text{m}$ were successfully improved despite the unpredictable motions of the animal (Fig. 4.9). This technique was also used to perform calcium imaging of the neocortex (dendrites and spines) through the intact skull of adult mice and to image through the highly scattering white matter on the hippocampal surface (at a depth of $\sim 650\ \mu\text{m}$) [53]. Later on, IMPACT was combined with fast axial scanning (based on an optical phase-locked ultrasound lens) to obtain *in vivo* volumetric dynamic imaging at large depth of microglial in mouse brain cortex and mitochondrial network in mouse popliteal lymph node [54].

Another practical approach in strongly scattering samples is to use a coherence-gated wavefront sensor based on phase-shifting interferometry [55]. The procedure was able to correct for aberrations up to a depth $>400\ \mu\text{m}$ and improve both MP images from rat brain slices [56].

Apart from these AO techniques, other schemes have been developed in order to enhance MP neural imaging and understand brain functions at deep locations in rodent models. These include differential-aberration imaging [57], electric-field PSF assessment [58], large multi-pupil AO [59], aberration correction and divergence control [60], and gradient-index (GRIN) lenses [61], among others.

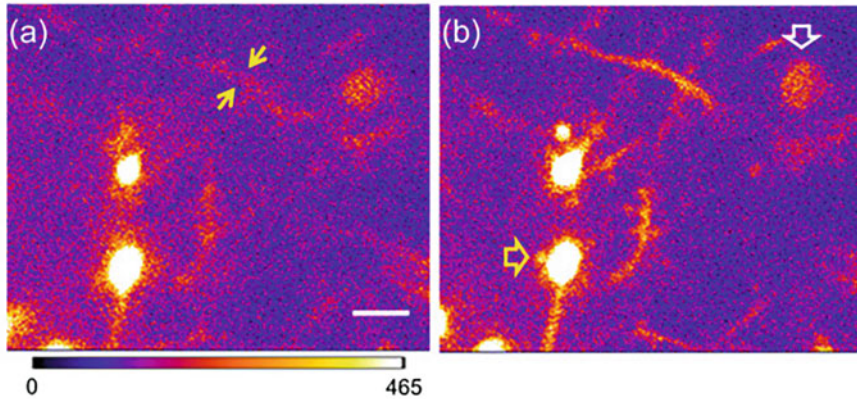


Fig. 4.9 MP images of the mouse S1 cortex were acquired at $\sim 656 \mu\text{m}$ under the dura. Images acquired with AO system correction (a) and full AO correction (b). Scale bar: $5 \mu\text{m}$. Yellow and white arrows mark a spine on the apical dendrite and the soma of the layer five pyramidal cells. (Adapted with permission from Kong and Cui [52] © The Optical Society)

4.4 Adaptive Optics Procedure for *Drosophila* Brain Enhanced Imaging

As stated above in this chapter, MP microscopy (with and without AO modules) is being broadly used to visualize brain structures of mammal animal models (mainly rodents). However, there is also an increasing interest in exploring the *Drosophila* brain by means of MP techniques since it provides relevant information on neuronal networks. Similar to mammal brains, *Drosophila* brain imaging also requires AO procedures to enhance features at deep locations since scattering and aberrations significantly limit the performance of the different imaging techniques used. In particular, the trachea induces strong aberration and scattering degradation making MP tools unable to reach locations deeper [62].

The amount of details that can be detected within the sample reduces with depth, as shown in Fig. 4.10. Since segmentation methods allow local analysis and quantification of the structures, the application of the Canny edge segmentation method to those images reveals a noticeable loss of details when using “regular” (i.e., non-AO) MP imaging microscopy [63]. Although AO schemes have been reported to be useful to enhance neural features, not many experiments dealing with *Drosophila* brain imaging and AO-MP microscopy can be found in the literature.

A sensor-less AO wide-field fluorescence (not MP imaging) microscope was able to get optical sections inside a living *Drosophila* brain (down to $50 \mu\text{m}$) through the compensation for specimen-induced aberrations, which were proved to be static [64]. Instead of using a single aberration correction pattern for the whole field of view (i.e., isoplanatic), Pozzi and co-authors [65] developed a sensor-less AO method based on an anisoplanatic aberration correction approach. It was

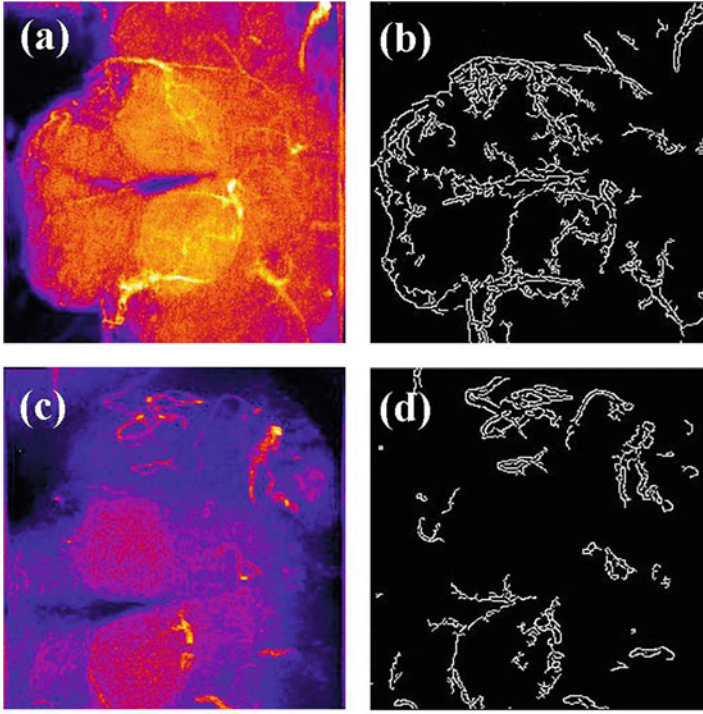


Fig. 4.10 MP imaging of the *Drosophila* brain was acquired at two different depth locations (**a**, **c**). Results of applying the Canny edge segmentation method (**b**, **d**). Imaged area: $180 \times 180 \mu\text{m}^2$

implemented in a confocal microscope and tested in fixed whole *Drosophila* brains (150- μm thick). Results showed a dramatic improvement in resolution and sharpness when compared to conventional isoplanatic adaptive optics (two-fold gain in selected patches). Stimulated Emission Depletion (STED) imaging was also combined with AO to allow performance improvement in thick tissue samples. In particular, the implementation of two AO elements enabled enhanced 3D STED images at depth in the *Drosophila* brain tissue [66].

Zheng et al. [67] demonstrated improved MP imaging in fixed *Drosophila* brain lobes by means of a direct AO scheme (nonlinear guide star, deformable mirror, and Hartmann-Shack sensor). The excitation laser power measured post objective was ~ 90 mW. They revealed that up to $\sim 65 \mu\text{m}$ from the coverslip, the dominant aberration was spherical and that the magnitude of the aberration progressively increased with depth. In addition, the plane-to-plane correction increased both contrast and resolution. The latter was improved $2\times$ and $4\times$ in lateral and axial directions, respectively, providing the visualization of fine, actin-enclosed structures that were not seen without AO.

The direct AO approach reported in [45, 46] was also used to image in vivo structural YFP-labeled neurons $70 \mu\text{m}$ below the surface of the fruit fly brain.

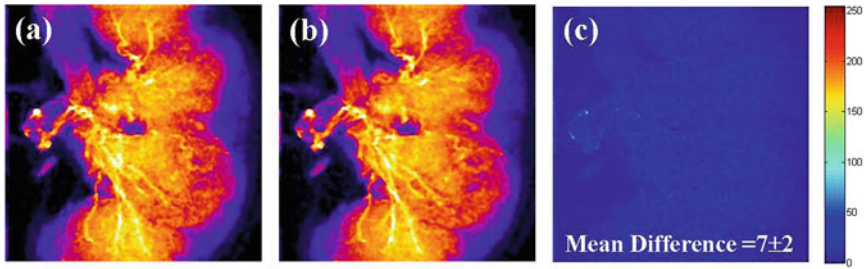


Fig. 4.11 MP images acquire without (a) and with (b) a broadband spectral filter placed in front of the detector unit. Right column shows the difference map (c). Depth location was arbitrarily chosen. Imaged area: $270 \times 270 \mu\text{m}^2$

Despite the fact that the values of the aberration peak-to-valley found were as large as $1.6 \mu\text{m}$, AO was able to effectively increase the imaging performance [68].

More recently, Bueno et al. [69] reported a sensor-less AO-MP instrument to improve images acquired at different depth locations within the fixed *Drosophila* brain. A hill-climbing algorithm looked for the optimal spherical aberration for each plane within the sample. Since this term is dominant in thick biological samples [32, 36, 38], including the *Drosophila* brain [67], the correction of other Zernike terms was not necessary.

Figure 4.11 shows two MP images of a fixed *Drosophila* brain acquired without and with a broadband spectral filter. Both images are similar, which indicates that the MP signal emitted by the specimen is associated with two-photon excitation fluorescence and collagen-based structures are not present in the brain. This occurs all along with the entire thick sample.

Despite the fact that MP signal decreases up to 80% at deeper layers, the AO procedure improved the quality of the TPEF images independently of the depth location of the imaged plane (Fig. 4.12). Aberrations hardly affected shallower locations, but the amount of aberration required to obtain the optimum image increased with depth. At $120 \mu\text{m}$ inside the *Drosophila* brain, the MP signal increased 60% when $0.6\text{-}\mu\text{m}$ of spherical aberration was compensated. Moreover, AO-MP sectioning provided optimized visualization of trachea branching and a number of brain structures (antennal lobe, protocerebral bridge, ellipsoidal body, etc.).

It is well-known that the plane-by-plane manipulation of the spherical aberration is a slow process in AO sensor-less algorithms. Then, an improved automatic procedure combining fast tomographic MP imaging and AO was implemented [70]. Since each tomography covered the entire *Drosophila* brain, the method used the intensity profiles as a function of depth to get an “averaged” optimum spherical aberration pattern. Although the image quality of planes close to the surface was slightly reduced, better images were obtained from deeper planes due to an increase in depth of focus. This compromise enabled the registration of enhanced volumetric MP images. As an example, Fig. 4.13 compares the improvement in the visualization

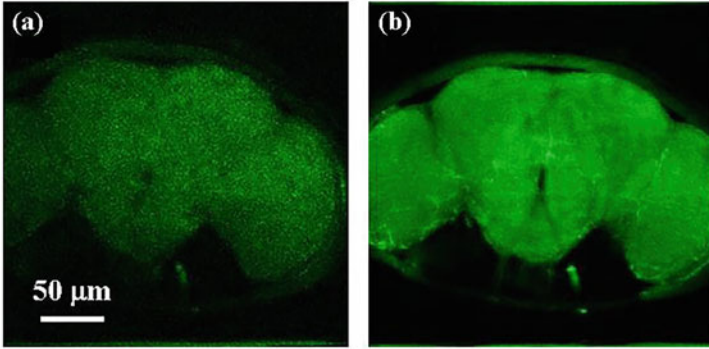


Fig. 4.12 MP images of the *Drosophila*'s brain before (a) and after (b) aberration correction

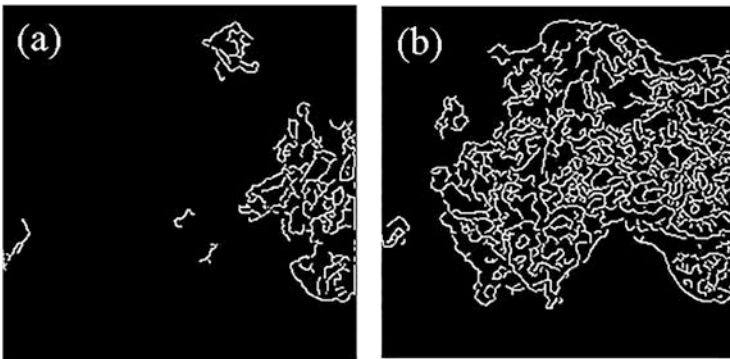


Fig. 4.13 Segmentation maps were obtained from MP images acquired before (a) and after SA correction (b). Imaged area: $270 \times 270 \mu\text{m}^2$. The segmentation evidences the benefit of using AO in the detection of spatial information at deeper locations within the *Drosophila* brain

of brain structures (through the Canny edge segmentation method) obtained from MP images recorded images at 115- μm depth before and after applying this AO procedure.

4.5 Conclusions

Drosophila is an important animal model in neuroscience. High-quality microscopy images are fundamental to visualizing neural connections, understanding functions, and analyzing processes and activities. Since the brain presents a three-dimensional circuit, imaging areas located at deep locations is highly desirable. MP imaging has been reported as a powerful tool to explore its structure and has found a niche in this research field during the last decade. However, although *Drosophila* brain

thickness is only about 200 μm , the non-homogeneity of the tissue reduces the efficiency of MP techniques to get single-cell resolution at deep locations. In this chapter, we have introduced the advantages of using AO to improve MP brain imaging.

By correcting aberrations, AO-MP microscopy can recover near-diffraction-limited performance by restoring the PSF sharpness effectively across the sample depth and demonstrating high-resolution imaging of neuronal structures. Among the different AO schemes, sensor-less ones are broadly used. Instead of being directly measured, the wavefront is inferred from the image variations.

The successful use of AO-MP has demonstrated its ability to improve the signal-to-noise ratio and enhance resolution at deep locations within the brain tissue, which led to the detection of fine brain features, otherwise invisible. Moreover, *in vivo* experiments have shown that this technique is indispensable for accurately assessing activity within deep cortex locations and recording activity from neurons in superficial cortical layers. This way of exploring detailed structural and functional information may open up new opportunities for deep tissue neuro-imaging.

References

1. Morgan TH (1910) Sex limited inheritance in *Drosophila*. *Science* 32(812):120–122
2. <https://www.animalresearch.info/en/medical-advances/nobel-prizes/>
3. Bellen HJ, Tong C, Tsuda H (2010) 100 years of *Drosophila* research and its impact on vertebrate neuroscience: a history lesson for the future. *Nat Rev Neurosci* 11(7):514–522
4. Prüßing K, Voigt A, Schulz JB (2013) *Drosophila melanogaster* as a model organism for Alzheimer's disease. *Mol Neurodegener* 8(1):35
5. Zheng Z, Lauritzen JS, Perlman E, Robinson CG, Nichols M, Milkie D, Torrens O, Price J, Fisher CB, Sharifi N, Calle-Schuler SA, Kmecova L, Ali IJ, Karsh B, Trautman ET, Bogovic JA, Hanslovsky P, Jefferis GSXE, Kazhdan M, Khairy K, Saalfeld S, Fetter RD, Bock DD (2018) A complete electron microscopy volume of the brain of adult *Drosophila melanogaster*. *Cell* 174(3):730–743.e22
6. Adams MD, Celniker SE, Holt RA, Evans CA, Gocayne JD, Amanatides PG, Scherer SE, Li PW, Hoskins RA, Galle RF, George RA, Lewis SE, Richards S, Ashburner M, Henderson SN, Sutton GG, Wortman JR, Yandell MD, Zhang Q, Chen LX, Brandon RC, Rogers YH, Blazej RG, Champe M, Pfeiffer BD, Wan KH, Doyle C, Baxter EG, Helt G, Nelson CR, Gabor GL, Abril JF, Agbayani A, An HJ, Andrews-Pfannkoch C, Baldwin D, Ballew RM, Basu A, Baxendale J, Bayraktaroglu L, Beasley EM, Beeson KY, Benos PV, Berman BP, Bhandari D, Bolshakov S, Borkova D, Botchan MR, Bouck J, Brokstein P, Brottier P, Burtis KC, Busam DA, Butler H, Cadieu E, Center A, Chandra I, Cherry JM, Cawley S, Dahlke C, Davenport LB, Davies P, de Pablos B, Delcher A, Deng Z, Mays AD, Dew I, Dietz SM, Dodson K, Doup LE, Downes M, Dugan-Rocha S, Dunkov BC, Dunn P, Durbin KJ, Evangelista CC, Ferraz C, Ferriera S, Fleischmann W, Fosler C, Gabrielian AE, Garg NS, Gelbart WM, Glasser K, Glodek A, Gong F, Gorrell JH, Gu Z, Guan P, Harris M, Harris NL, Harvey D, Heiman TJ, Hernandez JR, Houck J, Hostin D, Houston KA, Howland TJ, Wei MH, Ibegwam C, Jalali M, Kalush F, Karpen GH, Ke Z, Kennison JA, Ketchum KA, Kimmel BE, Kodira CD, Kraft C, Kravitz S, Kulp D, Lai Z, Lasko P, Lei Y, Levitsky AA, Li J, Li Z, Liang Y, Lin X, Liu X, Mattei B, McIntosh TC, McLeod MP, McPherson D, Merkulov G, Milshina NV, Mobarry C, Morris J, Moshrefi A, Mount SM, Moy M, Murphy B, Murphy L,

- Muzny DM, Nelson DL, Nelson DR, Nelson KA, Nixon K, Nusskern DR, Pacleb JM, Palazzolo M, Pittman GS, Pan S, Pollard J, Puri V, Reese MG, Reinert K, Remington K, Saunders RD, Scheeler F, Shen H, Shue BC, Sidén-Kiamos I, Simpson M, Skupski MP, Smith T, Spier E, Spradling AC, Stapleton M, Strong R, Sun E, Svirskas R, Tector C, Turner R, Venter E, Wang AH, Wang X, Wang ZY, Wassarman DA, Weinstock GM, Weissenbach J, Williams SM, Woodage T, Worley KC, Wu D, Yang S, Yao QA, Ye J, Yeh RF, Zaveri JS, Zhan M, Zhang G, Zhao Q, Zheng L, Zheng XH, Zhong FN, Zhong W, Zhou X, Zhu S, Zhu X, Smith HO, Gibbs RA, Myers EW, Rubin GM, Venter JC (2000) The genome sequence of *Drosophila melanogaster*. *Science* 287(5461):2185–2195
7. Background on Comparative Genomic Analysis. <https://www.genome.gov/10005835/background-on-comparative-genomic-analysis>
 8. Mirzoyan Z, Sollazzo M, Allocca M, Valenza AM, Grifoni D, Bellosta P (2019) *Drosophila melanogaster*: a model organism to study cancer. *Front Genet* 10:51
 9. Feany MB, Bender WW (2000) A *Drosophila* model of Parkinson's disease. *Nature* 404(6776):394–398
 10. Tan FHP, Azzam G (2017) *Drosophila melanogaster*: deciphering Alzheimer's disease. *Malaysian J Med Sci* 24(2):6–20
 11. Chiang A-S, Lin C-Y, Chuang C-C, Chang H-M, Hsieh C-H, Yeh C-W, Shih C-T, Wu J-J, Wang G-T, Chen Y-C, Wu C-C, Chen G-Y, Ching Y-T, Lee P-C, Lin C-Y, Lin H-H, Wu C-C, Hsu H-W, Huang Y-A, Chen J-Y, Chiang H-J, Lu C-F, Ni R-F, Yeh C-Y, Hwang J-K (2011) Three-dimensional reconstruction of brain-wide wiring networks in *Drosophila* at single-cell resolution. *Curr Biol* 21(1):1–11
 12. FlyCircuit. <http://www.flycircuit.tw/>
 13. Buhmann J, Sheridan A, Malin-Mayor C, Schlegel P, Gerhard S, Kazimiers T, Krause R, Nguyen TM, Heinrich L, Lee W-CA, Wilson R, Saalfeld S, Jefferis GSX, Bock DD, Turaga SC, Cook M, Funke J (2021) Automatic detection of synaptic partners in a whole-brain *Drosophila* electron microscopy data set. *Nat Methods* 18(7):771–774
 14. Huang S-H, Irawati N, Chien Y-F, Lin J-Y, Tsai Y-H, Wang P-Y, Chu L-A, Li M-L, Chiang A-S, Tsia K, Chu S-W (2021) Optical volumetric brain imaging: speed, depth, and resolution enhancement. *J Phys D Appl Phys* 54(32):323002
 15. Simpson JH, Looger LL (2018) Functional imaging and optogenetics in *Drosophila*. *Genetics* 208(4):1291–1309
 16. Ueda HR, Ertürk A, Chung K, Gradinaru V, Chédotal A, Tomancak P, Keller PJ (2020) Tissue clearing and its applications in neuroscience. *Nat Rev Neurosci* 21(2):61–79
 17. Kobat D, Horton NG, Xu C (2011) In vivo two-photon microscopy to 1.6-mm depth in mouse cortex. *J Biomed Opt* 16(10):106014
 18. Hsu K-J, Lin Y-Y, Chiang A-S, Chu S-W (2019) Optical properties of adult *Drosophila* brains in one-, two-, and three-photon microscopy. *Biomed Opt Express* 10(4):1627–1637
 19. Duocastella M, Sancataldo G, Saggau P, Ramoino P, Bianchini P, Diaspro A (2017) Fast inertia-free volumetric light-sheet microscope. *ACS Photon*. 4(7):1797–1804
 20. Wu J, Liang Y, Chen S, Hsu C-L, Chavarha M, Evans SW, Shi D, Lin MZ, Tsia KK, Ji N (2020) KiloHertz two-photon fluorescence microscopy imaging of neural activity in vivo. *Nat Methods* 17(3):287–290
 21. Lu R, Liang Y, Meng G, Zhou P, Svoboda K, Paninski L, Ji N (2020) Rapid mesoscale volumetric imaging of neural activity with synaptic resolution. *Nat Methods* 17(3):291–294
 22. Kang S, Duocastella M, Arnold CB (2020) Variable optical elements for fast focus control. *Nat Photonics* 14(9):533–542
 23. Tsai T, McLeod E, Arnold CB (2006) Generating Bessel beams with a tunable acoustic gradient index of refraction lens. In: *Optical trapping and optical micromanipulation III*, 11 Sept 2006. <https://doi.org/10.1117/12.682945>. <https://www.spiedigitallibrary.org/conference-proceedings-of-spie/6326/63261F/Generating-Bessel-beams-with-a-tunable-acoustic-gradient-index-of-10.1117/12.682945.short>

24. Kong L, Tang J, Little JP, Yu Y, Lämmermann T, Lin CP, Germain RN, Cui M (2015) Continuous volumetric imaging via an optical phase-locked ultrasound lens. *Nat Methods* 12(8):759–762
25. Hsu K-J, Lin Y-Y, Lin Y-Y, Su K, Feng K-L, Wu S-C, Lin Y-C, Chiang A-S, Chu S-W (2019) Millisecond two-photon optical ribbon imaging for small-animal functional connectome study. *Opt Lett* 44(13):3190–3193
26. Tsai Y-H, Liu C-W, Lin W-K, Wang C-S, Chiang C-H, Singh VR, So PTC, Chou C-F, Chu S-W (2020) Two-photon microscopy at >500 volumes/second. *bioRxiv*. <https://doi.org/10.1101/2020.10.21.349712>
27. Huang C, Tai C-Y, Yang K-P, Chang W-K, Hsu K-J, Hsiao C-C, Wu S-C, Lin Y-Y, Chiang A-S, Chu S-W (2019) All-optical volumetric physiology for connectomics in dense neuronal structures. *iScience* 22:133–146
28. Lee EJ (2020) Novel optical microscopies to unravel brain function, 27 Jul 2021. <https://www.apctp.info/post/the-department-of-physics-at-northeastern-university-china>
29. Helmchen F, Denk W (2005) Deep tissue two-photon microscopy. *Nat Methods* 2(12):932–940
30. Booth MJ (2014) Adaptive optical microscopy: the ongoing quest for a perfect image. *Light Sci Appl* 3:e165
31. Tyson R (1991) Principles of adaptive optics. Academic Press, Boston
32. Neil MAA, Juskaitis R, Booth MJ, Wilson T, Tanaka T, Kawata S (2000) Adaptive aberration correction in a two-photon microscope. *J Microsc* 200(2):105–108
33. Avilés-Espinosa R, Andilla J, Porcar-Guezenc R, Olarte OE, Nieto M, Levecq X, Artigas D, Loza-Alvarez P (2011) Measurement and correction of in vivo sample aberrations employing a nonlinear guide-star in two-photon excited fluorescence microscopy. *Biomed Opt Express* 2(11):3135–3149
34. Cha JW, Ballesta J, So PTC (2010) Shack-Hartmann wavefront-sensor-based adaptive optics system for multiphoton microscopy. *J Biomed Opt* 15(4):046022
35. Tao X, Norton A, Kissel M, Azucena O, Kubby J (2013) Adaptive optical two-photon microscopy using autofluorescent guide stars. *Opt Lett* 38(23):5075–5078
36. Débarre D, Botcherby EJ, Watanabe T, Srinivas S, Booth MJ, Wilson T (2009) Image-based adaptive optics for two-photon microscopy. *Opt Lett* 34(16):2495–2497
37. Marsh PN, Burns D, Girkin JM (2003) Practical implementation of adaptive optics in multiphoton microscopy. *Opt Express* 11(10):1123–1130
38. Skorsetz M, Artal P, Bueno JM (2016) Performance evaluation of a sensorless adaptive optics multiphoton microscope. *J Microsc* 261(3):249–358
39. Ji N, Milkie DE, Betzig E (2010) Adaptive optics via pupil segmentation for high-resolution imaging in biological tissues. *Nat Methods* 7(2):141–147
40. Vellekoop IM, Mosk AP (2007) Focusing coherent light through opaque strongly scattering media. *Opt Lett* 32(16):2309–2311
41. Tang J, Germain RN, Cui M (2012) Superpenetration optical microscopy by iterative multiphoton adaptive compensation technique. *Proc Natl Acad Sci* 109(22):8434–8439
42. Girkin JM, Vijverberg J, Orazio M, Poland S, Wright AJ (2007) Adaptive optics in confocal and two-photon microscopy of rat brain: a single correction per optical section. *Proc SPIE* 6442: 0T1–0T7
43. Rodríguez C, Ji N (2018) Adaptive optical microscopy for neurobiology. *Curr Opin Neurobiol* 5:83–91
44. Tao X, Azucena O, Fu M, Zuo Y, Chen DC, Kubby J (2011) Adaptive optics microscopy with direct wavefront sensing using fluorescent protein guide stars. *Opt Lett* 36(17):3389–3391
45. Wang C, Liu R, Milkie DE, Sun W, Tan Z, Kerlin A, Chen T-W, Kim DS, Ji N (2014) Multiplexed aberration measurement for deep tissue imaging in vivo. *Nat Methods* 11:1037–1040
46. Wang K, Milkie DE, Saxena A, Engerer P, Misgeld T, Bronner ME, Mumm J, Betzig E (2014) Rapid adaptive optical recovery of optimal resolution over large volumes. *Nat Methods* 11:625–628

47. Wang K, Sun W, Richie CT, Harvey BK, Betzig E, Ji N (2015) Direct wavefront sensing for high-resolution *in vivo* imaging in scattering tissue. *Nat Commun* 6:7276
48. Liu R, Li Z, Marvin JS, Kleinfeld D (2019) Direct wavefront sensing enables functional imaging of infragranular axons and spines. *Nat Methods* 16:615–618
49. Sun W, Tan Z, Mensh BD, Ji N (2016) Thalamus provides layer 4 of primary visual cortex with orientation- and direction-tuned inputs. *Nat Neurosci* 19:308–315
50. Sinefeld D, Paudel HP, Wang T, Wang M, Ouzounov DG, Bifano TG, Xu C (2017) Nonlinear adaptive optics: aberration correction in three photon fluorescence microscopy for mouse brain imaging. *Proc SPIE* 10073:1007314-1–1007314-7
51. Ji N, Rodríguez C, Chen A, Rivera JA, Mohr MA, Liang Y, Sun W, Milkie DE, Bifano TG, Chen X (2020) An adaptive optics module for deep tissue multiphoton imaging *in vivo*, under review. <https://doi.org/10.21203/rs.3.rs-115556/v1>. <https://www.biorxiv.org/content/10.1101/2020.11.25.397968v1>
52. Kong L, Cui M (2014) *In vivo* fluorescence microscopy via iterative multi-photon adaptive compensation technique. *Opt Express* 22(20):23786–23794
53. Kong L, Cui M (2015) *In vivo* neuroimaging through the highly scattering tissue via iterative multiphoton adaptive compensation technique. *Opt Express* 23(5):6145–6150
54. Kong L, Tang J, Cui M (2015) *In vivo* volumetric imaging of biological dynamics in deep tissue via wavefront engineering. *Opt Express* 24(2):1214–1221
55. Rueckel M, Mack-Bucher JA, Denk W (2006) Adaptive wavefront correction in two-photon microscopy using coherence-gated wavefront sensing. *Proc Natl Acad Sci* 103(46):17137–17142
56. Fiolka R, Si K, Cui M (2012) Complex wavefront corrections for deep tissue focusing using low coherence backscattered light. *Opt Express* 20(15):16532–16543
57. Leray A, Lillis K, Mertz J (2008) Enhanced background rejection in thick tissue with differential-aberration two-photon microscopy. *Biophys J* 94(4):1449–1458
58. Papadopoulos IN, Jouhanneau J-S, Poulet JFA, Judkewitz B (2017) Scattering compensation by focus scanning holographic aberration probing (F-SHARP). *Nat Photonics* 11:116–123
59. Park JH, Kong L, Zhou Y, Cui M (2017) Large-field-of-view imaging by multi-pupil adaptive optics. *Nat Methods* 14(6):581–583
60. Yang Y, Chen W, Fan JL, Ji N (2021) Adaptive optics enables aberration-free single-objective remote focusing for two-photon fluorescence microscopy. *Biomed Opt Express* 12(1):354–366
61. Chien YF, Lin JY, Yeh PT, Hsu KJ, Tsai YH, Chen SK, Chu SW (2020) Dual GRIN lens two-photon endoscopy for high-speed volumetric and deep brain imaging. *Biomed Opt Express* 12(1):162–172
62. Su K-J, Lin Y-Y, Chiang A-S, Chu S-W (2019) Optical properties of adult *Drosophila* brains in one-, two-, and three-photon microscopy. *Biomed Opt Express* 10(4):1627–1637
63. Canny JA (1986) Computational approach to edge detection. *IEEE Trans Pattern Anal Mach Intell* 8(6):679–698
64. Pedrazzani M, Lorette V, Tchenio P, Benrezzak S, Nutarelli D, Fragola A (2016) Sensorless adaptive optics implementation in widefield optical sectioning microscopy inside *in vivo* *Drosophila* brain. *J Biomed Opt* 21(3):036006
65. Pozzi P, Smith C, Carroll E, Wilding D, Soloviev O, Booth M, Vdovin G, Verhaegen M (2020) Anisoplanatic adaptive optics in parallelized laser scanning microscopy. *Opt Express* 28(10):14222–14236
66. Patton BR, Burke D, Oswald D, Gould TJ, Bewersdorf J, Booth MJ (2016) Three-dimensional STED microscopy of aberrating tissue using dual adaptive optics. *Opt Express* 24(8):8862–8876

67. Zheng W, Wu Y, Winter P, Fischer R, Nogare DD, Hong A, McCormick C, Christensen R, Dempsey WP, Arnold DB, Zimmerberg J, Chitnis A, Sellers J, Waterman C, Shroff H (2017) Adaptive optics improves multiphoton super-resolution imaging. *Nat Methods* 14:869–872
68. Wang K (2017) Adaptive optical microscope for brain imaging *in vivo*. In: Proceedings of SPIE, vol 10251, Biomedical imaging and sensing conference, 18 Apr, p 102510H
69. Bueno JM, Ávila FJ, Chen PC, Chu S-W, Artal P (2019) Adaptive optics multiphoton microscopy of the *Drosophila* brain. In: Focus on microscopy: FOM 2019. Program and abstract book, p 59
70. Bueno JM, Skorsetz M, Palacios R, Gualda EJ, Artal P (2014) Multiphoton imaging microscopy at deeper layers with adaptive optics control of spherical aberration. *J Biomed Opt* 19(1): 011007



Valeria Piazza and Victor H. Hernandez

Abstract

Central myelin is an envelope composed of dozens of superimposed layers of the plasma membrane of oligodendrocytes around the neural axons. This sheath functions as an insulator that increases the efficiency and speed of the electrical impulse. Several traditional staining methods have been available to observe myelin in tissue sections for many years. However, most of what we know about the structure and organization of myelin comes from transmission electron microscopy images. Nowadays, specific molecular components of myelin can be identified and visualized by fluorescence microscopy. Even though, their lipidic nature is much more difficult to observe by this kind of microscopy technique. In the last years, superresolution and other imaging techniques were developed and applied to the study of myelin. Thanks to these and other advances in imaging that are described in this chapter, new structural details as well as many of the fine steps involved in myelination are now visually accessible.

Keywords

Myelin · Lipids · Proteins · Fluorescence microscopy · Nonlinear optics microscopy · X-rays

V. Piazza (✉)

Biophotonics Lab, Centro de Investigaciones en Óptica A.C., León, Guanajuato, Mexico
e-mail: vpiazza@cio.mx

V. H. Hernandez

Neuroscience Lab, División de Ciencias e Ingenierías, Universidad de Guanajuato, León, Guanajuato, Mexico

5.1 Myelin

Since the first observation of myelinated fibers by Leeuwenhoek in the eighteenth century [1], until very recently, myelin has been envisaged as an isolating sheath for the axons, which conferred them the ability of fast conduction. However, nowadays, it is well known that myelin is a much more complex structure than initially conceived. When myelin defects affect the nervous system, the relevance of these complexities can be easily understood.

In the central nervous system, oligodendrocytes (OLCs) are the myelin-forming cells. Myelin is actually an extension of the plasma membrane of these glial cells that wraps around the axon. The lipid composition of myelin is different from other biological membranes. It is rich in cholesterol which forms more than 40% of the membrane and stabilizes the sheath, increasing its viscosity. Together with galactosylceramide, and plasmalogen it constitutes more than 65% of the fat content; the presence of organized functional lipid regions known as lipid rafts is another trademark of this peculiar plasma membrane [2].

Even though transmission electron microscopy has clearly shown how myelin is organized around the axon, the myelination process still lacks a clear understanding. The process of myelination includes several events, going from generation of oligodendrocyte progenitor cells (OPCs) in the neurogenic zones of the brain [3, 4] to their differentiation, proliferation, and migration [5, 6]. Once the OLCs contact the neuronal process, the myelin leading edge wraps around the axon and insinuates underneath the previous layer, creating this way a sheath composed of one hundred or more highly compacted superposed layers of the oligodendrocyte membrane [7].

5.2 Traditional Methods: Electron Microscopy, Immunohistochemistry, and Fluorescence Microscopy

Transmission electron microscopy images show a successive superposition of electron-dense and light layers, the major dense line, and the intraperiod line, respectively. This ultrastructural aspect reflects the high adhesion between compacted intracellular and extracellular membrane surfaces. However, myelin compaction is not uniform along the covered surface of the axon. As a result, non-compact myelin channels are formed at the lateral edges of the myelinated section, leaving nude regions named Ranvier nodes or simply nodes. These paranodal channels are arranged in a spiral that appears as a series of loops when sliced.

Improvements in tissue preparations have broadened the understanding of the myelin structure. For example, samples for electron microscopy are traditionally fixed with aldehydes and then dehydrated, stained, included in a resin, and sectioned in ultra-thin slices. Nevertheless, this method could introduce artifacts that change the intracellular volumes. An alternative is to avoid chemical processing and use instead cryofixation by high-pressure freezing, thus immobilizing complex

macromolecular assemblies in their native state in intact cells and tissues [8–10]. This method allows also to generate 3D tomograms [11]. A modification to this protocol is focused ion beam-scanning electron microscopy (FIB-SEM) which makes possible the generation of 3D images of ultrastructural details of cells and tissues [12]. This has allowed, for example, to describe pathologic changes in myelin diseases [13].

The oldest system for generating myelin images is immunocytochemistry. Several traditional staining methods are available for the visualization of myelin in tissue sections: the Weil stain, the Pal-Weigert Method, Luxol fast blue, Baker's acid hematin method, Sudan Black B as well as silver staining, which is preferred when thin processes need to be visualized. The Pal-Weigert stain [14, 15] and some of its modification for paraffin embedded sections, known as the Weil stain [16, 17], are based on the reduction of chrome salt to chromium dioxide at the white matter. The dioxide then works as mordant for hematoxylin. The result is a reliable black stain of myelin, useful especially for low resolution images, with blue nuclei and yellowish background. Luxol fast blue is a phthalocyanine dye of sulfonated copper, soluble in alcohol. When in contact with the tissue, the dye is attracted by the bases contained in the phospholipids of myelin. The excess can be removed with 95% ethanol and a subsequent wash in lithium carbonate and ethanol is performed until the gray matter is colorless. With this protocol [18], myelin is stained blue-green and the neurons become purple.

It is believed that hematin reacts with the phosphate radical of phospholipids in the Baker's acid hematin method [19]. After fixing the material with formalin-calcium to preserve phospholipids, the sample is placed in a solution of calcium chloride and dichromate, followed by staining in acid hematin. Myelin will be blue-black with a brown-yellow background and bluish nuclei. The diazo-dye Sudan black B [20] is not uniquely specific for phospholipids, but it is widely used for membrane and myelin staining, conferring gray color to phospholipids and blue-black to neutral fats. The silver staining method could in principle be applied to frozen and embedded samples. Among the basic staining techniques, it is the one that provides the best results when small caliber fibers need to be highlighted, and with time some drawbacks of the technique, like the difficulty in controlling the level and speed of staining and the background levels were improved with the addition of a bleaching step [21–23] and an additional fixation [23]. When specificity and resolution are the critical imaging parameters, classic optical microscopy provides another solution: immunofluorescence. By putting together, the high specificity conferred by antibody-mediated staining and the contrast and resolution provided by fluorescence techniques, like epifluorescence and confocal microscopy, molecular components of myelin can be identified and visualized in the brain.

Perhaps the major paradox lies in the fact that a method that marks proteins is used to highlight the presence of membranes made by over 70% lipids. The lipidic nature of myelin represents a hurdle for the straightforward application of fluorescence techniques: the fluorescent lipophilic dyes available have technical limitations, it is very difficult to stain specific phospholipids and many of the protocols for immunofluorescence cannot preserve optimally the lipidic components of cells and

tissues. Various examples can be cited: the loss of lipidic component is unavoidable when using organic solvents like acetone or methanol for the fixation step which is often necessary depending on the antibodies to use or the molecules to be stabilized; clearing protocols, so important for implementing imaging in thicker samples, often do not guarantee good preservation of the lipidic components of cells and tissues, etc. As a consequence, central myelin may be revealed by specific staining of some of its constituent proteins, as the oligodendrocyte pan-marker Olig-2 [24] or the stage-dependent markers chondroitin sulfate proteoglycan 4 (NG2 or CSPG4) [25] for oligodendrocyte-precursor cells (OPCs); 2',3'-cyclic-nucleotide 3'-phosphodiesterase (CNPase) for pre- and myelinating oligodendrocytes [26], myelin basic protein (MBP), proteolipid protein (PLP), myelin-associated glycoprotein (MAG), and myelin oligodendrocyte glycoprotein (MOG), along with others such as CNPase (cell body and myelin); and the mature somatic marker APC (or CC1) [27].

The possibility of visualizing myelin through its proteins opens the door to other fluorescence techniques, like light sheet microscopy, superresolution approaches, and combinations of both. The need of visualizing large portions of the brain could be satisfied by means of light sheet microscopy, a technique that relies on the use of a blade of excitation light to illuminate a thin, two-dimensional section of the entire sample, this way reducing drastically the time needed to acquire images and at the same time the photodamage caused by light in the regions not imaged (for a recent review, see [28]). Superresolution approaches, on the other hand, allow to describe the smallest image details that optical microscopy can handle; Werner et al. recently wrote an introductory review of superresolution techniques in neurosciences [29]. The brain, with its structures that are spatially heterogeneous as far as the refractive index, depends on clearing protocols to become suitable for volumetric imaging. However, as mentioned, the clearing processes used to prepare a large sample for imaging are only partially compatible with myelin preservation. Rusch and coworkers made a comparison among various clearing techniques to try to define which one could work best to prepare an aged human brain for light sheet microscopy [30]. While CLARITY and iDISCO resulted the best ones, specific visualization of myelin signals associated to PLP and MBP remains the most difficult task. Ryan and collaborators [31] provided a solution to the problem of first-order defocusing in light sheet microscopy, which causes loss of co-planarity between excitation and detection and affects the sharpness of the image. The authors show that the problem, particularly important in the brain, can be solved with Cleared tissue Digital Scanned Light-sheet Microscopy (C-DSLM), and demonstrated the robustness of this method with brains that were only partially cleared to preserve myelination and the associated fluorescence signal.

In 2019, the work of Gao, Asano, Upadhyayula et al. established a new scenario for microscopy of large specimens conjugated to the visualization of subcellular detail [32]. In this case, the superresolution was achieved by expanding the samples in a controlled fashion while imaging via lattice light sheet microscopy allowed rapid scanning with reduced photobleaching. This system, together with preliminary expansion of the sample, proved useful to image myelin and observe a lack in concentricity with axons that may be the structural cause in longitudinal changes

in capacitance and impedance, which in turn may affect signal propagation; it also revealed a certain heterogeneity in myelination patterns among neurons of the same region. Among the superresolution applications for the study of myelin, the spatial and functional relationship between PLP, mitochondria, and ER in the context of the Pelizaeus-Merzbacher leukodystrophy was studied by means of SIM microscopy, albeit in an *in vitro* mesenchymal cell system [33]; however, also structural alteration of brain tissue can be detected with the same technique, as shown for the study of myelinated axons architecture following optogenetic stimulation of striatal medium spiny neurons [34]. Besides rodent models, fine measurements of axons and myelin sheath diameters are possible also in human brain tissues, as performed with either STORM or SOFI strategies [35]. STED microscopy has allowed to study the interplay between MBP and the lipid constituents of myelin in cultured epithelial cells and primary oligodendrocytes [36].

5.3 Nonlinear Optics Solutions

Various types of nonlinear microscopy can circumvent the limitations of linear optical microscopy, namely the limitation in depth penetration and the contrast loss due to scattering tissues. Using the nonlinear signal confers several possible advantages. Imaging of thick samples can be made without the need of a confocal pinhole, increasing this way the signal-to-noise ratio and simplifying the setup downsizing to *in vivo* applications. The wavelength used, typically around 800 nm is barely absorbed in most tissues and also allows more penetration depth in tissue sections. Finally, the high energies required for the phenomena are fulfilled only at the focal volume, so undesired signal as well as photodamage are reduced out-of-focus. In many cases, exogenous stains are not required since most of the nonlinear interactions are specifically associated to certain biological molecules, for example, second harmonic generation and collagen, third harmonic generation and lipids.

These techniques take advantage of the possibility of exciting electrons in the imaged material by the simultaneous absorption of more than one photon, so that the photons released at decay will have a higher energy than those used for excitation. This is valid for two photon excitation fluorescence (TPEF), second harmonic generation (SHG), and third harmonic generation (THG) microscopies although the three are based on fundamentally different physical phenomena. Perhaps one of the most relevant differences lies in the fact that two photons need to be synchronously adsorbed in TPEF, with associated energy deposition in the adsorbing atoms and consequent release of fluorescence at slightly less than half the energy of the incident light, while the two or three photons that interact simultaneously in SHG and THG are upconverted and a single photon of exactly twice (or thrice) the energy is generated via a virtual state and without energy deposition. A slightly different situation is that of coherent anti-Stokes Raman scattering (CARS), where multiple photons are employed to address the molecular vibrations of the region under study and produce a coherent signal. Two simultaneous laser beams, the pump and the Stokes, with selected intensities and wavelengths are used to excite

molecules to a first virtual state and then populate vibrational levels of the ground state, in a way that is specific to the chemical properties of the illuminated molecule. A third laser beam (or alternatively the pump beam itself) elevates the molecules in the illuminated region from the vibrational sub-states to a second, higher virtual state, from which they relax to the ground state by releasing a detectable amount of energy, the so-called anti-Stokes signal, which carries information about the bonds probed (Fig. 5.1).

Two photon excitation fluorescence microscopy is perhaps the most popular nonlinear technique so far. Its use to reveal myelin staining is derived from the use of dyes that could selectively stain the lipid insulator since myelin itself doesn't provide intrinsic contrast for this technique. With this approach, it is possible to follow the changes in intracellular calcium that characterize glial cells, as it has been done in rat dissected optic nerve and spinal dorsal column axons [37]. TPEF is often used in multimodal imaging modalities along with CARS or SHG to highlight stained myelin sheaths or axons (see [38–42]) and could be used for microendoscopy approaches [43] to longitudinally study the fate of myelin after spinal cord injury *ex vivo* [44, 45].

Second harmonic generation (SHG) microscopy is used to observe noncentrosymmetric molecular arrangements. Lipids and lipidic membranes are not included among the few biological molecules that work as harmonophores for this technique, despite some scant *in vitro* tests performed decades ago seemed to indicate otherwise [46, 47]. Some effort has been made to image membranes with SHG with the help of specific dyes [48, 49]; further refinements of dye design including elimination of the TPEF contributions to the SHG signal [50] are a good indication that dyes suitable for myelin-specific SHG imaging should be available soon.

Recent findings in our lab have revealed another interesting aspect of this nonlinear imaging approach applied to myelin. SHG was used to study the only spontaneous animal model of H-ABC tubulinopathy, the taiep rat [51]. The rodent, as well as the patients suffering from this leukodystrophy, presents serious dysmyelination, deriving from a mutation in the tubulin beta 4A gene that causes microtubule accumulation in oligodendrocytes. The phenomenon of harmonic generation is robust enough to reveal the tubulin signal in tissue sections and also shows a very promising diagnostic potential since much stronger intensities are associated with the oligodendrocytes of the mutant tissue, compared to the healthy correspondent (unpublished, Fig.5.2).

Third harmonic generation (THG) microscopy is an imaging option for myelin, with many advantages. The pros include those dependent on the physical phenomenon, like the intrinsic optical sectioning capability, and those related to the sample, like the fact that invasive manipulations, like embedding or staining, are not required. The samples that are suitable for this type of observation are those that present inhomogeneities due to a refractive index (RI) mismatch [52], as is the case when imaging the interface between lipids and interstitial fluids. Visualizing membranes is therefore a natural application for this technique, which could also take advantage of the relatively simple use and modification of multiphoton optical

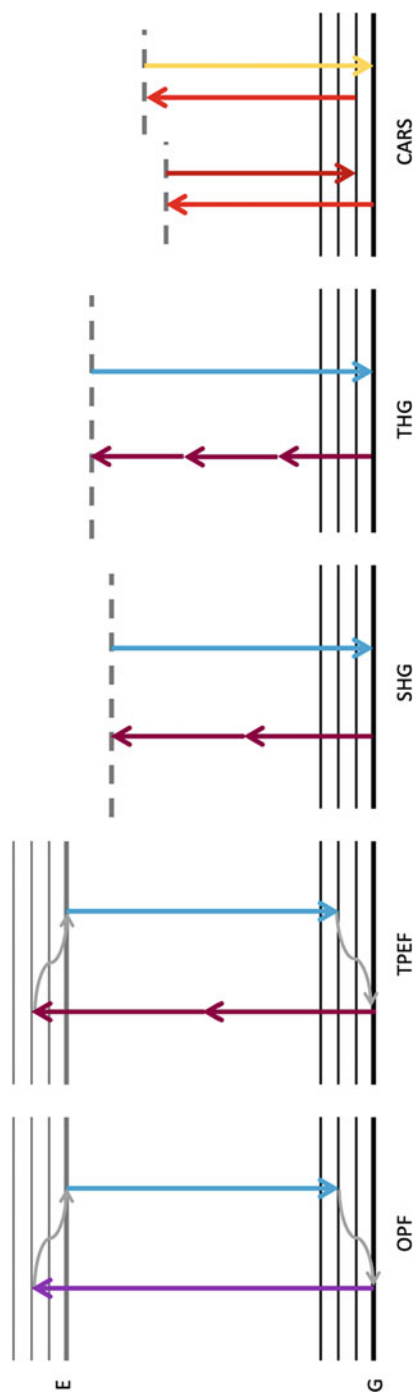


Fig. 5.1 General scheme for the fluorescence transitions that could be used for myelin imaging. *OPF* one photon fluorescence, *TPEF* two photon excitation fluorescence, *SHG* second harmonic generation, *THG* third harmonic generation, *CARS* coherent anti-Stokes Raman scattering

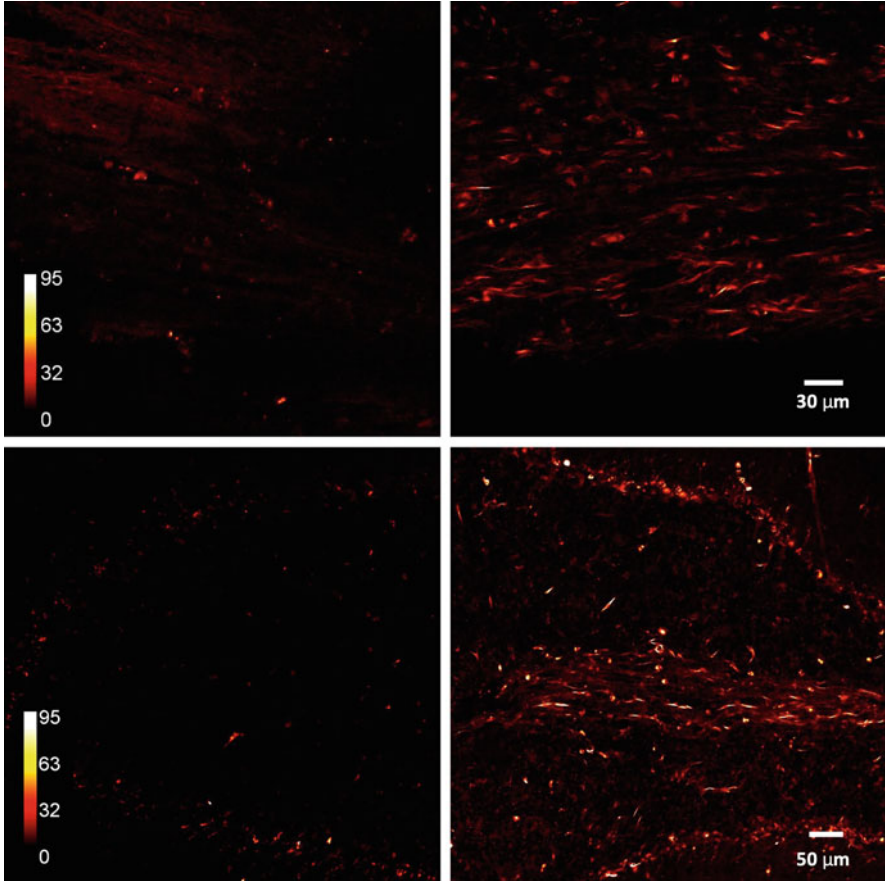


Fig. 5.2 Representative SHG micrographs from 10-month-old WT and tubulin mutant rats. (a) Image from a section of the corpus callosum of a WT rat. (b) Image from a section of the corpus callosum of a taiep rat. (c) Cerebellar folium from a WT rat. The only nonlinear signal detectable is at the level of the Purkinje cells. (d) From a correspondent region of a taiep cerebellum, the folium appears drastically different, with the signal from the central region, corresponding to the white matter, emitting a much stronger signal. Brighter colors represent the highest signal intensity in the calibration bars. Scale bars: (a, b) 30 μm , (c, d) 50 μm

setups to convert them in THG microscopes if a pulsed laser source with appropriate wavelength is available.

Examples of the use of THG for the study of myelin include *in vitro* and *in vivo* imaging of healthy and damaged CNS of mice and zebrafish [53], simultaneous imaging of neurons, white-matter structures, and blood vessels [54], evaluation of remyelination in axons regenerated after spinal cord injury [55], study of gray matter myeloarchitecture from fixed tissue sections and directly on the exposed brain cortex [56], visualization of oligodendrocytes in deeper layers of the cortex (up to 500 μm , *ex vivo*) [57] and early myelin ensheathment in the *Xenopus laevis* model [58].

CARS microscopy is a technique which combines noninvasive, chemical specificity with high-resolution imaging for biological samples. Like other nonlinear techniques, CARS takes advantage of the spatial and temporal control of the illuminating photons, so that intrinsic optical sectioning and minimal thermal damage are achieved when imaging. One major drawback, however, is the complexity and cost of the laser systems which still hinders the widespread application of CARS microscopy in most biomedical laboratories.

C–H bonds stretches display a strong CARS signal. For this reason, the majority of research utilizing CARS microscopy for cell biology has examined lipids and their dynamics (reviewed in [59]), allowing accurate imaging and quantification. This represents an interesting advantage over conventional fluorescent microscopy, where the lack of reliable lipid-specific markers makes it difficult to label lipids without affecting their localization and function.

With CARS microscopy, myelinated axons from the spinal cord of guinea pigs could be imaged and their g -ratio measured [60], with sharper contrast and less photobleaching than images obtainable with stained tissue in TPEF [38]; with small modifications in the setup corresponding to the implementation of SLAM-CARS, resolution can be improved to subdiffraction levels and contrast enhanced, as shown with myelinated axons in the mouse brainstem [61]. Other system that could be interrogated include the auditory brainstem, as it was the case in a work aimed at studying the main sensory issue of Fragile X syndrome [62]. The changes in lipids caused by the inflammation consequent to spinal cord injury can be visualized by CARS, allowing differentiation of myelin sheaths, myelin debris, and lipid droplets [63].

5.4 Novel Solutions for Optical Microscopy

As mentioned before, the lipophilic chemical probes used for myelin staining are not the most reliable, and this is particularly true when trying to image large volumes, because of the inefficient diffusion and unspecific binding of the dyes. Besides the development of the label-free techniques like THG and CARS, other solutions are continuously tested and, in this section, we describe some recent, interesting findings about old reagents and techniques.

The observation that glycerol removal from previously fixed and embedded samples causes a significant enhancement of myelin autofluorescence brought Costantini et al. to the elaboration of the MAGIC (Myelin Autofluorescence imaging by Glycerol Induced Contrast enhancement) protocol [64]. The procedure includes a first fixation step in paraformaldehyde, a subsequent embedding in glycerol and a final removal of glycerol by extensive washing in saline solution. FLIM and even more Raman spectroscopy analysis of MAGIC-treated samples point to a differential interaction of glycerol with myelinated fibers, compared to the surrounding cells and interstitial substance: glycerol has high affinity with myelinated fibers and remains confined into the sheaths, causing the increased autofluorescence.

The advantages of this method are its versatility: could be applied for the study of different samples, with different techniques (e.g., OPF, TPEF) and compatible with other staining systems, like immunofluorescence or the use of other lipophilic dyes like FluoroMyelin Red (trademark). It is applied postmortem without the need for specific preliminary treatment of the tissue, allowing for the analysis of stored fixed tissues. The only possible drawback for the application of this protocol stems from the long times involved in the MAGIC steps, which for a small brain like the rat's encompasses 5 weeks.

Another interesting finding has to do with Nile Red, a dye known for its affinity to lipids and used extensively to mark intracellular lipids and membranes with red fluorescence [65, 66].

Due to the solvatochromism of this dye, i.e., the tendency of shifting fluorescent emission wavelength depending on the chemical environment, the dye can be used as a reporter of myelin local perturbations which cause a change in polarity of the sheaths [67]. This sensitivity is very important for early detection of myelin disorders since it could be used to study physiochemical alteration of the insulator prior to its structural change, like in the early phases of MS or other leukodystrophies. This type of spectral analysis with the use of Nile Red cannot be performed directly with true color images taken with a fluorescent microscope but requires the capability to acquire multiwavelength data with good spectral resolution and to analyze it with a dedicated software for the pseudo-color rendering of the polarization states of myelin.

5.5 X-Rays

The limitations of the use of visible light to study myelin and other components of the nervous system are evident at large scales. Studies addressing sizeable volumetric portions of the brain are usually performed by serial sectioning of the sample, which not only causes some de-structuration and distortion of the sample, i.e., the cutting, profound modifications like clearing and staining but also extensive work for the purpose of aligning the images from the sections to reconstruct the original volume. While all these steps are necessary when looking for a signal with high molecular specificity, studies that pursue the reconstruction of the cytoarchitecture of brain regions may benefit from other technical approaches. In particular, thanks to the technological advancements, the use of X-rays has been demonstrated as a feasible complement to optical and electron microscopy when quantification and high resolution are needed, compatible with the visualization of subcellular structures [68], in analyses of brain tissues that could span from a single nerve [69] to an entire brain [70, 71]. The potential of small-angle X-ray scattering computed tomography can be exploited for the analysis of myelin [69, 72], revealing the details of its molecular organization, like the relative abundance at each position analyzed, the period and the thickness of the myelin sheaths in regions of the brain. With hard X-rays, radiation with wavelengths below 0.2 and 0.1 nm is also possible to perform tomography in phase contrast mode, which allows the efficient generation

of series of images with large fields of view (FOV) and a resolution that exceeds that of optical microscopy, in parallel to the possibility of penetrating entire tissues. Modifications of the technique including the use of a crystal X-ray interferometer and sample fixation in ethanol have shown to yield images of myelin with much higher contrast with respect to formaldehyde-fixed tissues [73].

References

1. Boullerne AI (2016) The history of myelin. *Exp Neurol* 283:431–445
2. Poitelon Y, Kopec AM, Belin S (2020) Myelin fat facts: an overview of lipids and fatty acid metabolism. *Cell* 9:812
3. Delgado AC et al (2021) Release of stem cells from quiescence reveals gliogenic domains in the adult mouse brain. *Science* 372:1205–1209
4. Mizrak D et al (2019) Single-cell analysis of regional differences in adult V-SVZ neural stem cell lineages. *Cell Rep* 26:394–406.e5
5. Bergles DE, Richardson WD (2016) Oligodendrocyte development and plasticity. *Cold Spring Harb Perspect Biol* 8:a020453
6. Nishiyama A, Shimizu T, Sherfat A, Richardson WD (2021) Life-long oligodendrocyte development and plasticity. *Semin Cell Dev Biol* 116:25–37
7. Hildebrand C, Remahl S, Persson H, Bjartmar C (1993) Myelinated nerve fibres in the CNS. *Prog Neurobiol* 40:319–384
8. Studer D, Humbel BM, Chiquet M (2008) Electron microscopy of high pressure frozen samples: bridging the gap between cellular ultrastructure and atomic resolution. *Histochem Cell Biol* 130:877–889
9. Möbius W et al (2010) Electron microscopy of the mouse central nervous system. In: *Methods in cell biology*, vol 96. Elsevier, Burlington, MA, pp 475–512
10. Möbius W, Nave K-A, Werner HB (2016) Electron microscopy of myelin: structure preservation by high-pressure freezing. *Brain Res* 1641:92–100
11. Lučić V, Leis A, Baumeister W (2008) Cryo-electron tomography of cells: connecting structure and function. *Histochem Cell Biol* 130:185–196
12. Kizilyaprak C, Daraspe J, Humbel BM (2014) Focused ion beam scanning electron microscopy in biology: focused ion beam scanning electron microscopy. *J Microsc* 254:109–114
13. Steyer AM et al (2020) Pathology of myelinated axons in the PLP-deficient mouse model of spastic paraplegia type 2 revealed by volume imaging using focused ion beam-scanning electron microscopy. *J Struct Biol* 210:107492
14. Weigert C (1885) Eine vergessener der Haematoxylin Blutlaugen-salzmethode für das Centralnervensystem. *Fortschr Deutsch Med* 3:236–239
15. Clark SL, Ward JW (1934) A variation of the Pal Weigert method for staining myelin sheaths. *Stain Technol* 9:53–55
16. Weil A (1928) A rapid method for staining myelin sheaths. *Arch Neurol Psychiatry* 20:392
17. Berube GR, Powers MM, Clark G (1965) Iron hematoxylin chelates: II. Histochemistry of myelin sheath stains. *Stain Technol* 40:235–238
18. Klüver H, Barrera E (1953) A method for the combined staining of cells and fibers in the nervous system. *J Neuropathol Exp Neurol* 12:400–403
19. Hori SH (1963) A simplified acid Hematein test for phospholipids. *Stain Technol* 38:221–225
20. Meier C (1976) Some observations on early myelination in the human spinal cord. Light and electron microscope study. *Brain Res* 104:21–32
21. Meywald T, Scherthan H, Nagl W (2004) Increased specificity of colloidal silver staining by means of chemical attenuation. *Hereditas* 124:63–70
22. Jain N (1998) A histologically visible representation of the fingers and palm in primate area 3b and its immutability following long-term deafferentations. *Cereb Cortex* 8:227–236

23. Pistorio AL, Hendry SH, Wang X (2006) A modified technique for high-resolution staining of myelin. *J Neurosci Methods* 153:135–146
24. Valério-Gomes B, Guimarães DM, Szczupak D, Lent R (2018) The absolute number of oligodendrocytes in the adult mouse brain. *Front Neuroanat* 12:90
25. Nishiyama A, Lin X-H, Giese N, Heldin C-H, Stallcup WB (1996) Co-localization of NG2 proteoglycan and PDGF α -receptor on O2A progenitor cells in the developing rat brain. *J Neurosci Res* 43:299–314
26. Scherer SS et al (1994) Differential regulation of the 2',3'-cyclic nucleotide 3'-phosphodiesterase gene during oligodendrocyte development. *Neuron* 12:1363–1375
27. Bhat RV et al (1996) Expression of the APC tumor suppressor protein in oligodendroglia. *Glia* 17:169–174
28. Stelzer EHK et al (2021) Light sheet fluorescence microscopy. *Nat Rev Methods Primers* 1:73
29. Werner C, Sauer M, Geis C (2021) Super-resolving microscopy in neuroscience. *Chem Rev* 121:11971–12015
30. Rusch H et al (2022) Finding the best clearing approach—towards 3D wide-scale multimodal imaging of aged human brain tissue. *NeuroImage* 247:118832
31. Ryan DP et al (2017) Automatic and adaptive heterogeneous refractive index compensation for light-sheet microscopy. *Nat Commun* 8:612
32. Gao R et al (2019) Cortical column and whole-brain imaging with molecular contrast and nanoscale resolution. *Science* 363:eaau8302
33. Duan R et al (2021) Novel insight into the potential pathogenicity of mitochondrial dysfunction resulting from PLP1 duplication mutations in patients with Pelizaeus–Merzbacher disease. *Neuroscience* 476:60–71
34. Abe Y et al (2019) Correlative study using structural MRI and super-resolution microscopy to detect structural alterations induced by long-term optogenetic stimulation of striatal medium spiny neurons. *Neurochem Int* 125:163–174
35. Hainsworth AH et al (2018) Super-resolution imaging of subcortical white matter using stochastic optical reconstruction microscopy (STORM) and super-resolution optical fluctuation imaging (SOFI). *Neuropathol Appl Neurobiol* 44:417–426
36. Steshenko O et al (2016) Reorganization of lipid diffusion by myelin basic protein as revealed by STED nanoscopy. *Biophys J* 110:2441–2450
37. Micu I et al (2007) Real-time measurement of free Ca²⁺ changes in CNS myelin by two-photon microscopy. *Nat Med* 13:874–879
38. Fu Y, Huff TB, Wang H-W, Cheng J-X, Wang H (2008) Ex vivo and in vivo imaging of myelin fibers in mouse brain by coherent anti-Stokes Raman scattering microscopy. *Opt Express* 16:19396
39. Zhai Y-H et al (2011) Multimodal coherent anti-Stokes Raman spectroscopic imaging with a fiber optical parametric oscillator. *Appl Phys Lett* 98:191106
40. Meyer T et al (2013) Expanding multimodal microscopy by high spectral resolution coherent anti-stokes Raman scattering imaging for clinical disease diagnostics. *Anal Chem* 85:6703–6715
41. Micu I, Brideau C, Lu L, Stys PK (2017) Effects of laser polarization on responses of the fluorescent Ca²⁺ indicator X-Rhod-1 in neurons and myelin. *Neurophoton* 4:025002
42. Wu W, Li X, Qu JY, He S (2021) In vivo imaging of biological tissues with combined two-photon fluorescence and stimulated Raman scattering microscopy. *J Vis Exp* 178:63411. <https://doi.org/10.3791/63411>
43. Bélanger E et al (2012) Live animal myelin histomorphometry of the spinal cord with video-rate multimodal nonlinear microendoscopy. *J Biomed Opt* 17:021107
44. Okada SLM, Stivers NS, Stys PK, Stirling DP (2014) An ex vivo laser-induced spinal cord injury model to assess mechanisms of axonal degeneration in real-time. *J Vis Exp* 93:52173. <https://doi.org/10.3791/52173>
45. Stivers NS et al (2017) The toll-like receptor 2 agonist Pam3CSK4 is neuroprotective after spinal cord injury. *Exp Neurol* 294:1–11


46. Chu S-W et al (2002) Nonlinear bio-photonic crystal effects revealed with multimodal nonlinear microscopy. *J Microsc* 208:190–200
47. Huang JY, Chen Z, Lewis A (1989) Second-harmonic generation in purple membrane-poly (vinyl alcohol) films: probing the dipolar characteristics of the bacteriorhodopsin chromophore in bR570 and M412. *J Phys Chem* 93:3314–3320
48. Jin L et al (2006) Characterization and application of a new optical probe for membrane lipid domains. *Biophys J* 90:2563–2575
49. Moen EK, Ibey BL, Beier HT (2014) Detecting subtle plasma membrane perturbation in living cells using second harmonic generation imaging. *Biophys J* 106:L37–L40
50. Nuriya M et al (2016) Multimodal two-photon imaging using a second harmonic generation-specific dye. *Nat Commun* 7:11557
51. Garduno-Robles A et al (2020) MRI features in a rat model of H-ABC tubulinopathy. *Front Neurosci* 14:555
52. Rehberg M, Krombach F, Pohl U, Dietzel S (2011) Label-free 3D visualization of cellular and tissue structures in intact muscle with second and third harmonic generation microscopy. *PLoS One* 6:e28237
53. Farrar MJ, Wise FW, Fetcho JR, Schaffer CB (2011) In vivo imaging of myelin in the vertebrate central nervous system using third harmonic generation microscopy. *Biophys J* 100:1362–1371
54. Witte S et al (2011) Label-free live brain imaging and targeted patching with third-harmonic generation microscopy. *Proc Natl Acad Sci* 108:5970–5975
55. Anzalone A et al (2018) Feasibility study on mouse live imaging after spinal cord injury and poly(lactide-co-glycolide) bridge implantation. *J Biomed Opt* 23:1
56. Redlich MJ, Lim H (2019) A method to measure myeloarchitecture of the murine cerebral cortex in vivo and ex vivo by intrinsic third-harmonic generation. *Front Neuroanat* 13:65
57. Redlich MJ et al (2021) High-pulse-energy multiphoton imaging of neurons and oligodendrocytes in deep murine brain with a fiber laser. *Sci Rep* 11:7950
58. Chorghay Z et al (2021) Activity-dependent alteration of early myelin ensheathment in a developing sensory circuit. *J Comp Neurol* 530:25253. <https://doi.org/10.1002/cne.25253>
59. Pezacki JP et al (2011) Chemical contrast for imaging living systems: molecular vibrations drive CARS microscopy. *Nat Chem Biol* 7:137–145
60. Wang H, Fu Y, Zickmund P, Shi R, Cheng J-X (2005) Coherent anti-Stokes Raman scattering imaging of axonal myelin in live spinal tissues. *Biophys J* 89:581–591
61. Gasecka A, Daradich A, Dehez H, Piché M, Côté D (2013) Resolution and contrast enhancement in coherent anti-Stokes Raman-scattering microscopy. *Opt Lett* 38:4510
62. Lucas A, Poleg S, Klug A, McCullagh EA (2021) Myelination deficits in the auditory brainstem of a mouse model of fragile X syndrome. *Front Neurosci* 15:772943
63. Tamosaityte S et al (2016) Inflammation-related alterations of lipids after spinal cord injury revealed by Raman spectroscopy. *J Biomed Opt* 21:061008
64. Costantini I et al (2021) Autofluorescence enhancement for label-free imaging of myelinated fibers in mammalian brains. *Sci Rep* 11:8038
65. Fowler SD, Greenspan P (1985) Application of Nile red, a fluorescent hydrophobic probe, for the detection of neutral lipid deposits in tissue sections: comparison with oil red O. *J Histochem Cytochem* 33:833–836
66. Prioli S, Reinholdt P, Hornum M, Kongsted J (2019) Rational design of Nile red analogs for sensing in membranes. *J Phys Chem B* 123:10424–10432
67. Teo W et al (2021) Nile red fluorescence spectroscopy reports early physicochemical changes in myelin with high sensitivity. *Proc Natl Acad Sci USA* 118:e2016897118
68. Sakdinawat A, Attwood D (2010) Nanoscale X-ray imaging. *Nat Photon* 4:840–848
69. Dučić T et al (2011) Structure and composition of myelinated axons: a multimodal synchrotron spectro-microscopy study. *J Struct Biol* 173:202–212

70. Töpperwien M et al (2017) Three-dimensional mouse brain cytoarchitecture revealed by laboratory-based X-ray phase-contrast tomography. *Sci Rep* 7:42847
71. Carboni E et al (2017) Imaging of neuronal tissues by X-ray diffraction and X-ray fluorescence microscopy: evaluation of contrast and biomarkers for neurodegenerative diseases. *Biomed Opt Express* 8:4331
72. Jensen TH et al (2011) Brain tumor imaging using small-angle X-ray scattering tomography. *Phys Med Biol* 56:1717–1726
73. Lwin T-T, Yoneyama A, Maruyama H, Takeda T (2021) Visualization ability of phase-contrast synchrotron-based X-ray imaging using an X-ray interferometer in soft tissue tumors. *Technol Cancer Res Treat* 20. <https://doi.org/10.1177/15330338211010121>



Brainbow: Principle, Technique, and Applications

6

Kausalya Neelavara Makkithaya, Saina Rath,
Sathya Sandilya Garemula, Sai Sowmya, S. Keerthana,
and Nirmal Mazumder 

Abstract

In the field of neuroscience, studying the intricate architecture of neuronal and glial cells forming a network in the nervous system can be extremely useful to understand the networking of neurons within the brain and other parts of the nervous system. However, this is an extremely arduous task due to the complexity of the brain and nerve tissue. To this end, optical techniques combined with genetic labeling techniques can be used to obtain a visual representation of the neurons in the tissue. Brainbow is one such strategy that uses Cre-lox recombination to stochastically express two to four fluorescent proteins in cells of the same tissue. This expression is combinatorial and depends on the copy number of the loxP sites present in each cell, thereby resulting in a myriad of colors and hues, which are unique to each cell, making it easier to visually distinguish each neuron within the complex arrangement of the tissue. This multicolor labeling technique otherwise referred to as the “Brainbow” technique is briefly discussed in the following chapter, along with the principle, techniques, and various applications in the field of neuroscience.

K. N. Makkithaya · N. Mazumder (✉)

Department of Biophysics, Manipal School of Life Sciences, Manipal Academy of Higher Education, Manipal, Karnataka, India

S. Rath

National Institute of Science Education and Research, Bhubaneswar, Jatni, Odisha, India

S. S. Garemula · S. Sowmya

Gitam University, Visakhapatnam, Andhra Pradesh, India

S. Keerthana

University of Madras, Chennai, Tamil Nadu, India

Keywords

Brainbow · Brain studies · Confocal microscopy · Multicolor labeling · Cre-recombination

6.1 Introduction

The ability to visualize and make observations is one of the oldest and most powerful methods for the brain to comprehend complex structures. Human beings possess a complex and accurate visual system that processes the myriad visual stimuli received intelligible to the brain. This perhaps is the reason for the preference of visualization tools to study the complex and dynamic nature of biological systems. The ability to visualize the minute cells and their morphological details began with the advent of the microscope. Cells undergo various processes such as proliferation, differentiation, growth, and maturation throughout the embryological stages and the life span of the organism. For instance, the nerves and the nervous system develop in the embryo at stages as early as the third week in the case of human embryos. These nerves and neurons create and become an integral part of an intricate and complex network wherein hundreds and thousands of nerve connections are formed, which overlap with each other within a restricted space [1]. The task of visually distinguishing the various pathways of the complex juxtaposed neurons and the network organization of the glial cells precisely among the intricate networks is humongous, and one which cannot be accomplished simply by using the staining procedures used to visualize and distinguish cells under various microscopes [2, 3].

However, with the isolation of fluorescent proteins, these proteins have been widely applied in microscopy for the visualization of biological tissues and labeling the cells, and organelles [4]. Furthermore, the modifications made to the fluorescent proteins allowed them to be utilized for genetic targeting, thereby labeling only specific cell types or proteins which usually interact with each other [5]. In most biological tissues, cells with similar functions are arranged together to form tissues. This gives rise to a shared genetic expression of these cells when labeled with the same color, making it difficult to distinguish one cell from another due to their shared expression. The same problem becomes extremely challenging when faced with the task of deciphering neurons from one another to visualize and map the connectome [6].

Brain studies require the visualization of the morphology of multiple neurons in a circuit to understand the neuronal pathways. Thus, the intention is to accentuate only a certain set of neurons, while simultaneously distinguishing them from the rest of the connectome. Several staining techniques were proposed [7, 8]. But none were perhaps as effective as the brainbow technique. This technique is designed specifically to label cells with different fluorescent proteins like cyan (CFP), yellow (YFP), or red fluorescent proteins (RFP), which express color based on the copy number of specific genes present in the individual cells. This idea is somewhat of an artistic method developed by neuroscientists to visualize the connectome in the brain. This

was achieved by “allowing” individual neurons to create and express their special mix of fluorescent protein paint, which when visualized under a microscope, manifests as a rainbow-colored brain, or “Brainbow.” This technique thereby separates individual neurons by color. These colors work as identification tags for each cell. The principle and applications of the brainbow technique are further discussed in the following sections.

6.2 Principle: Biology of Brainbow

Brainbow is a technique of color-coding neurons in the brain to analyze the brain connectome. The neurons are tagged with a fluorescent protein and are allowed to express a fluorescent color corresponding to the loxP sites present in them. The concept of brainbow has been inspired by the fact that the primary colors red (R), green (G), and blue (B) are combined in various ratios to form most colors we see digitally and otherwise. Brainbow achieves the aim of color-coding each neuron by the amalgamation of three or four differently colored fluorescent proteins (FPs) and allowing them to be expressed differently in each cell. This differential expression gives a distinct color to each neuron based on the genetic marker present in them [9, 10]. These colors can be visualized under a light microscope.

The primary components to form a brainbow are the “Cre-recombinase” enzyme, and the “Lox” sites present in the genome of the cells. Together, they are called the “Cre-Lox” system. The “Cre recombinase” enzyme was discovered being produced by the Cre gene in the P1 bacteriophage genome [11, 12]. It is known to identify the loxP sites that flank specific genes and cause the deletion, inversion, or translocation of the genes, depending on the position and orientation of the loxP sites, which are 34 bp long DNA sequences, with two palindrome recognition sites, separated by an 8 bp spacer, that gives directionality to the sequence. If the sites flank a gene in the same orientation, the gene is excised by the Cre-recombinase, resulting in an irreversible gene knockout. Whereas, if the loxP sites flanking the gene are in opposing orientations, the Cre-recombinase causes gene reversible inversion. The reversible nature of this process makes it impractical to be used for genetic manipulation. Reversible gene translocation is mediated by the Cre-recombinase if the loxP sites are present on separate DNA strands [13, 14]. The brainbow technique utilizes this Cre-lox recombination principle to visualize the distinct morphology of each neuron in the brain, while distinguishing them from each other as they wind their way into the brain tissues, forming a part of the brain’s connectome. The brainbow 1.0 technique uses three fluorescent proteins that are arranged sequentially arranged in a transgene, flanked by two pairs of the loxP recognition sites, which can be identified by the Cre-recombinase enzyme. The enzyme causes the DNA excision, depending on the spatial arrangement of the loxP sites, thereby causing the fluorescent proteins to express in different combinations of colors. This basic strategy can be expanded by using over four fluorescent proteins that can flank about three pairs of recognition sites.

Brainbow 2.0 technique uses the DNA inversion ability of the Cre-recombinase enzyme when the loxP sites flank the fluorescent proteins in opposing directions. Here, the interspaced protein is flipped instead of being excised by the recombinase. In this case, the FPs are arranged such that the inversion of the protein leads to the expression of only one of the two FPs. A combination of inversion and excision of the recognition sites by the recombinase enzyme can be used to employ four FPs, thereby creating the possibility of many more colors, as seen in brainbow 2.1 [15]. The difference in the number and arrangement of the recognition sites and the DNA excision or translocation caused by the recombinases are what causes the fluorescent proteins to be expressed in different combinations and ratios in each cell, thereby giving rise to a multitude of colors [16]. The palette of colors to be expressed in the brainbow depends on the number of FPs used, along with the function of the Cre-recombinase. A combinatorial function of excision and inversion would require a larger number of FPs, and result in a larger palette of colors expressed, thereby allowing for better differentiation among the neurons. This has resulted in up to 100 shades of different colors. These potential colors can give rise to a specific barcode for each cell, thus making it easy to distinguish between very closely related cells [16]. The intensity of colors expressed thereby depends on the copy number of the fluorescent protein (XFP) genes. Insertion of multiple copies of the transgenic cassette results in stochasticity and their synergistic expression thereby resulting in the distinct colors seen as brainbow.

6.3 Techniques Used in Brainbow

Light microscopes have been a constant tool for the visualization of biological structures, and deciphering cells of a tissue, to an entire organism. Light microscopes along with fluorescence proteins have further enhanced the ability of these microscopes to resolve fairly complex biological structures to a great extent. However, the ability of these microscopes to decipher cells in highly complex biological structures such as nerve tissues has been hampered simply by the sheer complexity of these structures [17]. This has given rise to the need for different techniques to enhance the capacity of these microscopes to visualize the nervous system in its entirety, which was made difficult by the complex arrangement of the nerve cells.

The advances in optical microscopy have made it possible to visualize complex microscopic structures, with the use of fluorescent dyes. However, in the case of complex biological tissues, it is important to obtain the spatiotemporal arrangement of the cells and other components of the tissue. Confocal Laser Scanning Microscopy (CLSM) is therefore used to obtain the surface topography of biological tissues. Most applications of confocal microscopy function on the principle of a pinhole for the discrimination of height or girth of the sample. The pinhole is used to refocus light on a specific area of the sample, thereby aiding in the formation of a clearer image of the “optical section.” The stacking of many such images results in the formation of a 3D image [18]. Recent advances in the field of microscopy have opened new avenues, permitting the greater depth of imaging, and the usage of live



Fig. 6.1 In vivo brain expression of the hindbrain of the zebrafish as viewed under a confocal microscope. In vivo brainbow expression in the hindbrain, shown in maximum intensity projections representing 41 μm in sparsely labeled 51 hpf zebrafish (above), and 81 μm in 63.5 hpf zebrafish (below). In both panels, the dorsal is up and the rostral is to the left. (Reproduced with permission from Brockway et al. [49])

samples, wherein a section of the tissue of interest is windowed [19]. Cook et al., in their work, have developed a novel protocol to visualize the progenitor cells and nerve cells of the hindbrain of the zebrafish in vivo (Fig. 6.1). The paper discussed the application of brainbow fluorescent dye techniques and time-lapse confocal microscopy for much clearer visualization of the tissues undergoing various physiological processes such as cell death (Fig. 6.2) [20].

6.4 Brain Tissue Optical Clearing

Confocal laser scanning microscopy is popularly used for the visualization of complex tissues. The quality of the images generated can be augmented by certain clearing agents [21]. The tissue clearing agents perform the dual tasks of enhancing the expression of the fluorescent dyes as well as increasing the resolution of the

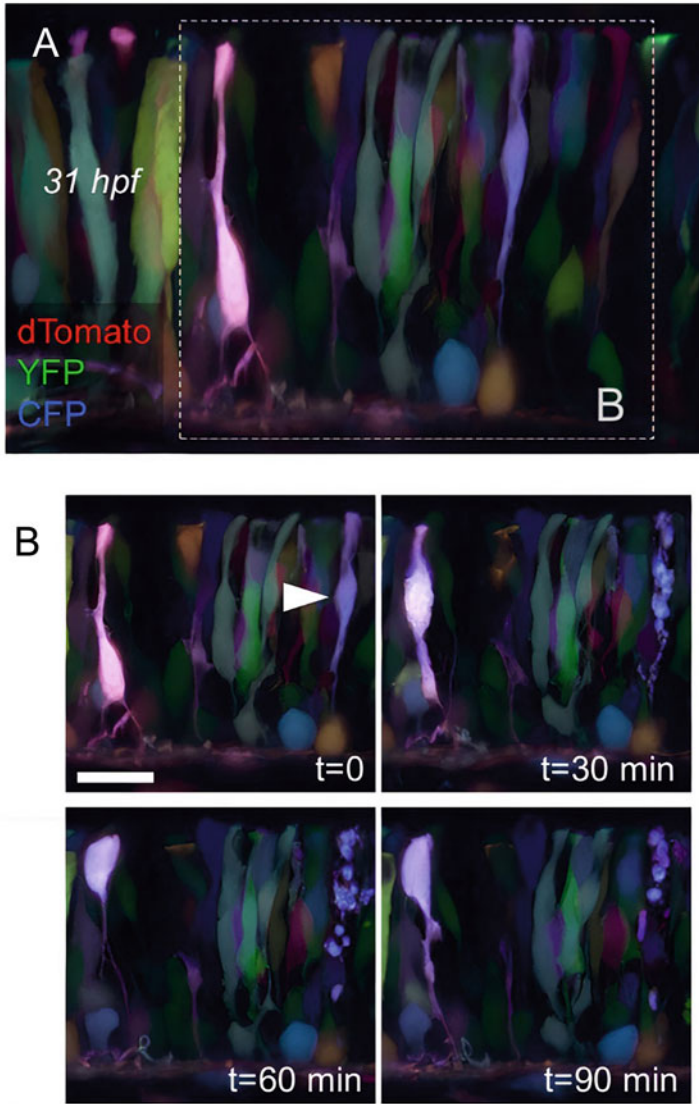


Fig. 6.2 Brainbow technique allows us to visualize physiological processes such as cell death. (a) Depiction of the zebrafish hindbrain brainbow at 31 hpf. (b) Gradual apoptosis of the lavender-colored cell (pointed) over a time. The image has been taken at a time interval of 30 min. (Reproduced with permission from Brockway et al. [49])

images being generated. This approach is called optical tissue clearing [22]. The optical clearing is a method where it reduces the tissue's opacity, reduces scattering, and makes it transparent, so it will be clear to see the biological sample. When light illuminates through biological tissues, it is scattered and absorbed. Because of the

light scattering, the biological tissues get opaque as the tissue is made up of water, lipids, and proteins. The refractive index of these components is different. Since the refractive indices mismatch, the light propagates at different speeds and angles, causing opacity in the mammalian tissue. The optical clearing technique is effective in removing the high refractive index components from the tissue [23]. Besides, this approach provides better tissue heterogeneity, reduces tissue scattering, increases the depth of light penetration, and makes the tissue transparent.

When brain tissue is incubated in a chemical bath, it tends to decrease its optical scattering property. Due to this, the optical imaging depth and tissue transparency increase. However, optical clearing provides transparency of the tissues, such that every single neuron is traceable. When a neuron combines with any fluorescent protein, the tissue gets labeled by color. To know the neuron's brainbow (or) color, the optical clearing technique will make the tissue transparent without tissue damage. Ke et al. developed SeeDB, a tissue clearing agent which was used to enable clearer visualization of brain tissue samples. Its ability to clear fixed brain tissue samples without quenching or diluting the fluorescent proteins and dyes which are used for color-coding neurons was reported. Ke et al. also conducted studies to investigate the tissue clearing performed by SeeDB, and it was found that the clearing agent did not compromise on the morphological integrity of the cells, thereby keeping the neural circuit intact [24]. Another technique for the optical clearing of formalin-fixed adult cortical tissue, called MASH (Multiscale Architectonic Staining of Human Cortex) was proposed by Hildebrand et al. It was found to be suitable for the cytoarchitectonic labeling of slightly thicker and larger cortical brain samples for deep volume imaging using a combination of cytoplasmic dyes and refractive index matching solutions. It was found that MASH reduced the cost and time taken for imaging cytoarchitecture in thick samples [25]. SHANEL (small-micelle-mediated human organ efficient clearing and labeling) is another technique for the optical clearing of the brain tissue. Zhao et al. developed the technique based on chemical tissue permeabilization and were successful in rendering adult human brain tissues and kidneys transparent [26].

Despite the uses of the brainbow technique, the brightness of the fluorescent proteins was found to be generally low. On investigation, it was found that the stochastic and combinatorial expressions of the fluorescent proteins were effective only at lower copy numbers of the genes, which was not always the case, thereby resulting in low fluorescent protein expression levels [27]. In order to enhance the expression of the fluorescent proteins (XFPs) forming brainbow, the tetracycline activator system was used. The technique developed is now called Tetbow (Tetracycline trans-activator brainbow) [28]. The Tetbow system employed the use of tetracycline response element (TRE), instead of the CAG promoter which is commonly used in the case of Brainbow. This ensured higher expression levels of the XFPs. Furthermore, spherical aberrations observed while viewing the connectome in the microscope were overcome by the application of the optical clearing agents and techniques. Additionally, Sakaguchi et al. also demonstrated that the use of the unmodified XFPs, instead of modified membrane-bound XFPs, accomplished better

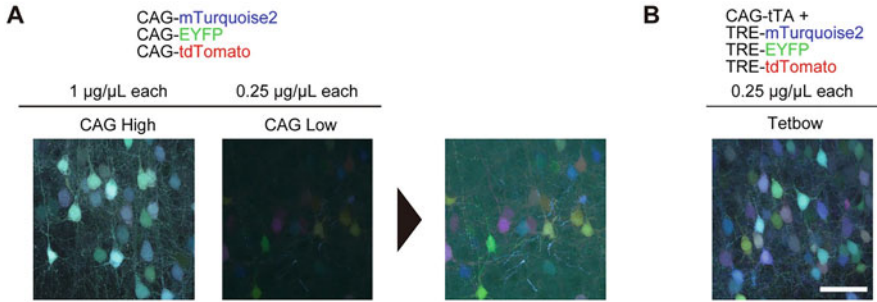


Fig. 6.3 Labeling of neurons via Tetbow technique (a) L2/3 neurons labeled with CAG-Turquoise2, EYFP, and tdTomato (1 or 0.25 µg/µL each). When each plasmid was introduced at 0.25 µg/µL, the color variation was increased, however, the fluorescence levels were reduced. Enhanced images are shown on the right. (b) CAG-tTA, TRE-Turquoise2, EYFP, and tdTomato were introduced at 0.25 µg/µL each. In utero electroporation was performed at E15 and the mice were analyzed at P21. (Reproduced with permission from Sakaguchi et al. [28])

expression levels compared to those obtained by the use of the CAG promoter plasmids (Fig. 6.3).

Further investigation for the standardization of the Tetbow protocol revealed that the technique is most effective when introduced employing in utero electroporation at an optimum concentration of 0.25 µg/µL, which enabled better axon tracing. Despite all the aforementioned advantages of the Tetbow staining technique, it is yet to be developed and used to its full potential. Currently, the brainbow technique is employed more frequently for various applications such as connectome mapping, studies of developmental biology, and other physiological pathways effectively [28].

6.5 Applications

6.5.1 Connectome Mapping

A human brain houses a million networks. A connectome explains the structural connections through nerve fibers (axons/physical wirings) between brain regions that help us in navigating the human brain. Besides dyeing cells with a unique color, the brainbow can spot and differentiate dendritic and neural processes. Hence, we can visualize neural circuitry with immense intricacy. It provides detailed information about the neurons and their connectivity, which helps in understanding the neuronal interactions and their impact on behavior and function. The versatility of this technique can be seen in its wide applications on various model organisms such as a mouse, fruit fly, plants, and zebrafish [9, 16]. Human beings, however, cannot be used for these manipulations for obvious ethical reasons.

6.5.1.1 Mice

The brain of all mammals almost has the same connectome organization which makes it easier to obtain insights about the human brain functioning from the data obtained from the model mouse brain. It is rather simple to map an entire mouse connectome than that of a human being. Brainbow is extensively used for retrograde tracing in the mouse brain [29, 30]. Further, it can help distinguish adjacent axons which help in mapping projections of a neuron at two levels in the same synaptic circuit. For an instance, the brainbow was used to label the preganglionic neurons with unique colors that aided the study of the relation between axons of postganglionic neurons and their preganglionic innervations [27].

6.5.1.2 *Drosophila*

Brainbows' multicolor labeling technique is combined with the genetic targeting tools from *Drosophila melanogaster* commonly known as the fruit fly. In the brainbow of *drosophila* (dBrainbow), endogenous fluorescence is replaced by the use of antibody-labeled epitopes which help in tracing the finer processes of neurites over long distances [31]. Genetic variants of fruit flies called Gal-4 lines use the Gal-4/UAS (Upstream activation stream) to study the connectome (esp. the neural interactions) through controlled expression of reporter line genes by specific cells and tracing them using brainbow [32]. For instance, dBrainbow is used to study the activity of motor neurons connecting suboesophageal ganglion to the proboscis's muscles that underlay its feeding behavior [33, 34]. Brainbow has also been used to study and follow the cell lineages of multiple cells in the wing imaginal disc while concurrently inhibiting the expression of UAS-regulated constructs in a subset of labeled cells. This allowed distinct visualization of the mutant and normal cells based on the differences in their expressions [35].

6.5.1.3 Zebrafish

Brainbow obtained of the zebrafish, known as "Zebrabow" was developed such that it included Gal4-inducible transgenic cell lines and standardized parameters for the diversity of the brainbow colors expressed [36]. This demonstrated that the color profiles of the cell lineages remain constant even after cell division and growth, thereby aiding in the effective tracking of the cell's lineage. Other zebrabows have been generated with transgenic cell lines modified specifically to follow cell migration, proliferation, and growth [37]. This is known to be useful for the study of extensive axon branching in the somatosensory and visual nerves [38].

6.5.2 Developmental Biology

Cellular dynamics such as orderly proliferation, cellular migration, positioning, and rearrangement carry a lot of biochemical and mechanical cues that help us trace its lineage better. Conventional viral and fluorescent labeling methods can be used to study the lineage of the cell from a single or a limited number of clones. Hence clearly, cells having complex intermingled lineages obtained from multiple clones

cannot be traced using these methods. Brainbow multicolor labeling method can be targeted to specific cells and developmental stages using Cre-lox recombination [9].

6.5.3 Deciphering Neural Heterogeneity

During the development of the nervous system from the neural stem cells, the neural progenitor cells progressively commit themselves to specific lineages and populations which have more limited proliferation and differentiation potential [39, 40]. This is achieved by symmetric and asymmetric divisions producing identical and non-identical sibling cells, respectively. This causes the production of a pool of cells with multiple lineages, making the human brain heterogeneous in origin [41]. Heterogeneity of the brain decides the shape and structure of brain tissues over proliferation. Recent studies using machine learning have also found out that heterogeneity helps in making learning (especially tasks with a temporal structure) more stable and robust. Brainbow helps in labeling the cells of different lineages in different hues and distinguishes them from neighboring neural cells. Advanced versions of the brainbow also produce vivid images that depict the morphology of each neural cell [42]. Information obtained from cell mapping using the brainbow technique is used to understand the progression of a lineage and its impact on the successive neural heterogeneity.

6.5.4 Lineage Tracing in Developing Embryos

In addition to its varied applications, brainbow is increasingly used as a multicolor clonal analysis technique to study the contribution of each cardiomyocyte in the morphogenesis of primitive embryonic heart to complex adult form. Brainbow is used to study the cellular mechanisms of organ morphogenesis after birth/hatching. This can be used to study the proliferative histories of cardiomyocytes as vertebrate hearts progress from a simpler to complex adult form [37].

6.5.5 Neural Diseases and Disorders

In healthy aging, some neurons are lost, producing changes in brain connections. But in neurodegenerative diseases, the loss of neurons is widespread, with simultaneous loss of functionality and connections ultimately leading to the death of neurons. The human brain is highly complex with intermingled networks, which makes it difficult to trace the original part of the brain which excites a particular behavior. Hence, it is important to understand the whole connectome to justify functions to structures and find a better cure for diseases. With recent advancements like improved color balance [31] color discrimination [43], it is easier to monitor the activity of each neuron under certain developmental and genetically modified conditions. Brainbow can help to label axons of each neuron with a different color, which makes it easier to

trace the origin of the neuron. So, when a neuron undergoes degeneration, the information obtained from the brainbow wiring diagrams of the nervous system helps us in identifying the source and potential loss of function that may lead to change in behavioral patterns and cognitive deficit. This helps to identify treatments for diseases like Alzheimer's and Parkinson's [44] where the symptoms usually manifest at later stages of the disease when it becomes almost incurable. Sometimes viruses and bacteria can invade the nervous system, causing infections such as encephalitis, meningitis, and brain TB. Viral vectors such as the West Nile virus [43, 45, 46] pseudorabies virus [47] can be incorporated with specific brainbow constructs to study the progression of the disease in model organisms (mice, zebrafish, etc.). Thus, the model organism is infected with the viral vector, followed by incubation of a specific nervous tissue for a defined period. This time is required by the vectors to express the fluorescent proteins and stain the neurons. If the incubation is done with fluorescent antibodies, the neurons are immuno-stained, and the immune response of the model organism can be studied. Further, when the cells are studied at an interval of days post-incubation, we can observe the percentage of target cells which are affected, which can help us find remedies and develop potential therapeutics [48].

6.6 Conclusion

The possibilities of scientific inventions are endless. It is rather the contemplation of the human brain which sees things in a different light. A myriad of labeling techniques was used since the advent of the brainbow technique, but none could produce a satisfactory detailed architecture of the human connectome. Over the years, scientists have engineered various brainbow constructs which can visualize neural circuitry at micro- and macroscopic levels in an artistic way, allowing the amalgamation of visual observation via color and genomic analyses. The recent advancements to the original brainbow constructs and techniques have improved our ability to visualize the nervous systems significantly, eventually increasing their practical applications. Brainbow is most effective when used to visualize a single cell in a complex multicellular background. Hence, picturing the entire connectome in high resolution at once is still a challenge.

Acknowledgments We thank Global Innovation and Technology Alliance (GITA), Department of Science and Technology (DST), India [Project Number-GITA/DST/TWN/P-95/2021], and Indian Council of Medical Research (ICMR), (Project Number-ITR/Ad-hoc/43/2020-21, ID No. 2020-3286) Government of India, India for financial support.

References

1. Stiles J, Jernigan TL (2010) The basics of brain development. *Neuropsychol Rev* 20(4): 327–348

2. Morris GB, Ridgway EJ, Suvama SK (2019) Traditional stains and modern techniques for demonstrating microorganisms in histology. In: Bancroft's theory and practice of histological techniques, vol 254(1). Elsevier, Amsterdam, pp 1–5
3. Yurt KK, Kivrak EG, Altun G, Mohamed H, Ali F, Gasmalla HE, Kaplan S (2018) A brief update on physical and optical disector applications and sectioning-staining methods in neuroscience. *J Chem Neuroanat* 93(1):16–29
4. Shimomura O, Johnson FH, Saiga Y (1962) Extraction, purification and properties of aequorin, a bioluminescent protein from the luminous hydromedusa, *Aequorea*. *J Cell Comp Physiol* 59(3):223–239
5. Goedhart J, Von Stetten D, Noirclerc-Savoie M, Lelimosin M, Joosen L, Hink MA, Van Weeren L, Gadella TW, Royant A (2012) Structure-guided evolution of cyan fluorescent proteins towards a quantum yield of 93%. *Nat Commun* 3(1):1–9
6. Luo L (2007) Fly MARCM and mouse MADM: genetic methods of labeling and manipulating single neurons. *Brain Res Rev* 55(2):220–227
7. Lee H, Oh WC, Seong J, Kim J (2016) Advanced fluorescence protein-based synapse-detectors. *Front Synaptic Neurosci* 8(1):16
8. Uemura T, Mori T, Kurihara T, Kawase S, Koike R, Satoga M, Cao X, Li X, Yanagawa T, Sakurai T, Shindo T (2016) Fluorescent protein tagging of endogenous protein in brain neurons using CRISPR/Cas9-mediated knock-in and in utero electroporation techniques. *Sci Rep* 6(1):1–3
9. Livet J, Weissman TA, Kang H, Draft RW, Lu J, Bennis RA, Sanes JR, Lichtman JW (2007) Transgenic strategies for combinatorial expression of fluorescent proteins in the nervous system. *Nature* 450(7166):56–62
10. Lichtman JW, Livet J, Sanes JR (2008) A technicolour approach to the connectome. *Nat Rev Neurosci* 9(6):417–422
11. Sternberg N, Hamilton D (1981) Bacteriophage P1 site-specific recombination: I. Recombination between loxP sites. *J Mol Biol* 150(4):467–486
12. Sternberg N, Sauer B, Hoess R, Abremski K (1986) Bacteriophage P1 cre gene and its regulatory region: evidence for multiple promoters and for regulation by DNA methylation. *J Mol Biol* 187(2):197–212
13. Nagy A (2000) Cre recombinase: the universal reagent for genome tailoring. *Genesis* 26(2):99–109
14. Branda CS, Dymecki SM (2004) Talking about a revolution: the impact of site-specific recombinases on genetic analyses in mice. *Dev Cell* 6(1):7–28
15. Van Duyne GD (2015) Cre recombinase. *Microbiol Spectrum* 3(1):3–1
16. Loulier K, Barry R, Mahou P, Le Franc Y, Supatto W, Matho KS, Ieng S, Fouquet S, Dupin E, Benosman R, Chédotal A (2014) Multiplex cell and lineage tracking with combinatorial labels. *Neuron* 81(3):505–520
17. Hillman EM, Voleti V, Li W, Yu H (2019) Light-sheet microscopy in neuroscience. *Annu Rev Neurosci* 42(2):295–313
18. Gleichgerrcht E, Fridriksson J, Rorden C, Bonilha L (2017) Connectome-based lesion-symptom mapping (CLSM): a novel approach to map neurological function. *NeuroImage Clin* 16(5):461–467
19. Elliott AD (2020) Confocal microscopy: principles and modern practices. *Curr Protoc Cytom* 92(1):68
20. Cook ZT, Brockway NL, Weissman TA (2020) Visualizing the developing brain in living zebrafish using brainbow and time-lapse confocal imaging. *J Vis Exp* (157):60593
21. Susaki EA, Tainaka K, Perrin D, Kishino F, Tawara T, Watanabe TM, Yokoyama C, Onoe H, Eguchi M, Yamaguchi S, Abe T (2014) Whole-brain imaging with single-cell resolution using chemical cocktails and computational analysis. *Cell* 157(3):726–739
22. Richardson DS, Lichtman JW (2015) Clarifying tissue clearing. *Cell* 162(2):246–257
23. Costa EC, Silva DN, Moreira AF, Correia IJ (2019) Optical clearing methods: an overview of the techniques used for the imaging of 3D spheroids. *Biotechnol Bioeng* 116(10):2742–2763

24. Ke MT, Fujimoto S, Imai T (2013) SeeDB: a simple and morphology-preserving optical clearing agent for neuronal circuit reconstruction. *Nat Neurosci* 16(8):1154–1161
25. Hildebrand S, Schueth A, Herrler A, Galuske R, Roebroek A (2019) Scalable labeling for cytoarchitectonic characterization of large optically cleared human neocortex samples. *Sci Rep* 9(1):1
26. Zhao S, Todorov MI, Cai R, Rami AM, Steinke H, Kemter E, Mai H, Rong Z, Warmer M, Stanic K, Schoppe O (2020) Cellular and molecular probing of intact human organs. *Cell* 180(4):796–812
27. Cai D, Cohen KB, Luo T, Lichtman JW, Sanes JR (2013) Improved tools for the Brainbow toolbox. *Nat Methods* 10(6):540–547
28. Sakaguchi R, Leiwe MN, Imai T (2018) Bright multicolor labeling of neuronal circuits with fluorescent proteins and chemical tags. *elife* 7:e40350
29. Wickersham IR, Finke S, Conzelmann KK, Callaway EM (2007) Retrograde neuronal tracing with a deletion-mutant rabies virus. *Nat Methods* 4(1):47–49
30. Wickersham IR, Lyon DC, Barnard RJ, Mori T, Finke S, Conzelmann KK, Young JA, Callaway EM (2007) Monosynaptic restriction of transsynaptic tracing from single, genetically targeted neurons. *Neuron* 53(5):639–647
31. Hampel S, Chung P, McKellar CE, Hall D, Looger LL, Simpson JH (2011) Drosophila Brainbow: a recombinase-based fluorescence labeling technique to subdivide neural expression patterns. *Nat Methods* 8(3):253–259
32. Förster D, Luschnig S (2012) Src42A-dependent polarized cell shape changes mediate epithelial tube elongation in Drosophila. *Nat Cell Biol* 14(5):526–534
33. Rajashekhar KP, Singh RN (1994) Neuroarchitecture of the tritocerebrum of Drosophila melanogaster. *J Comp Neurol* 349(4):633–645
34. Miller A (1950) The internal anatomy and histology of the imago of Drosophila melanogaster. In: *The biology of Drosophila*. Wiley, New York, pp 421–534
35. Worley MI, Setiawan L, Hariharan IK (2013) TIE-DYE: a combinatorial marking system to visualize and genetically manipulate clones during development in Drosophila melanogaster. *Development* 140(15):3275–3284
36. Pan YA, Freundlich T, Weissman TA, Schoppik D, Wang XC, Zimmerman S, Ciruna B, Sanes JR, Lichtman JW, Schier AF (2013) ZebraBow: multispectral cell labeling for cell tracing and lineage analysis in zebrafish. *Development* 140(13):2835–2846
37. Gupta V, Poss KD (2012) Clonally dominant cardiomyocytes direct heart morphogenesis. *Nature* 484(7395):479–484
38. Robles E, Filosa A, Baier H (2013) Precise lamination of retinal axons generates multiple parallel input pathways in the tectum. *J Neurosci* 33:5027–5039
39. Gage FH (2000) Mammalian neural stem cells. *Science* 287(5457):1433–1438
40. Temple S (2001) The development of neural stem cells. *Nature* 414(6859):112–117
41. Franco SJ, Müller U (2013) Shaping our minds: stem and progenitor cell diversity in the mammalian neocortex. *Neuron* 77(1):19–34
42. Snippert HJ, Van Der Flier LG, Sato T, Van Es JH, Van Den Born M, Kroon-Veenboer C, Barker N, Klein AM, Van Rheenen J, Simons BD, Clevers H (2010) Intestinal crypt homeostasis results from neutral competition between symmetrically dividing Lgr5 stem cells. *Cell* 143(1):134–144
43. García-Moreno F, Vasistha NA, Begbie J, Molnár Z (2014) CLoNe is a new method to target single progenitors and study their progeny in mouse and chick. *Development* 141(7):1589–1598
44. Vijjaratnam N, Simuni T, Bandmann O, Morris HR, Foltyniy T (2021) Progress towards therapies for disease modification in Parkinson’s disease. *Lancet Neurol* 20(7):559–572
45. Blakely PK, Kleinschmidt-DeMasters BK, Tyler KL, Irani DN (2009) Disrupted glutamate transporter expression in the spinal cord with acute flaccid paralysis caused by West Nile virus infection. *J Neuropathol Exp Neurol* 68(10):1061–1072

46. Kleinschmidt-DeMasters BK, Beckham JD (2015) West Nile virus encephalitis 16 years later. *Brain Pathol* 25(5):625–633
47. Boldogkői Z, Balint K, Awatramani GB, Balya D, Busskamp V, Viney TJ, Lagali PS, Duebel J, Pásti E, Tombácz D, Tóth JS (2009) Genetically timed, activity-sensor and rainbow transsynaptic viral tools. *Nat Methods* 6(2):127–130
48. Vig PJ, Lu D, Paul AM, Kuwar R, Lopez M, Stokic DS, Leis AA, Garrett MR, Bai F (2019) Differential expression of genes related to innate immune responses in ex vivo spinal cord and cerebellar slice cultures infected with west nile virus. *Brain Sci* 9(1):1
49. Brockway NL, Cook ZT, O’Gallagher MJ, Tobias ZJ, Gedi M, Carey KM, Unni VK, Pan YA, Metz MR, Weissman TA (2019) Multicolor lineage tracing using in vivo time-lapse imaging reveals coordinated death of clonally related cells in the developing vertebrate brain. *Dev Biol* 453(2):130–140



Photoacoustic Imaging of Brain

7

Mridula Sunder, Nirmal Mazumder, Yury V. Kistenev,
and Denis A. Vrazhnov

Abstract

Photoacoustic imaging (PAI) is a high-tech medical instrument which combines laser absorption spectroscopy and ultrasound imaging, commonly used to assess the function of the brain. It provides a contactless and diffraction-limited resolution visualization of tissues. In this chapter, various PAI experiments have been described to learn the in vivo brain activity, the peculiarities in brain, and the current state in persisting brain disorders. Each PAI method has shown excellent results in specific studies. The chapter helps to assess and predict the importance PAI in the clinical trials as well as medical field itself.

Keywords

Photoacoustic imaging · Cranial window · Neurodegenerative diseases · Ischemic stroke · Spinal cord injury · Epilepsy · Brain tumors

7.1 Introduction

Photoacoustic imaging (PAI) combines optical and acoustic phenomena for tissue analysis. When a laser pulse propagates through the biological tissue, a part of its energy is absorbed by definite tissue molecular components which further causes local periodical temperature variation and consequent thermoelastic expansion or

M. Sunder · N. Mazumder

Department of Biophysics, Manipal School of Life Sciences, Manipal Academy of Higher Education, Manipal, Karnataka, India

Y. V. Kistenev (✉) · D. A. Vrazhnov

Tomsk State University, Tomsk, Russia

e-mail: yuk@iao.ru

compression. As a result, an ultrasonic wave, with an approximate range of 1–100 MHz, is generated. The wave produced can be detected on the tissue surface by an ultrasound (US) transducer in the same manner as in conventional US imaging. PAI sensitivity is defined by the incident laser fluence, imaging depth, wavelength, absorption cross-section of a target molecule, and the US transducer efficiency [1]. According to the configurations of acoustic detection and optical excitation methods, the executions of PAI are classified into the following groups:

- photoacoustic computed tomography (PAT)
- optical-resolution photoacoustic microscopy (OR-PAM)
- acoustic-resolution photoacoustic microscopy (AR-PAM)
- photoacoustic remote sensing (PARS)
- volumetric photoacoustic microscopy (V-PAM)

7.1.1 Types of PA Instruments

PAT combines wide-field pulsed optical illumination and US multi-element-array detector enabling a whole imaging plane acquisition but having quite low spatial resolution of hundreds of micrometers and high penetration depth of several centimeters [2–4]. Tight beam focusing improves spatial resolution, and the typical ratio of the tomography depth to the spatial resolution in PAT is approximately 200 [5]. Oppositely to PAT, PAM combines focused both acoustic detection and optical illumination that offers high spatial resolution from several micrometers to tens of micrometers with comparatively small penetration from one to several millimeters [6]. PAM mainly consists of two types of microscopy, the OR-PAM and the AR-PAM.

The distinction between OR- and AR-PAM is the size of the focused laser spot on the object [6, 7]. In OR-PAM, the optical focus is much firmer than the acoustic focus although in AR-PAM, the acoustic focus is smaller than the optical beamwidth. In both the cases, the axial resolution is defined acoustically. In OR-PAM, the optically controlled lateral resolution is characteristically much better than the axial resolution. The optical focusing can be either strong or weak, depending on the desired spatial resolution and penetration. In contrast, in AR-PAM, the axial resolution is normally better than the lateral resolution [5, 8]. It was shown to provide up to 5 mm depth, 7 μm axial, and 30 μm lateral resolutions [9]. PARS combines a pulsed sensing laser beam illumination and a US wave detection on a body surface by a continuous wave probing beam reflected from the air/body surface interface [10, 11]. This approach provides contactless diffraction-limited resolution at distances of up to 2.5 cm to the body surface. The latter is convenient for intraoperative applications [2–13]. When a two-dimensional array of US detectors is placed on a spherical surface, a whole volume image can be recorded without scanning, using a single laser pulse illumination [14, 15]. This approach, called V-PAM is attractive for whole-brain animal neuroimaging

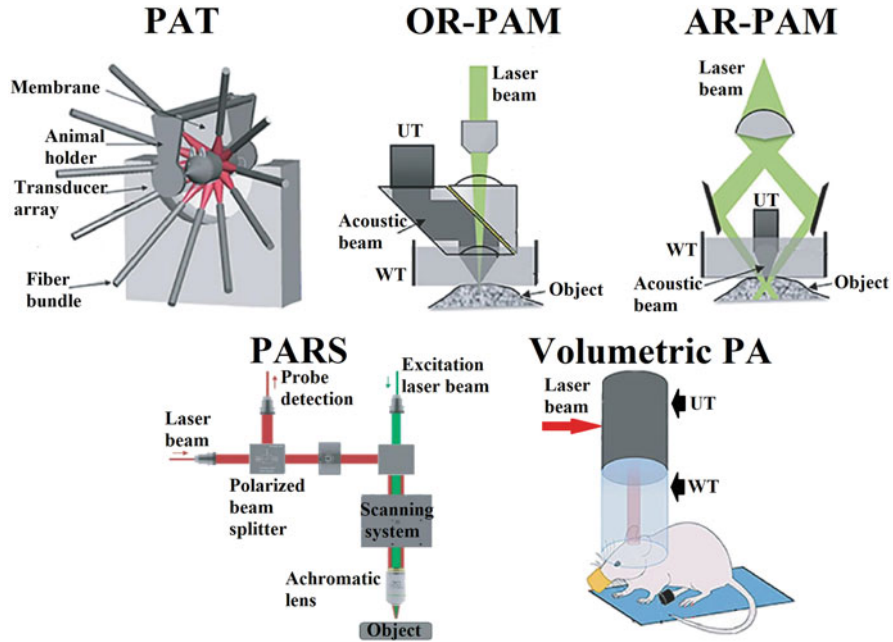


Fig. 7.1 Experimental setup of various types of PAI for different applications. (The figure was adapted with permission from Ref. [2])

[2]. Typical experimental implementations of PAI methods are explained further in the next section (Fig. 7.1).

PAI has the following benefits compared to other imaging methods [16]:

1. In contrast to US imaging, PAI can distinguish molecular substances with the same acoustic impedance by their unique absorption spectra.
2. Safer when compared to X-ray and other ionization imaging methods.
3. Compared with MRI, PAI has higher sensitivity and no contraindications.
4. Deeper penetration compared to conventional optical imaging due to backward signal is an ultrasound, which undergoes less scattering than an optical wave.

7.2 Instrumentation

A specific engineering task for brain imaging with PAI is a wearable head-mounted device that allows free movement of the animal under study and does not produce discomfort, which might affect brain imaging results. Wang et al. proposed a miniaturized head-mounted PAI (hmPAI) system for cortical layer hemodynamic response studies in freely moving rats. Additionally, the system can provide front and rear horizontal planes B-scan images via PA probe with a US transducer and

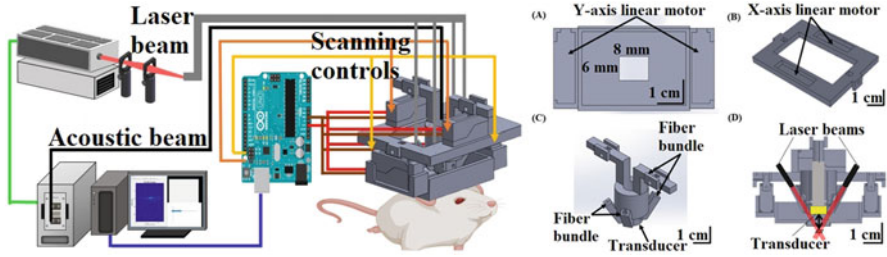


Fig. 7.2 Scheme of head-mounted system, including size, component, and assembly. (a, b) are y-axis and x-axis linear motor holders, respectively, (c) transducer and fiber bundles holders, (d) hmPAI system cross-sectional view. (The figure was adapted with permission from Ref. [17])

fiber-based illumination. The scanning area is up to 8 by 6 mm with a lateral resolution of 0.12 mm. It takes 56 min to obtain a full scan [17] (Fig. 7.2).

The direct, longitudinal *in vivo* studies of the brain activities require implantation of chronic cranial windows (CCW) [18, 19]. The CCW are used in multiphoton imaging, NIRS, EEG, and OR-PAM [20–26]. The OR-PAM CCW requires not only optically but acoustically transparent. A soft, micro- and nanostructured, conductive elastomer films constructed by depositing gold on nanometer thiol-functionalized polydimethylsiloxane (PDMS) make a good mechanical match between neural tissue and implant [27]. The thicknesses of the implants may cause severe acoustic attenuation, so ultrathin (50 μm) PDMS films were fabricated [26]. The PDMS film was fixed to the skull with cyanoacrylate glue, sterilized, and cleaned with ethanol. The gap between the imaging probe and PDMS film was filled with a coupling medium. Air bubbles on a cortical surface can affect visualization, so the space between the dura and PDMS film was filled with saline. The comparison of the maximum amplitude projection images of the proposed technology and glass-based CCW shows that PDMS films are optically and acoustically transparent for OR-PAM. It was mentioned that due to postoperative inflammation, CCW blurring was observed.

Another CCW with a soft film made from polymethyl pentene polymer (PMP) was reported [28]. An advantage of PMP is that it is less permeable to air compared to PDMS. The disadvantage of soft polymer films is the possible degradation of the penetration depth. For example, it was shown for multiphoton imaging at 800 nm that initially tissues can be visualized up to the 600 μm depth, 400 μm after 6 months, and only 200 μm after 1 year. The glass CCW shows no degradation after 6 months. The benefits of glass CCW lead to the idea of using ultrasonic detectors with optically transparent micro-ring resonators [29, 30]. The unresolved problems were easy contamination, high cost, poor sensitivity, and low yield [31]. Further development of the technique was done by Li et al. [32] by the invention of an integrated transparent nanophotonic ultrasonic detector with a 5 μm thin UV-curable PDMS protective film. It provides a tenfold increase in sensitivity (Fig. 7.3). A very simple yet productive idea for hidden CCW based on skull removal and suturing the incision on the scalp was suggested in [32]. The proposed technique can be used for

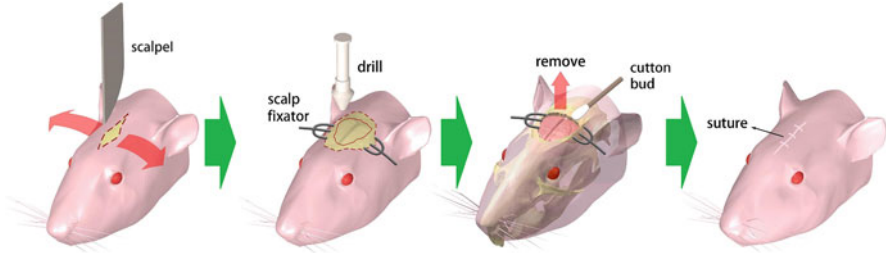


Fig. 7.3 Procedure for creating the chronic cranial window. (The figure was adapted with permission from Ref. [32])

ring-array PACT, photoacoustic mesoscopic, functional PACT, and ultrasound imaging.

A procedure of thinning cranial bone up to 25 μm was found to be complicated because it requires repetition over time and is applicable for small CCW sizes only [33]. Alternative to the invasive CCW technique is various optical clearing agents (OCA), which are capable of enhancing visualization quality by infiltrating studied samples with high-refractive-index substances, which increases the induced acoustic wave and the transmission of light. In the study [34], the following OCAs were applied to mouse skulls two-photon imaging: collagenase, EDTA disodium, and glycerol. The primary substance in the inorganic part of the skull was shown to be calcium hydroxyapatite (CH), and collagen is dominant in the organic part. During mouse aging, the quantity of collagen lowers while CH increases, so infant mice are treated by collagenase and later by EDTA disodium for decalcification (Fig. 7.4).

The *in vitro* study of propylene glycol (PG) as OCA in application to the cranial bone [35] shows a significant reduction (by 20–30%) of absorption and scattering. Both *in vivo* and *in vitro* tests of various OCA compositions of EDTA, laurinol, dimethyl sulfoxide, weak alkaline substances, EDTA, alcohol, sorbitol, glucose, glycerol, and PG during USAF visualization were performed and discovered the leading role of the laurinol the skull optical clearing in 25 min after application [36]. OCAs are also applied to the head skin, i.e., glycerol–water solution can increase lateral resolution and imaging depth of OR-PAM [37, 38]. It can be used along with craniotomy with head skin covering the wound. Yang et al. show that ultrasonic signal in PAI of cerebral microvasculature of intact skulls can be improved 1.58-fold by application of complex OCA consisting of laurinol, dimethylsulfoxide, sorbitol, alcohol, glucose, and sodium dodecyl benzene sulfonate [39]. The acoustic wave distortion in the turbid skull can be corrected by computational techniques [40, 41]. Main problems are described below:

- Cranial bone is a dispersive barrier for the acoustic waves, which alters both phase and amplitude. The magnitude of the acoustic waves is affected by the attenuation of an acoustic signal, which is a result of scattering in skull tissue. The phase of the acoustic wave is distorted because of the acoustic dispersion [42, 43].

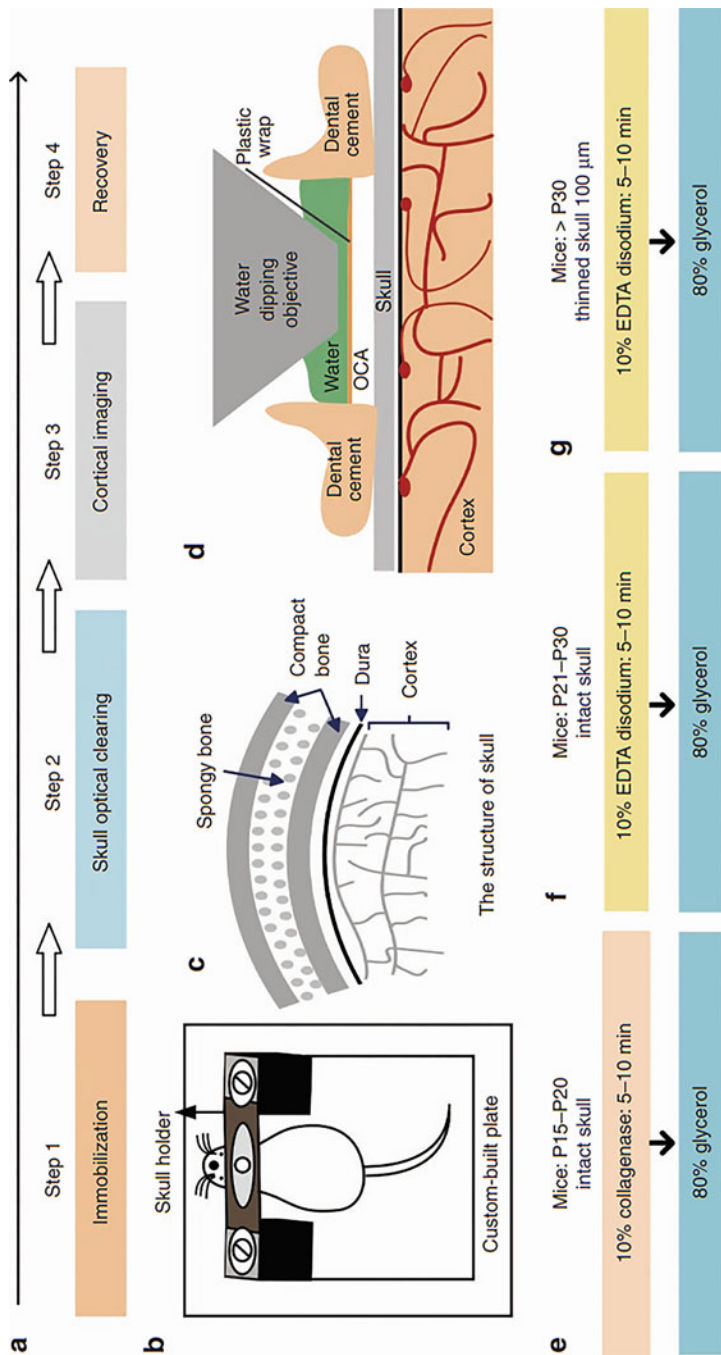


Fig. 7.4 Scheme of OCA application for cortical imaging. (a) Four-step procedure. (b) A head immobilization device. (c) The anatomical structure of mouse skull. (d) Schematic of the OCA application, including OCA administration protocols for mice of age: (e) - 15-20 days; (f) - 21-30 days; (g) older than 30 days

- The attenuation and dispersion depend on the density, porosity, and thickness of the skull [43, 44].
- The received acoustic signal is broadened because acoustic wave amplitude is reduced, and this process is frequency-dependent. Another broadening effect occurs due to almost twice difference in propagation speed in the brain and skull tissues [44, 45].
- Further, reverberations will be generated due to the reflection of acoustic waves from the cranial bone interface. The longitudinal wave can transform into a transverse one when it propagates from the brain to the cranial bone, not normal to the last [46].
- Longitudinal to shear wave mode translation occurs when materials with different acoustic impedances with an incident angle is produced as it gets encountered with the wave [46, 47].

Manwar et al. studied *ex vivo* distorting an acoustic signal generated by Nd:YAG tunable laser in the range 690–900 nm controlled by an internal OPO in the sheep skull with three thicknesses: 0.7, 1.0, and 1.3 mm [41]. Brain tissue was modeled by mimicking a phantom made from 8% gelatin water solution with 4% fiber in a transparent acrylic cube without an upper side. The maximum thickness of cranial bone was 0.7 mm to obtain feasible PAI visualization. Mohammadi et al. used a vector space similarity model and ray-tracing modeling to correct acoustic distortions in transcranial PA [47]. Other methods include ray- and wave-based simulations [48]. The great potential has modern deep learning methods, which can reconstruct images [49], but they are not applied to the cranial bone PA images yet. Current computational methods lack accuracy and need improvement to be suitable for *in vivo* imaging [47].

7.3 Photoacoustic Brain Disorders Imaging

PAI allows measuring deoxyhemoglobin (Hb), oxyhemoglobin (HbO₂), oxygen saturation (sO₂), melanin, fat, water, nucleic acids, controlling oxygen metabolism (MRO₂), and blood flow when laser is absorbed by an individual molecule [50–55]. These vital parameters determining tissue's physiological status are essential in neurodegenerative, tumor, and other brain disorders' diagnosis. For example, changes in Hb levels in an ischemic brain were established with PAI combined with electrocorticography [56, 57]. On reperfusion, arterial oxygen reached the baseline, whereas venous oxygen crossed the baseline.

7.3.1 Neurodegenerative Disease Studies

Neurodegenerative diseases are an emerging field for research. Alzheimer's disease (AD) being one of them is the most widely studied research topics. An accumulation of misfolded amyloid β protein, called as amyloid plaques, is used as an AD

biomarker. PAI showed that these plaques could be resolved by cranial opening, and it can be used for AD animal models' whole-brain studies [58]. Neuro-ferritin and neuro-melanin control by PAI can be helpful for neurodegenerative disease detection. Recognizing endogenous chromophores can be beneficial for neurodegenerative disease studies. Loss of neuro-melanin dopaminergic neurons in substantia nigra can be used as a key biomarker of Parkinson's disease (PD). Hence, these techniques can be utilized for deep structure imaging like midbrain, basal ganglia, and hindbrain nuclei which cannot be performed by other high-resolution optical neuroimaging techniques [59].

7.3.2 Ischemic Stroke Studies

Stroke is the second most common cause of death worldwide [60]. A stroke is a neurological dysfunction, which occurs when the blood flow in brain blood vessels is reduced or stopped, causing hypoxia and brain cell necrosis. Transient ischemic attack (TIA) produces stroke-like symptoms lasting for a few minutes up to 1 day. About 10–15% of TIA patients experience a stroke within 3 months. A photochemically initiated thrombosis was used to induce ischemia and study reperfusion (Fig. 7.5C) [61, 62]. The cerebral blood flow and somatosensory evoked potentials were studied by functional photoacoustic microscopy (fPAM) combined with micro-electrocorticography (μ ECoG) after a TIA during spontaneous reperfusion recovering accompanied by local cerebral blood volume and hemoglobin oxygen saturation [63, 64]. The μ ECoG-fPAM system was applied to analyze a neurovascular function in the right hemisphere of the forelimb region of the primary somatosensory cortex at pre- and post-ischemia. This fPAM system assesses the changes in blood flow at both deep and superficial layers. μ ECoG-fPAM techniques can be used for disease monitoring and neural activity recovery after the treatment with diagnostic compounds and other disorders like epilepsy, migraine, involving imbalance in neurovascular function.

In another case, recombinant tissue plasminogen activator (rtPA), the only drug for thrombolytic therapy approved by the US FDA, was studied [65]. It was helpful for acute ischemia in a narrow clinical therapeutic time window of 3–4.5 h. Conventional MRI, computed tomography, positron emission tomography techniques fail to monitor hemodynamic changes and cerebral blood flow in extreme depth whereas fPAM allowed analyzing cerebral blood volume and hemoglobin oxygen saturation in the ischemic region [66]. fPAM was combined with electrocorticography (ECoG) to monitor neurovascular function. A neurovascular function before, during, and after rtPA thrombolysis was assessed using the photothrombic ischemia (PTI) rat model. ECoG-fPAM was applied to study this function by measuring the hemodynamic responses in the bilateral primary somatosensory cortex. Major findings are: (1) partial recovery from PTI on early rtPA infusion, (2) improvement of neurovascular functions with rtPA treatment between 1 and 3 h after PTI, (3) delayed rtPa infusion worsens the state. ECoG-fPAM showed improved cerebral blood volume and brain symmetry index in the second findings. Improved physiological

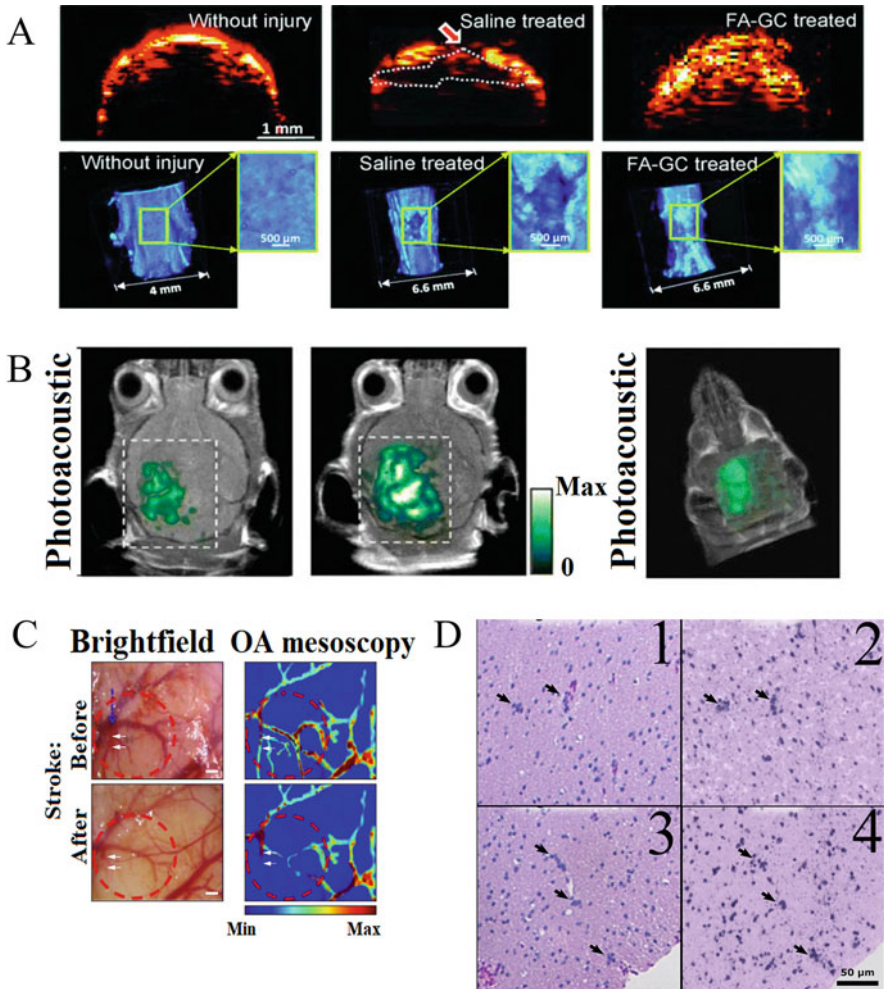


Fig. 7.5 (A) B-scan PA image of normal spinal cord tissue and injured tissue with or without treatment. 3D PA image showing the white matter loss in normal spinal cord and in injured spinal cord. Dashed lines signify white matter loss (The figure was adapted with permission from Ref. [69]). (B) Optoacoustic (OA) images of the brain of tumor-bearing mice before and after i.v. injection with multimodal probe. The post-injection images exhibited clear tumor visualization. The OA images were overlapped with the MR image, displaying good co-localization among the three modalities (The figure was adapted with permission from Ref. [78]). (C) Open-skull photograph of the cerebral cortical surface. The blue dashed arrow denotes the location for photothrombotic stroke; white double arrows indicate the ablated artery. In vivo optoacoustic C-scan image of the resultant cortical region with the blood vessels on the surface obtained at 570 nm (The figure was adapted with permission from Ref. [59]). (D) Comparison of brightfield histology with PARS H&E. (1, 3) White matter tissue including gliosis brightfield histology; perivascular oligodendrocytes are designated by the black arrows. (2, 4) PARS H&E images of nearby tissue sections showing perivascular oligodendrocytes, shown with black arrows (The figure was adapted with permission from Ref. [13])

brain functions in the second finding were also established, whereas the first finding showed a saturation point [67].

7.3.3 Spinal Cord Injury Studies

Spinal cord injury progression comprises two phases, first is a primary injury, a mechanical injury leading to loss or damage to the gray matter. In severe cases, the primary injury is followed by secondary injury caused by multiple causative events like oxidative stress, inflammation, explicitly leading to damage of white matter. PAI was applied to analyze the structure and spectral characteristics of the normal rat spinal cord. The rich white matter had two spectral peaks corresponding to CH_2 : the first overtone at 1730 nm and the second at 1200 nm. The 1730 nm spectral peak had a higher amplitude than the second [68]. The rat spinal cord was assessed with a C-scan PAI to estimate the difference between gray matter and white matter under 1730 nm illumination and found that the white matter comprised abundant CH_2 bonds in the myelinated axons (Fig. 7.5A).

Further, normal and injured spinal cord samples were used to assess the pathophysiology and recovery of the injury after treatment with ferulic-acid-conjugated glycol chitosan (FA-GC) by PA imaging. PA B-scan imaging of the spinal cords showed that the dorsal surface of the saline treated spinal cord exhibited twice the lower PA signal than that of the normal spinal cord due to a lower concentration of CH_2 molecules, implying a consecutive loss in WM myelination error in the injured spinal cord. In contrast, FA-GC treated spinal cord showed no unexpected PA signal on the dorsal plane, which led to the overall conclusion that FA-GC showed recovery of white matter leading to maintenance of CH_2 bonds [69]. On the whole, the spinal cord PA imaging was used to assess WM physiology in a label-free approach and using CH_2 as the signaling molecules.

7.3.4 Epilepsy Studies

Epilepsy is a brain disorder met in 1% of the worldwide population according to the World Health Organization (2009) [70]. Since the epileptic signal is concise, conventional imaging techniques, such as functional PET, MRI, and single-photon emission computed tomography have a low temporal resolution for fixation of paroxysmal epileptiform events [51, 71, 72]. An acute epilepsy rat model was studied using a real-time PAI system, having a spatial resolution of about 0.2 mm [73]. The area induced by bicuculline methiodide injection seizure was successfully identified using this system [74]. Hemodynamic changes are closely associated with seizures [51]. A link between de-oxygenation level measured by 755 nm PAI and an increasing the EEG spikes amplitude was established [75]. The vasodilation of small blood vessels caused by epileptic seizures was studied by PAI [76].

7.3.5 Brain Tumors Detection

The comprehensiveness of surgical resection is a crucial factor in brain tumors treatment. A multiwavelength PARS system was used for cellular and nuclear structure imaging in human tissue preparations without the stain [11, 77]. Formalin-fixed paraffin-embedded (FFPE) brain tissue samples were analyzed by this system [13]. Sample properties such as cellular composition, nuclear density, inter-nuclear distance, and cellular organization were observed, allowing differentiation of neoplastic or necrotic tissue from healthy tissue.

In the PARS images, the microvascular proliferation and tumor margins can be detected as in H&E staining images (Fig. 7.5D). Glioma comprises of three varied regions [79, 80]: the main glioma bulk, peritumoral zone including glioma cells and endothelial cell proliferated and hyper-vascularized, area of perifocal edema consisting of brain parenchyma, individual tumor cells, tumor-initiating cells and precursor cells. The latter region is crucial for treatment. An extensive network of blood vessels surrounds the glioma. It can be used to detect glioma margins during surgery. A multiwavelength LED-based PAI was used to discover small blood vessel structures [81]. The 1064 nm PAI channel provided visualization of deeper tumor margins, and the 532 nm PAI channel was suitable for tumor margins visualization closer to the surface. A combination of PAI and fluorescence molecular imaging (FMI) had been used to detect glioma on cell level [80]. An animal glioma model provoked by injection of human glioma cells, U87MG-Luc-mCherry was assessed by a multi-spectral photoacoustic tomography system for imaging. FMI images were collected *ex vivo* via frozen tissue sections and *in vivo* by a spectrum system. IRDye800-HFn nanoparticles were used for tumor area contrasting via the tail vein of tumor-bearing mouse. The authors stated that assessment of tumor morphology by MRI was observed to be unclear leading to the application of PAI for better morphology, depth, and spatial location of glioma (Fig. 7.5B). FMI was more accurate than histology analysis. Mesenchymal stem cells (MSCs) are proven to be useful against glioblastoma multiform identifying brain tumors [82]. A combination of MSCs from bone marrow and gold-coated superparamagnetic iron oxides (SPIO) can be used as distinguishable agents in photoacoustic and magnetic-resonance dual imaging [83]. The NIR region in SPIO nanoshells are the source of surface plasmon resonance and strong magnetic resonance signals were generated by SPIO nanocores penetrating the cranial bone. SPIO@Au-loaded MSCs injected into the carotid artery (4 $\mu\text{g}/\text{mL}$) were safe for the cells and can be visualized *in vivo* by this technique. In addition, gold nanoshells are used in photothermal ablation therapy for cancer cell destruction.

7.4 Conclusion

PAI elucidates contrasting results between a healthy and unhealthy brain and provides information on brain disorders, trauma effects, ischemic attacks, and other neurodegenerative disease states. In this chapter, we touched on several

brain disorders using photoacoustic techniques to assess different neurological diseases. PAI measures and quantifies vital physiological parameters like deoxyhemoglobin (HbR), oxyhemoglobin (HbO₂), and oxygen saturation (sO₂) which determine the tissue's physiological status as well as a precise diagnosis for various neuro-disorders and tumors. Also, PAI is a label-free detection method that provides image contrast due to the specific absorption by the targeted molecules. Furthermore, integration of PAI with other techniques can also improve the future of further studies.

Acknowledgments NM thanks the Global Innovation and Technology Alliance (GITA), Department of Science and Technology (DST) [Project Number-GITA/DST/TWN/P-95/2021], Government of India, India, for financial support. YVK thanks Decree of the Government of the Russian Federation No. 220 of 9 April 2010 (Agreement No. 075-15-2021-615 of 4 June 2021) for support. YVK thanks the Government of the Russian Federation for financial support (Agreement No. 075-15-2021-615 of 4 June 2021).

References

1. Yao J, Wang LV (2013) Photoacoustic microscopy. *Laser Photonics Rev* 7(5):758–778. <https://doi.org/10.1002/lpor.201200060>
2. Bodea SV, Westmeyer GG (2021) Photoacoustic neuroimaging—perspectives on a maturing imaging technique and its applications in neuroscience. *Front Neurosci* 15. <https://doi.org/10.3389/fnins.2021.655247>
3. Kruger RA, Liu P, Fang YR, Appledorn CR (1995) Photoacoustic ultrasound (PAUS)—reconstruction tomography. *Med Phys* 22(10):1605–1609. <https://doi.org/10.1118/1.597429>
4. Buehler A, Herzog E, Razansky D, Ntziachristos V (2010) Video rate optoacoustic tomography of mouse kidney perfusion. *Opt Lett* 35(14):2475–2477. <https://doi.org/10.1364/OL.35.002475>
5. Wang LV, Yao J (2016) A practical guide to photoacoustic tomography in the life sciences. *Nat Methods* 13(8):627–638. <https://doi.org/10.1038/nmeth.3925>
6. Liu W, Yao J (2018) Photoacoustic microscopy: principles and biomedical applications. *Biomed Eng Lett* 8(2):203–213. <https://doi.org/10.1007/s13534-018-0067-2>
7. Bigio IJ, Mourant JR (2003) Optical biops. *Encycl Opt Eng* 1577:1593. <https://doi.org/10.1081/E-EOE120009717>
8. Park S, Lee C, Kim J, Kim C (2014) Acoustic resolution photoacoustic microscopy. *Biomed Eng Lett* 4(3):213–222. <https://doi.org/10.1007/s13534-014-0153-z>
9. Omar M, Soliman D, Gateau J, Ntziachristos V (2014) Ultrawideband reflection-mode optoacoustic mesoscopy. *Opt Lett* 39(13):3911–3914. <https://doi.org/10.1364/OL.39.003911>
10. Bell KL, Hajireza P, Shi W, Zemp RJ (2017) Temporal evolution of low-coherence reflectrometry signals in photoacoustic remote sensing microscopy. *Appl Opt* 56(18):5172–5181. <https://doi.org/10.1364/AO.56.005172>
11. Hajireza P, Shi W, Bell K, Paproski RJ, Zemp RJ (2017) Non-interferometric photoacoustic remote sensing microscopy. *Light Sci Appl* 6(6):–e16278. <https://doi.org/10.1038/lsa.2016.278>
12. Abbasi S, Le M, Sonier B, Dinakaran D, Bigras G, Bell K, Mackey JR, Reza PH (2019) All-optical reflection-mode microscopic histology of unstained human tissues. *Sci Rep* 9(1): 1–11. <https://doi.org/10.1038/s41598-019-49849-9>
13. Ecclestone BR, Bell K, Abbasi S, Dinakaran D, van Landeghem FK, Mackey JR, Fieguth P, Reza PH (2020) Improving maximal safe brain tumor resection with photoacoustic remote sensing microscopy. *Sci Rep* 10(1):1–7. <https://doi.org/10.1038/s41598-020-74160-3>

14. Deán-Ben XL, Ford SJ, Razansky D (2015) High-frame rate four dimensional optoacoustic tomography enables visualization of cardiovascular dynamics and mouse heart perfusion. *Sci Rep* 5(1):1–9. <https://doi.org/10.1038/srep13240>
15. Deán-Ben XL, Razansky D (2013) Portable spherical array probe for volumetric real-time optoacoustic imaging at centimeter-scale depths. *Opt Express* 21(23):28062–28071. <https://doi.org/10.1364/OE.21.028062>
16. Du J, Yang S, Qiao Y, Lu H, Dong H (2021) Recent progress in near-infrared photoacoustic imaging. *Biosens Bioelectron* 191:113478. <https://doi.org/10.1016/j.bios.2021.113478>
17. Wang Y, Chu TS, Lin YR, Tsao CH, Tsai CH, Ger TR, Chen LT, Chang WSW, Liao LD (2021) Assessment of brain functional activity using a miniaturized head-mounted scanning photoacoustic imaging system in awake and freely moving rats. *Biosensors* 11(11):429. <https://doi.org/10.3390/bios11110429>
18. Heo C, Park H, Kim YT, Baeg E, Kim YH, Kim SG, Suh M (2016) A soft, transparent, freely accessible cranial window for chronic imaging and electrophysiology. *Sci Rep* 6(1):1–11. <https://doi.org/10.1038/srep27818>
19. Roome CJ, Kuhn B (2014) Chronic cranial window with access port for repeated cellular manipulations, drug application, and electrophysiology. *Front Cell Neurosci* 8:379. <https://doi.org/10.3389/fncel.2014.00379>
20. Shih AY, Driscoll JD, Drew PJ, Nishimura N, Schaffer CB, Kleinfeld D (2012) Two-photon microscopy as a tool to study blood flow and neurovascular coupling in the rodent brain. *J Cereb Blood Flow Metab* 32(7):1277–1309. <https://doi.org/10.1038/jcbfm.2011.196>
21. Li M, Liu F, Jiang H, Lee TS, Tang S (2017) Long-term two-photon imaging in awake macaque monkey. *Neuron* 93(5):1049–1057. <https://doi.org/10.1016/j.neuron.2017.01.027>
22. Koletar MM, Dorr A, Brown ME, McLaurin J, Stefanovic B (2019) Refinement of a chronic cranial window implant in the rat for longitudinal in vivo two-photon fluorescence microscopy of neurovascular function. *Sci Rep* 9(1):1–12. <https://doi.org/10.1038/s41598-019-41966-9>
23. Hong G, Diao S, Chang J, Antaris AL, Chen C, Zhang B, Zhao S, Atochin DN, Huang PL, Andreasson KI, Kuo CJ (2014) Through-skull fluorescence imaging of the brain in a new near-infrared window. *Nat Photonics* 8(9):723–730. <https://doi.org/10.1038/nphoton.2014.166>
24. Holtmaat A, Bonhoeffer T, Chow DK, Chuckowree J, De Paola V, Hofer SB, Hübener M, Keck T, Knott G, Lee WCA, Mostany R (2009) Long-term, high-resolution imaging in the mouse neocortex through a chronic cranial window. *Nat Protoc* 4(8):1128–1144. <https://doi.org/10.1038/nprot.2009.89>
25. Park H, You N, Lee J, Suh M (2019) Longitudinal study of hemodynamics and dendritic membrane potential changes in the mouse cortex following a soft cranial window installation. *Neurophotonics* 6(1):015006. <https://doi.org/10.1117/1.NPh.6.1.015006>
26. Wang Y, Liang G, Liu F, Chen Q, Xi L (2020) A long-term cranial window for high-resolution photoacoustic imaging. *IEEE Trans Biomed Eng* 68(2):706–711. <https://doi.org/10.1109/TBME.2020.3012663>
27. Osmani B, Schiff H, Vogelsang K, Guzman R, Kristiansen PM, Crockett R, Chacko A, Bucher S, Töpfer T, Müller B (2020) Hierarchically structured polydimethylsiloxane films for ultra-soft neural interfaces. *Micro Nano Eng* 7:100051. <https://doi.org/10.1016/j.mne.2020.100051>
28. Kılıç K, Desjardins M, Tang J, Thunemann M, Sunil S, Erdener ŞE, Postnov DD, Boas DA, Devor A (2021) Chronic cranial windows for long term multimodal neurovascular imaging in mice. *Front Physiol* 1813. <https://doi.org/10.3389/fphys.2020.612678>
29. Li H, Dong B, Zhang Z, Zhang HF, Sun C (2014) A transparent broadband ultrasonic detector based on an optical micro-ring resonator for photoacoustic microscopy. *Sci Rep* 4(1):1–8. <https://doi.org/10.1038/srep04496>
30. Wang Y, Xi L (2021) Chronic cranial window for photoacoustic imaging: a mini review. *Vis Comput Ind Biomed Art* 4(1):1–9. <https://doi.org/10.1186/s42492-021-00081-1>

31. Zhang C, Chen SL, Ling T, Guo LJ (2015) Imprinted polymer microrings as high-performance ultrasound detectors in photoacoustic imaging. *J Lightwave Technol* 33(20):4318–4328. <https://doi.org/10.1109/JLT.2015.2466661>
32. Wang X, Luo Y, Chen Y, Chen C, Yin L, Yu T, He W, Ma C (2021) A skull-removed chronic cranial window for ultrasound and photoacoustic imaging of the rodent brain. *Front Neurosci* 15:642. <https://doi.org/10.3389/fnins.2021.673740>
33. Drew PJ, Shih AY, Driscoll JD, Knutsen PM, Blinder P, Davalos D, Akassoglou K, Tsai PS, Kleinfeld D (2010) Chronic optical access through a polished and reinforced thinned skull. *Nat Methods* 7(12):981–984. <https://doi.org/10.1038/nmeth.1530>
34. Zhao YJ, Yu TT, Zhang C, Li Z, Luo QM, Xu TH, Zhu D (2018) Skull optical clearing window for in vivo imaging of the mouse cortex at synaptic resolution. *Light Sci Appl* 7(2): 17153–17153. <https://doi.org/10.1038/lsa.2017.153>
35. Genina EA, Bashkatov AN, Tuchin VV (2008) Optical clearing of cranial bone. *Adv Opt Technol* 2008. <https://doi.org/10.1155/2008/267867>
36. Wang J, Zhang Y, Xu TH, Luo QM, Zhu D (2012) An innovative transparent cranial window based on skull optical clearing. *Laser Phys Lett* 9(6):469. <https://doi.org/10.7452/lapl.201210017>
37. Zhou Y, Yao J, Wang LV (2013) Optical clearing-aided photoacoustic microscopy with enhanced resolution and imaging depth. *Opt Lett* 38(14):2592–2595. <https://doi.org/10.1364/OL.38.002592>
38. Zharov VP, Galanzha EI, Shashkov EV, Khlebtsov NG, Tuchin VV (2006) In vivo photoacoustic flow cytometry for monitoring of circulating single cancer cells and contrast agents. *Opt Lett* 31(24):3623–3625. <https://doi.org/10.1364/OL.31.003623>
39. Yang X, Zhang Y, Zhao K, Zhao Y, Liu Y, Gong H, Luo Q, Zhu D (2016) Skull optical clearing solution for enhancing ultrasonic and photoacoustic imaging. *IEEE Trans Med Imaging* 35(8): 1903–1906. <https://doi.org/10.1109/tmi.2016.2528284>
40. Odabae M, Odabae M, Pelekanos M, Leinenga G, Götz J (2018) Modeling ultrasound propagation through material of increasing geometrical complexity. *Ultrasonics* 90:52–62. <https://doi.org/10.1016/j.ultras.2018.05.014>
41. Manwar R, Kratkiewicz K, Avanaki K (2020) Investigation of the effect of the skull in transcranial photoacoustic imaging: a preliminary ex vivo study. *Sensors* 20(15):4189. <https://doi.org/10.3390/s20154189>
42. Fry FJ, Barger JE (1978) Acoustical properties of the human skull. *J Acoust Soc Am* 63(5): 1576–1590. <https://doi.org/10.1121/1.381852>
43. Mohammadi L, Behnam H, Tavakkoli J, Avanaki M (2019) Skull's photoacoustic attenuation and dispersion modeling with deterministic ray-tracing: towards real-time aberration correction. *Sensors* 19(2):345. <https://doi.org/10.3390/s19020345>
44. Treeby BE (2013) Acoustic attenuation compensation in photoacoustic tomography using time-variant filtering. *J Biomed Opt* 18(3):036008. <https://doi.org/10.1117/1.JBO.18.3.036008>
45. Deán-Ben XL, Razansky D, Ntziachristos V (2011) The effects of acoustic attenuation in photoacoustic signals. *Phys Med Biol* 56(18):6129. <https://doi.org/10.1088/0031-9155/56/18/021>
46. Estrada H, Huang X, Rebling J, Zwack M, Gottschalk S, Razansky D (2018) Virtual craniotomy for high-resolution photoacoustic brain microscopy. *Sci Rep* 8(1):1–9. <https://doi.org/10.1038/s41598-017-18857-y>
47. Mohammadi L, Behnam H, Tavakkoli J, Avanaki K (2020) Skull acoustic aberration correction in photoacoustic microscopy using a vector space similarity model: a proof-of-concept simulation study. *Biomed Opt Express* 11(10):5542–5556. <https://doi.org/10.1364/BOE.402027>
48. Yoon K, Lee W, Croce P, Cammalleri A, Yoo SS (2018) Multi-resolution simulation of focused ultrasound propagation through ovine skull from a single-element transducer. *Phys Med Biol* 63(10):105001. <https://doi.org/10.1088/1361-6560/aabe37>

49. Antholzer S, Haltmeier M, Nuster R, Schwab J (2018) Photoacoustic image reconstruction via deep learning. In: Photons plus ultrasound: imaging and sensing. International Society for Optics and Photonics, Washington
50. Yao L, Xi L, Jiang H (2014) Photoacoustic computed microscopy. *Sci Rep* 4(1):1–8. <https://doi.org/10.1038/srep04960>
51. Qiu T, Lan Y, Gao W, Zhou M, Liu S, Huang W, Zeng S, Pathak JL, Yang B, Zhang J (2021) Photoacoustic imaging as a highly efficient and precise imaging strategy for the evaluation of brain diseases. *Quant Imaging Med Surg* 11(5):2169. <https://doi.org/10.21037/qims-20-845>
52. Strohm EM, Berndt ES, Kolios MC (2013) High frequency label-free photoacoustic microscopy of single cells. *Photoacoustics* 1(3–4):49–53. <https://doi.org/10.1016/j.pacs.2013.08.003>
53. Guggenheim JA, Allen TJ, Plumb A, Zhang EZ, Rodriguez-Justo M, Punwani S, Beard PC (2015) Photoacoustic imaging of human lymph nodes with endogenous lipid and hemoglobin contrast. *J Biomed Opt* 20(5):050504. <https://doi.org/10.1117/1.jbo.20.5.050504>
54. Xu Z, Li C, Wang LV (2010) Photoacoustic tomography of water in phantoms and tissue. *J Biomed Opt* 15(3):036019. <https://doi.org/10.1117/1.3443793>
55. Cao R, Kilroy JP, Ning B, Wang T, Hossack JA, Hu S (2015) Multispectral photoacoustic microscopy based on an optical–acoustic objective. *Photoacoustics* 3(2):55–59. <https://doi.org/10.1016/j.pacs.2014.12.004>
56. Burton NC, Patel M, Morscher S, Driessen WH, Claussen J, Beziere N, Jetzfellner T, Taruttis A, Razansky D, Bednar B, Ntziachristos V (2013) Multispectral opto-acoustic tomography (MSOT) of the brain and glioblastoma characterization. *NeuroImage* 65:522–528. <https://doi.org/10.1016/j.neuroimage.2012.09.053>
57. Kneipp M, Turner J, Hambauer S, Krieg SM, Lehmborg J, Lindauer U, Razansky D (2014) Functional real-time optoacoustic imaging of middle cerebral artery occlusion in mice. *PLoS One* 9(4):e96118. <https://doi.org/10.1371/journal.pone.0096118>
58. Hu S, Yan P, Maslov K, Lee JM, Wang LV (2009) Intravital imaging of amyloid plaques in a transgenic mouse model using optical-resolution photoacoustic microscopy. *Opt Lett* 34(24):3899–3901. <https://doi.org/10.1364/OL.34.003899>
59. Ovsepian SV, Olefir I, Westmeyer G, Razansky D, Ntziachristos V (2017) Pushing the boundaries of neuroimaging with optoacoustics. *Neuron* 96(5):966–988. <https://doi.org/10.1016/j.neuron.2017.10.022>
60. Donnan GA, Fisher M, Macleod M (2008) Stroke. *Lancet* 371(9624):1612–1623. [https://doi.org/10.1016/s0140-6736\(08\)60694-7](https://doi.org/10.1016/s0140-6736(08)60694-7)
61. Watson BD, Dietrich WD, Busto R, Wachtel MS, Ginsberg MD (1985) Induction of reproducible brain infarction by photochemically initiated thrombosis. *Ann Neurol* 17(5):497–504. <https://doi.org/10.1002/ana.410170513>
62. Liao LD, Bandla A, Ling JM, Liu YH, Kuo LW, Chen YY, King NK, Lai HY, Lin YR, Thakor NV (2014) Improving neurovascular outcomes with bilateral forepaw stimulation in a rat photothrombotic ischemic stroke model. *NeuroPhotonics* 1(1):011007. <https://doi.org/10.1117/1.NPh.1.1.011007>
63. Jasanoff A (2007) MRI contrast agents for functional molecular imaging of brain activity. *Curr Opin Neurobiol* 17(5):593–600. <https://doi.org/10.1016/j.conb.2007.11.002>
64. Lin CY, Lin MH, Cheung WM, Lin TN, Chen JH, Chang C (2009) In vivo cerebromicrovasculature visualization using 3D ΔR_2 -based microscopy of magnetic resonance angiography (3D ΔR_2 -mMRA). *NeuroImage* 45(3):824–831. <https://doi.org/10.1016/j.neuroimage.2008.12.030>
65. Del Zoppo GJ, Saver JL, Jauch EC, Adams HP Jr (2009) Expansion of the time window for treatment of acute ischemic stroke with intravenous tissue plasminogen activator: a science advisory from the American Heart Association/American Stroke Association. *Stroke* 40(8):2945–2948. <https://doi.org/10.1161/STROKEAHA.109.192535>
66. Burrows FE, Bray N, Denes A, Allan SM, Schiessl I (2015) Delayed reperfusion deficits after experimental stroke account for increased pathophysiology. *J Cereb Blood Flow Metab* 35(2):277–284. <https://doi.org/10.1038/jcbfm.2014.197>

67. Bandla A, Liao LD, Chan SJ, Ling JM, Liu YH, Shih YYI, Pan HC, Wong PTH, Lai HY, King NKK, Chen YY (2018) Simultaneous functional photoacoustic microscopy and electrocorticography reveal the impact of rtPA on dynamic neurovascular functions after cerebral ischemia. *J Cereb Blood Flow Metab* 38(6):980–995. <https://doi.org/10.1177/0271678X17712399>
68. Wang P, Wang HW, Sturek M, Cheng JX (2012) Bond-selective imaging of deep tissue through the optical window between 1600 and 1850 nm. *J Biophotonics* 5(1):25–32. <https://doi.org/10.1002/jbio.201100102>
69. Wu W, Wang P, Cheng JX, Xu XM (2014) Assessment of white matter loss using bond-selective photoacoustic imaging in a rat model of contusive spinal cord injury. *J Neurotrauma* 31(24):1998–2002. <https://doi.org/10.1089/neu.2014.3349>
70. Lozano AM, Hallett M (2013) Brain stimulation. In: *Handbook of clinical neurology*. Elsevier, Amsterdam
71. Devous MD, Thisted RA, Morgan GF, Leroy RF, Rowe CC (1998) SPECT brain imaging in epilepsy: a meta-analysis. In: *Database of abstracts of reviews of effects (DARE): quality-assessed reviews* [internet]. Centre for Reviews and Dissemination, York
72. Jackson GD, Connelly A, Cross JH, Gordon I, Gadian DG (1994) Functional magnetic resonance imaging of focal seizures. *Neurology* 44(5):850–850. <https://doi.org/10.1212/WNL.44.5.850>
73. Wang B, Xiang L, Jiang MS, Yang J, Zhang Q, Carney PR, Jiang H (2012) Photoacoustic tomography system for noninvasive real-time three-dimensional imaging of epilepsy. *Biomed Opt Express* 3(6):1427–1432. <https://doi.org/10.1364/BOE.3.001427>
74. Zhang Q, Liu Z, Carney PR, Yuan Z, Chen H, Roper SN, Jiang H (2008) Non-invasive imaging of epileptic seizures in vivo using photoacoustic tomography. *Phys Med Biol* 53(7):1921. <https://doi.org/10.1088/0031-9155/53/7/008>
75. Xiang L, Ji L, Zhang T, Wang B, Yang J, Zhang Q, Jiang MS, Zhou J, Carney PR, Jiang H (2013) Noninvasive real time tomographic imaging of epileptic foci and networks. *NeuroImage* 66:240–248. <https://doi.org/10.1016/j.neuroimage.2012.10.077>
76. Tsytsarev V, Rao B, Maslov KI, Li L, Wang LV (2013) Photoacoustic and optical coherence tomography of epilepsy with high temporal and spatial resolution and dual optical contrasts. *J Neurosci Methods* 216(2):142–145. <https://doi.org/10.1016/j.jneumeth.2013.04.001>
77. Reza PH, Bell K, Shi W, Shapiro J, Zemp RJ (2018) Deep non-contact photoacoustic initial pressure imaging. *Optica* 5(7):814–820. <https://doi.org/10.1364/OPTICA.5.000814>
78. Razansky D, Klohs J, Ni R (2021) Multi-scale optoacoustic molecular imaging of brain diseases. *Eur J Nucl Med Mol Imaging*:1–19. <https://doi.org/10.1007/s00259-021-05207-4>
79. Eyüpoglu IY, Buchfelder M, Savaskan NE (2013) Surgical resection of malignant gliomas—role in optimizing patient outcome. *Nat Rev Neurol* 9(3):141–151. <https://doi.org/10.1038/nrneurol.2012.279>
80. Jia X, Fan K, Zhang R, Zhang D, Zhang J, Gao Y, Zhang T, Li W, Li J, Yan X, Tian J (2020) Precise visual distinction of brain glioma from normal tissues via targeted photoacoustic and fluorescence navigation. *Nanomed Nanotechnol Biol Med* 27:102204. <https://doi.org/10.1016/j.nano.2020.102204>
81. Najafzadeh E, Ghadiri H, Alimohamadi M, Farnia P, Mehrmohammadi M, Ahmadian A (2020) Evaluation of multi-wavelengths LED-based photoacoustic imaging for maximum safe resection of glioma: a proof of concept study. *Int J Comput Assist Radiol Surg* 15:1053–1062. <https://doi.org/10.1007/s11548-020-02191-2>
82. Zhao Z, Myllylä T (2021) Recent technical progression in photoacoustic imaging—towards using contrast agents and multimodal techniques. *Appl Sci* 11(21):9804. <https://doi.org/10.3390/app11219804>
83. Duan Y, Hu D, Guo B, Shi Q, Wu M, Xu S, Liu X, Jiang J, Sheng Z, Zheng H, Liu B (2020) Nanostructural control enables optimized photoacoustic–fluorescence–magnetic resonance multimodal imaging and photothermal therapy of brain tumor. *Adv Funct Mater* 30(1):1907077. <https://doi.org/10.1002/adfm.201907077>



Photodynamic Therapy of Brain Diseases

8

Valeria V. Telnova, Alexander I. Dubrovsky, Andrey V. Terskov,
Anna S. Tsven, Oxana V. Semyachkina-Glushkovskaya,
and Valery V. Tuchin

Abstract

Photodynamic therapy is a highly perspective tool for cancer treatment. The PDT method has been used for more than 30 years to treat patients with brain cancer. In recent years, the active study of reactive oxygen species and, in particular, the properties of singlet oxygen have opened up new prospects for the use of PDT, and also opened the veil of mystery of the mechanisms behind the action of this method. In addition, the recent discovery of meningeal lymphatic vessels, the properties of PDT to violate the integrity of the blood–brain barrier, and the incompatibility of this with the purification of brain tissue, turned PDT into a method of fighting not only cancer but also other neurodegenerative diseases.

Keywords

Photodynamic therapy · Singlet oxygen · Brain cancer · Meningeal lymphatic · Stroke

V. V. Telnova (✉) · A. I. Dubrovsky · A. V. Terskov · A. S. Tsven ·
O. V. Semyachkina-Glushkovskaya
Science Medical Center, Saratov State University, Saratov, Russia

V. V. Tuchin
Science Medical Center, Saratov State University, Saratov, Russia

Laboratory of Laser Diagnostics of Technical and Living Systems, Institute of Precision Mechanics and Control of the FRS “Saratov Scientific Center” of the Russian Academy of Sciences, Saratov, Russia

Laboratory of Laser Molecular Imaging and Machine Learning, National Research Tomsk State University, Tomsk, Russia

A.N. Bach Institute of Biochemistry, Research Center of Biotechnology of the Russian Academy of Sciences, Moscow, Russia

8.1 Introduction

Photodynamic therapy (PDT) is a minimally invasive therapeutic tool that combines light irradiation and photosensitizer agents (porphyrins, chlorins, and many other photodynamic dyes). The PDT is a technique developed to treat the ever-increasing global incidence of cancer [1–4].

The PDT theory was created by Niels Finsen, winner of the 1903 Nobel Prize for his discoveries in the treatment of cutaneous tuberculosis with light. Oscar Raab was the first to use PDT, in 1898, by combining a light source with acridine dyes, which caused a toxic reaction in the unicellular microorganism paramecium. Oscar Raab then worked in the laboratory of Hermann von Tappeiner in Munich, who in 1904 discovered that the process depends on oxygen. Von Tappeiner was the first to describe the phenomenon of oxygen-dependent photosensitization with the term “photodynamic therapy.” He was also the first to apply PDT on people with skin cancer using eosin as a photosensitizing agent. The physical properties of hematoporphyrin as a photosensitizer were first described in 1908. The biological activity of hematoporphyrin was demonstrated several years later, in 1913, by the German physician Meyer-Betz, who injected himself with 200 mg of hematoporphyrin and remained sensitive to light for 2 months [5].

Until the 1960s of the last century, the primary mechanisms of photodynamic reactions were the subject of heated discussions. Currently, we know that in the vast majority of cases of PDT use, it is necessary to have a photosensitizer (PS). Photosensitizers are agents capable of absorbing light of a specific wavelength and converting it [6] and transferring it as useful energy to an oxygen molecule with the formation of reactive oxygen species (ROS) include oxygen-based free radicals and non-radical forms and electronically excited singlet oxygen [7] in target tissues (tumors). The excitation of PS by light leads its electron to transition to the first excited singlet state. The next intersystem intersection leads to a triplet state. PS in the triplet state transfers energy to the triplet oxygen, which leads to the formation of reactive singlet oxygen ($^1\text{O}_2$) [8].

There are two mechanisms of oxidation of biomolecules using photosensitizers. Type I is a radical mechanism in which a photosensitizer transfers light energy directly to biomolecules through electron/hydrogen transfer in direct contact reactions, which leads to specific damage to biomolecules by initiating radical chain reactions. In the type II mechanism, energy is transferred to molecular triplet oxygen ($^3\text{O}_2$), which leads to the formation of excited singlet oxygen ($^1\text{O}_2$), which can cause damage to membranes, proteins, and DNA [9].

Such parameters as the type and dose of photosensitizer, intensity of light used, route of administration, type of tumor, and concentration of cytoplasmic oxygen affect the effectiveness of PDT. The ideal photosensitizers should have an absorption spectrum in the 650–800 nm range, rapid elimination rates. It also should be pharmacologically inactive without light irradiation, selectively present in tumor cells, and water soluble [10].

Photosensitizers can be divided into porphyrin photosensitizers and non-porphyrin photosensitizers. First-generation PSs (such as hematoporphyrin)

have been introduced for more than 40 years even though they have some disadvantages, such as poor penetration into cancer cells, low elimination rates, low chemical stability, causing skin hypersensitivity reactions, and a long half-life [10].

To overcome most of these disadvantages, porphyrin-like photosensitizers of the second generation (chlorin, bacteriochlorin, tetraazaporphyrin, tetrabenzoporphyrin, phthalocyanine, and naphthalocyanine) have been developed. 5-Aminolevulinic acid (ALPHA), methyl aminolevulinic acid (MAIL; Matrix), and Hexvix/Cysview are precursors of protoporphyrin IX, which absorb light at 630 nm [10].

The newly developed third-generation photosensitizers are conjugates of second-generation photosensitizers and biological target groups such as carbohydrates, peptides, or antibodies. Such changes led to an increase in the selectivity of photosensitizers and the minimization of undesirable effects [10].

Non-porphyrin photosensitizers include cyanines, chalcogenopyrylium dyes, and phenothiazinium dyes.

The PDT method has been studied as an auxiliary for the treatment of cancer and glioblastoma, in particular, for about 35 years, so it has the widest application in this area. But currently, PDT has a much wider application. There are many vascular effects of PDT to induce a thrombotic stroke model to study the neuroprotective effects of pharmacological agents against stroke, many intriguing cerebrovascular effects of $^1\text{O}_2$, exciting results on the discovery of the blood-brain barrier caused by PDT, and the effect of PDT on newly discovered meningeal lymphatic vessels.

Currently, PDT cancer treatment is based on the photodynamic effect (PDE), which involves damage to photosensitized cells (by the mechanism of apoptosis and damage to the endothelium of cancer cells) in the presence of light and oxygen. To date, it is believed that singlet oxygen becomes a key agent for PDE [11] (Fig. 8.1).

However, PS the majority of times is a necessary element of PDT, absorbed by both healthy and tumor tissues. One of the most important and complicated issues in modern PDT is the prevention of PS accumulation in healthy tissues and the prevention of corresponding undesirable effects. This problem can be solved by encapsulating PS in polymer nanoparticles, in which the substance will be protected from degradation by the physiological environment [12].

However, despite the already long history of PDT, there is a need for further improvement of the PDT method due to existing limitations such as high internal toxicity, prolonged hypersensitivity to intense light, low penetration of activating light into tissues (630 nm), the low specificity of the photosensitizer to cancer cells, and high cost of PSs administration [10].

But new opportunities in photodynamic cancer therapy have opened up with the development of laser diodes with quantum dots (QD) (LDS) emitting with a center of about 1268 nm, which coincides with the absorption band of NIR [2, 3] oxygen molecules. One of the new directions is the activation of cell apoptosis by direct photo-excitation with molecular oxygen.

To date, the idea of direct $^1\text{O}_2$ activation has not been developed because direct $^3\text{O}_2 \rightarrow ^1\text{O}_2$ transition in molecular form of oxygen is forbidden due to spin-orbital selection rules. However, the selection rules governing intermolecular amplification

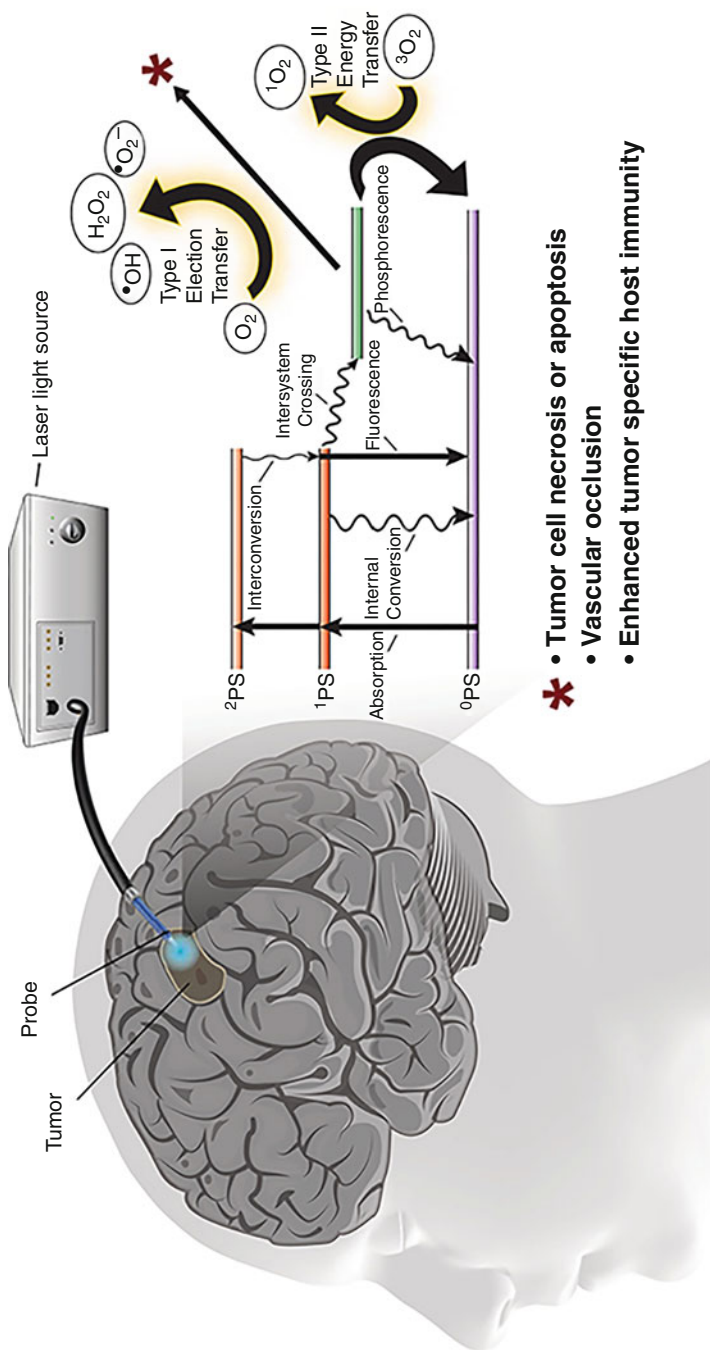


Fig. 8.1 Scheme of PDT of glioblastoma and simplified energy diagram of the oxygen-dependent photodynamic response. (The figure is reproduced with permission from [11])

changed after experimental studies of the solvent effect [3, 4]. The main contribution to the intensity comes from two-molecular collisions of O_2-O_2 , which mix states through intermolecular exchange interaction, introducing allowed states into previously forbidden transitions, which enhances the transition $^3O_2 \rightarrow ^1O_2$. In addition, the action spectra of some cell cultures recorded in the spectral range from 310 to 860 nm and the results demonstrated for low-intensity laser therapy [13, 14] suggest the transformation of cellular metabolism in response to low-power laser excitation in spectral intervals corresponding to the absorption bands of molecular oxygen. Formation of 1O_2 was also demonstrated by direct photo-excitation at 1265 nm in aerobic systems containing no pigments and in the condensed phase at 77 K at 1064 nm [15, 16]. It has recently been demonstrated that a laser with a wavelength of 1268 nm can provoke the death of cancer cells in an environment free of PSs [17, 18]. However, it is still unclear whether oxygen activation is direct from the laser or whether it is a more complex process in biosystems [13, 14].

This chapter is devoted to the study of PDT therapy for brain cancer, the mechanisms underlying the method, as well as recent discoveries in the field of PDT, which open up new possibilities for using the method both in preclinical studies and in clinical practice.

8.2 Singlet Oxygen Generation in Living Cells

Even though the process of photoactivation of oxygen in the PS-free medium in living cells remains extremely uncertain, the results of low-intensity laser therapy [19, 20], modification of erythrocyte membrane proteins [21], and suppression of cancer cell growth by photo-excitation in the NIR spectral range under PS-free conditions [22] refer to a more likely direct photo-oxidation in media containing molecular oxygen.

So, laser-induced 1O_2 production in living cells in PS-free conditions was shown on HaCaT and HeLa cell lines. 1O_2 production was monitored with dihydroethidium (DHE) which is specifically oxidized to dihydroxyethidium (DHOE) fluorescing at 585 nm by the superoxide anion [23].

Experiments conducted with HaCaT cells showed a substantial difference between non-irradiated and irradiated by a 1268 nm laser pulse of 47.7 J/cm² cells causing an increase in dihydroxyethidium (DHOE, oxidized DHE) fluorescence reaching a steady-state level after 8 min and continued post-termination of the laser pulse. Also, a strong donor of O_2 -NaOCl (100 μ M) induced a dramatic increase in DHOE fluorescence. The pre-incubation of HaCaT cells for 10 min with α -tocopherol (nonspecific ROS scavenger [24, 25]) diminished the laser-induced fluorescence to near background levels. This suggests that the 1268 nm laser irradiation photo-oxidizes triplet molecular oxygen inside the cell.

Furthermore, a laser pulse with a wavelength of 1268 nm caused O_2 -dependent fluorescence in all taken cell lines with the most impressive effect observed in HeLa cells, and no difference between HaCaT and PK. The fluorescence induced by the

NIR laser demonstrated a strong dose dependence, not reaching saturation over time, especially in HeLa cells [26].

In addition, PDT promotes the initiation of autophagy (or macroautophagy) in tumor cells. This occurs due to the suppression of AKT-mTOR signaling and increased regulation of the AMPK pathway [27]. PDT of early response genes by hyperactivation of the survival pathway, leading to overexpression of anti-apoptotic (BCL-2, survivin, BCL-XL) or autophagy-related proteins that cause resistance to PDT. It has recently been found that tumor resistance to certain antitumor drugs, such as cisplatin, oxaliplatin, carboplatin, doxorubicin, etoposide, rapamycin, everolimus, alpelisib, pictilisib, and AZD8055, is associated with increased and sustained activation of PI3K/mTOR signaling.

The International Committee on Cell Death postulates that the transformation of the initial protective mechanism of autophagy into a lethal one is autophagy-dependent cell death (ADCD). Using the term ADCD, it could be assumed that photo-induced cell death is carried out through autophagy and its mechanisms, whereas its pharmacological or genetic reduction will lead to lower mortality independently of other mechanisms of regulated cell death (RCD). Autophagy is characterized by massive vacuolization of the cytoplasm, which leads to the formation of an autophagosome with a double membrane that isolates cytoplasmic components and organelles and delivers them to lysosomes. The fusion of autophagosomes and lysosomes leads to the degradation of cytoplasmic components by lysosomal hydrolases. In adult organisms, autophagy functions as a self-digestion pathway that promotes cell survival in adverse conditions and as a quality control mechanism by removing damaged organelles, toxic metabolites, or intracellular pathogens. DAMPs indicate molecular patterns associated with damage; HSP, heat shock proteins; HMGB1, high mobility group B1 protein; IL, interleukin; ATP/MSU, sodium adenosine triphosphate/urate.

However, no studies have accurately established the autophagy process (or ADCD) as a mechanism of photo-induced cell death although the results of these studies show increased autophagic flow and point vacuoles. Therefore, before attributing a direct role to autophagy in death, it is recommended to determine the effectiveness status of the mechanism by a general inhibition of the autophagy pathway using genetic approaches (knockdown or knockout based on siRNA, shRNA, or CRISPR/Cas9). Other studies have shown that, depending on the stress level, some elements of autophagic cell death may contribute to other cell death programs, such as apoptosis or necrosis [28]. Necrosis, unlike apoptosis, is morphologically characterized by vacuolization of the cytoplasm, swelling, and destruction of the plasma membrane, which leads to an inflammatory reaction due to the release of cellular contents. Necrosis is believed to be the result of pathological disorders, such as depletion of adenosine triphosphate (ATP) to a level incompatible with cell survival. The biochemistry of necrosis is characterized by the release of cytochrome C and fragmentation of DNA oligonucleosomes.

ROS and singlet oxygen particularly can activate both ways of apoptosis. Apoptosis is morphologically characterized by chromatin condensation, cleavage of chromosomal DNA, rupture of membranes, and formation of apoptotic bodies

without destruction of the plasma membrane. Usually, cells subject to apoptosis secrete signaling molecules such as “find me” and “eat me,” which are necessary for the removal of cellular residues by phagocytic cells. At the biochemical level, the process of apoptosis is carried out due to the activation of caspases, which are proteases of a highly conserved cysteine-dependent aspartate-specific family.

$^1\text{O}_2$ can activate p53 and/or c-Jun N-terminal kinase (JNK), which promotes pro-apoptotic Bcl-2 proteins that inhibit the functions of anti-apoptotic proteins. ROS also causes depolarization of the mitochondrial membrane and/or the opening of Bax/Bak channels, which also leads to cell death. Transmembrane death receptors, which include Fas, TRAIL-R1/2, and TNF-R1, can be activated by ROS. Apoptosis mediated by death receptors energizes the involvement of the FADD adapter protein and procaspase-8 or -10 to the cytoplasmic surface of the receptor to form DISC. It leads to the activation of caspase-8/-10, which can directly promote caspases-3/-6/-7 and trigger the external pathway of apoptosis [29].

PDT also induces immunological reactions since cells of the immune system (macrophages, neutrophils, and dendritic cells) are attracted by the cell debris from tumor cells at the site of PDT, and tumor cell antigens are exposed to the immune system [7] (Fig. 8.2). Singlet oxygen has a distance of migration between 0.02 and 1.00 μm and a limited life span of 0.04–4.00 μs . As a result, PDT minimizes the risk of damage to normal tissue, while simultaneously targeting tumor tissues containing the photosensitizer [5, 13, 29]. Moreover, PDT can activate the immune system through Damage-Associated Molecular Patterns (DAMPs) released by or exposed to dying cells, which in turn stimulate both innate and adaptive immunity. The potential of this fact is enormous, taking into account that common cancer therapies tend to be immunosuppressive [30]. That mechanism could induce immunogenic cell death (ICD). ICD is characterized by the emission of various DAMPs, such as ASP and HMGB1. DAMPs function as adjuvants that promote the activation of antigen-presenting cells by absorbing dying cancer cells and cross-presenting antigenic peptides to CD8+ T cells, one of the main elements of antitumor immune responses [31].

8.3 PDT of Brain Tumors

PDT continues to be investigated as an adjunct therapy for the treatment of glioblastoma (GBM) for about 35 years [32–36]. In 1980, Perria et al. [19] conducted the first PDT study using Photofrin[®] as a photosensitizer (5 mg/kg, luminous flux 720–2400 J/cm²) on eight patients with anaplastic astrocytoma and GBM. Later, in 2005, Kaneko [37] and Stylli et al. [20] repeated PDT using Photofrin[®] (5 mg/kg, luminous flux 70–240 J/cm²) and added a combination of radiochemotherapy in 145 patients with GBM. They reported an MST of 14.9 months for patients with initial GBM and 13.5 months for patients with relapse. In 2006, Muller et al. [21] used the PDT method on 112 patients with GBM (Photofrin[®] (2 mg/kg, luminous flux 20 J/cm²) and showed an average survival time (AST) of 11 months for the PDT group and 8 months for the control group. In the same year, Kostron

Fig. 8.2 Effects of PDT on immune system. PDT can affect immune responses and induce antitumor immunity. It is also capable of inducing immunogenic cell death, which stimulates immune responses against dead cell antigens, which in turn are absorbed by antigen-presenting cells such as dendritic cells. Next, antigens are presented to T cells in secondary lymphoid organs. Activated T cells, as well as monocytes, mast cells, and neutrophils are recruited into the tumor microenvironment, which lead to inflammation. (The figure is reproduced with permission from [8])

et al. [3] performed PDT using another sensitizer—Foscan[®] (0.15 mg/kg, absorption wavelength 652 nm, 20 J/cm²) for patients with recurrent GB and reported that AST was 9 months for the PDT group compared to patients who did not receive treatment. In 2007, Stepp et al. [22] the prodrug 5-aminolevulinic acid (5-ALA, 20 mg/kg) was used for photodynamic diagnostics (PDD) of GBM. For PDD, specific 5-ALA fluorescence was monitored in the ultraviolet range 3–6 h after the introduction of per os (Fig. 8.3). This group also used PDT for GBM patients (635 nm laser with 100, 150, and 200 J/cm²) and demonstrated MST of 6 months for the PDT group compared to the control group.

The most successful and promising results were demonstrated in the work of Eljamel [39] in 2010, who performed PDT in 27 patients with GBM using Photofrin[®], 2 mg/kg, luminous flux of 100 J/cm². They achieved an MMSE score of 53 weeks in the PDT group and 24 weeks in the control group, i.e., survival increased by 1.5 years.

8.4 PDT and the Blood–Brain Barrier (BBB) Permeability

Another aptitude that PDT could help in brain cancer treatment is its effect on the blood–brain barrier (BBB) permeability. BBB is an integral part of the health of the central nervous system (CNS). BBB is semi-permeable, controlling the penetration of various agents from the blood into the brain, protecting the central nervous system from toxic substances and pathogens. On the other hand, the same semiconductor properties of the BBB limit the delivery of medications to brain tissues and the central nervous system as a whole, which creates a gap in the successful therapy of CNS diseases. The effects exerted on the ¹O₂ vessel during PDT may become a potential method of delivering therapeutic substances to the brain and the local tumor environment due to an increase in the permeability of the BBB to pharmacological agents. This explains the increased interest in the methods of BBB discovery in recent decades [39].

It has been found that PDT can effectively increase BBB permeability in specific areas. Hirschberg et al. using a quartz fiber with a flat end of 400 microns, transmitting light of 635 nm, and a stereotactic procedure, it is shown that PDT using ALA causes the opening of the BBB without any damage to brain tissue. Several other authors demonstrate PDT-mediated BBB discovery for macrophage migration from the blood to the brain, using these immune cells and as a transport system of gold nanoparticles through the BBB. Gold nanoparticles have great prospects for PDT [10]. It has also been demonstrated that the degree of increased BBB permeability has a direct dependence on the doses of the photosensitizer [40–43]. It is shown that the optimal laser doses (when using a powerful red continuous-wave LED with $\lambda = 635$ nm), which induced the opening of the BBB, was 10–15 J/cm². At the same time, it was shown that a further increase in the light dose to 40 J/cm² was not accompanied by more significant changes in the BBB. Hirschberg et al. using stereotactic PDT in healthy rats (632 nm + a high dose of 5-ALA 125 mg/kg, intravenously), an increase in BBB permeability for low-molecular gadolinium

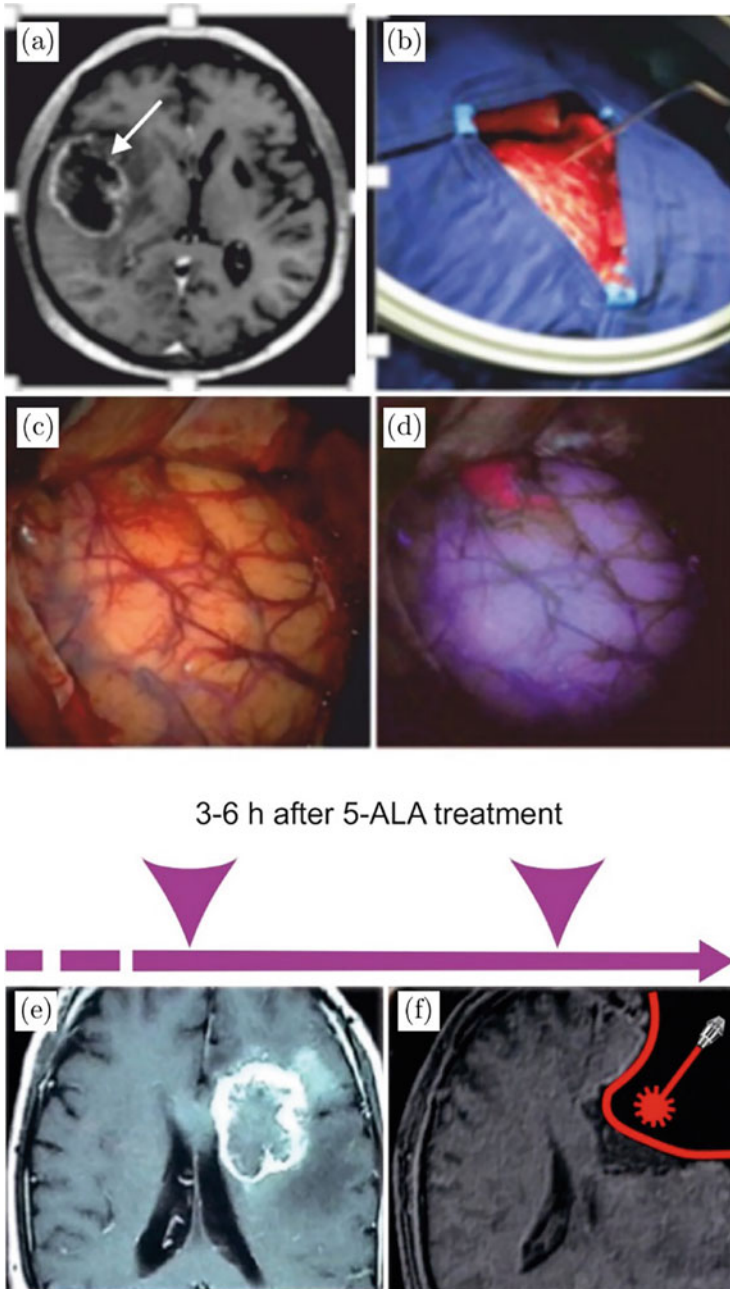


Fig. 8.3 The fluorescence-guided resection of GBM in the patient: (a) magnetic resonance imaging (MRI) of GBM (arrowed); (b) preparation of surgical area; (c) the surface of brain after craniotomy; (d) specific fluorescence of 5-ALA in ultraviolet 3–6 h after 5-ALA administration per os; (e, f) PDT of GBM, where (e)—MRI of GBM and (f)—schematic illustration of post-surgical PDT of GBM. Panels (a)–(d) presented with the permission of Herbert Stepp, University Hospital of Munich, Germany. (The figure is reproduced with permission from [38])

was achieved 2 h after light exposure and restoration of normal BBB permeability after 72 h at the lowest flow level of 9 J/cm^2 [40]. High doses of radiation (17 and 26 J/cm^2) were accompanied by a longer restoration of the normal structure and function of the BBB (2 weeks) and serious damage to brain tissue (necrosis, hemorrhage).

BBB permeability after PDT is different under other PSs. Thus, compared variety of PSs for PDT-induced BBB opening for Evans Blue complex, GalZnPc gives a stronger increase in the BBB permeability than 5-ALA, AlPcS, and ZnPc (GalZnPc/AlPcS: 29.54 ± 0.02 vs. 18.64 ± 0.03 , $p < 0.001$ for 2.5 J/cm^2 ; 31.8 ± 0.03 vs. 20.37 ± 0.08 , $p < 0.001$ for 5 J/cm^2 ; 33.93 ± 0.05 vs. 23.18 ± 0.07 , $p < 0.001$ for 10 J/cm^2 ; GalZnPc/ZnPc: 29.54 ± 0.02 vs. 12.55 ± 0.05 , $p < 0.001$ for 2.5 J/cm^2 ; 31.8 ± 0.03 vs. 14.12 ± 0.01 , $p < 0.001$ for 5 J/cm^2 ; 33.93 ± 0.05 vs. 15.44 ± 0.05 , $p < 0.001$ for 10 J/cm^2 ; GalZnPc/5-ALA: 29.54 ± 0.02 vs. 1.18 ± 0.02 , $p < 0.001$ for 2.5 J/cm^2 ; 31.8 ± 0.03 vs. 1.09 ± 0.02 , $p < 0.001$ for 5 J/cm^2 ; 33.93 ± 0.05 vs. 8.97 ± 0.05 , $p < 0.001$ for 10 J/cm^2) [44].

Up to now, the mechanisms responsible for the PDT-induced opening of the BBB remain poorly understood. In some studies, it was assumed that PDT exposure leads to an increase in the gaps between vascular endothelial cells, acting on the cytoskeleton depolarization of microtubules and rounding cells [19, 20, 36]. In other studies, it was assumed that singlet oxygen formed as a result of PDT causes a violation of the endothelial regulation of vascular relaxation, which reduces vascular resistance to oxidative stress. This leads to a decrease in the influx and release of calcium from the intracellular storage [28, 45].

It is demonstrated that photoactivation of the Bengal Rose photosensitizer by light contributed to significant ultrastructural damage to endothelial cells. The damage was accompanied by swelling of the mitochondria with the destruction and adhesion of the cristae, the development of necrosis, degranulation of mast cells, loss of calcium with the appearance of precipitation of the mitochondria (normally localized in the sarcolemma). Photoactivation of the Bengal rose leads not only to the formation of $^1\text{O}_2$ but also to the synthesis of super anion, hydroxyl radical, hydrogen peroxide, which causes oxidative stress and vascular endothelial dysfunction [28].

8.5 PDT-Induced Opening of the BBB and the Meningeal Lymphatic System

It has been shown that after PDT-induced BBB opening, the purification of brain tissues through meningeal lymphatic vessels increases. The main function of the lymphatic system is the outflow of fluid. However, the situation with the brain is different.

For more than 200 years, scientists have believed that the structures of the lymphatic system are absent inside the central nervous system. However, later

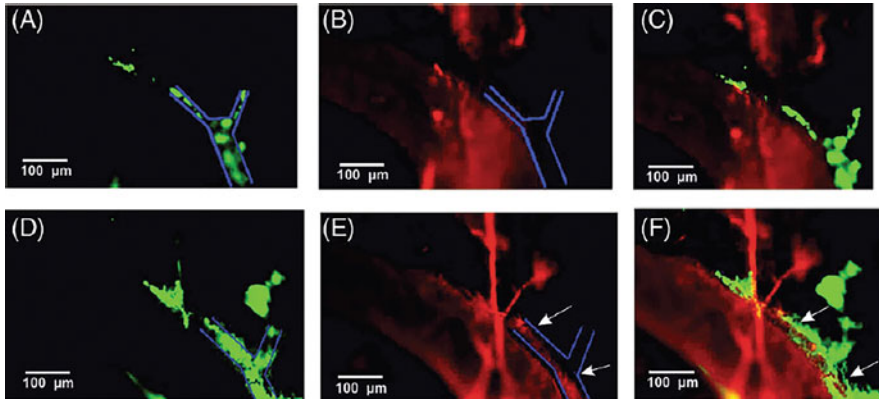


Fig. 8.4 Fluorescent microscopy of the brain clearing from the FITC-dextran through the meningeal lymphatic vessels after PDT-induced BBB opening. Before PDT-induced BBB opening: (a) meningeal lymphatic vessels marked by specific lymphatic antibodies (LYVE-1—green color, blue lines delineate the boundaries of the lymphatic vessel); (b) FITC-dextran presence inside the Sagittal sinus (the main cerebral vein), but not in the meningeal lymphatic vessel after its intravenous injection; (c) merged pictures of (a) and (b). After PDT-opening of the BBB: (d) the same as in (a); (e) FITC-dextran presence inside the Sagittal sinus and in the meningeal lymphatic vessel (arrowed) after its extravasation from the cerebral vessels into the brain parenchyma; (f) merged pictures of (d) and (e) [46]

meningeal lymphatic vessels of the brain were discovered, which broke the dogma. And today, the literature is full of reports on the interrelation of the process of the brain and the work of the lymphatic system of the head and neck.

It has been shown that any opening of the BBB is accompanied by an increase in the diameter of the meningeal lymphatic vessels and the accumulation of cerebrospinal fluid in cisterna magna. Moreover, the increase in diameter and accumulation of fluid is proportional to the degree of opening of the BBB. Thus, 30 min after PDT of BBB opening for FITC-dextran, *ex vivo* (confocal data) and *in vivo* (fluorescence microscopy) experiments indicated the presence of a dye inside meningeal lymphatic vessels labeled with specific antibodies to lymphatic vessels (LYVE-1) (Fig. 8.4) [46].

8.6 PDT for Preclinical Study of Stroke

PDT, in addition to all of the above, can also be used to create models of diseases such as stroke. Stroke is a disease that affects the blood vessels of the brain. Despite the fact that stroke leads in the number of deaths due to its fault, which is a socio-economic problem, we still do not have enough medicines and therapies aimed at treating and eliminating the consequences of a cerebrovascular catastrophe [47–50]. The creation and use of stroke models on laboratory animals in recent years has made it possible to better understand the nature of stroke [51].

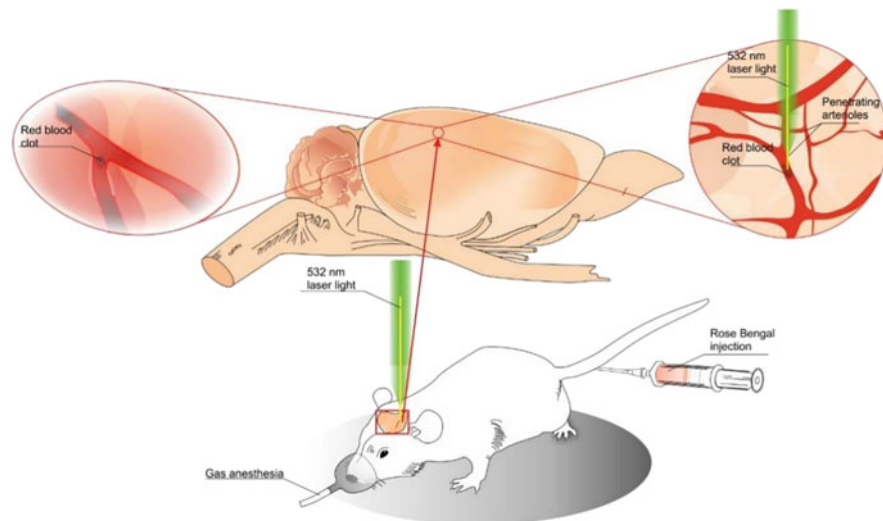


Fig. 8.5 The inducing of thrombotic stroke in rats. The rat underwent general anesthesia and intravenous injection of Rose Bengal. Then rat is exposed to a “cold” light source (wavelength 532 nm, second harmonic of Nd:YAG laser radiation). Rapidly, the endothelial damage and specifically stimulates platelet adhesion and aggregation with thrombus formation. (The figure was reproduced with permission from [28])

The use of PDT provokes the occurrence of stroke by photoactivation and intravenously administered photosensitizer or photosensitive dye. The most popular of them for the stroke model is Bengal pink—disodium tetrachlorotetraiodofluorescein with an absorption peak at 562 nm. In addition to Bengali pink, erythrosin B is also used, but it is less effective in the same concentration [50]. The Bengal rose to circulate in the bloodstream binds to the organelles of endothelial cells. The stained endothelium is irradiated with a source of “cold” light (green light at 562 nm from a filtered xenon arc lamp or at 532 nm second-harmonic generation from an Nd:YAG laser) and transmits light energy to an oxygen molecule (Fig. 8.5). Oxygen (O_2) in this case passes into excited singlet oxygen (1O_2), as in classical PDT. Singlet oxygen, in turn, interacts with the brain endothelium, peroxidizing lipids, and proteins, which causes damage to the endothelium (the process occurs within 40 min) and specifically stimulates platelet adhesion and aggregation with the formation of a thrombus, which causes local occlusion of pial vessels and acute stroke [50–53].

The photothrombotic stroke model does not require surgical intervention, such as trepanation or direct blood injection, and is a noninvasive method where only intravenous injection of a photosensitizer and light illumination of the intact skull is required. The model is well reproducible, all parameters are easily changed and controlled [54, 55]. Although the mortality rate is less than 10%, photothrombotic stroke causes prolonged sensorimotor disorders [55–58].

This model is used to study anti-stroke neuroprotective drugs, such as diazepam, a calcium channel blocker [59], memantine, an antagonist of the *N*-methyl-D-aspartate receptor [60], leptin, an inhibitor of protein kinase activated by adenosine monophosphate 50 [61], melatonin, a pineal gland hormone that controls sleep and reduces the expression of matrix metalloproteinase 9, responsible for the opening of the BBB [62].

8.7 Enhancement of Light Delivery to the Brain

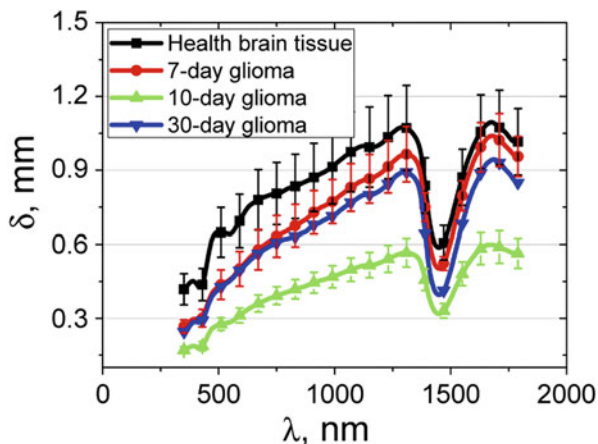
The correct determination of the glioma radiation dose during PDT depends, in addition to the initially supplied power, also on the depth of light penetration into the biological tissue [63]. The key to the therapeutic application of therapeutic diagnostics is the assessment of the ability of laser radiation to penetrate the brain based on knowledge about optical properties in a wide spectral range [63]. In the visible/infrared range, the depth of light penetration into healthy brain tissue is well characterized [64–70]. For glioma, in particular, the absorption and scattering coefficients and the scattering anisotropy coefficient were measured in vitro in the range of 350–1100 nm for human gliomas of II degree [65, 71] and in the range of 400–800 nm for gliomas of III degrees [71]; absorption, scattering, and reduced scattering coefficients, as well as the depth of light penetration, were obtained in the range of 350–1300 nm [66, 68] for malignant human gliomas and in the range of 350–1000 nm for glioblastoma and oligodendroglioma [61]; the depth of light penetration was estimated in a narrow range of 610–710 nm for human astrocytomas of I–II and III degrees and glioblastoma [72]. Diffuse reflection spectra of human glioma in vivo were measured in the range of 400–800 nm [66].

An estimate of the penetration depth of laser radiation into the healthy and malignant brain tissue (δ) in healthy rats and rats with a C6 model glioblastoma (7, 10, and 30 days), defined as a depth for which intensity of a light beam is attenuated in 2.7-fold, has been performed using equation written in the diffusion approximation $\delta = \frac{1}{\sqrt{(3\mu_a(\mu_a + \mu'_s))}}$, where μ'_s is the reduced scattering coefficient, μ_a is the absorption coefficient (see Fig. 8.6) [63].

The penetration depth varies significantly depending on the wavelength of the probing light. For healthy tissue, the maximum penetration depth is approximately 1.0 ± 0.2 mm, for the spectral range of 1000–1300 nm. In the areas of the water absorption band with a maximum of 1450 nm and the hemoglobin absorption band with a maximum of 420 nm, the penetration depth is significantly reduced to 0.4–0.5 mm [63].

Light attenuation caused by the skull in laboratory animals can be reduced by the open-skull glass window and the thinned-skull cranial window techniques. The associated inflammatory response and the complexities in surgical procedures related to these two techniques are mitigated in the skull optical clearing window technique [73].

Fig. 8.6 The light penetration depth into the healthy brain tissues and 7–10–30 days after glioma cells implantation. The solid line corresponds to the averaged experimental data and the vertical lines show the standard deviation values. (The figure was reproduced with permission from [63])



Skull optical clearing window is a derivative of the tissue optical clearing technique [74–76]. Strong scattering in the mouse skull is produced by its structural heterogeneity. The skull consists of two layers of compact bone sandwiching a layer of spongy bone with all layers containing an inorganic matrix and an organic matrix. The main component of the inorganic matrix is calcium hydroxyapatite. Collagen is the main component in an organic matrix. As the laboratory animal grows older, the ratio of inorganic matrix to organic matrix increases. For example, for the infantile mice (<P20), collagenase can be used to dissolve collagenous fiber; for the elder mice (>P20), EDTA disodium can be used to chelate calcium ions (decalcification). In addition, glycerol is used to match the refractive index [73].

The process of optical cleansing of the skull window is carried out in two stages: the first is the cleansing of the outer layer of the skull, the second is the selection of the refractive index. Because the composition and thickness of the skull bones change with age, different methods of optical cleaning are selected for mice of different age groups. So, for mice aged P15–P20, an intact skull is topically treated with 10% collagenase for 5–10 min. The reagent is replaced by 10% disodium EDTA for mice aged P21–P30. As mice age, the thickness of their skulls increases. In mice older than P30, the skull is thinned to about 100 μm before optical purification and treatment of 10% EDTA disodium for 5–10 min [73].

Head optics, describing the contribution of various layers of the head, such as the scalp, skull, dura mater, gray and white matter, to light attenuation and optical clearing of the tissues, are discussed in Ref. [77]. All these data are of great importance for the efficient delivery of light to the tags in the brain and for the effective action of PDT.

8.8 Conclusion and Perspectives

PDT is definitively less invasive compared to surgery, and more precise than chemotherapy and, finally, as opposed to radiotherapy, may be repeated several times. Despite the wide application of the PDT method in today's clinical practice, it is extremely necessary to do further detailed investigations for the understanding of the fundamental mechanisms of PDT effect and action.

It is not yet clear how to explain the direct generation of $^1\text{O}_2$, since the rules of spin-orbit selection prevent the direct $^3\text{O}_2 \rightarrow ^1\text{O}_2$ transition in molecular oxygen. In addition, the physiological effects of directly generated $^1\text{O}_2$ are also poorly understood.

The cerebrovascular effects of $^1\text{O}_2$ are the highly perspective for the urgent medical application of PDT, but using it in clinical practice as well strongly needs optimization and adaptation due to negative complications such as perivascular edema, constriction of brain vessels, thrombosis, small cerebral hemorrhages.

Another application of the effects caused by $^1\text{O}_2$ is the stroke model. However, even though this model has been used for more than 30 years to conduct preclinical studies of the neuroprotective effects of pharmacological agents and medications to mitigate the effects of stroke, the mechanisms of action of $^1\text{O}_2$ on vascular damage are unclear.

The newly discovered effects of PDT on BBB permeability open novel strategies for drug-brain delivery, especially for the post-surgical treatment of GBM.

Recent discoveries of connection between BBB opening and activation of lymphatic clearing also open a door to prospective application for PDT treatment of a variety of diseases such as Alzheimer's, stroke, and so on.

So, despite the already long-term use of PDT, there are still mysteries about the mechanisms, and there are all new possibilities for using the method, which will require further study.

Funding This work was supported by RF Governmental Grant No. 075-15-2019-1885, Grant from RSF Nos. 20-15-00090 and 21-75-10088, RFBR Grant No. 19-515-55016 China a, 20-015-00308-a.

References

1. Uzdensky AB, Berezhnaya E, Kovaleva V, Neginskaya M, Rudkovskii M, Sharifulina S (2015) Photodynamic therapy: a review of applications in neurooncology and neuropathology. *J Biomed Opt* 20:61108
2. Zakharov SD, Ivanov AV (1999) Light-oxygen effect in cells and its potential applications in tumour therapy (review). *Quant Electron* 29:1031
3. Kostron H, Hasan T (eds) (2016) Photodynamic medicine: from bench to clinic. The Royal Society of Chemistry, Cambridge
4. Zavadskaya TS (2015) Photodynamic therapy in the treatment of glioma. *Exp Oncol* 37:234–241

5. Abdurashitov A, Tuchin V, Semyachkina-Glushkovskaya O (2020) Photodynamic therapy of brain tumors and novel optical coherence tomography strategies for in vivo monitoring of cerebral fluid dynamics. *J Innov Opt Health Sci* 13:2030004
6. Kwang J (2012) *Int Rev Cell Mol Biol* 295:139–174
7. Edge R, Truscott TG (2021) The reactive oxygen species singlet oxygen, hydroxy radicals, and the superoxide radical anion—examples of their roles in biology and medicine. *Oxygen* 1:77–95
8. Gunaydin G, Gedik M, Seylan A (2021) Photodynamic therapy—current limitations and novel approaches. *Front Chem* 9:691697
9. Ferreira dos Santos A, de Almeida DRQ, Terra LF, Baptista MS, Labriola L (2019) Photodynamic therapy in cancer treatment—an update review. *J Cancer Metastasis Treat* 5:25–45
10. Fahmy SA, Azzazy HM, Schaefer J (2021) Liposome photosensitizer formulations for effective cancer photodynamic therapy. *Pharmaceutics* 13:1345
11. Cramer SW, Chen CC (2020) Photodynamic therapy for the treatment of glioblastoma. *Front Surg* 6:81–92
12. Ailioaie LM, Ailioaie C, Litscher G (2021) Latest innovations and nanotechnologies with curcumin as a nature-inspired photosensitizer applied in the photodynamic therapy of cancer. *Pharmaceutics* 23:1562
13. Chung H, Dai T, Sharma SK, Huang Y, Carroll JD, Hamblin MR (2012) The nuts and bolts of low-level laser (light) therapy. *Ann Biomed Eng* 40:516–533
14. Cotler HB, Chow RT, Hamblin MR, Carroll J (2015) The use of low-level laser therapy (LLLT) for musculoskeletal pain. *MOJ Orthop Rheumatol* 2:188–194
15. Matheson BC, Lee J (1971) Comparison of the pressure dependences of the visible and infrared electronic absorption spectra of oxygen in gas and in Freon solution. *Chem Phys Lett* 7:235–239
16. Jockusch S, Turro NJ, Thompson EK, Gouterman M, Callis JB, Khalil GE (2008) Singlet molecular oxygen by direct excitation. *Photochem Photobiol Sci* 7:235–239
17. Anquez F, El Yazidi-Belkoura I, Randoux S, Suret P, Courtade E (2012) Cancerous cell death from sensitizer free photoactivation of singlet oxygen. *Photochem Photobiol* 88:167–174
18. Sokolovski SG, Zolotovskaya SA, Goltsov A, Pourreyron C, South AP, Rafailov EU (2013) Infrared laser pulse triggers excessive singlet oxygen production selectively targeting tumour cells. *Sci Rep* 3:3484
19. Perria C, Capuzzo T, Cavagnaro G, Datti R, Francaviglia N, Rivano C, Tercero VE (1980) Fast attempts at the photodynamic treatment of human gliomas. *J Neurosurg Sci* 24:119–129
20. Stylli SS, Kaye AH, MacGregor L, Howes M, Rajendra P (2005) Photodynamic therapy of high grade glioma—long term survival. *J Clin Neurosci* 12:389–398
21. Muller PJ, Wilson BC (2006) Photodynamic therapy of brain tumor—a work in progress. *Laser Surg Med* 38:384–389
22. Stepp H, Beck T, Pongratz T, Meinel T, Kreth F, Tonn J, Stummer W (2007) ALA and malignant glioma: fluorescence-guided resection and photodynamic treatment. *J Environ Pathol Toxicol Oncol* 26:157–164
23. Peshavariya HM, Dusting GJ, Selemidis S (2007) Analysis of dihydroethidium fluorescence for the detection of intracellular and extracellular superoxide produced by NADPH oxidase. *Free Radic Res* 41:699–712
24. Halliwell B, Gutteridge GM (2007) *Free radicals in biology and medicine*, 3rd edn. Oxford University Press, Oxford
25. Adams JC, Watt FM (1998) An unusual strain of human keratinocytes which do not stratify or undergo terminal differentiation in culture. *J Cell Biol* 107:1927–1938
26. Semyachkina-Glushkovskaya OV, Sokolovski SG, Goltsov A, Gekaluyk AS, Saranceva EI, Bragina OA, Tuchin VV, Rafailov EU (2017) Laser-induced generation of singlet oxygen and its role in the cerebrovascular physiology. *J Progr Quant Electron* 55:112–128
27. Agostinis P, Berg K, Cengel KA (2011) Photodynamic therapy of cancer: an update. *CA Cancer J Clin* 61:250–281

28. Waleska KM, Belotto R, Silva MN, Grasso D, Suriani MD, Lavor TS, Itri R, Baptista MS, Tsubone TM (2021) Autophagy regulation and photodynamic therapy: insights to improve outcomes of cancer treatment. *Front Oncol* 10:610472
29. Yanovsky RL, Bartenstein DW, Rogers GS, Isakoff SJ, Chen ST (2019) Photodynamic therapy for solid tumors: a review of the literature. *Photodermatol Photoimmunol Photomed* 35:295–303
30. Algorri JF, Ochoa M, Roldán-Varona P (2021) Photodynamic therapy: a compendium of latest reviews. *Cancers (Basel)* 13:4447
31. Turubanova VD, Mishchenko TA, Balalaeva IV, Efimov I, Peskova NN, Klapshina LG, Lermontova SA, Bachert C, Krysko O, Vedunova MV, Krysko DV (2021) Novel porphyrazine-based photodynamic anti-cancer therapy induces immunogenic cell death. *Sci Rep* 11:7205
32. Eljamel MS, Goodman C, Moseley H (2008) ALA and photofrin fluorescence-guided resection and repetitive PDT in glioblastoma multiforme: a single Centre phase III randomised controlled trial. *Lasers Med Sci* 23:361–367
33. Muragaki Y, Akimoto J, Maruyama T (2013) Phase II clinical study on intraoperative photodynamic therapy with talaporfin sodium and semiconductor laser in patients with malignant brain. *J Neurosurg* 119:845–852
34. Bechet D, Mordon SR, Guillemin F (2014) Photodynamic therapy of malignant brain tumors: a complementary approach to conventional therapies. *Cancer Treat Rev* 40:229–241
35. Quirk BJ, Brandal G, Donlon S (2015) Photodynamic therapy (PDT) for malignant brain tumors—where do we stand? *Photodiagn Photodyn Ther* 12:530–544
36. Gasper LE, Fisher BJ, Macdonald DR (1992) Supratentorial malignant glioma: patterns of recurrence and implications for external beam local treatment. *Int J Radiat Oncol Biol Phys* 24:55–57
37. Kaneko S (2012) Safety guidelines for diagnostic and therapeutic laser applications in the neurosurgical field. *Laser Ther* 21:129–136
38. Akimoto J (2016) Photodynamic therapy for malignant brain tumors. *Neurol Med Chir* 56:151–157
39. Eljamel S (2010) Photodynamic applications in brain tumors: a comprehensive review of the literature. *Photodiagn Photodyn Ther* 7:76–85
40. Zhang C, Feng W, Vodovozova E (2018) Photodynamic opening of the blood-brain barrier to high weight molecules and liposomes through an optical clearing skull window. *Biomed Opt Express* 9:4850–4862
41. Bors L, Tóth K, Tóth EZ (2018) Age-dependent changes at the blood-brain barrier. A comparative structural and functional study in young adult and middle aged rats. *Brain Res Bull* 139:269–277
42. Ruk I, Pockova P, Benes J (2019) Drug delivery systems for phthalocyanines for photodynamic therapy. *Anticancer Res* 39:3323–3339
43. Sansaloni-Pastor S, Bouilloux J, Lange N (2019) The dark side: photosensitizer prodrugs. *Pharmaceuticals* 12:148
44. Semyachkina-Glushkovskaya O, Borisova E, Mantareva V, Angelov I, Eneva I, Terskov A, Mamedova A, Shirokov A, Khorovodov A, Klimova M, Agranovich I, Blokhina I, Lezhnev N, Kurths J (2020) Photodynamic opening of the blood-brain barrier using different photosensitizers in mice. *Appl Sci* 10:33–45
45. Mathews MS, Chighvinadze D, Gach HM, Uzal FA, Madsen SJ, Hirschberg H (2011) Cerebral edema following photodynamic therapy using endogenous and exogenous photosensitizers in normal brain. *Lasers Surg Med* 43:892–900
46. Semyachkina-Glushkovskaya O, Chehonin V, Borisova E, Fedosov I, Namykin A, Abdurashitov A, Shirokov A, Khlebtsov B, Lyubun Y, Navolokin N, Ulanova M, Shushunova N, Khorovodov A, Agranovich I, Bodrova A, Sagatova M, Shareef AE, Saranceva E, Iskra T, Dvoryatkina M, Zhinchenko E, Sindeeva O, Tuchin V, Kurths J (2018)


- Photodynamic opening of the blood-brain barrier and pathways of brain clearing. *J Biophotonics* 10:33–41
47. Schwamm LH (2012) Stroke in 2011: major advances across the spectrum of stroke care. *Nat Rev Neurol* 8:63–64
 48. Tymianski M (2014) Stroke in 2013: disappointments and advances in acute stroke intervention. *Nat Rev Neurol* 10:66–68
 49. Mergenthaler PH, Meisel A (2012) Do stroke models model stroke? *Dis Models Mech* 5:718–725
 50. Bergeron M (2013) Inducing photochemical cortical lesions in rat brain. *Curr Protoc Neurosci* 9:16
 51. Watson BD, Dietrich WD, Busto R, Wachtel MS, Ginsberg MD (1985) Induction of reproducible brain infarction by photochemically initiated thrombosis. *Ann Neurol* 17:497–504
 52. Labatgest V, Tomasi S (2013) Photothrombotic ischemia: a minimally invasive and reproducible photochemical cortical lesion model for mouse stroke studies. *J Vis* 76:50370
 53. Yanlin WF (ed) (2008) Manual of stroke models in rats. CRC Press, Boca Raton
 54. Schmidt A, Hoppen M, Strecker J, Diederich K, Schäbitz W, Schilling M, Minnerup J (2012) Photochemically induced ischemic stroke in rats. *Exp Transl Stroke Med* 4:13
 55. Schroeter M, Jander S, Stoll G (2002) Non-invasive induction of focal cerebral ischemia in mice by photothrombosis of cortical microvessels: characterization of inflammatory responses. *J Neurosci Methods* 117:43–49
 56. Shanina EV, Redecker C, Reinecke S, Schallert T, Witte OW (2005) Long-term effects of sequential cortical infarcts on scar size, brain volume and cognitive function. *Behav Brain Res* 158:69–77
 57. Wood N, Sopesen BV, Roberts JC, Pambakian P, Rothaul AL, Hunter AJ, Hamilton TC (1996) Motor dysfunction in a photothrombotic focal ischaemia model. *Behav Brain Res* 78:113–120
 58. Minnerup J, Kim JB, Schmidt A, Diederich K, Bauer H, Schilling M, Strecker J, Ringelstein EB, Sommer C, Schöler HR, Schäbitz W (2011) Effects of neural progenitor cells on sensorimotor recovery and endogenous repair mechanisms after photothrombotic stroke. *Stroke* 42:1757–1763
 59. Aerden L, Kessels F, Rutten B, Lodder J, Steinbusch H (2004) Diazepam reduces brain lesion size in a photothrombotic model of focal ischemia in rats. *Neurosci Lett* 367:76–78
 60. Lopez-Valdes HE, Clarkson AN, Ao Y, Charles AC, Carmichael ST, Sofroniew MV, Brennan KC (2014) Memantine enhances recovery from stroke. *Stroke* 45:2093–2100
 61. Avraham Y, Davidi N, Lassri V, Vorobiev L, Kabesa M, Dayan M, Chernoguz D, Berry E, Leker R (2008) Leptin induces neuroprotection neurogenesis and angiogenesis after stroke. *Curr Neurovasc Res* 8:313–322
 62. Jang J-W, Lee J-K, Lee M-C, Piao M-S, Kim S-H, Kim H-S (2012) Melatonin reduced the elevated matrix metalloproteinase-9 level in a rat photothrombotic stroke model. *J Neurol Sci* 323:221–227
 63. Genina EA, Bashkatov AN, Tuchina DK, Timoshina PAD, Navolokin N, Shirokov A, Khorovodov A, Terskov A, Klimova M, Mamedova A, Blokhina I, Agranovich I, Zinchenko E, Semyachkina-Glushkovskaya OV, Tuchin VV (2019) Optical properties of brain tissues at the different stages of glioma development in rats: pilot study. *Biomed Opt Express* 10:5182–5197
 64. van der Zee P, Essenpreis M, Delpy DT (1993) Optical properties of brain tissue. *Proc SPIE* 1:117–123
 65. Yaroslavsky AN, Schulze PC, Yaroslavsky IV, Schober R, Ulrich F, Schwarzmaier HJ (2002) Optical properties of selected native and coagulated human brain tissues in vitro in the visible and near infrared spectral range. *Phys Med Biol* 47:2059–2073
 66. Gebhart SC, Lin WC, Mahadevan-Jansen A (2006) In vitro determination of normal and neoplastic human brain tissue optical properties using inverse adding-doubling. *Phys Med Biol* 51:2011–2027

67. Honda N, Ishii K, Kajimoto Y, Kuroiw T, Awazu K (2018) Determination of optical properties of human brain tumor tissues from 350 to 1000 nm to investigate the cause of false negatives in fluorescence-guided resection with 5-aminolevulinic acid. *J Biomed Opt* 23:1–10
68. Sterenborg HJ, Gemert M, Kamphorst W, Wolbers J, Hogervorst W (1989) The spectral dependence of the optical properties of human brain. *Lasers Med Sci* 4:221–227
69. Madsen SJ (ed) (2013) *Optical methods and instrumentation in brain imaging and therapy*. Springer, New York
70. Golovynskiy S, Golovynska I, Stepanova LI, Datsenko O, Liwei Liu JQ, Ohulchanskyy T (2018) Optical windows for head tissues in near-infrared and short-wave infrared regions: approaching transcranial light applications. *J Biophotonics* 11:201800141
71. Schwarzmaier H, Eickmeyer F, Fiedler V, Ulrich F (2002) Basic principles of laser induced interstitial thermotherapy in brain tumors. *Med Laser Appl* 108:201–208
72. Svaasand LO, Ellingsen R (1983) Optical properties of human brain. *Photochem Photobiol* 38: 293–299
73. Zhao Y-J, Yu T-T, Zhang C, Li Z, Luo Q-M, Xu T-H, Zhu D (2018) Skull optical clearing window for in vivo imaging of the mouse cortex at synaptic resolution. *Light Sci Appl* 7:17153
74. Tuchin VV (ed) (2005) *Optical clearing of tissues and blood*. SPIE Press, Bellingham, WA
75. Oliveira L, Tuchin VV (2019) *The optical clearing method: a new tool for clinical practice and biomedical engineering*. Springer Nature Switzerland AG, Basel
76. V. V. Tuchin, Dan Zhu, E. A. Genina (ed), *Handbook of tissue optical clearing: new prospects in optical imaging*. (CRC Press, Boca Raton, 2022)
77. Sabeeh A, Tuchin VV (2020) Recent advances in the laser radiation transport through the head tissues of humans and animals. *J Biomed Photon* 6:40201



Advanced Magnetic Resonance Imaging (MRI) of Brain

9

Navdeep Kaur , Soumya Swaroop Sahoo,
and Shailendra Singh Rana

Abstract

Magnetic Resonance Imaging (MRI) uses the principle of nuclear magnetic resonance to generate high-resolution images of brain. Due to abundance of water in human body, current MR imaging is based on proton imaging. MRI enables non-invasive structural as well as functional evaluation of brain parenchyma. T₁WI provide detailed structural evaluation of brain. Advanced sequences such as Diffusion Weighted Imaging (DWI), MR Perfusion, MR Spectroscopy, Diffusion Tensor Imaging and functional MRI enable the evaluation of metabolic, haemodynamic and cytoarchitecture of brain parenchyma in a non-invasive manner. This book chapter aims to provide insight into basic and various advanced MRI sequences along with its potential applications in neuroimaging.

Keywords

Magnetic Resonance Imaging · MR perfusion · MR spectroscopy · DTI · Functional MRI

N. Kaur (✉)

Department of Radiodiagnosis, All India Institute of Medical Sciences, Bathinda, Punjab, India

S. S. Sahoo

Department of Community and Family Medicine, All India Institute of Medical Sciences, Bathinda, Punjab, India

S. S. Rana

Department of Dentistry, All India Institute of Medical Sciences, Bathinda, Punjab, India

9.1 Introduction

The fine spatial resolution and non-invasiveness of Magnetic Resonance Imaging (MRI) makes it an integral component of the algorithm for evaluating patients with any neurological disease. Nowadays, MRI is not just limited to provide the anatomical details of tissues. Many advanced MRI sequences are being introduced to provide information about the cytoarchitecture, metabolic, haemodynamic and functional status of tissues to investigate the disease at molecular level.

9.2 Basic Principle

MRI is used to generate high-resolution images of human body. MRI is established on the principle of nuclear magnetic resonance (NMR). The two fundamental principles of NMR are as follows:

- Atoms with odd number of protons or neutrons have a spin.
- A moving electric charge generates a magnetic field.

Human body has many atoms such as ^1H , ^{13}C , ^{19}F , ^{23}Na and ^{31}P that can be used for MR imaging.

Currently, MR is primarily based on proton imaging. Hydrogen atom has only single proton, so one H^+ ion = one proton. Hydrogen ions are present in abundance in human body as water. So, out of all nuclei H^+ ion gives most intense signal on MR imaging (Fig. 9.1).

To localize from where the signal is coming from human body, three additional magnetic fields are superimposed on the principal magnetic field in X , Y and Z axes. These are called gradient fields which vary in strength with varying location. Slice selection gradient is used to select the slice and is sent at the time of Radiation Frequency (RF) pulse. Phase encoding gradient is turned on briefly after slice selection gradient. Frequency encoding/read out gradient is sent at the time of signal reception.

TR (Time to Repeat)—Time period between two RF pulses.

TE (Time to Echo)—Time gap between the start of RF pulse and reception of signal.

Varying combinations of TR and TE are used to generate different MR images.

T_1 -weighted images—Short TR and short TE.

T_2 -weighted images—Long TR and long TE.

Proton density images—Long TR and short TE.

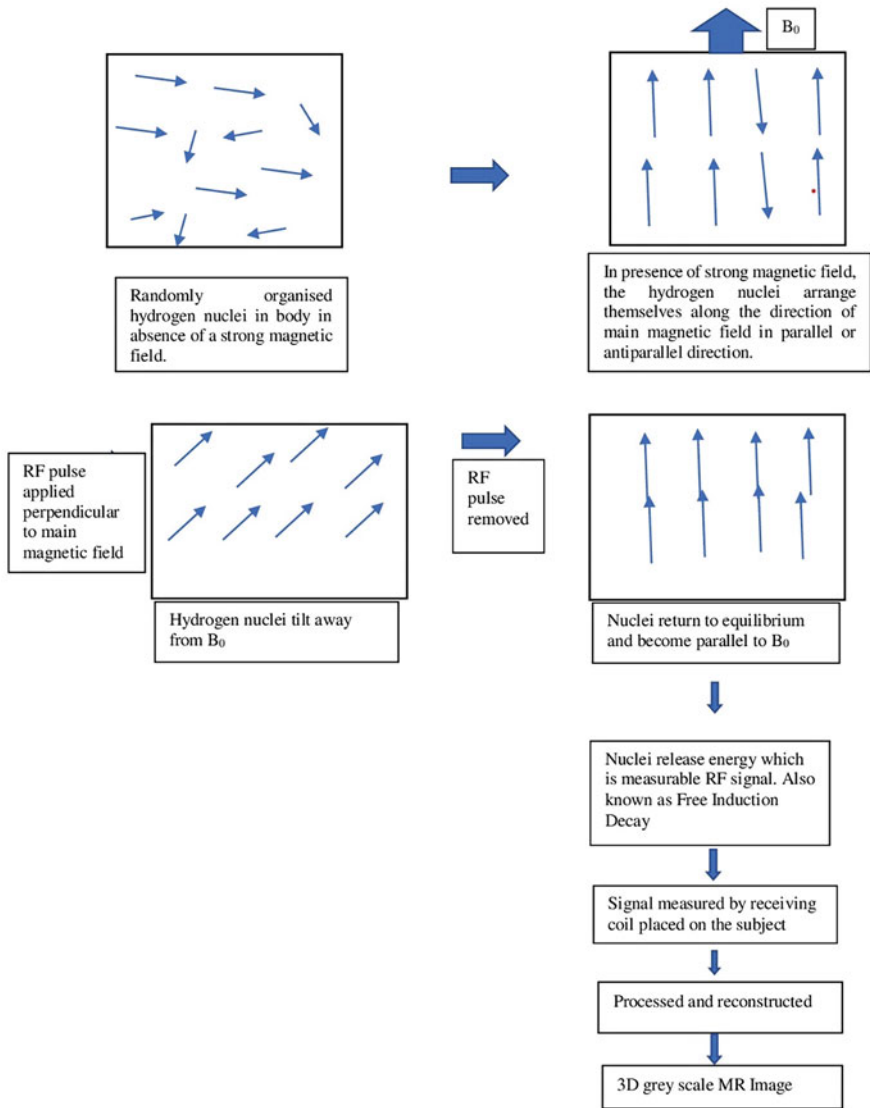


Fig. 9.1 Generation of magnetic resonance signal

9.3 Various MR Sequences

9.3.1 T₁ Weighted Images (T₁WI)

Short Repetition Time (TR) and short Time to Echo (TE) generate T₁WI. Fluid appears dark and fat appears bright on T₁WI (Fig. 9.2a). T₁WI best depict the normal anatomy of brain parenchyma. Grey matter appears intermediate in signal intensity, while white matter appears hyperintense as compared to grey matter. Gadolinium decreases T₁ of the tissues and appear bright on T₁WI. So, post-contrast images can be used for depiction of vascular changes. In various pathologies such as tumours and inflammation, breakdown of blood–brain barrier can lead to leakage of contrast into the brain parenchyma causing its enhancement and thus localization of pathology on post-contrast T₁WI.

9.3.2 T₂ Weighted Images (T₂WI)

Long TR and long TE generate T₂WI. Fluid appears bright and fat appears dark on T₂WI. Grey matter appears intermediate signal intensity, while white matter appears hypointense as compared to grey matter (Fig. 9.2). As most pathologies are associated with cerebral oedema, i.e. increased signal on T₂WI, they are more easily picked up on T₂WI.

9.3.3 Fluid Attenuation Inversion Recovery (FLAIR) Sequence

FLAIR is a special inversion recovery sequence which suppresses the cerebrospinal fluid (CSF) (Fig. 9.2). So, it enables us to detect cerebral oedema without glaring high signal from CSF particularly in periventricular regions and in periphery near

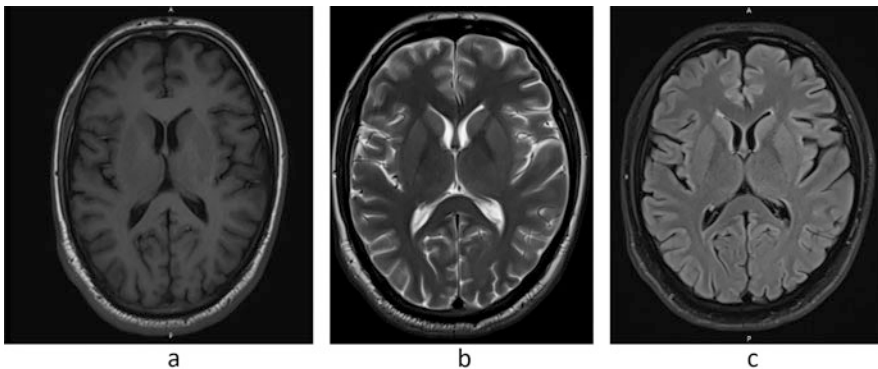


Fig. 9.2 Axial MRI of brain at level of lateral ventricles showing cerebrospinal fluid as dark signal on T₁WI (a), bright on T₂WI (b) and suppression on FLAIR (c) images

sulcal spaces. FLAIR sequence is very useful in evaluating various diseases of central nervous system such as infarction, demyelination and subarachnoid haemorrhage in trauma patients [1–3]. Post-contrast FLAIR images have been used for evaluating leptomeningeal diseases as early meningitis as it enables us to detect which even subtle meningeal enhancement [4].

9.3.4 Diffusion Weighted Imaging (DWI)

DWI is based on the principle of measuring Brownian, i.e. random motion of water molecules in each voxel of tissue. Since microarchitecture of cerebral tissues affect the Brownian motion of water molecules, it may be used to study the cellular integrity. Any pathology such as inflammation or mass lesion restricts the free motion of water molecules in tissues causing bright signal on DWI.

However, few tissues which are bright on T_2 WI, appear bright on DWI without any apparent reduced water diffusion. This is specified as T_2 shine through. Misinterpretation of T_2 shine through for true restricted diffusion can be avoided by using Apparent Diffusion Coefficient (ADC) maps. These ADC images demonstrate actual diffusion values of tissues. Any pathology appears dark on ADC images.

DWI plays a major role in evaluating the following diseases [5–7]:

1. Diagnosis of early stroke, distinguishing acute from chronic stroke and stroke mimics—the vasogenic oedema in acute stroke restricts the free motion of water molecules in affected brain tissue, thus appearing bright on DWI images and dark on ADC maps (Fig. 9.3).
2. Differentiating epidermoid cyst from arachnoid cyst—both the lesions will appear hyperintense on T_2 WI. Epidermoid cyst shows diffusion restriction on DWI/ADC as compared to arachnoid cyst which does not show diffusion restriction.
3. Assessment of active demyelinating lesions as in multiple sclerosis which will show restricted diffusion as compared to the chronic plaques.
4. Grading of diffuse gliomas and meningiomas—extent of tumour cellularity is used for quantitative assessment with DWI. Glioma grade is inversely related with ADC values [8]. Higher the tumour grade—more the cellularity, more the diffusion restriction and lower the ADC values.

9.3.5 Susceptibility Weighted Imaging (SWI)

Compounds having paramagnetic, diamagnetic and ferromagnetic properties distort the local magnetic field altering the phase of local tissues and thus resulting in change of signal [9]. SWI aids in detecting structures that have separate susceptibility in comparison to the surrounding structures like deoxygenated blood, ferritin, haemosiderin and calcium [10]. Calcium can be easily picked up on SWI images which may not be visible on routine images.

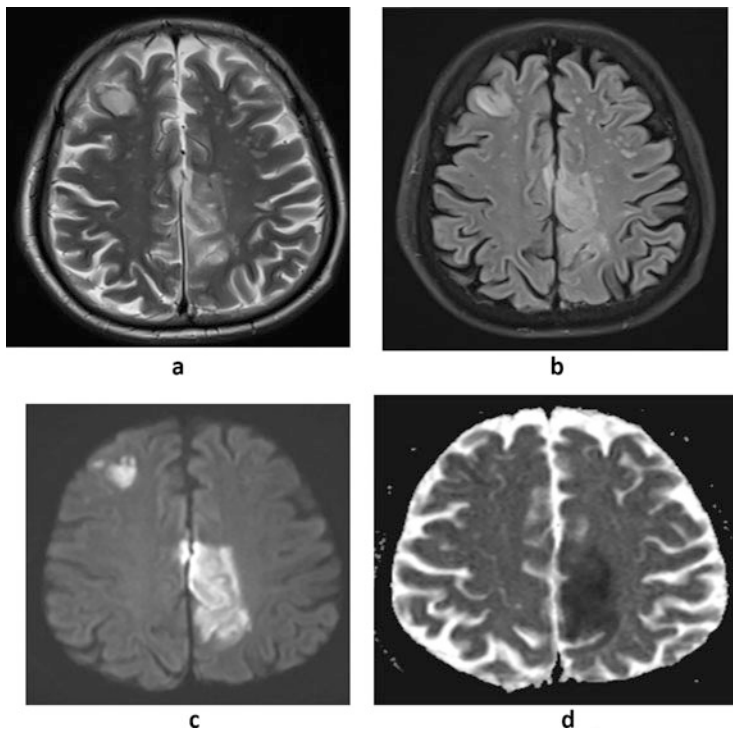


Fig. 9.3 Axial MRI of brain showing area of altered signal intensity involving right frontal lobe and left parietal lobe. It appears hyperintense on T₂WI (a) and FLAIR (b) images. The area shows restriction on DWI (c) and ADC (d) images consistent with acute infarct

SWI is also known as high-resolution blood oxygen level-dependent (BOLD) venography. Paramagnetic deoxyhaemoglobin in veins cause shift in resonant frequency between venous channels and the surrounding brain parenchyma thus aiding in detecting various vascular malformations such as deep venous anomaly.

It is exquisitely sensitive in detecting small haemorrhagic contusions in traumatic brain injury. Identification of small haemorrhages along with their location provides valuable information concerning the mechanism of injury and prognosis of the patient [11].

SWI has the ability to detect minute bleeds within the infarct thus precluding the use of revascularization therapies in case of early haemorrhagic transformation of infarct [12] (Fig. 9.4).

9.3.6 MR Perfusion Imaging

MR perfusion imaging enables us to non-invasively measure cerebral perfusion through assessment of multiple haemodynamic parameters such as cerebral blood

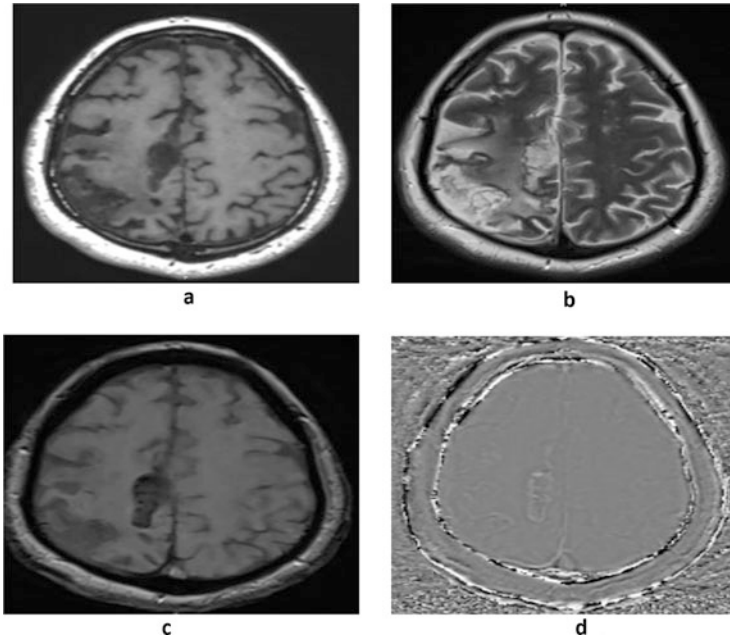


Fig. 9.4 Axial MRI of brain showing area of altered signal intensity involving right parietal lobe. It is hypointense on T₁WI (a), and hyperintense on T₂WI (b) consistent with infarct. Foci of blooming seen in it in right parasagittal location on SWI (c) and appearing bright on phase images (d) indicating haemorrhagic transformation

volume, cerebral blood flow and mean transit time. Exogenous tracer method involving the use of paramagnetic contrast material may be used or magnetically labelled blood may be used as endogenous tracer material [13].

9.3.6.1 Dynamic Susceptibility Contrast (DSC) MR Perfusion

It is the most frequently used technique for MR perfusion study. It uses the regional susceptibility-induced signal loss due to paramagnetic contrast material (such as gadolinium) on T₂ or T₂* WI. Gadolinium containing contrast medium is injected intravenously and rapid repeat sequences of brain are acquired during the first pass of the contrast. Signal in each voxel represents the intrinsic tissue T₂/T₂* signal attenuated by susceptibility induced signal loss proportional to the amount of contrast in the vessels [14, 15].

After image acquisition, signal intensity-time curve is generated from area of interest and various parameters such as regional cerebral blood volume, cerebral blood flow and mean transit time can be calculated. Also, we can use these values to generate coloured maps of area of interest.

9.3.6.2 Dynamic Contrast Enhanced (DCE) MR Perfusion

DCE MR perfusion calculates cerebral perfusion parameters by assessing T_1 shortening effects of gadolinium. Gadolinium-based contrast media is injected intravenously and repeated T_1 WI are obtained. The most frequently calculated parameter is k -trans, i.e. measure of capillary permeability.

9.3.6.3 Arterial Spin Labelling (ASL)

It does not require use of any exogenous contrast medium. Water molecules in incoming blood are magnetically tagged using a radiofrequency pulse which saturates the water protons. Labelled or tagged images and control images are obtained in which the signal from static tissues is identical but of inflowing blood is different. Subtraction of labelled and control images removes the signal from static tissues and the remaining signal measures perfusion which is proportional to cerebral blood flow (CBF).

Compared to other methods, ASL has very low signal-to-noise ratio but is very useful in paediatric patients or patients with impaired renal function who require serial follow-ups [16].

9.3.6.4 Uses

- In acute stroke, perfusion-diffusion mismatch can help in identifying ischaemic penumbra, i.e. surrounding viable ischaemic tissue which is at risk of infarction [17, 18]. Area with reduced cerebral blood volume and cerebral blood flow and increased mean transit time represents the infarcted core as well as the reversible surrounding ischaemic tissue, whereas the area with diffusion restriction represents irreversibly infarcted core.
- Cerebral blood volume maps help us to assess neovascularity within the tumour that correlates well with tumour grade and malignant histology and to localize tumour area expected to yield positive results on stereotactic biopsy. It can enable us to differentiate radiation necrosis from recurrent tumour.
- While evaluating patients with migraine headaches, during the aura, patients show decreased cerebral blood flow and blood volume as compared to post-aural state.
- Its role is being evaluated in dementia patients. Alzheimer's disease patients have shown decreased cerebral blood volume in the temporal and parietal lobes. The results are consistent with findings of single-photon emission computerized tomography (SPECT) studies in these patients [19, 20].

9.3.7 Magnetic Resonance Spectroscopy (MRS)

^1H -MRS is an advanced non-invasive imaging tool which provides information about biochemical composition of tissue being imaged. The main metabolites of brain parenchyma include *N*-acetyl aspartate (NAA), Choline (Cho) and Creatine (Cr) which show peaks at different parts per million (ppm) (Fig. 9.5). The metabolic changes precede the anatomical changes during the development of disease as well

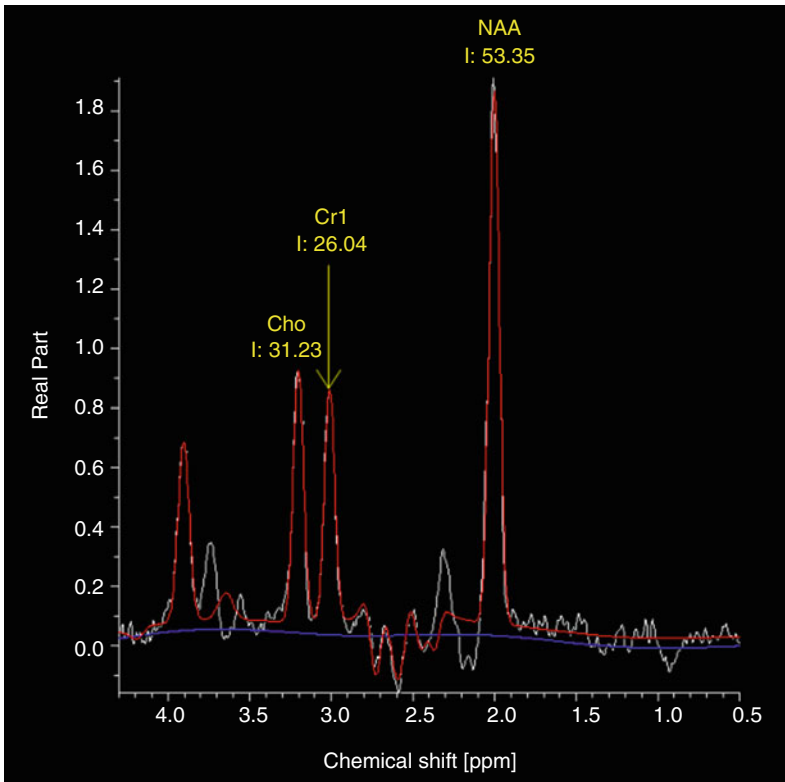


Fig. 9.5 MR spectroscopy image of normal brain parenchyma showing *N*-acetyl aspartate (NAA) peak at 2.01 ppm, Choline peak at 3.20 ppm and Creatine peak at 3.03 ppm

as during response to treatment. So, MRS is a highly sensitive tool to assess these changes at an early stage (Table 9.1).

9.3.8 Diffusion Tensor Imaging (DTI)

DTI is utilized to map and characterize three-dimensional diffusion of water molecules as a function of spatial localization [37, 38]. Diffusion of water in biological tissues is produced by random thermal fluctuations and is hindered by cellular structures and cell membranes. Thus, it leads to anisotropy, i.e. varying magnitude in different directions.

In cerebral white matter, diffusion of water is relatively less restricted in the direction parallel to fibre orientation, while it is exceedingly impeded in the direction perpendicular to the white matter. Major diffusion eigenvector is presumed to be parallel to the orientation of white matter tracts in homogenous white matter

Table 9.1 Magnetic resonance spectroscopy peaks

Metabolite	Peaks at	Significance
NAA (<i>N</i> -acetyl aspartate)	2.01 ppm ^a	Recognized as neuronal marker as it is predominantly found in neurons, axons and dendrites in the central nervous system [21]. Elevated in Canavan's Disease [22].
Choline	3.20 ppm	Elevated in gliomas and in active demyelination [23]. Low levels in hepatic encephalopathy [24].
Lactate	1.31 ppm	Not detectable under normal conditions in brain parenchyma. Elevated in acute hypoxia, ischaemic injury, in brain tumours or mitochondrial diseases [25–30].
Myo-inositol	3.5– 3.6 ppm	Reduced in hepatic encephalopathy [31]. Elevated in Alzheimer's dementia and demyelinating diseases [32, 33].
Creatine	3.03 ppm	Involved in energy metabolism. Glial cells have higher concentration than neurons [34]. Higher levels of creatine in cerebellum as compared to supratentorial brain parenchyma.
Glutamate and glutamine	2.2– 2.4 ppm	Most abundant amino acid in brain. Glutamate is the dominant neurotransmitter. Glutamate is elevated in multiple sclerosis plaques [35]. Elevated glutamine is found in hepatic encephalopathy and Reye's syndrome [31, 36].

^appm: parts per million

[39]. Tractography algorithms are used to generate estimates of the white matter trajectories in human brain.

Tractography methods are applied primarily to generate reconstructions of the major projection pathways, i.e. corticospinal tract, corona radiata, commissural pathways (corpus callosum and anterior commissure) and also association pathways such as arcuate fasciculus, uncinate fasciculus and inferior longitudinal fasciculus [40–44] (Fig. 9.6). Any pathology causing change in tissue microarchitecture alters the anisotropy, thus making DTI a highly efficient tool for indicating the effects of disease on tissue microarchitecture (Fig. 9.7). DTI has a high sensitivity but low specificity which poses a unique challenge to its applications in neurology.

9.3.8.1 Uses

1. Brain tumours—The customary clinical application of DTI is characterization of white matter tracts in persons with brain tumours. DTI maps and tractography help to localize white matter fibre tracts involved in critical functions such as vision, language and motion [44–46]. This information enables the neurosurgeon to plan the surgery accordingly minimizing damage to these critical tracts such as corticospinal tracts [47].
2. Stroke—Diagnosis and characterization of acute ischaemic lesions can be done in the brain parenchyma. During acute phase of the disease, the mean diffusivity significantly reduces in the lesion [48]. After few days (5–7 days), the mean diffusivity normalizes and significantly increases in chronic phase when

Fig. 9.6 Diffusion tractography image showing anteroposterior fibres as green, transverse fibres as red and craniocaudal fibres as blue in color

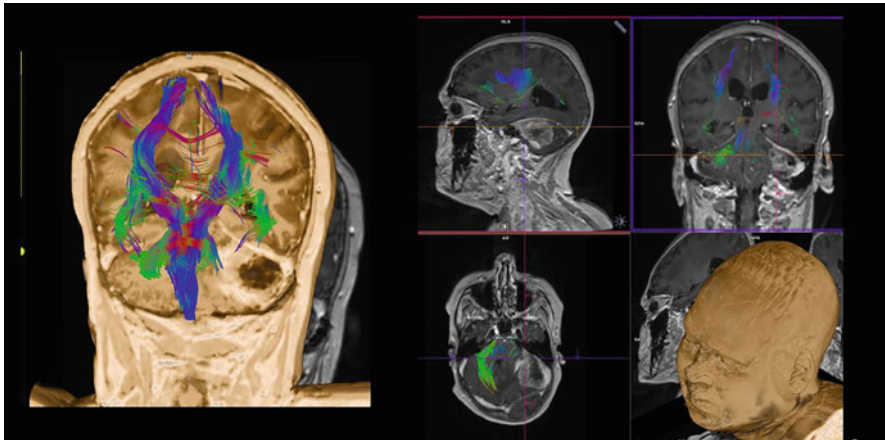
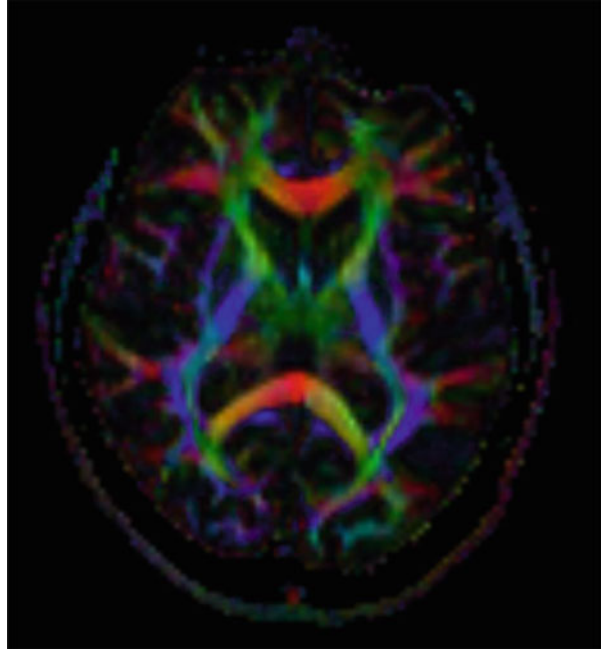


Fig. 9.7 Diffusion tractography image of brain showing destruction of left middle cerebellar peduncle by the mass lesion in left cerebellar hemisphere

encephalomalacia ensues. Fractional anisotropy increases during the acute phase and decrease below the baseline level during chronic phase [49–51].

3. Demyelination—Parallel organization of white matter fibres forms the ground for diffusion anisotropy and myelin modulates the degree of anisotropy [52]. Any

disease process causing dysmyelination or demyelination will cause increased radial diffusivity and decrease in anisotropy. This has been particularly seen in relapsing-remitting multiple sclerosis, periventricular frontal white matter in early Alzheimer's disease, in periventricular white matter in hydrocephalus, in extratemporal white matter in temporal lobe epilepsy, in genu of corpus callosum in cocaine addicts and in the corpus callosum of patients with autism [53–58].

9.3.9 Functional MRI (fMRI)

fMRI as a technique is used to obtain functional imaging by visualizing alterations in blood flow in cerebral cortex in response to stimuli or actions (Fig. 9.8).

In this technique, the patient is instructed to perform a particular task. In response to the task, there is an increase in regional cortical activity which increases the oxygen requirement of the activated cortex leading to drop in oxyhaemoglobin concentration and an increase in deoxyhaemoglobin concentration. Following a delay of 2–6 s, there is an increase in cerebral blood flow (CBF) thus washing away deoxyhaemoglobin. This rebound in tissue oxygenation is measured [59, 60].

fMRI utilizes the difference in paramagnetic properties of oxyhaemoglobin and deoxyhaemoglobin. Deoxygenated haemoglobin is basically paramagnetic causing

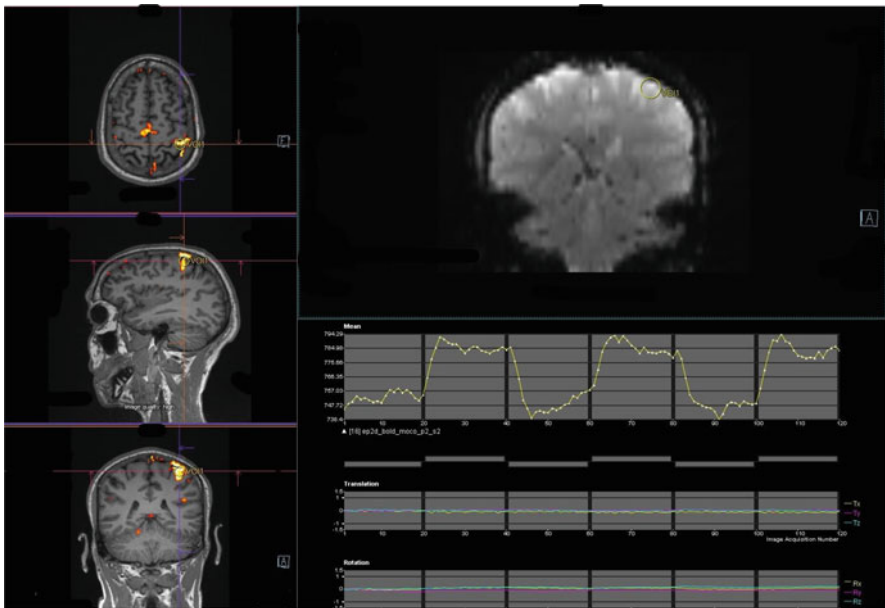


Fig. 9.8 Functional MRI showing activation of corresponding motor cortex with movement of right index finger

local dephasing of protons and thus reducing the signal returned from surrounding tissues. Heavy T_2^* weighted sequences are used for imaging in fMRI.

This imaging technique is used to look for the extent of involvement of eloquent areas (such as those involved in speech or motor function) by the tumour for presurgical planning.

9.4 Conclusion

Today MRI is not just limited to providing the anatomical details. Advanced MRI sequences also enable us to evaluate the metabolic and functional status of tissues at molecular level in a non-invasive manner. Use of advanced MRI techniques forms an essential component of diagnostic algorithm of neurological diseases both for diagnosis and assessment of response to treatment before anatomical changes set in.

Declaration All the figures described in the text have been obtained by the authors at their institute.

References

1. Bakshi R, Ariyaratana S, Benedict RHB, Jacobs L (2001) Fluid-attenuated inversion recovery magnetic resonance imaging detects cortical and juxtacortical multiple sclerosis lesions. *Arch Neurol* 58:742–748
2. Okuda T, Korogi Y, Ikushima I, Murakami R, Nakashima K, Yasunaga T, Kondo Y, Takahashi M (2014) Use of fluid-attenuated inversion recovery (FLAIR) pulse sequences in perinatal hypoxic-ischaemic encephalopathy. *Br J Radiol* 71:282–290. <https://doi.org/10.1259/bjr718439616237>
3. Bangerter NK, Hargreaves BA, Gold GE, Stucker DT, Nishimura DG (2006) Fluid-attenuated inversion-recovery SSFP imaging. *J Magn Reson Imaging* 24:1426–1431
4. Vaswani AK, Nizamani WM, Ali M, Aneel G, Shahani BK, Hussain S (2014) Diagnostic accuracy of contrast-enhanced FLAIR magnetic resonance imaging in diagnosis of meningitis correlated with CSF analysis. *ISRN Radiol* 2014:1–7
5. Moritani T, Ekholm S, Westesson PL (2009) Diffusion-weighted MR imaging of the brain, 2nd edn. Springer, New York, pp 1–401
6. Neurology | Handbook of Neurosurgery. <https://www.thieme.com/books-main/neurology/product/5411-handbook-of-neurosurgery>. Accessed 27 Sept 2021
7. Diffusion MRI: theory, methods, and applications—Oxford medicine. <https://oxfordmedicine.com/view/10.1093/med/9780195369779.001.0001/med-9780195369779>. Accessed 27 Sept 2021
8. Cha S (2006) Update on brain tumor imaging: from anatomy to physiology. *Am J Neuroradiol* 27:475–487. <http://www.ajnr.org/content/27/3/475>. Accessed 27 Sept 2021
9. Tong KA, Ashwal S, Obenaus A, Nickerson JP, Kido D, Haacke EM (2008) Susceptibility-weighted MR imaging: a review of clinical applications in children. *Am J Neuroradiol* 29:9–17
10. Haacke EM, Mittal S, Wu Z, Neelavalli J, Cheng Y-CN (2009) Susceptibility-weighted imaging: technical aspects and clinical applications, part 1. *Am J Neuroradiol* 30:19–30
11. Tong KA, Ashwal S, Holshouser BA, Nickerson JP, Wall CJ, Shutter LA, Osterdock RJ, Haacke EM, Kido D (2004) Diffuse axonal injury in children: clinical correlation with hemorrhagic lesions. *Ann Neurol* 56:36–50

12. Santhosh K, Kesavadas C, Thomas B, Gupta AK, Thamburaj K, Kapilamoorthy TR (2009) Susceptibility weighted imaging: a new tool in magnetic resonance imaging of stroke. *Clin Radiol* 64:74–83
13. Rosen BR, Belliveau JW, Chien D (1989) Perfusion imaging by nuclear magnetic resonance. *Magn Reson Q* 5:263–281
14. Essig M, Shiroishi MS, Nguyen TB et al (2013) Perfusion MRI: the five Most frequently asked technical questions. *Am J Roentgenol* 200:24–34. <https://doi.org/10.2214/AJR129543>
15. Petrella JR, Provenzale JM (2000) MR perfusion imaging of the brain: techniques and applications. *AJR Am J Roentgenol* 175:207–219
16. Petcharunpaisan S, Ramalho J, Castillo M (2010) Arterial spin labeling in neuroimaging. *World J Radiol* 2:384–398. <http://www.wjngnet.com/>
17. Sorensen AG, Buonanno FS, Gonzalez RG et al (1996) Hyperacute stroke: evaluation with combined multisection diffusion-weighted and hemodynamically weighted echo-planar MR imaging. *Radiology* 199:391–401. <https://doi.org/10.1148/radiology19928668784>
18. Sorensen AG, Copen WA, Østergaard L, Buonanno FS, Gonzalez RG, Rordorf G, Rosen BR, Schwamm LH, Weisskoff RM, Koroshetz WJ (1999) Hyperacute stroke: simultaneous measurement of relative cerebral blood volume, relative cerebral blood flow, and mean tissue transit time. *Radiology* 210:519–527. <https://doi.org/10.1148/radiology2102.r99fe06519>
19. Mattay VS, Frank JA, Duyn JH et al (1996) Three-dimensional “BURST” functional magnetic resonance imaging: initial clinical applications. *Acad Radiol* 3:S379–S383
20. Harris GJ, Lewis RF, Satlin A, English CD, Scott TM, Yurgelun-Todd DA, Renshaw PF (1998) Dynamic susceptibility contrast MR imaging of regional cerebral blood volume in Alzheimer disease: a promising alternative to nuclear medicine. *Am J Neuroradiol* 19(9):1727–1732
21. Simmons MLL, Frondoza CGG, Coyle JTT (1991) Immunocytochemical localization of N-acetyl-aspartate with monoclonal antibodies. *Neuroscience* 45:37–45
22. Reddy N, Calloni SF, Vernon HJ, Boltshauser E, Huisman TAGM, Soares BP (2018) Neuroimaging findings of organic acidemias and aminoacidopathies. *Radiographics* 38:912–931. <https://doi.org/10.1148/rg.2018170042>
23. Davie CA, Barker GJ, Tofts PS, Hawkins CP, Brennan A, Miller DH, McDonald WI (1993) Detection of myelin breakdown products by proton magnetic resonance spectroscopy. *Lancet* 341:630–631
24. Kreis R, Ross BD, Farrow NA, Ackerman Z (1992) Metabolic disorders of the brain in chronic hepatic encephalopathy detected with H-1 MR spectroscopy. *Radiology* 182:19–27. <https://doi.org/10.1148/radiology18211345760>
25. Penrice J, Cady EB, Lorek A, Wylezinska M, Amess PN, Aldridge RF, Stewart A, Wyatt JS, Reynolds EOR (1996) Proton magnetic resonance spectroscopy of the brain in normal preterm and term infants, and early changes after perinatal hypoxia-ischemia. *Pediatr Res* 40(40):6–14
26. Barker PB, Gillard JH, van Zijl PC, Soher BJ, Hanley DF, Agildere AM, Oppenheimer SM, Bryan RN (1994) Acute stroke: evaluation with serial proton MR spectroscopic imaging. *Radiology* 192:723–732. <https://doi.org/10.1148/radiology19238058940>
27. Petroff OAC, Graham GD, Blamire AM, Al-Rayess M, Rothman DL, Fayad PB, Brass LM, Shulman RG, Prichard JW (1992) Spectroscopic imaging of stroke in humans. *Neurology* 42:1349–1349
28. Alger JR, Frank JA, Bizzi A, Fulham MJ, DeSouza BX, Duhaney MO, Inscow SW, Black JL, van Zijl PC, Moonen CT (1990) Metabolism of human gliomas: assessment with H-1 MR spectroscopy and F-18 fluorodeoxyglucose PET. *Radiology* 177:633–641. <https://doi.org/10.1148/radiology17732243962>
29. Lin DDM, Crawford TO, Barker PB, Morgan RH, Lin DM, Hopkins J (2003) Proton MR spectroscopy in the diagnostic evaluation of suspected mitochondrial disease. *AJNR Am J Neuroradiol* 24:33–41
30. Matthews PM, Andermann F, Silver K, Karpati G, Arnold DL (1993) Proton MR spectroscopic characterization of differences in regional brain metabolic abnormalities in mitochondrial encephalomyopathies. *Neurology* 43:2484–2484

31. Ross B, Michaelis T (1994) Clinical applications of magnetic resonance spectroscopy. *Magn Reson Q* 10:191–247
32. Shonk TK, Moats RA, Gifford P, Michaelis T, Mandigo JC, Izumi J, Ross BD (1995) Probable Alzheimer disease: diagnosis with proton MR spectroscopy. *Radiology* 195:65–72. <https://doi.org/10.1148/radiology19517892497>
33. Kruse B, Hanefeld F, Christen HJ, Bruhn H, Michaelis T, Hänicke W, Frahm J (1993) Alterations of brain metabolites in metachromatic leukodystrophy as detected by localized proton magnetic resonance spectroscopy in vivo. *J Neurol* 241:68–74
34. Magistretti PJ, Pellerin L, Rothman DL, Shulman RG (1999) Energy on demand. *Science* 283:496–497
35. Srinivasan R, Sailasuta N, Hurd R, Nelson S, Pelletier D (2005) Evidence of elevated glutamate in multiple sclerosis using magnetic resonance spectroscopy at 3 T. *Brain* 128:1016–1025
36. Kreis R, Pfenninger J, Herschkowitz N, Boesch C (1995) In vivo proton magnetic resonance spectroscopy in a case of Reye’s syndrome. *Intensive Care Med* 21:266–269
37. Basser PJ, Mattiello J, LeBihan D (1994) Estimation of the effective self-diffusion tensor from the NMR spin echo. *J Magn Reson B* 103:247–254
38. Basser PJ, Mattiello J, LeBihan D (1994) MR diffusion tensor spectroscopy and imaging. *Biophys J* 66:259–267
39. Alexander AL, Eun Lee J, Lazar M, Field AS (2007) Diffusion tensor imaging of the brain. *Neurotherapeutics* 4:316–329
40. Mori S, Kaufmann WE, Davatzikos C et al (2002) Imaging cortical association tracts in the human brain using diffusion-tensor-based axonal tracking. *Magn Reson Med* 47:215–223
41. Catani M, Howard RJ, Pajevic S, Jones DK (2002) Virtual in vivo interactive dissection of white matter fasciculi in the human brain. *NeuroImage* 17:77–94
42. Stieltjes B, Kaufmann WE, van Zijl PCM, Fredericksen K, Pearlson GD, Solaiyappan M, Mori S (2001) Diffusion tensor imaging and axonal tracking in the human brainstem. *NeuroImage* 14:723–735
43. Wakana S, Jiang H, Nagae-Poetscher LM, van Zijl PCM, Mori S (2004) Fiber tract-based atlas of human white matter anatomy. *Radiology* 230:77–87. <https://doi.org/10.1148/radiol2301021640>
44. Jellison BJ, Field AS, Medow J, Lazar M, Salamat MS, Alexander AL (2004) Diffusion tensor imaging of cerebral white matter: a pictorial review of physics, fiber tract anatomy, and tumor imaging patterns. *Am J Neuroradiol* 25:356–369
45. Witwer BP, Mofhtakhar R, Hasan KM et al (2002) Diffusion-tensor imaging of white matter tracts in patients with cerebral neoplasm. *J Neurosurg* 97:568–575
46. Lazar M, Alexander AL, Thottakara PJ, Badie B, Field AS (2006) White matter reorganization after surgical resection of brain tumors and vascular malformations. *Am J Neuroradiol* 27:1258–1271
47. Laundre BJ, Jellison BJ, Badie B, Alexander AL, Field AS (2005) Diffusion tensor imaging of the corticospinal tract before and after mass resection as correlated with clinical motor findings: preliminary data. *Am J Neuroradiol* 26:791–796
48. Van Gelderen P, de Vleeschouwer MH, DesPres D, Pekar J, van Zijl PC, Moonen CT (1994) Water diffusion and acute stroke. *Magn Reson Med* 31:154–163
49. Liu Y, D’Arceuil HE, Westmoreland S, He J, Duggan M, Gonzalez RG, Pryor J, de Crespigny AJ (2007) Serial diffusion tensor MRI after transient and permanent cerebral ischemia in nonhuman primates. *Stroke* 38:138–145
50. Sorensen AG, Wu O, Copen WA, Davis TL, Gonzalez RG, Koroshetz WJ, Reese TG, Rosen BR, Wedeen VJ, Weisskoff RM (1999) Human acute cerebral ischemia: detection of changes in water diffusion anisotropy by using MR imaging. *Radiology* 212:785–792. <https://doi.org/10.1148/radiology2123.r99se24785>
51. Yang Q, Tress BM, Barber PA, Desmond PM, Darby DG, Gerraty RP, Li T, Davis SM (1999) Serial study of apparent diffusion coefficient and anisotropy in patients with acute stroke. *Stroke* 30:2382–2390

52. Beaulieu C, Allen PS (1994) Determinants of anisotropic water diffusion in nerves. *Magn Reson Med* 31:394–400
53. Henry RG, Oh J, Nelson SJ, Pelletier D (2003) Directional diffusion in relapsing-remitting multiple sclerosis: a possible in vivo signature of Wallerian degeneration. *J Magn Reson Imaging* 18:420–426
54. Choi SJ, Lim KO, Monteiro I, Reisberg B (2016) Diffusion tensor imaging of frontal white matter microstructure in early Alzheimer's disease: a preliminary study. *J Geriatr Psychiatry Neurol* 18:12–19. <https://doi.org/10.1177/0891988704271763>
55. Assaf Y, Ben-Sira L, Constantini S, Chang LC, Beni-Adani L (2006) Diffusion tensor imaging in hydrocephalus: initial experience. *AJNR Am J Neuroradiol* 27:1717
56. Gross DW, Concha L, Beaulieu C (2006) Extratemporal white matter abnormalities in mesial temporal lobe epilepsy demonstrated with diffusion tensor imaging. *Epilepsia* 47:1360–1363
57. Moeller FG, Hasan KM, Steinberg JL, Kramer LA, Valdes I, Lai LY, Swann AC, Narayana PA (2007) Diffusion tensor imaging eigenvalues: preliminary evidence for altered myelin in cocaine dependence. *Psychiatry Res Neuroimaging* 154:253–258
58. Alexander AL, Lee JE et al (2006) Diffusion tensor imaging of the corpus callosum in autism. *NeuroImage* 34:61–73. <https://doi.org/10.1016/j.neuroimage.2006.08.032>
59. Moonen CTW, Chrit TW, Bandettini PA, Peter A, Aguirre GK, Geoffrey K (1999) *Functional MRI*. Springer, Berlin, p 575
60. Stippich C (2015) *Clinical functional MRI: presurgical functional neuroimaging*. Springer, Berlin, p 351



Yan Peng, Chenjun Shi, Yury V. Kistenev, Denis A. Vrazhnov,
and Olga P. Cherkasova

Abstract

Methods of the indirect imaging of cancers are based on the control of molecular biomarkers in tissue associated with cancer-specific variations from proteomic, genomic, and metabolomic aspects. Basic knowledge about current techniques for indirect cancer imaging is presented in this chapter.

Keywords

Immunohistochemistry · Flow cytometry · Enzyme-linked immunosorbent assay · Next-generation sequencing · Atomic force microscopy · Nuclear magnetic resonance · Chromatography · Mass Spectrometry

10.1 Introduction

In the last part, we have introduced direct imaging methods. These methods can identify different tissue samples and effectively differentiate cancerous tissues. However, besides the effective spatial division of the cancerous area, during cancer

Y. Peng · C. Shi

University of Shanghai for Science and Technology, Shanghai, China

Y. V. Kistenev · D. A. Vrazhnov

Tomsk State University, Tomsk, Russia

O. P. Cherkasova (✉)

Institute for Problems of Laser and Information Technologies of the Russian Academy of Sciences, Branch of Federal Scientific Research Center “Crystallography and Photonics” of the RAS, Shatura, Russia

Institute of Laser Physics of the Siberian Branch of the Russian Academy of Sciences, Novosibirsk, Russia

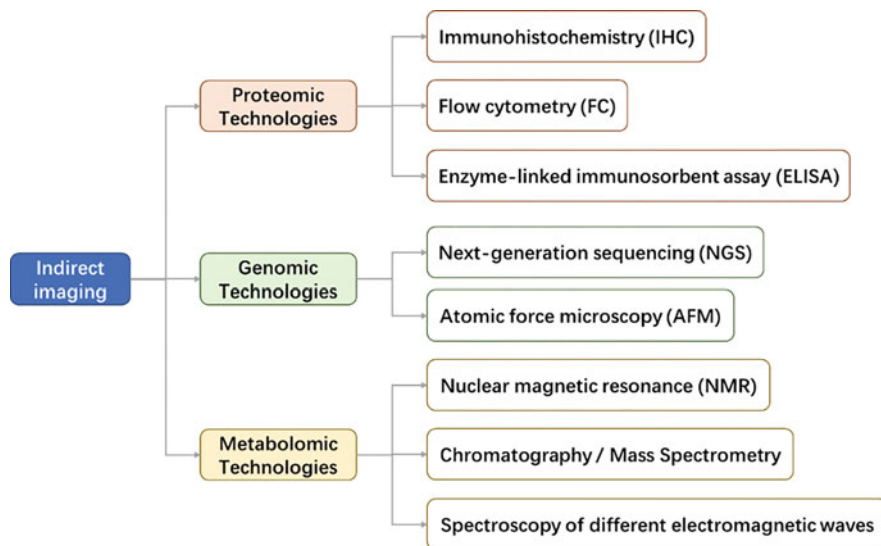


Fig. 10.1 Current technologies for indirect imaging of cancer biomarkers

research or diagnosis/treatment, sometimes other information needs to be focused on, such as cancer biomarkers. The research on cancer biomarkers helps to study the interactions between proteins, gene expression, pharmacokinetics in the treatment process, etc. This information is helpful for cancer diagnosis, treatment, and prognosis. Direct imaging cannot provide information on tissue samples such as biomarkers expression. Therefore, indirect imaging methods are proposed for identifying these biomarkers.

Targeting identification of different kinds of biomarkers, currently, there are three kinds of technologies, as shown in Fig. 10.1, namely Genomic Technologies, Proteomic Technologies, and Metabolomic Technologies [1]. Genomic technologies explore the differences in overall or gene fragment expression in DNA sequences between tumor cells and normal cells and use next-generation sequencing (NGS) technologies. Proteomic technologies study the specific protein expression in cancer, and the commonly used methods are immunohistochemistry (IHC), enzyme-linked immunosorbent assay (ELISA), flow cytometry (FC), etc. Metabolomic technologies recognize and diagnose cancer by studying the metabolites of cancer cells. The main methods are nuclear magnetic resonance, chromatography/mass spectrometry, and spectroscopy. In addition, another popular technology: atomic force microscopy, is currently reported to realize the detection of DNA mutations in cancer tissues.

In this part, we will introduce indirect imaging techniques targeting cancer biomarkers, their basic principles, and their pros and cons.

10.2 Immunohistochemistry (IHC)

IHC utilizes monoclonal and polyclonal antibodies to detect specific antigens in tissue sections, widely used to diagnose cancers [2]. Using the staining method combined with IHC reaction, tissue imaging with biomarker distribution can be realized, thereby recognizing a specific cancerous area [3].

The conventional method of Hematoxylin and eosin (H&E) stain can label the nucleus of each cell in the tissue so that the cancer area can be identified by the distribution of cells (cells distribute more densely in the cancerous area). The limitation of this approach is that the stain label is the same for any cell, and therefore it cannot distinguish different cancers. For IHC stain, due to its feature of antibody reaction, it can label the specific cells, so that particular target imaging antigens can be realized. Reference [4] describes a method to analyze biomarkers in tumor neurospheres (NS) produced from glioma tissue of patients and animals (see Fig. 10.2). Embedding the NS in paraffin blocks was used. This technology makes it possible to store samples for a long time and preserves the 3D structure of tumor tissues.

Based on the specific response of antibodies to cancer markers, these works based on IHC have achieved an accurate division of cancerous tissue regions with high specificity. However, IHC lacks an effective quantitative analysis method, so it can only perform tissue imaging but cannot provide a quantitative analysis of biomarkers.

10.3 Flow Cytometry

Flow cytometry (FC) is the technology used for counting a population of cells. These cells are labeled with fluorescent markers and then injected into the instrument. The channels were designed ideally to pass a single cell each time to be counted through

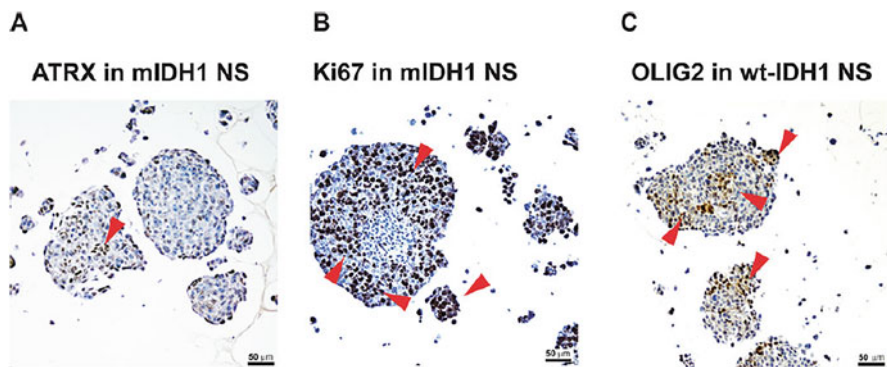


Fig. 10.2 The immunohistochemistry of paraffin-embedded glioma NS stained for biomarker: (a) ATRX; (b) Ki67; (c) OLIG2. The positive cells are pointed by red arrows. (Cited from Ref. [4])

the fluorescent markers. This technique can be combined with antibodies to quantify specific cancer cells/proteins in cancer diagnosis. Application of FC for prognosis in patients with neuroblastoma and medulloblastoma are presented in [5]. Detection of synaptic proteins in microglia by FC under homeostasis and in various mouse models of brain disease is demonstrated in [6]. FC has a high specificity and can confirm lymphoma diagnosis in brain biopsies significantly faster than immunohistochemistry [7]. The multicolor FC was used to measure the surface markers of glioblastoma stem-like cells CD133, CD44, CD15, CD36, and ITGA6. Glioblastoma patients with an enrichment of the molecular signature CD44+/CD133+/ITGA6+/CD36+ had a significantly worse survival outcome [8].

FC can provide a high-throughput rapid analysis to distinguish and count cancer cells from normal cells, which is of great value for cancer early diagnosis and prognosis. However, limitations are that the machines are costly, and the training needed to use them properly is extensive [9].

10.4 Enzyme-Linked Immunosorbent Assay (ELISA)

ELISA is also a technology based on the reaction of antibodies and antigens. In ELISA, the antibody is also bonded with an enzyme, and the enzymatic substrate is used to estimate the quantity of the antigen in a sample. This process is demonstrated in Fig. 10.3.

ELISA is now a mature technology used for cancer detection. Many commercial ELISA kits target various cancer markers, including Alpha-fetoprotein (AFP), β -2microglobulin (B2M), CA15-3, CA19-9, etc. These ELISA kits can be used to screen and early detect cancer, the prognosis for cancers or effectiveness of the treatment, and detect recurrent cancer.

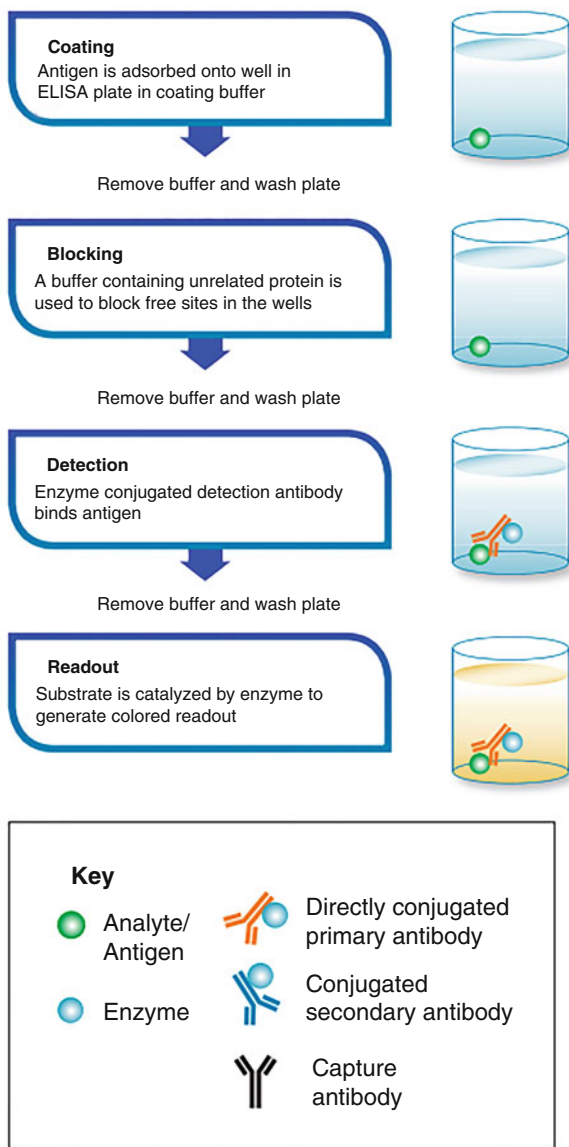
It has been shown that the determination of some proteins by ELISA, such as Vascular Endothelial Growth Factor and angiogenesis-associated proteins, matrix metalloproteinases, and extracellular matrix proteins, is helpful for the diagnosis and prognosis of glioma, especially with unclear biopsy results [11].

Overall, ELISA has a simple processing, high specificity, and high sensitivity. The limitations are high cost for labeling and antibody design, short storage time because of the protein inside the ELISA, and false results associated with possible cross-reactions [12].

10.5 Next-Generation Sequencing (NGS)

Cancer is often caused by somatic mutations [13]; therefore, genomic technology can diagnose early cancer. NGS is a method of simultaneously sequencing millions of DNA (or complementary DNA) fragments. NGS represents various sequencing techniques with different ways to realize. Still, the basic principle is the same: breaking the gene into random fragments, and then other platforms use different analysis methods for reconstruction and sequencing. Compared with the traditional

Fig. 10.3 The specific process of ELISA. (Cited from Ref. [10])



Sanger sequencing using capillary electrophoresis, the massively parallel sequencing of NGS has dramatically improved the efficiency and cost, so it has been used in clinical laboratories to test various tumor mutations [14].

In the current research, the oncogenes of different cancers have been discovered through NGS. Here we enumerated the related research works, as shown in Table 10.1. These works demonstrate the promise of NGS technology in cancer research:

Table 10.1 Cancer research works based on NGS

Samples	Targets	Results	Reference
121 glioma biopsy samples	Glioma-tailored 20-gene panel	The targeted NGS panel allows gliomas classification	[18]
106 glioma patients (grade II: 19 cases, grade III: 23 cases, grade IV: 64 cases)	Glioma-tailored 48-gene NGS panel	NGS panel for detecting 1p/19q codeletion and gene mutations on a single platform was created for molecular classifications of glioblastomas	[19]
126 paraffin-embedded glioma tissues	The ion AmpliSeq, a custom primer panel including 468 amplicons covering the crucial genes, was used.	NGS technologies provide more accurate diagnosis and classification of glioma	[20]

1. For some cancers that have DNA mutations at an early stage, this technology is expected to achieve cancer early diagnosis.
2. In the process of targeted therapy with mutation inhibitors, NGS can monitor the effectiveness of the treatment.

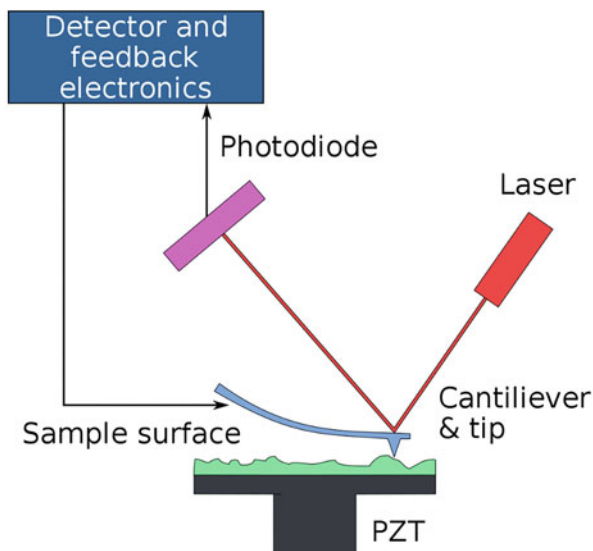
NGS technology enables efficient and accurate detection of new and rare somatic mutations, discovers many novel genetic aberrations and related potential therapeutic targets, therefore has the advantage of designing personalized cancer treatment based on the test results [15]. But for current NGS platforms, some limitations also exist. For example, the mutation discovered could result from technical variations (different sequencing methods) instead of tumor heterogeneity [16]. Also, gene mutations found in cancer may be caused by other non-cancer factors, such as a normal phenotype of aging [17]. These factors can lead to misdiagnosis of cancer and have a severe impact.

10.6 Atomic Force Microscopy

Atomic force microscopy (AFM) can scan samples with nanometer resolution. It is more than 1000 times better than the optical diffraction limit. The AFM consists of a cantilever with a tip as the probe, which is used for scanning the samples (see Fig. 10.4). When the tip is scanning a sample surface, it exhibits a force between the tip and the sample, deflecting the cantilever. This force can be attributed to molecular forces such as van der Waals forces and chemical bonding. The photodiode receives the light reflected by the cantilever, which amplifies the change of the cantilever's bending caused by force. Therefore, AFM has the ability of molecular identification.

Currently, AFM is mainly used as direct imaging: the structural difference such as density or elasticity between cancer cells and normal cells will lead to different intensities of mechanical force between tips and cells. But based on the molecular

Fig. 10.4 The scheme of an AFM. (Cited from OverlordQ at the Wikipedia project)



identification ability and high-resolution imaging ability, AFM can also be used for the indirect detection of cancers. For example, the tip can be combined with different aptamers to realize genomic identification. A hybrid binding domain-tethered tip designed by Koo et al. exhibits special forces to realize miRNAs, whose expression level will be altered in pathological conditions, including cancer [21]. Apart from genomic changes, AFM can also detect cancer-associated proteins when the tip is combined with a specific antibody, and the protein will interact with the tip targetly [22]. On the other side, AFM can be combined with different electromagnetic spectroscopies such as infrared spectroscopy to identify different biomarker molecules based on the resonance between tips and molecular vibration/rotation modes.

Overall, AFM advantages are 3D imaging, non-destructive, nanometer-scale resolution, and high specificity in cancer research. But currently, some limitations hinder its application for actual usage: time-consuming; tip can be damaged if sample's thickness changes significantly at different points; water in tissue samples affects the final signal, causing a noise.

10.7 Nuclear Magnetic Resonance (NMR)

Many cancers are associated with specific metabolites, and these small molecules can also be used as cancer biomarkers. The analysis of metabolites in clinics is often performed using nuclear magnetic resonance spectroscopy (NMR spectroscopy). NMR spectroscopy is sensitive to molecules' chemical shifts, reflecting the atomic groups' composition within the molecule. Figure 10.5 shows the current routine cancer analysis process based on NMR spectroscopy, including sample collection, data analysis, pattern recognition, and verification [23].

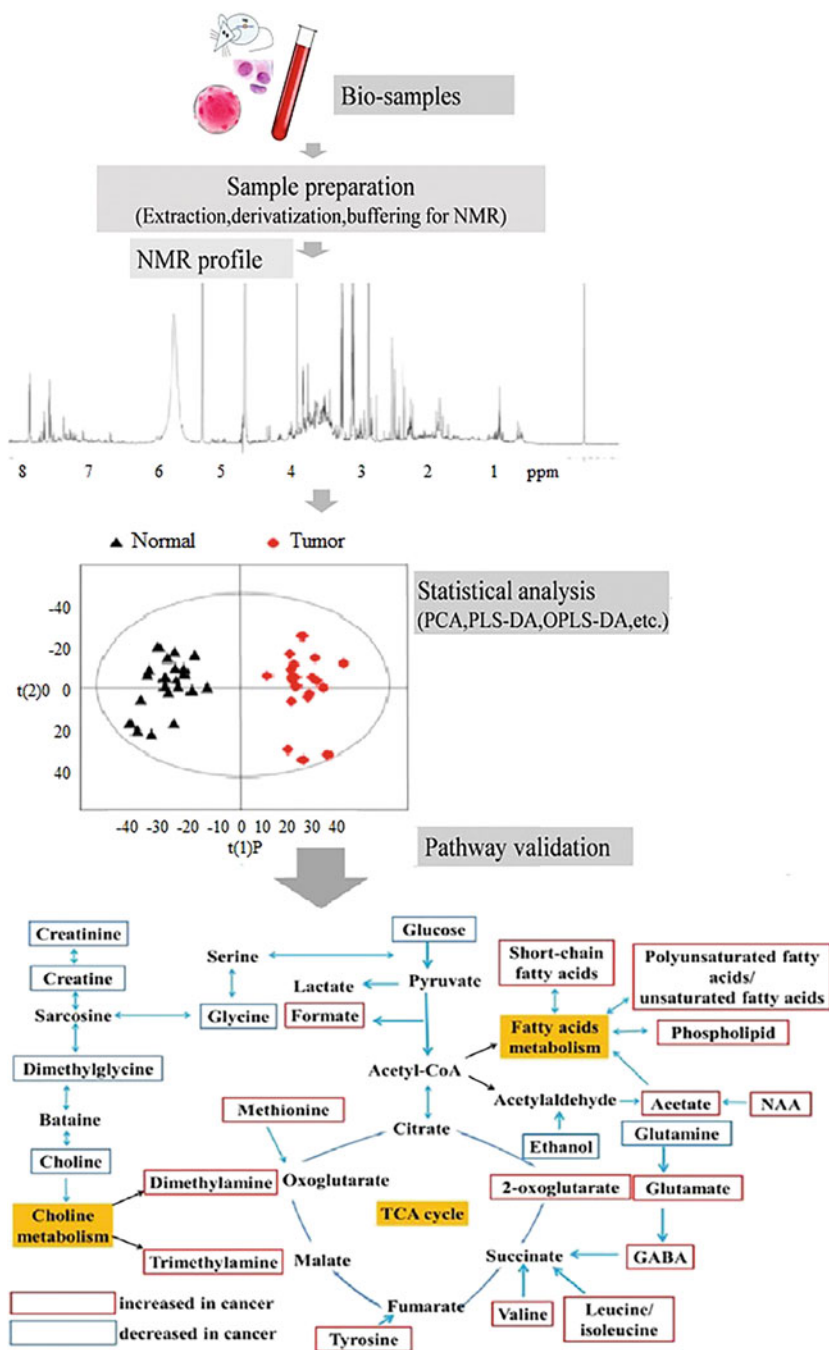


Fig. 10.5 Tumor metabolism studies by NMR spectroscopy. (Cited from Ref. [23])

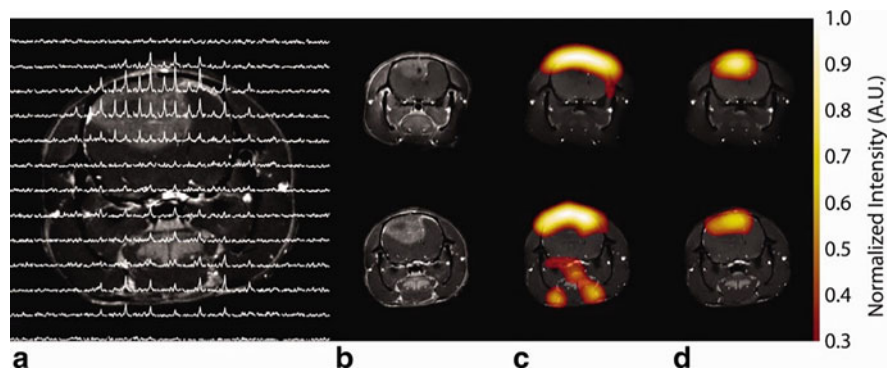


Fig. 10.6 ^{13}C chemical shift images (a) of the brain in a C6 glioma-bearing rat before (top) and 96 h after radiotherapy (bottom); T1-weighted proton images (b); pyruvate (c); lactate (d). (Cited from Ref. [24])

Detection of cancer biomarkers in body fluids is vital for non-invasive diagnostics. NMR was used to measure the profile of metabolites in 60 plasma samples from patients with glioma [24]. For comparison, the blood plasma of 28 healthy volunteers was measured. The authors concluded that the following metabolic pathways are disrupted in glioma: taurine/hypotaurine, D-glutamine/D-glutamate, alanine/aspartate/glutamate, glycine/serine/threonine, and pyruvate metabolism [25]. Plasma levels of tyrosine and phenylalanine were elevated in glioblastoma.

Some researchers have also tried to perform *in vivo* studies based on NMR. Figure 10.6 shows the changes in the treatment of brain tumors injected with pyruvate by Day et al. It was found that the tumor lactate signal was diminished after treatment [26].

NMR studies in glioma patients showed that the level of 2-hydroxyglutarate (2HG), currently recognized glioma biomarkers, is increased with tumor progression and falls in response to therapy [27, 28]. It was shown that detection of 2HG and glutamate by NMR spectroscopy resulted in the diagnosis of IDH1 mutant glioma with a sensitivity of 72% and specificity of 96% [29]. NMR spectroscopy makes it possible to determine the degree of glioma malignancy by the ratio of several metabolites. A relatively high concentration of *N*-acetyl aspartate (NAA), low levels of choline (Cho), and the absence of lactate (Lac) and lipids have been shown to be characteristic of low-grade glioma. With the progression of tumor growth, there is a decrease in the level of NAA and myo-inositol and an increase of Cho, Lac, and lipids [30]. While the Cho/NAA ratio quantitatively correlated with the percentage of tumor infiltration in biopsy samples [31]. The same ratio made it possible to detect proliferative remnants of glioma in the resection margin [31].

Therefore, detailed molecular information provided by NMR spectroscopy allows the comprehensive studies of cancer metabolites. The drawbacks are:

1. Body water limits the detection sensitivity of metabolites contained in tissues in submillimolar and to a large extent of micromolar concentration [32].
2. The measurements are conducted in a high magnetic field, and ferromagnetic objects should be removed from a test environment.

3. The usage of enhancer during the biopsy will remain in the body, which may be harmful.
4. The complexity of NMR equipment limits real-time imaging during surgery.

10.8 Chromatography/Mass Spectrometry

Chromatography is a laboratory technique for mixture components separation. The chromatography has different chromatographic columns, which serve as the channel to let fluid pass through. The columns were specially designed so that different molecules have different affinities to the columns. They pass through the column at different speeds, and the mixture is separated into individual components. The chromatography can be divided into liquid and gas chromatography.

Mass spectrometry is a method for studying the composition of samples, which is based on the ionization of components and the measurement of the ratio of the charge of ions to their mass for quantitative determination. It consists of an ion source, a mass analyzer, and a detector. The ion source provides electron beams that can ionize the test sample. According to their mass-to-charge ratio, the mass analyzer separates the ions (fragments from an ionized sample). Then the separated ions are identified by the detector (i.e., an electron multiplier). Detailed molecule information can be obtained by analyzing these ions.

These two techniques are usually combined as liquid/gas chromatography-mass spectrometry (GC-MS/LC-MS) in cancer research. Chromatography-mass spectrometry can detect a wide range of molecules, even those with the same molecular structures (such as enantiomers). Take gliomas as an example, the IDH1 and IDH2 mutations make cells metabolize 2-hydroxyglutarate (2HG), an enantiomer, and only D-2-hydroxyglutarate has a relation with the gliomas [33]. After a series of derivative processing, the 2HG in human brain tissues can be separated and identified through GC-MS, as shown in Fig. 10.7 [34]. The quantitative

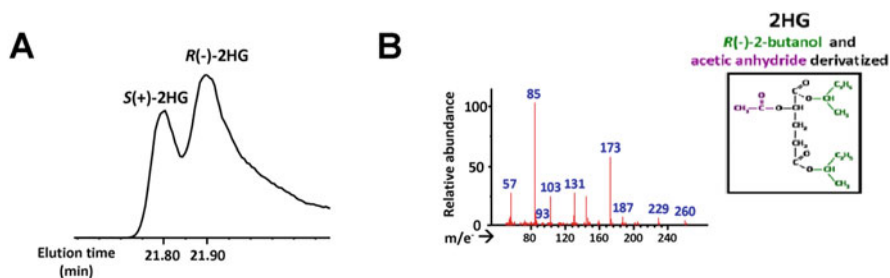


Fig. 10.7 GC separation of derivatized 2HG enantiomers isolated from cell lysates (a); the mass spectrum of substances having a retention time of 21.8 and 21.9 min. (b) It is identical to the mass spectrum of derivatized 2HG standard, the structural formula of which is shown in the inset on the right. (Cited from Ref. [34])

determination of enantiomers of 2HG in blood serum and cerebrospinal fluid using gas/liquid chromatography-tandem mass spectrometry was demonstrated in [35–37].

Liquid chromatography and ion spectra mass spectrometry (SWATH-MS) were used for proteomic analysis of blood plasma and brain tissues of 14 glioblastoma patients. It has been shown that tumor size is significantly positively correlated with the concentration of a number of proteins in the blood, namely C-reactive protein, alpha-2-glycoprotein, and C9 complement component [38].

Urinary biomarkers of glioma have been detected using LC-MS/MS analysis [39–41]. It was identified 27 urinary proteins whose concentration changed after surgery to remove the tumor. Six proteins provided the best accuracy in diagnosing glioma, namely alpha-2-glycoprotein and alpha-1-antichymotrypsin, galectin-1 and calreticulin, malate dehydrogenase, and thrombospondin-4.

Blood plasma from patients with glioma was analyzed by LC-QQQ-MS [42]. Five important metabolites were obtained, the concentrations of which differed significantly between samples of low- and high-grade gliomas. These include uracil, lactate, cystamine, arginine, and ornithine. The most significant changes were observed in the metabolic pathways associated with the development of glioma, namely the metabolism of amino acids, nucleotides, and carbohydrates [43, 44]. When studying the blood plasma of 159 patients with glioblastoma, it was shown that high levels of arginine and methionine in the blood of patients are associated with the increased probability of 2-year overall survival. The metabolite kynurenate was reduced that chance [45].

Blood serum and tumor tissues from glioma patients were analyzed using GC-time of flight mass spectrometry to differentiate glioma grades [46]. Tissue samples from glioblastoma multiforms (GBMs) patients have higher phenylalanine levels compared to oligodendrogliomas. On the contrary, concentrations of 2-hydroxyglutaric acid, 4-aminobutyric acid, creatinine, ribitol, and myo-inositol were increased in oligodendrogliomas compared to GBM. It was demonstrated serum cysteine concentration was higher in GBMs. Serum lysine and 2-oxoisocaproic acid concentration were higher in oligodendrogliomas [46]. It has been shown that radiation treatment at GBMs decreased the concentration of several metabolites in the blood serum [47].

The excellent separation ability of the chromatography ensures that there are almost no interfering substances during the measurement, and combined with mass spectrometry, it can achieve the detection limit in nanogram order. Such high sensitivity makes chromatography-mass spectrometry an effective tool in analyzing cancer metabolites. However, this technique is mainly used in research rather than clinical diagnosis because of three shortages:

1. A time-consuming analysis: the separation processing usually takes more than 30 min.
2. A requirement of a high-skill operator during the test because of the complicated processing protocol.
3. A specialized test process needs to be developed for purification and separation for different biomarkers, which takes time and costs.

10.9 Spectroscopy Using Electromagnetic Waves

Many molecules have vibration modes in the infrared band. Combined with the advantages of low photon energy (non-destructive), good penetration ability, and spectral fingerprinting ability, infrared spectroscopy can be used to identify these molecules. The infrared range can be divided into far-infrared ($10\text{--}400\text{ cm}^{-1}$), mid-infrared ($400\text{--}4000\text{ cm}^{-1}$), and near-infrared ($4000\text{--}12,800\text{ cm}^{-1}$). For example, the bending/stretching frequencies of chemical bonds of molecules are located in the mid-infrared band (see Table 10.2) [48]. The molar absorptivity in the near-IR region is quite small, resulting in poor sensitivity. Therefore, most studies in biomedical research based on infrared spectroscopy used mid-infrared spectroscopy.

Figure 10.8 demonstrates a mid-infrared spectrum of the human blood serum sample. By analyzing absorption peaks, we can recognize vibration modes of specific substances and identify biomarkers molecules. Bellisola et al. summarized the vibrational frequencies for some functional groups frequently seen within the infrared band, as listed in Table 10.2 [49]. While most cancer metabolites are small organic molecules with these functional groups, infrared spectroscopy can effectively identify these molecules.

Attenuated total reflectance Fourier-transform infrared (ATR-FTIR) spectroscopy of blood serum allows brain cancer diagnosis with 81.0% sensitivity and 80.0% specificity [50, 51]. It was demonstrated that ATR-FTIR spectroscopy combined with machine learning allows discriminating cancer patients from controls and differentiating specific tumor types [52, 53]. ATR-FTIR spectroscopy was established to identify both small and low-grade gliomas [54]. The serums of 177 patients with low-grade or high-grade glioma were measured by ATR-FTIR spectroscopy coupled with supervised learning methods and machine learning algorithms. Cancer patients with tiny tumor volumes (0.2 cm^3) were identified correctly with sensitivities and specificities better than 88%.

At a lower frequency of infrared band (below 600 cm^{-1}), there's a gap between infrared and microwave, namely the "terahertz gap" ($10^{11}\text{--}10^{13}\text{ Hz}$). Terahertz waves exhibit similar advantages to infrared waves: non-invasive and high-penetrative. Compared with infrared spectroscopy, THz spectroscopy detects the collective behavior of molecules [55, 56]. Therefore, THz spectroscopy can differentiate substances with different molecular structures and polymorph and chiral substances, even those with the same elements and molecular bonds. For example, terahertz spectroscopy can also identify the 2HG mentioned above in the GC-MS test. As shown in Fig. 10.9, Chen et al. test S-2HG (L-2HG) and R-2HG (D-2HG) and showed that they have different characteristic peaks [57]. However, because THz spectroscopy detects the collective behavior of molecules, we cannot infer the molecular structure of unknown substances from its terahertz spectrum—for different molecules, the same function group may have different frequencies.

For both infrared and terahertz spectroscopy, one limitation that hinders their applications in clinical usage is the influence of water existence, just like the NMR spectroscopy. The strong water signal covers the useful spectral information from target biomarkers, making these characteristic peaks hard to be recognized.

Table 10.2 A summary of the vibrational frequencies for some functional groups frequently seen within the infrared band

Wavenumber (cm ⁻¹)	Functional group	Vibrational mode	Typical component
3500–2500	X–H stretching vibrations (where X is C, O, or N)		
~3300	N–H	$\nu(\text{N–H})$	Amide A: peptide, protein
~3100	N–H	$\nu(\text{N–H})$	Amide B: peptide, protein
2957	C–CH ₃	$\nu_{\text{as}}(\text{CH}_3)$	
2920	–(CH ₂) _n –	$\nu_{\text{as}}(\text{CH}_2)$	
2872	C–CH ₃	$\nu_{\text{s}}(\text{CH}_3)$	Lipids
2851	–(CH ₂) _n –	$\nu_{\text{s}}(\text{CH}_2)$	
2000–1500	Fundamental stretching vibrations of double bonds (e.g., C=O, C=C, C=N)		
~1740	–CH ₂ –COOR	$\nu(\text{C=O})$	Phospholipid esters
~1655	O=C–N–H	80% $\nu(\text{CO})$, 20% $\nu(\text{CN})$	Amide I peptide, protein
~1645	H–O–H	$\gamma(\text{HOH})$	Water
~1545	O=C–N–H	60% $\nu(\text{N–H})$, 30% $\nu(\text{C–N})$, 10% $\nu(\text{C–C})$	Amide II peptide, protein
1500–600	The “fingerprinting region”: many overlapped vibrations		
~1450	–(CH ₃) _n –	$\delta_{\text{as}}(\text{CH}_3)$	Lipid, protein
	–(CH ₂) _n –	$\delta_{\text{as}}(\text{CH}_3)$	
~1395	–(CH ₃) _n –	$\delta_{\text{s}}(\text{CH}_3)$	Lipid, protein
	–(CH ₂) _n –	$\delta_{\text{s}}(\text{CH}_3)$	
	–O–C=O	$\nu(\text{C=O})$	
~1380	C–CH ₃	$\gamma_{\text{s}}(\text{CH}_3)$	Phospholipid, fatty acid, triglyceride
1400–1200	O=C–N–H, CH ₃	$\gamma(\text{N–H})$, $\nu(\text{C–N})$, $\gamma(\text{C=O})$, $\nu(\text{C–C})$ and $\nu(\text{CH}_3)$	Amide III peptide, protein, collagen
1245–1230	RO–PO ₂ [–] –OR	$\nu_{\text{as}}(\text{PO}_2^-)$	DNA, RNA, phospholipid, phosphorylated protein
~1170	R–COO–R'	$\nu_{\text{as}}(\text{C–O})$	Ester
1160–1120	C–O, C–O–H	$\nu(\text{C–O})$	RNA ribose
~1150		$\nu(\text{CO})$, $\gamma(\text{COH})$	Carbohydrates
~1095	RO–PO ₂ [–] –OR	$\nu_{\text{s}}(\text{PO}_2^-)$	DNA, RNA, phospholipid, phosphorylated protein
~1084			
~1070			
~1078	C–C	$\nu(\text{CC})$	Glycogen
~1060	C–O	$\nu(\text{CO})$	DNA and RNA ribose
~1050			
~1015			
~1050	C–O–P	$\nu(\text{COP})$	Phosphate ester

(continued)

Table 10.2 (continued)

Wavenumber (cm ⁻¹)	Functional group	Vibrational mode	Typical component
~1028	C–O–H	def(CHO)	Glycogen
~965	PO ₃ ²⁻	ν(PO ₃ ²⁻)	DNA and RNA ribose
~950	P–O	ν(PO ₃ ²⁻)	Phosphorylated protein
~920	C–O–P	ν(COP)	Phosphorylated protein

Abbreviation: ν, stretching; δ, bending; γ, wagging, twisting, and rocking; def, deformation; as, antisymmetric; s, symmetric

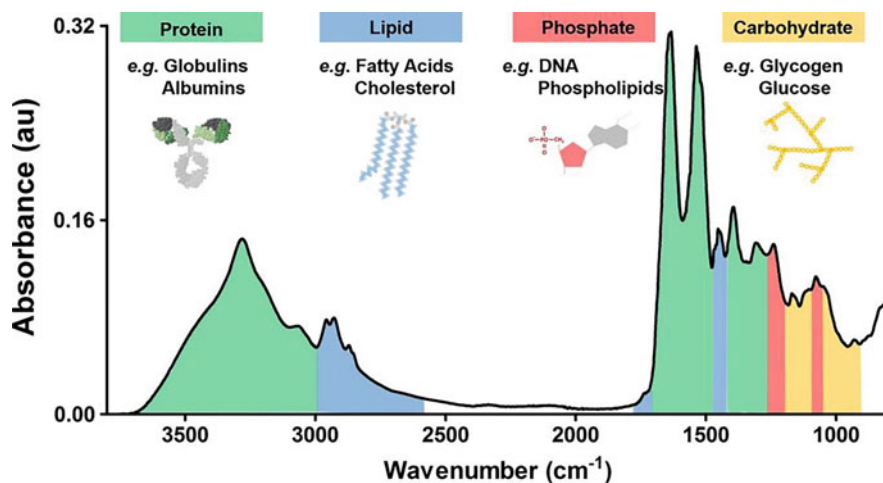


Fig. 10.8 ATR-FTIR spectrum of human blood serum. Spectral regions that correspond to known biomolecules are highlighted in color. (Cited from Ref. [50])

Raman spectroscopy is another technique used in cancer research. Raman spectroscopy profiles molecules' vibrational motion that arises from an inelastic scattering, even depending on nuclear vibrations, which change a molecule's polarizability as it vibrates/rotates [58]. The water signal from Raman spectroscopy is weak, and therefore the water won't be the problem during the Raman test for tissue samples.

Many molecular biomarkers can also be recognized by Raman spectroscopy, such as proteins, nucleic acids, lipids, and carbohydrates [59]. It allows differentiating cancerous tissues from normal tissues using the characteristics of cancer metabolisms by Raman spectroscopy.

Machine learning techniques can distinguish glioma tissues from normal brain tissues with high sensitivity, specificity, and accuracy [60]. Visible resonance Raman spectroscopy was used to identify glioma margins and grades. The vibrational band assigned to carotenoids, tryptophan, amide I–amide III, and lipids are observed in the Raman spectra (see Fig. 10.10).

The limitation of Raman spectroscopy is that the weak Raman signal leads to low sensitivity and long acquisition times and makes it unsuitable for real-time imaging.

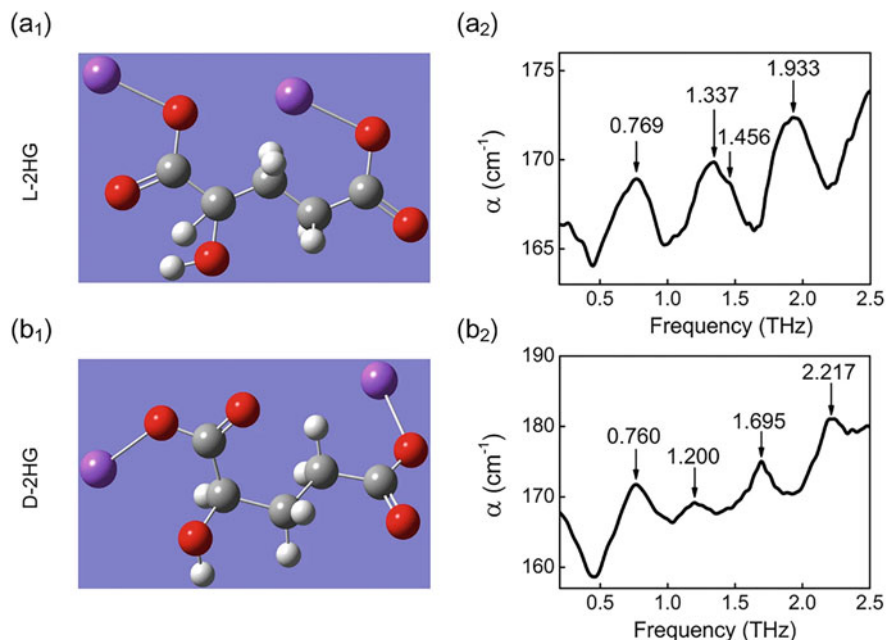


Fig. 10.9 The molecular structure (**a₁**) and THz spectrum of L-2HG (**a₂**). The molecular structure (**b₁**) and THz spectrum of D-2HG (**b₂**) [57]

Therefore, cancer biomarkers can be recognized through different electromagnetic spectroscopies using resonances between electromagnetic waves and molecule vibrations/rotations. Current spectroscopy techniques used in cancer research mainly are infrared, terahertz, and Raman spectroscopy. These spectroscopy techniques provide effective non-invasive methods for cancer metabolomic analysis. Table 10.3 summarizes the advantages and limitations of several indirect imaging methods.

10.10 Summary

We introduced various techniques used in the indirect imaging of cancers, providing detailed information on tissue cancer-specific changes. These techniques analyze cancer-specific variations from proteomic, genomic, and metabolomic aspects. We hope that readers can get the basic knowledge about current techniques for indirect cancer imaging through this chapter.

Acknowledgments This work was partly supported by a grant under the Decree of the Government of the Russian Federation No. 220 of 9 April 2010 (Agreement No. 075-15-2021-615 of 4 June 2021), the Ministry of Science and Higher Education of the Russian Federation within the State assignment FSRC “Crystallography and Photonics” RAS, Russian Foundation for Basic

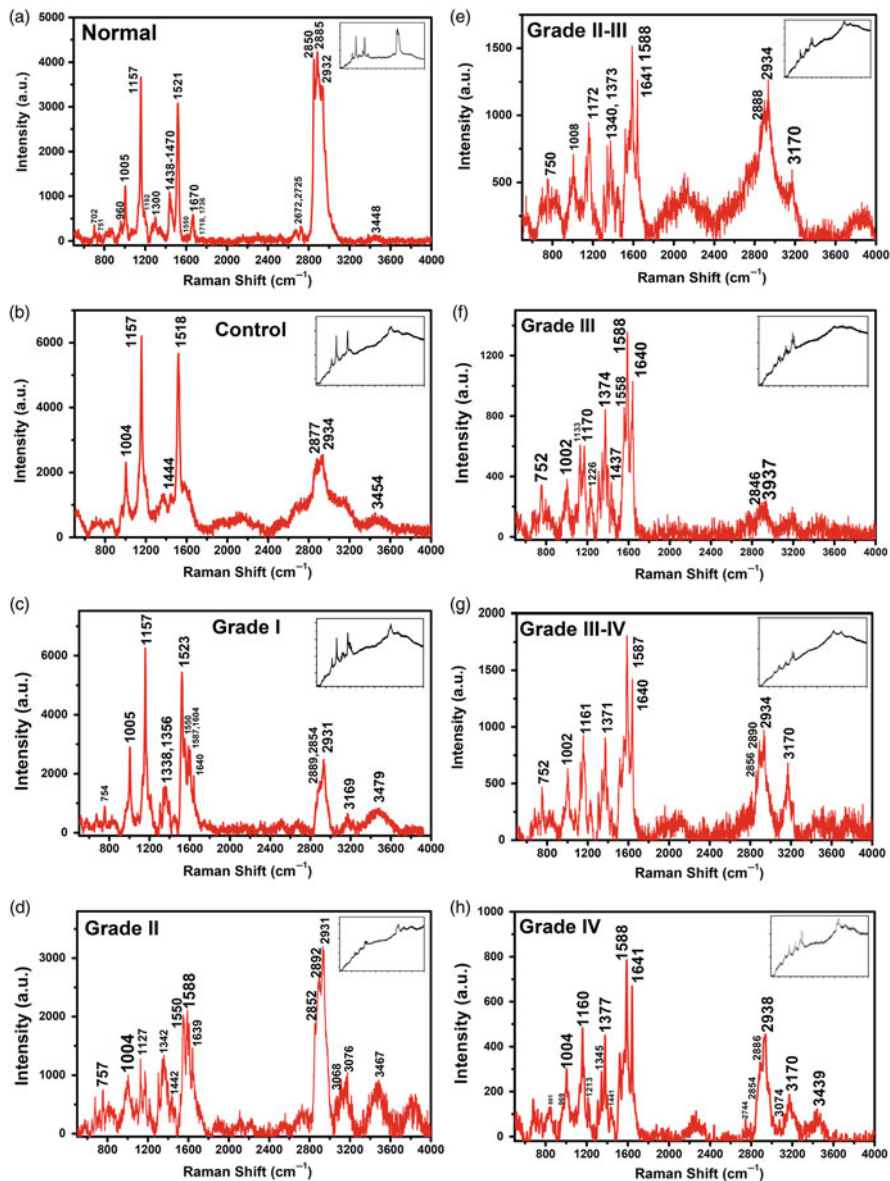


Fig. 10.10 Visible resonance Raman spectra: healthy human brain tissue (a); normal control tissue (b); human brain glioma tumors of grade I (c), grade II (d), grade II–III (e), grade III (f), grade III–IV (g), and grade IV (h). Insets are the raw spectra [60]

Table 10.3 Advantages and disadvantages of indirect imaging techniques

Analysis technique	Advantages	Disadvantages	
Proteomic-based technologies	Immunohistochemistry (IHC)	High specificity	Quantification unavailable
	Flow cytometry (FC)	Quantification ability with high specificity	High cost and complexity in operation
	Enzyme-linked immunosorbent assay (ELISA)	Simple processing, high specificity, and high sensitivity	High cost, short storage time, and the possibility of false results
Genomic-based technologies	Next-generation sequencing (NGS)	High specificity and high effectiveness	Possibility of false results
	Atomic force microscopy (AFM)	3D imaging, non-destructive, nanometer-scale resolution, and high specificity	A time-consuming probe is easy to be damaged
Metabolomic-based technologies	Nuclear magnetic resonance (NMR)	Non-invasive, non-ionizing method, detailed molecular information	Limitation in sensitivity, ferromagnetic objects should be avoided
	Chromatography/mass spectrometry	Well separation ability, high sensitivity, high detection limit	Long testing time, complexity in operation, a customized process for different substances
	Spectroscopy of different electromagnetic waves	High specificity, high effectiveness, and noninvasiveness	Limited sensitivity caused by water or signal intensity

Research (Grant No. 19-52-55004) and National Natural Science Foundation of China (Grant No. 81961138014 and 61922059).

References

1. Maruvada P, Wang W, Wagner PD, Srivastava S (2005) Biomarkers in molecular medicine: cancer detection and diagnosis. *Biotechniques* 38(4S):S9–S15
2. Duraiyan J, Govindarajan R, Kaliyappan K, Palanisamy M (2012) Applications of immunohistochemistry. *J Pharm Bioallied Sci* 4(Suppl 2):S307–S309
3. Magaki S, Hojat SA, Wei B, So A, Yong WH (2019) An introduction to the performance of immunohistochemistry. *Methods Mol Biol* 1897:289–298. https://doi.org/10.1007/978-1-4939-8935-5_25
4. Núñez FJ, Mendez FM, Garcia-Fabiani MB et al (2019) Evaluation of biomarkers in glioma by immunohistochemistry on paraffin-embedded 3D glioma neurosphere cultures. *J Vis Exp* 143. <https://doi.org/10.3791/58931>
5. Rabson AR (1994) Flow cytometry in the diagnosis of brain tumors. *Neurosurg Clin N Am* 5(1):135–146. [https://doi.org/10.1016/S1042-3680\(18\)30547-3](https://doi.org/10.1016/S1042-3680(18)30547-3)
6. Briochi S, d'Errico P, Amann LS, Janova H, Wojcik SM, Meyer-Luehmann M, Rajendran L, Wieghofer P, Paolicelli RC, Biber K (2020) Detection of synaptic proteins in microglia by flow cytometry. *Front Mol Neurosci* 13:149. <https://doi.org/10.3389/fnmol.2020.00149>

7. van der Meulen M, Bromberg JEC, Lam KH, Dammers R, Langerak AW, Doorduijn JK, Kros JM, van den Bent MJ, van der Velden VHJ (2018) Flow cytometry shows added value in diagnosing lymphoma in brain biopsies. *Cytometry B Clin Cytom* 94(6):928–934. <https://doi.org/10.1002/cyto.b.21641>
8. Erhart F et al (2019) Gliomasphere marker combinatorics: multidimensional flow cytometry detects CD44+/CD133+/ITGA6+/CD36+ signature. *J Cell Mol Med* 23(1):281–292
9. Collins L, Alvarez D, Chauhan A (2014) Phycoremediation coupled with generation of value-added products. In: Das S (ed) *Microbial biodegradation and bioremediation*. Elsevier, Oxford, pp 341–387
10. ELISA: Procedure (2021) US Bio-Rad Laboratories, Hercules, California. <https://www.bio-rad-antibodies.com/elisa-procedure.html>. Accessed 20 Sept 2021
11. Touat M, Duran-Peña A, Alentorn A, Lacroix L, Massard C, Idhahbi A (2015) Emerging circulating biomarkers in glioblastoma: promises and challenges. *Expert Rev Mol Diagn* 15: 1311–1323. <https://doi.org/10.1586/14737159.2015.1087315>
12. Sakamoto S et al (2018) Enzyme-linked immunosorbent assay for the quantitative/qualitative analysis of plant secondary metabolites. *J Nat Med* 72(1):32–42
13. Behjati S, Tarpey PS (2013) What is next generation sequencing? *Arch Dis Child Educ Pract Ed* 98(6):236–238
14. Yohe S, Thyagarajan B (2017) Review of clinical next-generation sequencing. *Arch Pathol Lab Med* 141(11):1544–1557
15. Guan Y-F et al (2012) Application of next-generation sequencing in clinical oncology to advance personalized treatment of cancer. *Chin J Cancer (in Eng)* 31(10):463–470
16. Stetson D et al (2019) Orthogonal comparison of four plasma NGS tests with tumor suggests technical factors are a major source of assay discordance. *JCO Precis Oncol* 3:1–9
17. Kennedy SR, Zhang Y, Risques RA (2019) Cancer-associated mutations but no cancer: insights into the early steps of carcinogenesis and implications for early cancer detection. *Trends Cancer* 5(9):531–540
18. Zacher A et al (2017) Molecular diagnostics of gliomas using next generation sequencing of a glioma-tailored gene panel. *Brain Pathol* 27:146–159. <https://doi.org/10.1111/bpa.12367>
19. Higa N, Akahane T, Yokoyama S, Yonezawa H, Uchida H, Takajo T, Kirishima M, Hamada T, Matsuo K, Fujio S, Hanada T, Hosoyama H, Yonenaga M, Sakamoto A, Hiraki T, Tanimoto A, Yoshimoto K (2020) A tailored next-generation sequencing panel identified distinct subtypes of wildtype IDH and TERT promoter glioblastomas. *Cancer Sci* 111(10):3902–3911. <https://doi.org/10.1111/cas.14597>
20. Dubbink HJ et al (2016) Molecular classification of anaplastic oligodendroglioma using next-generation sequencing: a report of the prospective randomized EORTC Brain Tumor Group 26951 phase III trial. *Neuro-Oncology* 18(3):388–400. <https://doi.org/10.1093/neuonc/nov182>
21. Koo H et al (2016) Visualization and quantification of microRNA in a single cell using atomic force microscopy. *J Am Chem Soc* 138(36):11664–11671
22. Deng X et al (2018) Application of atomic force microscopy in cancer research. *J Nanobiotechnol* 16(1):102
23. Li T, Deng P (2016) Nuclear magnetic resonance technique in tumor metabolism. *Genes Dis (in Eng)* 4(1):28–36
24. Baranovicová E et al (2019) Metabolomic profiling of blood plasma in patients with primary brain tumours: basal plasma metabolites correlated with tumour grade and plasma biomarker analysis predicts feasibility of the successful statistical discrimination from healthy subjects—a preliminary study. *IUBMB Life* 71:1994–2002
25. Lee JE, Jeun SS, Kim SH, Yoo CY, Baek H-M, Yang SH (2019) Metabolic profiling of human gliomas assessed with NMR. *J Clin Neurosci* 68:275–280
26. Day SE et al (2011) Detecting response of rat C6 glioma tumors to radiotherapy using hyperpolarized [1-¹³C]pyruvate and ¹³C magnetic resonance spectroscopic imaging. *Magn Reson Med* 65(2):557–563. <https://doi.org/10.1002/mrm.22698>

27. Choi C, Raisanen JM, Ganji SK, Zhang S, McNeil SS, An Z, Madan A, Hatanpaa KJ, Vemireddy V, Sheppard CA et al (2016) Prospective longitudinal analysis of 2-hydroxyglutarate magnetic resonance spectroscopy identifies broad clinical utility for the management of patients with IDH-mutant glioma. *J Clin Oncol* 3:4030–4039
28. Andronesi OC, Loebel F, Bogner W, Marjańska M, Vander Heiden MG, Iafrate AJ, Dietrich J, Batchelor TT, Gerstner ER, Kaelin WG et al (2016) Treatment response assessment in IDH-mutant glioma patients by non-invasive 3D functional spectroscopic mapping of 2-hydroxyglutarate. *Clin Cancer Res* 22:1632–1641
29. Nagashima H et al (2016) Diagnostic value of glutamate with 2-hydroxyglutarate in magnetic resonance spectroscopy for IDH1 mutant glioma. *Neuro-Oncology* 18:1559–1568
30. Bulik M, Jancalek J, Vanicek J, Skoch A, Mechl M (2013) Potential of MR spectroscopy for assessment of glioma grading. *Clin Neurol Neurosurg* 115:146–153
31. Stadlbauer A, Gruber S, Nimsky C, Fahlbusch R, Hammen T, Buslei R, Tomandl B, Moser E, Ganslandt O (2006) Preoperative grading of gliomas by using metabolite quantification with high-spatial-resolution proton MR spectroscopic imaging. *Radiology* 238:958–969
32. Chatham JC, Blackband SJ (2001) Nuclear magnetic resonance spectroscopy and imaging in animal research. *ILAR J* 42(3):189–208
33. Dang L et al (2009) Cancer-associated IDH1 mutations produce 2-hydroxyglutarate. *Nature* 462(7274):739–744
34. Ward PS et al (2010) The common feature of leukemia-associated IDH1 and IDH2 mutations is a neomorphic enzyme activity converting α -ketoglutarate to 2-hydroxyglutarate. *Cancer Cell* 17(3):225–234
35. Strain SK, Groves MD, Olino KL, Emmett MR (2019) Measurement of 2-hydroxyglutarate enantiomers in serum by chiral gas chromatography-tandem mass spectrometry and its application as a biomarker for IDH mutant gliomas. *Clin Mass Spectrom* 15:16–24. <https://doi.org/10.1016/j.clinms.2019.11.002>
36. Poinsignon V, Mercier L, Nakabayashi K, David MD, Lalli A, Penard-Lacronique V, Quivoron C, Saada V, DeBotton S, Broutin S et al (2016) Quantitation of isocitrate dehydrogenase (IDH)-induced D and L enantiomers of 2-hydroxyglutaric acid in biological fluids by a fully validated liquid tandem mass spectrometry method, suitable for clinical applications. *J Chromatogr B Analyt Technol Biomed Life Sci* 1022:290–297. <https://doi.org/10.1016/j.jchromb.2016.04.030>
37. Nakamizo S, Sasayama T, Shinohara M, Irino Y, Nishiumi S, Nishihara M, Tanaka H, Tanaka K, Mizukawa K, Itoh T et al (2013) GC/MS-based metabolomic analysis of cerebrospinal fluid (CSF) from glioma patients. *J Neuro-Oncol* 113:65–74. <https://doi.org/10.1007/s11060-013-1090-x>
38. Miyauchi E, Furuta T, Ohtsuki S, Tachikawa M, Uchida Y, Sabit H, Obuchi W, Baba T, Watanabe M, Terasaki T et al (2018) Identification of blood biomarkers in glioblastoma by SWATH mass spectrometry and quantitative targeted absolute proteomics. *PLoS One* 13: e0193799
39. Wu J, Zhang J, Wei J, Zhao Y, Gao Y (2020) Urinary biomarker discovery in gliomas using mass spectrometry-based clinical proteomics. *Chin Neurosurg J* 6(11):1–10
40. Zhao M, Li M, Yang Y, Guo Z, Sun Y, Shao C, Li M, Sun W, Gao Y (2017) A comprehensive analysis and annotation of the human normal urinary proteome. *Sci Rep* 7:3024
41. An M, Gao Y (2015) Urinary biomarkers of brain diseases. *Genom Proteom Bioinform* 13:345–354
42. Zhao H, Heimberger AB, Lu Z, Wu X, Hodges TR, Song R, Shen J (2016) Metabolomics profiling in plasma samples from glioma patients correlates with tumor phenotypes. *Oncotarget* 7:20486–20495
43. Kwon H, Oh S, Jin X, An YJ, Park S (2015) Cancer metabolomics in basic science perspective. *Arch Pharm Res* 38:372–380
44. Ali JS, Ain NU, Naz S, Zia M (2020) Biomarker selection and imaging design in cancer: a link with biochemical pathways for imminent engineering. *Heliyon* 6:e03340

45. Shen J, Song R, Hodges TR, Heimberger AB, Zhao H (2018) Identification of metabolites in plasma for predicting survival in glioblastoma. *Mol Carcinog* 57:1078–1084
46. Mören L, Bergenheim AT, Ghasimi S, Brännström T, Johansson M, Antti H (2015) Metabolomic screening of tumour tissue and serum in glioma patients reveals diagnostic and prognostic information. *Metabolites* 5:502–520
47. Mören L, Wibom C, Bergström P, Johansson M, Antti H, Bergenheim AT (2016) Characterization of the serum metabolome following radiation treatment in patients with high-grade gliomas. *Radiat Oncol* 11(1):1–9
48. Türker-Kaya S, Huck CW (2017) A review of mid-infrared and near-infrared imaging: principles, concepts and applications in plant tissue analysis. *Molecules* (Basel, Switzerland) 22(1):168
49. Bellisola G, Sorio C (2012) Infrared spectroscopy and microscopy in cancer research and diagnosis. *Am J Cancer Res* 2(1):1–21
50. Gray E, Butler HJ, Board R, Brennan PM, Chalmers AJ, Dawson T, Goodden J, Hamilton W, Hegarty MG, James A et al (2018) Health economic evaluation of a serum-based blood test for brain tumour diagnosis: exploration of two clinical scenarios. *BMJ Open* 8:e017593
51. Gray E, Cameron JM, Butler HJ, Jenkinson MD, Hegarty MG, Palmer DS, Brennan PM, Baker MJ (2021) Early economic evaluation to guide the development of a spectroscopic liquid biopsy for the detection of brain cancer. *Int J Technol Assess Health Care* 37:E41
52. Cameron JM, Butler HJ, Smith BR, Hegarty MG, Jenkinson MD, Syed K, Brennan PM, Ashton K, Dawson T, Palmer DS et al (2019) Developing infrared spectroscopic detection for stratifying brain tumour patients: glioblastoma multiforme vs. lymphoma. *Analyst* 144:6736–6750
53. Butler HJ, Brennan PM, Cameron JM, Finlayson D, Hegarty MG, Jenkinson MD, Palmer DS, Smith BR, Baker MJ (2019) Development of high-throughput ATR-FTIR technology for rapid triage of brain cancer. *Nat Commun* 10:1–9
54. Theakstone AG, Brennan PM, Jenkinson MD, Mills SJ, Syed K, Rinaldi C, Xu Y, Goodacre R, Butler HJ, Palmer DS et al (2021) Rapid spectroscopic liquid biopsy for the universal detection of brain tumours. *Cancers* 13:3851. <https://doi.org/10.3390/cancers13153851>
55. Lee S-H et al (2020) Label-free brain tissue imaging using large-area terahertz metamaterials. *Biosens Bioelectron* 170:112663
56. Cherkasova O et al (2021) Diagnosis of glioma molecular markers by terahertz technologies. *Photonics* 8(22). <https://doi.org/10.3390/photonics8010022>
57. Chen W, Peng Y, Jiang X, Zhao J, Zhao H, Zhu Y (2017) Isomers identification of 2-hydroxyglutarate acid disodium salt (2HG) by terahertz time-domain spectroscopy. *Sci Rep* 7:12166
58. Auner GW et al (2018) Applications of Raman spectroscopy in cancer diagnosis. *Cancer Metastasis Rev* 37(4):691–717
59. Kuhar N, Sil S, Verma T, Umopathy S (2018) Challenges in application of Raman spectroscopy to biology and materials. *RSC Adv* 8(46):25888–25908
60. Zhou Y et al (2019) Optical biopsy identification and grading of gliomas using label-free visible resonance Raman spectroscopy. *J Biomed Opt* 24(9):095001. <https://doi.org/10.1117/1.JBO.24.9.095001>



Multimodal Noninvasive Imaging Strategies for Clinically Monitoring Degenerative Disorders of the Brain

11

Pratik Purohit and Prasun K. Roy

Abstract

Magnetic resonance imaging (MRI) is a valuable tool in a clinical environment for noninvasive monitoring and assessment of neurodegenerative disorders, an umbrella term for diseases causing neural degeneration. Different MRI modalities provide information about underlying neuropathology from different perspectives. Structural MRI (sMRI) is sensitive towards anatomical alterations and assesses neural degeneration-induced tissue atrophy. In addition to volumetric and cortical thickness variations, several quantitative assessments and grading systems are available to calculate disease severity using MRI scans. Furthermore, functional MRI (fMRI) indirectly measures neurotransmission in the functional brain networks and shows differential regional activation in the neurodegenerative brain. In contrast, diffusion tensor imaging (DTI) furnishes the mapping of white matter tracts and anatomical connectivity in the brain networks by measuring aqueous diffusion along the tract scaffold. On the other hand, arterial spin labeling (ASL) is a vascular perfusion MRI technique and safe substitute for invasive FDG-PET that needs vein catheter resection with radioactive tracer administration. Like fMRI, the signals from DTI and ASL show differential anatomical and perfusion patterns in neurodegenerative diseases. Large-scale

P. Purohit

Computational Neuroscience and Neuroimaging Laboratory, School of Bio-Medical Engineering, Indian Institute of Technology (BHU), Varanasi, Uttar Pradesh, India

P. K. Roy (✉)

Computational Neuroscience and Neuroimaging Laboratory, School of Bio-Medical Engineering, Indian Institute of Technology (BHU), Varanasi, Uttar Pradesh, India

Centre for Tissue Engineering, Indian Institute of Technology (BHU), Varanasi, Uttar Pradesh, India

e-mail: pkroy.bme@iitbhu.ac.in

clinical trials are now enabling precise quantification, making sMRI, fMRI, DTI, and ASL much more reliable in clinical settings.

Keywords

Neuroimaging of dementia · Neurodegenerative disease · Alzheimer's disease · Vascular dementia · Mild cognitive impairment · Lewy body disease · Frontotemporal dementia · MRI · Diffusion tensor imaging · fMRI · Arterial spin labeling

11.1 Introduction

The brain is the most critical organ in the human body. Therefore, any disease related to it can become potentially life-threatening, making clinical monitoring of such disorders extremely important. From a ready clinical office perspective, a physician can often diagnose the disease by neurobehavioral assessment. Standard functional and cognitive examinations are available for this purpose, which do not need the more involved diagnostic methods as brain imaging. For example, Montreal Cognitive Assessment Test was developed to identify mild cognitive impairment. Other screening tools in the same category are Mini-Mental State Examination Extended, St. Louis University Mental Status Examination, and the likewise. These assessment techniques are generally helpful in identifying the possibility of neurological disorders in the patient.

Nevertheless, there may be appreciable chances of misidentification and misclassification, depending upon the type of test, clinician's bias, etc. [1]. Therefore, in a clinical setting, one cannot rely only on behavioral or psychological tests only. Therefore, several neuroimaging techniques are required to make decisions about recognizing the disease and planning the treatment. Imaging the brain at different times during the medication duration also helps monitor the disease progression and assess the effectiveness of the clinical intervention. In addition, the accurate detection of neurodegenerative disorders is possible using different neuroimaging paradigms, which may furnish meticulous diagnostic signals which may not manifest at the gross cognitive and behavioral variations when one administers the psychological test batteries at the primary stage of the disease.

11.2 Common Noninvasive Neuroimaging Modalities

In neurodegenerative disorders, the patient progressively loses functional neural tissue in the brain, resulting in cognitive and motor impairment. Some noteworthy examples of such disorders are Frontotemporal Dementia (Pick's Disease), Alzheimer's disease, Dementia with Lewy bodies, Parkinson's disease, Vascular Dementia, Progressive Supranuclear Palsy, Posterior Cortical Atrophy, and

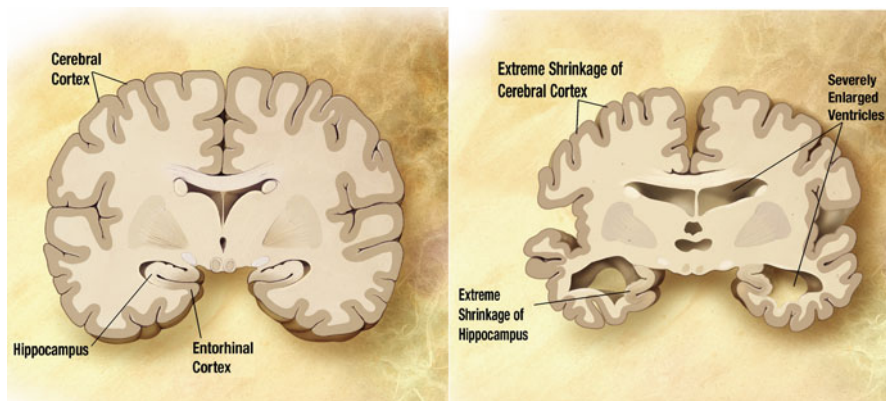


Fig. 11.1 Clip-art schema showing the contraction of cortical areas in the Alzheimer's disease-affected brain (right) compared to normal brain (left) [in Public Domain]

Amyotrophic Lateral Sclerosis. In general, people above mid-age are more susceptible, seriously affecting their quality of life. One of the significant hurdles to prevent disease progression is early detection before clinical symptoms are visible, that generally happens in pathologically later stages of the disease when disease-modifying therapies are not much effective. This hurdle can be overcome by in vivo observation of the brain using various noninvasive neuroimaging techniques. Neurodegenerative disorders are readily visible as deformations in the brain anatomy in Structural Magnetic Resonance Imaging (sMRI) (Fig. 11.1).

Anatomical imaging of the brain detects the physical changes, but it has limitations to capture the alterations in the neuropathology or neurophysiology of the brain. Therefore, imaging the brain from different perspectives gives better insight into the state of brain pathology. Accordingly, other magnetic resonance imaging modalities like diffusion-weighted, perfusion-weighted, and functional MRI are emerging tools apart from standard structural MRI. Diffusion-weighted Imaging (DWI) estimates the directionally varying or anisotropic diffusion of water molecules at the different spatial locations in the brain. The diffusion of water molecules in gray matter is more isotropic than diffusion in white matter. Therefore, white matter tracts can be visualized using diffusion-weighted MRI scanning after applying different tractography image-analysis algorithms. This enables quantifying neuronal connectivity, which may get damaged under neurodegenerative disorders. Underlying neuropathology alters the diffusion properties of the affected brain region which can be measured using diffusion-weighted imaging.

Similarly, perfusion-weighted Imaging (PWI) gives a different perspective and estimates vascular status or blood perfusion in tissue which can be analyzed to get different parameters about the blood flow like blood volume, mean transit time, perfusion rate, etc. Abnormal blood perfusion in the particular brain region indicates towards altered functionality. In contrast, Functional Magnetic Resonance Imaging

(fMRI) indirectly measures hemoglobin's oxygenation level in specific brain tissue by utilizing the difference in magnetic resonance properties of the oxygenated and de-oxygenated hemoglobin. Altered default mode network connectivity can also be mapped using fMRI. Neuroimaging analysis enables one to have important clues to:

1. Diagnosis of a disorder
2. Therapy Monitoring regarding clinical efficacy
3. Planning of corrective modification of treatment
4. Prognosis of the susceptibility of the patient to a disease condition
5. Rehabilitation performance of different interventions

We shall now elucidate how the successive noninvasive imaging modalities (sMRI, fMRI, DTI, ASL) can be utilized for investigating neurodegenerative disorders.

11.3 Characterizing Neurodegeneration Using Noninvasive Imaging

Structural MRI is a fundamental modality of the magnetic resonance imaging paradigm with widespread clinical availability, enabling in vivo anatomical investigation of the brain tissues. It can be performed using the various pulse sequences: T_1 relaxation weighted, T_2 relaxation weighted, Proton Density, FLAIR (Fluid-attenuated Inversion Recovery), etc. Each pulse sequence has its clinical significance. Structural MRI helps preliminary study about the cause of underlying symptoms, whether it is due to reasons other than neurodegeneration or not, like hemorrhage or space-occupying lesions, like tumors. Initially, neural degeneration can be assessed by cerebral or region-wise atrophy or volume loss due to neuronal damage. Alteration of brain regions needs to be scanned and analyzed across the three planes (coronal, sagittal, and axial) (Fig. 11.2).

11.3.1 Volumetry

Since common neurodegenerative disorders primarily affect certain brain regions, volumetric MRI scans have the potential to reveal the pathological condition. Many brain areas in the Limbic System, such as the entorhinal cortex and hippocampus, lose their volume due to neurons death in Alzheimer's disease or dementia [2, 3]. Hippocampal volume loss starts before behavioral and cognitive symptoms [4]. Similarly, volumetric loss of the Precuneus region of the cerebrum is a good indicator of the early onset of Alzheimer's disease [5]. Volumetric analysis requires T_1 weighted MRI scans of the patient, and to extract the region of interest, several automated and manual tools are available like SPM (Statistical Parametric Mapping) and FSL (FMRI-brain Software Library). Volumetric variations are an indicator of the change

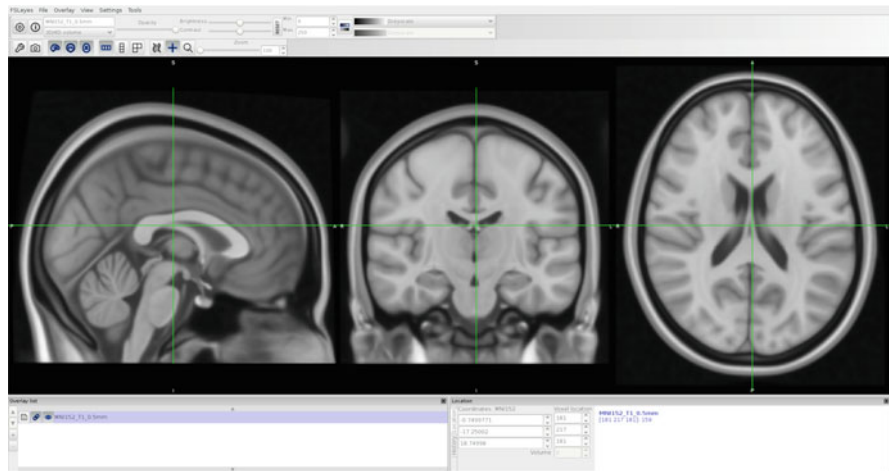


Fig. 11.2 T₁ weighted MRI scan of the human brain shown in sagittal, coronal, and axial views

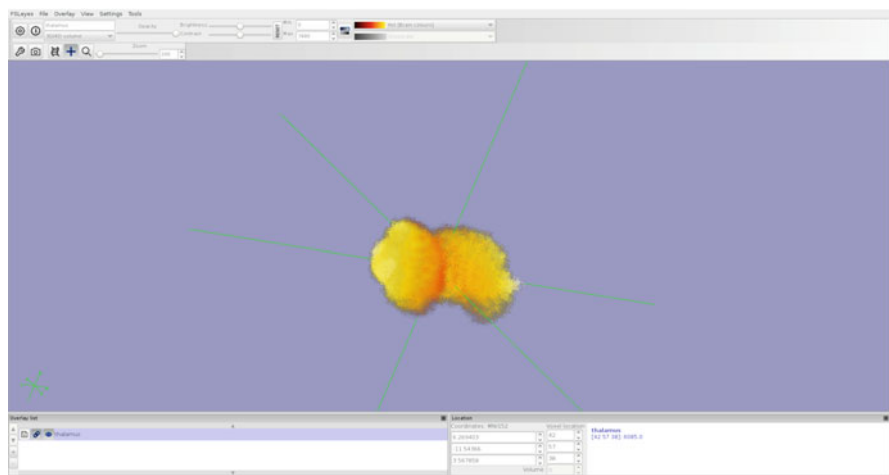


Fig. 11.3 The 3D extraction of the thalamus from T₁ MRI scan for volumetric analysis

in the shape of a particular brain region (Fig. 11.3). Thus, shape analysis is another tool for the identification and monitoring of neurodegenerative disorders. Sub-regional alteration in a brain region varies, depending upon the type of neurodegenerative disorder. For example, hippocampal shape analysis in different diseases reveals sub-structural variations [6]. These sub-structural variations could help classify neurodegenerative disorders more accurately.

11.3.2 Cortical Thickness

Cortical thickness is also a helpful parameter for assessing disease progression. Analysis of structural MRI scans can evaluate cortical thickness. Neurodegenerative disorders such as Alzheimer's disease reduce cortical thickness in parietal, frontal, and orbitofrontal lobes [7]. Cortical thinning patterns vary across different neurodegenerative disorders like in Alzheimer's disease and Frontotemporal dementia [8]. Since cortical thinning correlates with the disease intensity, it can quantify disease severity [9].

11.3.3 Specific Signature Changes in Different Disorders

Degeneration of neural tissue affects normal brain functions, manifesting in the behavioral symptoms after disease progresses to a certain level. Volume measurement, shape analysis, and cortical thickness assessment are some ways to estimate the extent of neuronal damage. Neurodegenerative disorders have some differences in cognitive and behavioral symptoms due to variations in the brain regions getting affected. For instance, Parkinson's disease reduces the volume of substantia nigra pars compacta (thus affecting movement or walking), while Alzheimer's disease predominantly affects the hippocampus and entorhinal cortex (hence affecting memory). Although some of the disorders may involve some common regions, though not other areas, nevertheless these specific regional atrophy patterns vary among different diseases and are vital clues that can help in diagnosis and prognosis.

In a T_1 weighted MRI scan, Alzheimer's disease-based atrophy is observable in the medial parietal and temporal lobe [10]. However, in Pick's disease, atrophy in the anterior temporal lobe is a sign of the pathology; however, the patient's age at disease onset decreases accuracy in structural MRI [11]. On the other hand, preservation of the temporal lobe structures is an imaging marker in the case of Dementia with Lewy bodies, as detectable in the structural MRI [12]. To contrast, progressive supranuclear palsy has characteristic predominant atrophy in the midbrain compared to the pons [13]. In comparison, Huntington's disease mainly affects putamen and caudate in the early stage [14].

11.4 Quantitative Parameters for Clinical Evaluation by Imaging

Structural imaging of the brain helps to estimate the level of the disease process. Moreover, in a clinical setting, it is advisable to have some quantitative parameters that quantify the disease severity, so as to monitor disease progression conveniently. For this purpose, parameters and scoring systems are devised to help clinicians assess the current disease intensity quantitatively. However, most of them are exclusively for a particular disorder. Some of the measurement parameters are:

11.4.1 Ratio of Midbrain to Pons Area

Degeneration of the midbrain compared to the pons region in Progressive Supranuclear Palsy is measurable by a T_1 -weighted MRI scan in terms of the ratio between the area of the midbrain to the pons [15]. This ratio can be measured on midsagittal T_1 MRI slice by manually drawing the midbrain and pons boundary on the computer, then calculating the area. In Progressive Supranuclear Palsy, the ratio is lower than either normal subjects or patients of Multiple System Atrophy and Parkinson's disease. For Progressive Supranuclear Palsy-affected the brain, this ratio is less than 0.16, while for normal, Multiple System Atrophy and Parkinson's Disease patients, the ratio is more than 0.16. Another way is to find the ratio of the minor axis of the midbrain to the pons, in which case the ratio is less than 0.52 in the case of Progressive Supranuclear Palsy [16].

11.4.2 Magnetic Resonance Parkinsonism Index (MRPI)

MRPI improves the classification accuracy of the midbrain to pons area ratio. MRPI can differentiate between Progressive Supranuclear Palsy and Parkinson's disease patient or normal subject [17, 18]. The T_1 MRI scan of the subject is needed to calculate MRPI using the following formula:

$$\text{MRPI} = \frac{\text{Pons}_{\text{area}}}{\text{Midbrain}_{\text{area}}} * \frac{\text{Middle Cerebellar Peduncle}_{\text{width}}}{\text{Superior Cerebellar Peduncle}_{\text{width}}}$$

The width of the Middle Cerebellar Peduncle can be calculated in the sagittal plane, while a coronal section is needed in the case of the Superior Cerebellar Peduncle. The Midsagittal section is required for calculating the area of the midbrain and pons. The value of $\text{MRPI} > 13.27$ strongly indicates that the subject will develop Progressive Supranuclear Palsy.

11.4.3 Modified Parkinsonism Index

Recently, there has been proposed modifications in MRPI score to improve its accuracy further [19]. This incorporates the width of the frontal horn and third ventricle, as follows:

$$\text{MRPI}_{\text{new}} = \text{MRPI} * \frac{\text{Width of the third ventricle}}{\text{Left to right frontal horn width}}$$

If $\text{MRPI}_{\text{new}} > 2.18$ for a subject, then there is significantly increased probability of Progressive Supranuclear Palsy occurring, when compared to normal subjects.

11.4.4 Ratio of Intercaudate Distance to Inner Table Width

This ratio is used to assess Huntington's disease in which the caudate nuclei region degenerates [20]. A radiologist calculates the intercaudate distance and the inner table width on the axial plane of the T₁ MRI scan where the ACPC (anterior commissure–posterior commissure) line passes. The normal range of this ratio lies between 0.09 to 0.12, which increases in the case of Huntington's disease.

11.4.5 Anterior Ventricle–Intercaudate Ratio

Another similar index is the ratio between frontal horn width and intercaudate distance, whose normal values are 2.2–2.6.

11.5 Grading System for Evaluating Neural Degeneration Using Structural Imaging

In the above section, the various quantitative parameters need the time-consuming procedure of accurate measurement and accurate computations to calculate the indices from the T₁ MRI scan. This high-resource procedure is difficult to implement in a busy outdoor clinic where many patients demand attention from the medical professional in a short time frame. To circumvent this difficulty, non-parametric methods have been developed, where a clinician need not compute parameters, but can rapidly visually glance at an MRI image and quantitatively estimate the underlying disease condition using a scoring system. Some of the scoring systems are as follows:

11.5.1 Fazekas Scale

White matter hyperintensities are the bright patches in white matter, visible in T₂ weighted or FLAIR-protocol MRI scans. White matter hyperintensities may appear with aging, but they are potential indicators of vascular dementia, including stroke or cognitive impairment. Depending upon the region where they occur, hyperintensities lie in three categories: (1) deep white matter hyperintensities, (2) periventricular hyperintensities, and (3) subcortical hyperintensities. The Fazekas scale grades the periventricular white matter and deep white matter hyperintensities depending upon the shape and size of the lesion [21, 22].

For periventricular white matter:

0—No hyperintensity signal

1—Thin line

2—Smooth halo

3—Asymmetric hyperintensities extending into deep white matter

For deep white matter:

- 0—No hyperintensity signal
- 1—Punctate foci
- 2—Beginning of overlap
- 3—Large overlapping areas

11.5.2 Global Cortical Atrophy (GCA) Scale

The GCA scale quantitatively assesses cerebral atrophy in the brain's degenerative diseases [23]. FLAIR MRI scan is needed to rate atrophy based on the sulci and ventricular enlargement in 13 brain regions. Sulcus and ventricular enlargement is considered in the frontal, parieto-occipital, and temporal lobe of both hemispheres, including ventricular enlargement in the third ventricle. The four-point GCA scale defines the acuteness of the atrophy. An average value of this scale for 13 brain regions gives an overall rating for the brain:

GCA Scale 0—Normal condition

GCA Scale 1—Slight sulci or ventricular widening

GCA Scale 2—Volume loss of gyri or moderate ventricular dilation

GCA Scale 3—Knife-blade atrophy of gyri, with sulci thickness greater than gyri

11.5.3 Scheltens's Scale or Medial Temporal Lobe Atrophy (MTA) Score

The MTA score is helpful to classify Alzheimer's patients from other patients [24]. It is also applicable in the case of MCI (Mild Cognitive Impairment). This scoring system rates hippocampus atrophy based on the width of the choroid fissure, the width of the lateral ventricle's temporal horn, and the length of the hippocampus [25]. These measurements must be made on the T₁-weighted MRI coronal section through the hippocampus at the level of the anterior pons and along the brainstem's axis [26]. The scoring system based on the measurements is as follows:

MTA Score 0—No CSF around the hippocampus

MTA Score 1—Mild dilation of the choroidal fissure

MTA Score 2—Moderate dilation of the choroidal fissure with mild loss of hippocampus length and mild temporal horn enlargement

MTA Score 3—Marked enlargement of the choroidal fissure with moderate hippocampus length decrement and moderate temporal horn enlargement

MTA Score 4—Marked enlargement of the choroidal fissure with severe hippocampal atrophy and temporal horn enlargement

For patients older than 75 years, a score greater than two is abnormal, while it is greater than three for others.

For subjects older than 75 years, a score greater than two is abnormal, while for subjects younger than 75 years, a score greater than three is abnormal.

11.5.4 Posterior Atrophy Score

The Posterior Atrophy Score or Koedam score rates parietal atrophy to assess the possibility of early-onset Alzheimer's disease and dementia [26]. It is beneficial in the case of younger Alzheimer's disease patients where sometimes medial temporal lobe atrophy scores are normal. Therefore, the Koedam score can accurately assess the situation. This score requires an MRI scan in three planes (coronal, sagittal, and axial) to inspect the various brain structures visually. Evaluated brain regions are:

1. *Sagittal section*: Posterior cingulate sulcus, parieto-occipital sulcus, precuneus gyrus
2. *Coronal section*: Posterior cingulate sulcus, parietal gyrus
3. *Axial section*: Posterior cingulate sulcus, parietal lobes

Based on the visual observation, the parietal atrophy is graded as given below:

Grade 0—Close sulci, no gyral atrophy

Grade 1—Mild sulcal dilation, mild gyral atrophy

Grade 2—Substantial sulcal widening, substantial gyral atrophy

Grade 3—Marked sulcal widening, knife-blade gyral atrophy

11.6 Functional Mapping (fMRI)

The fMRI procedure indirectly measures the neuronal activity in the brain based on the measuring change in hemoglobin oxygenation level in the tissue. The fMRI methodology uses a blood oxygenation-level-dependent (BOLD) signal as contrast, proportional to oxygenated hemoglobin flowing into brain tissue in response to metabolic demand of the neural activity. fMRI can be performed in two ways:

(A) Task-Based Condition

- (a) Event-design analysis
- (b) Block-design analysis

(B) Resting-State Condition

Task-based fMRI gives information about the brain regions active during a given cognitive task performed by the subject during scanning. Here, the task is presented continuously for an extended time interval (time-block), so as to continue cognitive engagement, and various task conditions are presented alternating in time-sequence. Block-design surpasses in terms of robustness, producing higher blood-oxygen-level-dependent (BOLD) signal, which produces higher statistical power. In contrast, during an event-related design, the investigator presents discrete and short-duration events, so that the time-gap

and order is randomized. Event-related design can identify transient variations in the BOLD signal and enable a proper analysis of a patient's personalized or idiosyncratic response to the stimulus, and the findings are less affected by head motion. Stimulations used in task-based studies are light, sound, touch, or warmth.

On the other hand, as the name suggests, resting-state fMRI provides information about active brain regions during rest or no task conditions. The brain activity has specific signatures even when a person is physically and mentally idle [27]. Any abnormal brain activity from an average level is a potential imaging marker for the possible underlying neurocognitive disorder [28–30]. The mathematical analysis of the resting-state fMRI along the temporal dimension shows the probabilistic connectivity between active brain regions, also known as the functional connectivity analysis, which is the basis for constructing resting-state brain network such as “Default Mode Network” (DMN). Default mode network is a large-scale “idling” network of the brain during the wakeful state, but not focused on performing any cognitive task [31]. Neurodegenerative disorders lead to neuronal dysfunction and affect the connectivity of the resting-state brain networks [32]. Functional atrophy patterns in the brain networks may vary with different neurodegenerative disorders. In Alzheimer's disease, the DMN has differential connectivity compared to the control subjects. It can be used for the classification of the Alzheimer's disease subject vis-a-vis the normal one [28, 33]. Resting-state neuronal network analysis indicates the possibility of the compensatory increase in the functional connectivity of the middle temporal lobe under mild cognitive impairment [34]. In addition, hyperactivity of the hippocampus and altered DMN correlates with the misfolded protein dynamics: amyloid deposition and tau accumulation [35–37]. Functional connectivity alterations of the DMN represent corresponding cognitive function impairment even in neurodevelopmental diseases such as autism [29].

Indeed, fMRI has the capability to provide much useful insight into the pathology of neural degeneration. However, its use in a rapid clinical context is minimal due to limitations like the low signal-to-noise ratio. In addition, the BOLD signal is an indirect measure of neuronal activity with an ambiguous accuracy [38].

11.7 Diffusion Tensor Imaging (DTI) and Neural Fiber Connectivity

Diffusion MRI encodes water diffusion displacement in terms of the image. The tensorial version, namely DTI, is a variant of diffusion MRI and is used to construct visualization of the white matter tracts and neural fiber connectivity. An important parameter is anisotropy or pointedness of the aqueous diffusion ellipsoid along the nerve fiber direction. More the neural fiber density, more the diffusion's anisotropy or pointedness since it is these packed fibers that provide the scaffold of water diffusion [39]. Color coding thus gives a map of the white matter fiber health (Fig. 11.4). White matter volume varies with aging, and its lesions influence

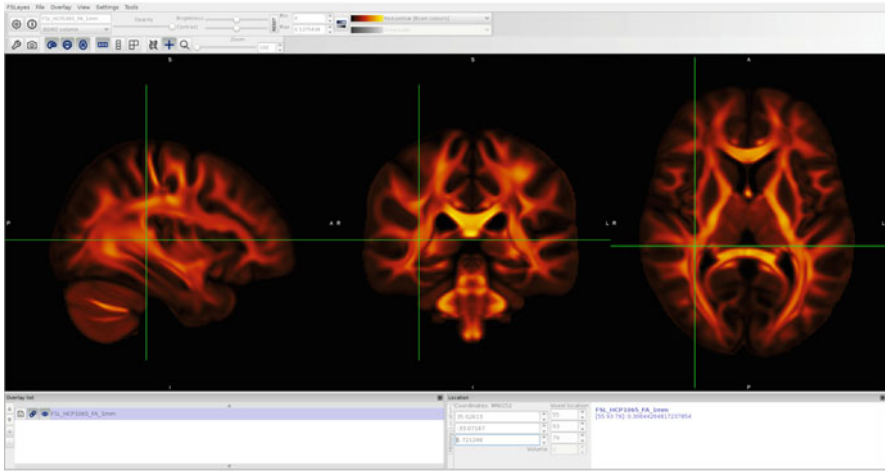


Fig. 11.4 Visualization of white matter tracts obtained after analyzing diffusion-weighted MRI. (These are anisotropy maps, whereby the color intensity is proportional to the fractional anisotropy which is an estimate of neural fiber density)

cognitive capabilities. Neurodegenerative diseases affect white matter integrity, which declines as the disease progresses [40].

Alzheimer's disease progression manifests as the changes in the diffusion parameters of white matter such as fractional anisotropy, mean diffusivity, and radial diffusivity [41, 42]. These white tract alterations coincide with amyloid-beta plaque formation and tau tangle accumulation in the early phase of Alzheimer's disease [43, 44]. Another neurodegenerative disease, amyotrophic lateral sclerosis, decreases the apparent diffusion coefficient in the bilateral centrum semiovale and frontoparietal lobe white matter. In addition, fractional anisotropy diminishes in the various brain regions, including the corpus callosum, cerebral peduncle, and frontal lobe deep white matter. These diffusion indices can classify amyotrophic lateral sclerosis patients from normal subjects [45].

Tractography based on the DTI assumes single fiber orientation in a given voxel. However, fiber may be crossing, touching, or diverting since the size of the voxel (in millimeters) is much higher than the diameter of the neural fiber (in micrometers) [46]. Due to this disadvantage of the DTI, recent methodologies of diffusion MRI acquisition techniques and fiber tracking algorithms have been developed which consider the possibility of the multidirectional fibers in a single voxel, thereby these procedures reduce the error in the fiber tracking. Further, the HARDI (High Angular Resolution Diffusion Imaging) method provides diffusion MRI scans with more diffusion directions and b -values which help to identify crossing fibers in a single voxel [47].

Indeed, higher order diffusion tensor at a voxel, instead of a second-order tensor (conventional DTI), could estimate multiple diffusion directions that correspond to

the possibility of different or varying orientations of neural tracts in a particular voxel. Higher order tensor requires diffusion MRI signal from multiple directions obtained by HARDI protocol [47]. Multiple tractography methods are available to estimate white matter pathways utilizing HARDI scans, such as diffusion spectrum imaging or Q-space imaging which relate the diffusion-MR signal and water molecules displacement. Generally, Q-ball imaging based on Funk Radon transform has more advantages than Q-space imaging [48]. These methods have the potential to overcome the limitations of conventional DTI which is based on a fixed single diffusion ellipsoid in a voxel [49, 50].

Nevertheless, DTI is helpful for clinicians to investigate dementia effects due to structural space-occupying lesions, as brain tumor, stroke hematoma, parasitic granuloma, and the like. DTI is a valuable tool for the *in vivo* study of neurodegenerative disorders in the research ecosystem. However, routine use of DTI biomarkers in the clinical context requires a quantitative and accurate relationship between the disease severity and white matter tract indices, the details of such interaction are now emerging from laboratory studies.

11.8 Vascular Dynamics: Arterial Spin Labeling

Arterial spin labeling (ASL) is an MRI technique for measuring blood perfusion, namely serum transport through tissue capillary bed. ASL is entirely noninvasive and does not need any intravenous tracer to be injected. Actually, ASL generates the contrast by magnetic tagging the arterial blood. Since tissue metabolism and cerebral capillary blood perfusion vary in synchrony, ASL can be a safer substitute for glucose metabolism measurement using injected fluoro-deoxy glucose, FDG, in a PET (positron emission tomography) scanner [51]. Neurodegenerative disorders generally show differential patterns of perfusion. In frontotemporal Dementia, ASL reveals a reduction of blood perfusion in the right frontal cortex compared to normal subjects. This reduction in perfusion correlates with cognitive deficits. When compared to Alzheimer's disease patients, frontotemporal dementia subjects have an elevated level of blood perfusion in the parietal cortex and posterior cingulate [52].

It has also been observed that ASL can reduce radiation exposure as well as provide similar clinical significance compared to PET. Nevertheless, for various neurodegenerative diseases, large-scale multi-country/multi-continent clinical trials are needed for rigorous standardization and validation for ASL-based clinical markers. Some of these trials are being initiated.

11.9 Dementia Imaging Matrix Parameters

Accurate identification of the neurodegenerative diseases manifesting as dementia is crucial for planning clinical intervention. Regional atrophy evaluation using MRI scans is standard clinical practice for this purpose. Crucial anatomical signs of the different neurodegenerative dementias are:

- (a) *Pick's disease (Frontotemporal Lobar Degeneration, FTLD)*: Asymmetrical frontal lobe and temporal pole atrophy.
- (b) *Vascular dementia*: White matter lesions, lacunar infarcts, and infarcts in the regions responsible for cognitive skills.
- (c) *Alzheimer's disease*: Parietal and medial temporal cortex atrophy.
- (d) *Lewy bodies dementia*: No specific atrophy.
- (e) *Mixed dementia*: Hippocampus atrophy, frontal and temporal lobe. Lacunes, Leukoaraiosis, and latent micro bleeding.

We construct Table 11.1 to summarize the different anatomical locations of various atrophies under assorted dementias. The different lobes of the brain are arranged as per their location along the neurodevelopment axis, while the various dementia types as per the intensity of vascular damage, with vascular dementia having the highest vascular damage (angiopathic axis); this dementia being often a post-stroke complication. The numerical values are the gradation of the intensity of atrophy. Table 11.1 shows the atrophy levels of different dementias when enumerated along the neurodevelopmental axis and the angiopathic axis, thus forming a matrix parametric representation.

11.10 Emerging Technique of Neuroimaging Genomics to Assess Brain Disorders

Numerous diseases of the human body have a genetic basis, and expressions and mutations of genes are critical factors in the disease initiation or progression. Imaging the brain aims to capture the current physiological or anatomical state. Therefore, identifying imaging features for the corresponding genetic traits helps may be a noninvasive correlate that can bypass invasive and time-consuming biopsies and also provide molecular insights into the disease mechanism. Neuroimaging genomics combines neuroimaging and genetic data to find the gene expression-modulated imaging characteristics in normal and diseased brains. For example, in neuroproliferative disorders as Glioblastoma, the definitive relationship observed between T_1 -weighted MRI scans and gene expression microarray data does indeed highlight the interlinking between targeted gene expression levels and MRI-derived characteristics such as the ratio of contrast-enhancing and necrotic tumor volume [53, 54]. Another study demonstrates that cortical thickness and surface area are genetically independent (i.e., statistically uncorrelated) in a normal brain [55]. In addition to finding the influence of a targeted gene in question, the discipline of neuroimaging genomics is a promising technique to explore the influence of gene networks on brain organization [56].

Neuroimaging genomics analysis can reveal genes associated with neural degeneration due to underlying disorders, which may ultimately help to understand disease-inducing mechanisms and refine treatment strategy. In the case of Alzheimer's disease, several Single Nucleotide Polymorphisms (rs2137962, rs1498853, rs288503, rs288496) are associated with focused neurodegeneration in

Table 11.1 Anatomical atrophies in different forms of dementia

Neurodevelopment axis (Caudal-Rostral) ↓		Brain regional atrophy	Lewy body dementia	Pick's disease (FTLD)	Alzheimer's disease	Mixed dementia	Vascular dementia	
	Limbic lobe	Hippocampus	2	3	2	2	2	
		Periventricle lacunes	1	0	2	3	3	
		Subthalamic lesions	0	0	1	3	3	
	Temporal lobe	Leukarosis	1	0	2	3	3	
		Parietal lobe	0	3	2	1	1	
		Frontal-prefrontal lobe	1	0	2	1	1	
			Angiopathic axis →	0	3	0	0	1

Atrophy gradation: 0: No significant change, 1: Low atrophy, 2: Moderate atrophy, 3: High atrophy

the hippocampi gyrus, parahippocampal gyrus, and left temporal gyrus [57]. Diffusion MRI-based white matter connectivity and genetic data analysis reveal that the *SPON1* gene variant (at rs2618516) affects the white matter integrity in dementia [58]. Similarly, neuroimaging integrated with genomics highlight the potential genes (MAPT, GRN, C9orf72, etc.) associated with frontotemporal dementia [59].

Although neuroimaging genomics looks very promising, it is still evolving and limited to research purposes. However, these research outcomes can help refine our understanding of gene aberration, biochemical dysfunction, and its consequent drug targets, in neurodegenerative disorders, and consequently affect the treatment strategies. Further advancements in neuroimaging genomics may go a long way to usher in personalized medicine in neurodegenerative disorders, for helping clinicians to tailor individual drugs and treatment schedules. The multidimensional nature of neuroimaging and genetic data requires the development of computationally efficient and novel algorithms. Large-scale imaging genomics datasets such as ADNI (Alzheimer's Disease Neuroimaging Initiative), UK Biobank, and ENIGMA (Enhancing Neuro Imaging Genetics through Meta-Analysis) consortium have unparalleled potentials for helping researchers worldwide to accelerate advancements in the frontier field of neuroimaging genomics.

11.11 Conclusion

Every imaging modality has its clinical advantage, and multimodal imaging can offer a combination of such benefits compared to the single modality. Multimodal imaging captures disease pathology more insightfully as it involves various pathological variables and thus improves diagnostic accuracy. However, the methodology to estimate disease becomes complex because of the higher number of variables. One way is to choose more imaging markers for a particular neurodegenerative disease: either positive or negative. Multimodal imaging does not give redundant information but instead provides complementarily neuroimaging markers, thus improving identification and monitoring accuracy. For example, in the case of Alzheimer's disease, integration of structural MRI, fMRI, and ASL scans more effectively predict conversion from mild cognitive impairment to dementia.

Therefore, multimodal imaging should be incorporated into a clinical setting to help clinicians identify the underlying disease and plan efficient diagnosis. However, there is a need to devise a clinical protocol to select the combination of the modalities from given signs or symptoms. In the case of sequential imaging (for instance, successively taking sMRI, fMRI, and DTI image acquisitions in one scanning session of 30–40 min), a given image modality should be chosen based on its availability and cost. A scanner that supports parallel imaging, such as integrated fMRI-DTI, needs only a single session for both modalities, and it is cost-effective. Apart from optimization proper permutation of which modalities can be combined to give a maximal diagnostic performance, the prospects of implementing multimodal imaging biomarkers for neurodegenerative disorders is now making seminal progress through multi-center multi-country investigations.

References

1. Ranson JM, Kuźma E, Hamilton W et al (2019) Predictors of dementia misclassification when using brief cognitive assessments. *Neurol Clin Pract* 9:109–117. <https://doi.org/10.1212/CPJ.0000000000000566>
2. Du AT, Schuff N, Amend D et al (2001) Magnetic resonance imaging of the entorhinal cortex and hippocampus in mild cognitive impairment and Alzheimer's disease. *J Neurol Neurosurg Psychiatry* 71:441–447. <https://doi.org/10.1136/JNPN.71.4.441>
3. Mosconi L (2013) Glucose metabolism in normal aging and Alzheimer's disease: methodological and physiological considerations for PET studies. *Clin Transl Imaging* 1:217–233. <https://doi.org/10.1007/S40336-013-0026-Y>
4. Ridha BH, Barnes J, Bartlett JW et al (2006) Tracking atrophy progression in familial Alzheimer's disease: a serial MRI study. *Lancet Neurol* 5:828–834. [https://doi.org/10.1016/S1474-4422\(06\)70550-6](https://doi.org/10.1016/S1474-4422(06)70550-6)
5. Karas G, Scheltens P, Rombouts S et al (2007) Precuneus atrophy in early-onset Alzheimer's disease: a morphometric structural MRI study. *Neuroradiology* 49:967–976. <https://doi.org/10.1007/S00234-007-0269-2>
6. Lindberg O, Walterfang M, Looi JCL et al (2012) Hippocampal shape analysis in Alzheimer's disease and frontotemporal lobar degeneration subtypes. *J Alzheimers Dis* 30:355–365. <https://doi.org/10.3233/JAD-2012-112210>
7. Lerch JP, Pruessner JC, Zijdenbos A et al (2005) Focal decline of cortical thickness in Alzheimer's disease identified by computational neuroanatomy. *Cereb Cortex* 15:995–1001. <https://doi.org/10.1093/CERCOR/BHH200>
8. Du AT, Schuff N, Kramer JH et al (2007) Different regional patterns of cortical thinning in Alzheimer's disease and frontotemporal dementia. *Brain* 130:1159–1166. <https://doi.org/10.1093/BRAIN/AWM016>
9. Im K, Lee JM, Seo SW et al (2008) Variations in cortical thickness with dementia severity in Alzheimer's disease. *Neurosci Lett* 436:227–231. <https://doi.org/10.1016/J.NEULET.2008.03.032>
10. McKhann GM, Knopman DS, Chertkow H et al (2011) The diagnosis of dementia due to Alzheimer's disease: recommendations from the National Institute on Aging-Alzheimer's Association workgroups on diagnostic guidelines for Alzheimer's disease. *Alzheimers Dement* 7:263–269. <https://doi.org/10.1016/J.JALZ.2011.03.005>
11. Rascovsky K, Hodges JR, Knopman D et al (2011) Sensitivity of revised diagnostic criteria for the behavioural variant of frontotemporal dementia. *Brain* 134:2456–2477. <https://doi.org/10.1093/BRAIN/AWR179>
12. McKeith IG, Boeve BF, Dickson DW et al (2017) Diagnosis and management of dementia with Lewy bodies. *Neurology* 89:88–100. <https://doi.org/10.1212/WNL.0000000000004058>
13. Höglinger GU, Respondek G, Stamelou M et al (2017) Clinical diagnosis of progressive supranuclear palsy: the movement disorder society criteria. *Mov Disord* 32:853–864. <https://doi.org/10.1002/MDS.26987>
14. Tan B, Shishegar R, Poudel GR et al (2021) Cortical morphometry and neural dysfunction in Huntington's disease: a review. *Eur J Neurol* 28:1406–1419. <https://doi.org/10.1111/ENE.14648>
15. Oba H, Yagishita A, Terada H et al (2005) New and reliable MRI diagnosis for progressive supranuclear palsy. *Neurology* 64:2050–2055. <https://doi.org/10.1212/01.WNL.0000165960.04422.D0>
16. Massey LA, Jager HR, Paviour DC et al (2013) The midbrain to pons ratio. *Neurology* 80:1856–1861. <https://doi.org/10.1212/WNL.0B013E318292A2D2>
17. Morelli M, Arabia G, Novellino F et al (2011) MRI measurements predict PSP in unclassifiable parkinsonisms. *Neurology* 77:1042–1047. <https://doi.org/10.1212/WNL.0B013E31822E55D0>
18. Morelli M, Arabia G, Salsone M et al (2011) Accuracy of magnetic resonance parkinsonism index for differentiation of progressive supranuclear palsy from probable or possible Parkinson disease. *Mov Disord* 26:527–533. <https://doi.org/10.1002/MDS.23529>

19. Quattrone A, Morelli M, Nigro S et al (2018) A new MR imaging index for differentiation of progressive supranuclear palsy-parkinsonism from Parkinson's disease. *Parkinsonism Relat Disord* 54:3–8. <https://doi.org/10.1016/J.PARKRELDIS.2018.07.016>
20. Ho VB, Chuang HS, Rovira MJ, Koo B (1995) Juvenile Huntington disease: CT and MR features. *Am J Neuroradiol* 16:1405–1412
21. Fazekas F, Chawluk JB, Alavi A et al (2012) MR signal abnormalities at 1.5 T in Alzheimer's dementia and normal aging. *Am J Roentgenol* 149:351–356. <https://doi.org/10.2214/AJR.149.2.351>
22. Kim KW, MacFall JR, Payne ME (2008) Classification of white matter lesions on magnetic resonance imaging in elderly persons. *Biol Psychiatry* 64:273–280. <https://doi.org/10.1016/J.BIOPSYCH.2008.03.024>
23. Pasquier F, Leys D, Weerts JGE et al (1996) Inter- and intraobserver reproducibility of cerebral atrophy assessment on MRI scans with hemispheric infarcts. *Eur Neurol* 36:268–272. <https://doi.org/10.1159/000117270>
24. Scheltens P, Launer LJ, Barkhof F et al (1995) Visual assessment of medial temporal lobe atrophy on magnetic resonance imaging: interobserver reliability. *J Neurol* 242:557–560. <https://doi.org/10.1007/BF00868807>
25. Wahlund LO, Julin P, Johansson SE, Scheltens P (2000) Visual rating and volumetry of the medial temporal lobe on magnetic resonance imaging in dementia: a comparative study. *J Neurol Neurosurg Psychiatry* 69:630–635. <https://doi.org/10.1136/JNPNP.69.5.630>
26. Scheltens P, Kuiper M, Ch Wolters E et al (1992) Atrophy of medial temporal lobes on MRI in "probable" Alzheimer's disease and normal ageing: diagnostic value and neuropsychological correlates. *J Neurol Neurosurg Psychiatry* 55:967–972. <https://doi.org/10.1136/JNPNP.55.10.967>
27. Ingvar DH (1979) "Hyperfrontal" distribution of the cerebral grey matter flow in resting wakefulness; on the functional anatomy of the conscious state. *Acta Neurol Scand* 60:12–25. <https://doi.org/10.1111/J.1600-0404.1979.TB02947.X>
28. Hojjati SH, Ebrahimzadeh A, Babajani-Feremi A (2019) Identification of the early stage of Alzheimer's disease using structural MRI and resting-state fMRI. *Front Neurol* 10:904. <https://doi.org/10.3389/FNEUR.2019.00904/BIBTEX>
29. Paul S, Arora A, Midha R et al (2021) Autistic traits and individual brain differences: functional network efficiency reflects attentional and social impairments, structural nodal efficiencies index systemising and theory-of-mind skills. *Mol Autism* 12:1–18. <https://doi.org/10.1186/S13229-020-00377-8>
30. Skudlarski P, Jagannathan K, Anderson K et al (2010) Brain connectivity is not only lower but different in schizophrenia: a combined anatomical and functional approach. *Biol Psychiatry* 68: 61–69. <https://doi.org/10.1016/J.BIOPSYCH.2010.03.035>
31. Raichle ME, MacLeod AM, Snyder AZ et al (2001) A default mode of brain function. *Proc Natl Acad Sci U S A* 98:676–682. <https://doi.org/10.1073/PNAS.98.2.676>
32. Hohenfeld C, Werner CJ, Reetz K (2018) Resting-state connectivity in neurodegenerative disorders: is there potential for an imaging biomarker? *Neuroimage Clin* 18:849–870. <https://doi.org/10.1016/J.NICL.2018.03.013>
33. Greicius MD, Srivastava G, Reiss AL, Menon V (2004) Default-mode network activity distinguishes Alzheimer's disease from healthy aging: evidence from functional MRI. *Proc Natl Acad Sci* 101:4637–4642. <https://doi.org/10.1073/PNAS.0308627101>
34. Das SR, Pluta J, Mancuso L et al (2013) Increased functional connectivity within medial temporal lobe in mild cognitive impairment. *Hippocampus* 23:1–6. <https://doi.org/10.1002/HIPO.22051>
35. Huijbers XW, Schultz AP, Papp KV et al (2019) Tau accumulation in clinically normal older adults is associated with hippocampal hyperactivity. *J Neurosci* 39:548–556. <https://doi.org/10.1523/JNEUROSCI.1397-18.2018>
36. Leal SL, Landau SM, Bell RK, Jagust WJ (2017) Hippocampal activation is associated with longitudinal amyloid accumulation and cognitive decline. *Elife* 6. <https://doi.org/10.7554/ELIFE.22978>

37. Sperling RA, LaViolette PS, O'Keefe K et al (2009) Amyloid deposition is associated with impaired default network function in older persons without dementia. *Neuron* 63:178–188. <https://doi.org/10.1016/J.NEURON.2009.07.003>
38. Bandettini PA (2009) Functional MRI limitations and aspirations, pp 15–38. https://doi.org/10.1007/978-3-540-68044-4_2
39. Nagy Z, Lindstrom K, Westerburg H (2005) Diffusion tensor imaging on teenagers, born at term with moderate hypoxic-ischemic encephalopathy. *Pediatr Res* 58:936–940. <https://doi.org/10.1203/01.pdr.0000186516.85702.61>
40. Filley CM, Fields RD (2016) White matter and cognition: making the connection. *J Neurophysiol* 116:2093–2104. <https://doi.org/10.1152/JN.00221.2016/ASSET/IMAGES/LARGE/Z9K0111638630003.JPEG>
41. Acosta-Cabronero J, Nestor PJ (2014) Diffusion tensor imaging in Alzheimer's disease: insights into the limbic-diencephalic network and methodological considerations. *Front Aging Neurosci* 6:266. <https://doi.org/10.3389/FNAGI.2014.00266/ABSTRACT>
42. Mayo CD, Garcia-Barrera MA, Mazerolle EL et al (2019) Relationship between DTI metrics and cognitive function in Alzheimer's disease. *Front Aging Neurosci* 11:436. <https://doi.org/10.3389/FNAGI.2018.00436/BIBTEX>
43. Jacobs HIL, Hedden T, Schultz AP et al (2018) Structural tract alterations predict downstream tau accumulation in amyloid-positive older individuals. *Nat Neurosci* 21:424–431. <https://doi.org/10.1038/s41593-018-0070-z>
44. Song Z, Farrell ME, Chen X, Park DC (2018) Longitudinal accrual of neocortical amyloid burden is associated with microstructural changes of the fornix in cognitively normal adults. *Neurobiol Aging* 68:114–122. <https://doi.org/10.1016/J.NEUROBIOLAGING.2018.02.021>
45. Tang M, Chen X, Zhou Q et al (2015) Quantitative assessment of amyotrophic lateral sclerosis with diffusion tensor imaging in 3.0T magnetic resonance. *Int J Clin Exp Med* 8:8295
46. O'Donnell LJ, Westin CF (2011) An introduction to diffusion tensor image analysis. *Neurosurg Clin N Am* 22:185–196. <https://doi.org/10.1016/J.NEC.2010.12.004>
47. Tuch DS, Reese TG, Wiegell MR et al (2002) High angular resolution diffusion imaging reveals intravoxel white matter fiber heterogeneity. *Magn Reson Med* 48:577–582. <https://doi.org/10.1002/MRM.10268>
48. Tuch DS (2004) Q-ball imaging. *Magn Reson Med* 52:1358–1372. <https://doi.org/10.1002/MRM.20279>
49. Fernandez-Miranda JC, Pathak S, Engh J et al (2012) High-definition fiber Tractography of the human Brain neuroanatomical validation and neurosurgical applications. *Neurosurgery* 71:430–453. <https://doi.org/10.1227/NEU.0B013E3182592FAA>
50. Tourmier JD, Yeh CH, Calamante F et al (2008) Resolving crossing fibres using constrained spherical deconvolution: validation using diffusion-weighted imaging phantom data. *NeuroImage* 42:617–625. <https://doi.org/10.1016/J.NEUROIMAGE.2008.05.002>
51. Anazodo UC, Finger E, Kwan BYM et al (2018) Using simultaneous PET/MRI to compare the accuracy of diagnosing frontotemporal dementia by arterial spin labelling MRI and FDG-PET. *Neuroimage Clin* 17:405–414. <https://doi.org/10.1016/J.NICL.2017.10.033>
52. Du AT, Jahng GH, Hayasaka S et al (2006) Hypoperfusion in frontotemporal dementia and Alzheimer disease by arterial spin labeling MRI. *Neurology* 67:1215–1220. <https://doi.org/10.1212/01.WNL.0000238163.71349.78>
53. Diehn M, Nardini C, Wang DS et al (2008) Identification of noninvasive imaging surrogates for brain tumor gene-expression modules. *Proc Natl Acad Sci* 105:5213–5218. <https://doi.org/10.1073/PNAS.0801279105>
54. Zinn PO, Majadan B, Sathyan P et al (2011) Radiogenomic mapping of edema/cellular invasion MRI-phenotypes in glioblastoma multiforme. *PLoS One* 6:e25451. <https://doi.org/10.1371/JOURNAL.PONE.002545>
55. Panizzon MS, Fennema-Notestine C, Eyer LT et al (2009) Distinct genetic influences on cortical surface area and cortical thickness. *Cereb Cortex* 19:2728–2735. <https://doi.org/10.1093/CERCOR/BHP026>

56. Paul S, Mukherjee S, Bhattacharyya S (2019) Network organization of co-opetitive genetic influences on morphologies of the human cerebral cortex. *J Neural Eng* 16:026028. <https://doi.org/10.1088/1741-2552/AAFF85>
57. Moon SW, Dinov ID, Kim J et al (2015) Structural neuroimaging genetics interactions in Alzheimer's disease. *J Alzheimers Dis* 48:1051–1063. <https://doi.org/10.3233/JAD-150335>
58. Jahanshad N, Rajagopalan P, Hua X et al (2013) Genome-wide scan of healthy human connectome discovers SPON1 gene variant influencing dementia severity. *Proc Natl Acad Sci USA* 110:4768–4773. <https://doi.org/10.1073/PNAS.1216206110/-/DCSUPPLEMENTAL>
59. Häkkinen S, Chu SA, Lee SE (2020) Neuroimaging in genetic frontotemporal dementia and amyotrophic lateral sclerosis. *Neurobiol Dis* 145:105063. <https://doi.org/10.1016/J.NBD.2020.105063>



Machine Learning Approach in Brain Imaging

12

Yury V. Kistenev and Denis A. Vrazhnov

Abstract

Machine learning is widely used in visual data image analysis, recognition, and classification. This chapter gives an introduction to this field and describes how machine learning can be used in brain disorders diagnostics based on MRI and optical imaging modalities.

Keywords

Machine learning · MRI · Brain optical imaging · Brain tumors · Disorders of consciousness · Autism spectrum disorder · Alzheimer's disease · Parkinson's disease · Multiple sclerosis

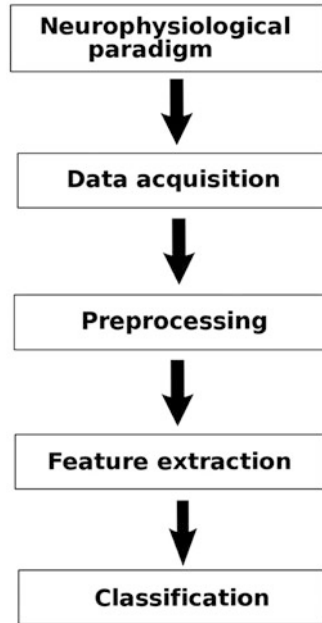
12.1 Introduction

Brain imaging helps achieve two goals: understanding brain functioning more deeply and extracting specific features from experimental data, which allows discriminating one brain state from another. The first breakthrough in brain imaging is connected with the analysis of **voxels** and parametric spatial mapping technique, allowing group analysis of brain structure and its functionality [1, 2]. The evident drawback is an inability to catch an individual human's brain state. A machine learning (ML) concept gives this issue a fundamental solution. The latter is associated with the so-called classification problem, solved by supervised ML methods.

In total, there are four branches of ML. Supervised ML allows making a decision about the belonging of a patient to one of the preliminarily determined classes.

Y. V. Kistenev · D. A. Vrazhnov (✉)
Tomsk State University, Tomsk, Russia

Fig. 12.1 Typical workflow for ML-based classification of brain imaging data [4]. (Reprinted under Elsevier license no. 5161970366985)



Supervised ML means that algorithms are trained on participants with established belonging to these classes. A typical workflow for ML-based classification of brain imaging data is shown in Fig. 12.1. Unsupervised ML algorithms allow us to make conclusions about the presence of possible classes with unknown origins in unlabeled data. Semi-supervised learning uses the benefits of both approaches mentioned above. It is useful when the volume of the training dataset is small [3]. Reinforcement learning uses a system of rewards and penalties to find an optimal solution for the given machine learning problem. The design of such a system varies and depends on the task.

Despite the achieved ML benefits, the following pitfalls exist in MP applications [1]:

1. *The best ML method does not exist.* You can find the most optimal method for specific data, but this method can fail in another situation.
2. *Overfitting.* A created data that fits the information well should have a necessary level of generalization. An illustration of the overfitting is shown in Fig. 12.2. In a small-volume dataset, we do not have enough information about the actual boundary between groups, and this uncertainty decreases when additional data appear. An appropriate split of dataset on training and testing samples and cross-validation methods is needed to evaluate this model performance correctly.
3. *Participants' labeling relatively belongs to a specific class.* Usually, it is conducted at the stage of a disease's evident clinical manifestations. A focus on imaging patterns in early pre-clinical brain states is preferable [1].

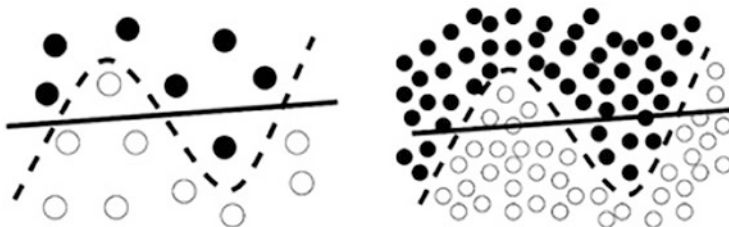


Fig. 12.2 An illustration of the overfitting [4]. (Reprinted under Elsevier license no. 5161970366985)

4. A majority of ML methods are “black-boxes.” Typical ML effectiveness criteria like the ROC-AUC confusion matrix give practically nothing about brain functionality disorder. A knowledge of informative features that affect brain state signatures is needed [1]. Deep learning networks, having a lot of free parameters, are good examples.
5. *Data heterogeneity.* When dealing with a very complicated biological system like the brain, it is tough to find a set of informative characteristics that characterize its current stage and functioning perfectly. As a rule, multiple concurrent features sets can be extracted from experimental data. High-dimensional data models and data fusion methods suit heterogeneous data analysis [5]. But the study of high-dimensional data is closely related to the “curse of dimensionality” problem [6]. The latter’s essence is associated with the exponential growth of the volume of data needed for the classifier training, when the feature vector’s dimension increases linearly. According to the central limit theorem, it is due to tending to zero the difference between two random vectors when their dimension is increased [7]. Data fusion can be conducted at three levels: merging the data itself, obtained by various experimental methods, combining informative features from different datasets, and merging various predictive models. All three levels are closely related to the stages of the ML pipeline.

12.2 Brain Optical Imaging

Brain optical imaging is a functional visualization tool that allows noninvasive imaging of hemodynamics and metabolism in the brain, studying its structure and function in vivo, especially in the animal brain [8].

The major limitation of brain optical imaging is connected with the effects of light scattering, causing image aberrations and penetration depth to decrease. A model-based technique for sensorless adaptive optics aberration corrections based on machine learning has been developed [9]. Similar aberrations are associated with an unknown phase function. This model mimics the acquisition of scanning microscope two-photon image, taking into account free parameters related to the sample’s aberration. Machine learning uses preliminarily defined associations between

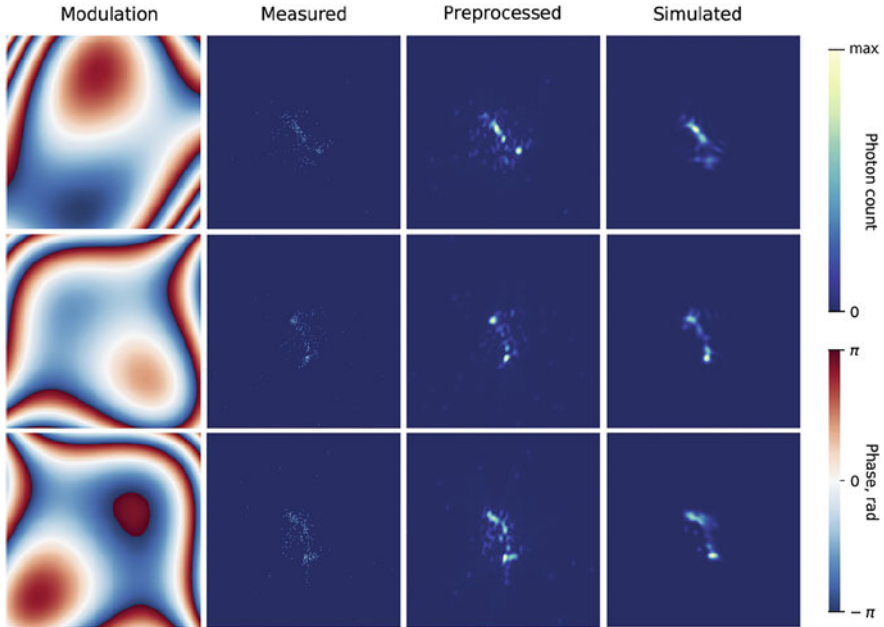


Fig. 12.3 Correspondence between computationally generated and experimentally measured. (Taken from [9])

randomly generated phase patterns and image aberrations. Twenty pairs of spatial light modulator (SLM) phase aberrations and reciprocal two-photon images were recorded in total by photon counting. The recording frame rate was 30 Hz. The sum of the first ten Zernike modes allows to compute probing phase modulations. The corresponding coefficients are calculated from a uniform random distribution in the $[-1, 1]$ interval. The fluorescent beads images and the relations of numerically simulated and experimental data are shown in Fig. 12.3.

The rows in Fig. 12.3 correspond to different examples of an aberration sample. The first column contains probing modulation on SLM. The second column displays photon counting images with the point spread function (PSF). The third column preprocessed demonstrates images prepared for model fitting. The optimized model simulation results are given in the fourth column. The size of the image is $40 \times 40 \mu\text{m}$ [9].

Near Infra-Red (NIR) light penetrates a biological tissue more actively than being visible due to light scattering and absorbance properties at longer wavelengths. The effective tissue penetration depth is about 1–2 cm because of a transparency window at wavelengths ranging from 650 to 950 nm. The second transparency window lies between 1000 and 1350 nm (Fig. 12.4) [10, 11]. The penetration depth depends on the photon propagation regime, from the (quasi)ballistic (typically ≤ 1 mm in soft tissue) to the diffusive regimes (typically ≥ 10 mm in soft tissue), up to the dissipation limit (~ 10 cm in soft tissue) [12]. Optical tissue clearing based on diffusion of

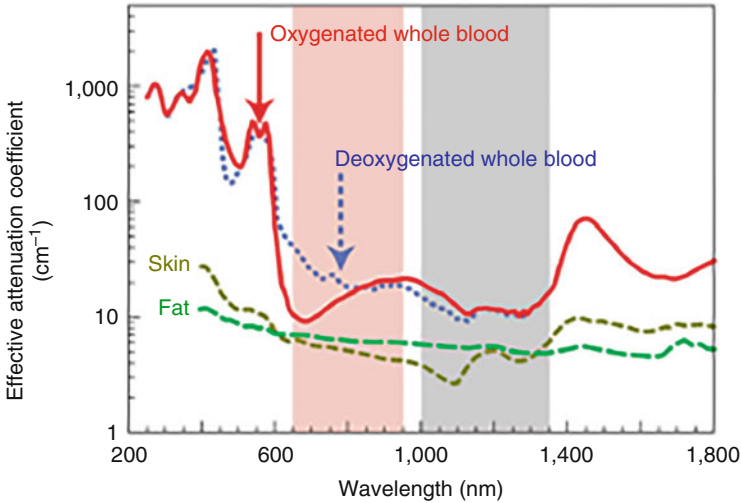


Fig. 12.4 The effective attenuation coefficient of tissue (on a log scale) versus wavelength [10, 11]. (Reprinted under Springer Nature license no. 5161970075140)

special agents into tissue, which cause temporal reducing its scattering and absorption properties, allows increasing depth of optical waves tissue penetration [13].

Neural activity can be studied by the neurovascular coupling (NVC) approach. The latter uses the spatial and temporal correlation between neural activity and hemodynamic responses [14]. The following are NVC optical methods: (a) intrinsic signal optical imaging, (b) functional near-infrared spectroscopy (fNIRS) [15], (c) diffuse correlation spectroscopy (DCS) [16]. The latter specificity is using speckle images of diffusely reflected light in tissue to analyze the motions of red blood cells with high temporal resolution (up to 100 Hz) and large penetration depth (up to ~ 1.5 cm). This approach uses a modification of the Beer-Lambert law, taking light scattering into account, to get correct estimations of relative oxygenation levels [17].

Neurons have a complicated spatial structure: the length of the axon (up to a few millimeters) is far larger than its diameter ($1 \mu\text{m}$) [18, 19]. Therefore, a neuron's conventional 3D optical imaging is impossible. Several direct hardware-oriented solutions were proposed. For example, the spinning disk scanning technique allows block-face serial microscopy tomography to acquire images of a mouse brain with a resolution of $0.7 \times 0.7 \times 5 \mu\text{m}$ and reduce imaging time up to several hours [20]. Structured illumination microscopy (SIM), using a high-speed micro-mirror device with a voxel size of $0.32 \times 0.32 \times 2 \mu\text{m}$, was created, providing a mouse whole-brain imaging in 77 h [21]. A deep learning big data processing has the potential to overcome this limitation of optical devices [22]. The combination of automatic histological sectioning and optical microscopy leads to a new hardware-oriented approach [23], for example, whole-brain imaging by deep-learning-based fluorescence micro-optical sectioning tomography (DL-fMOST) [24]. A comparison

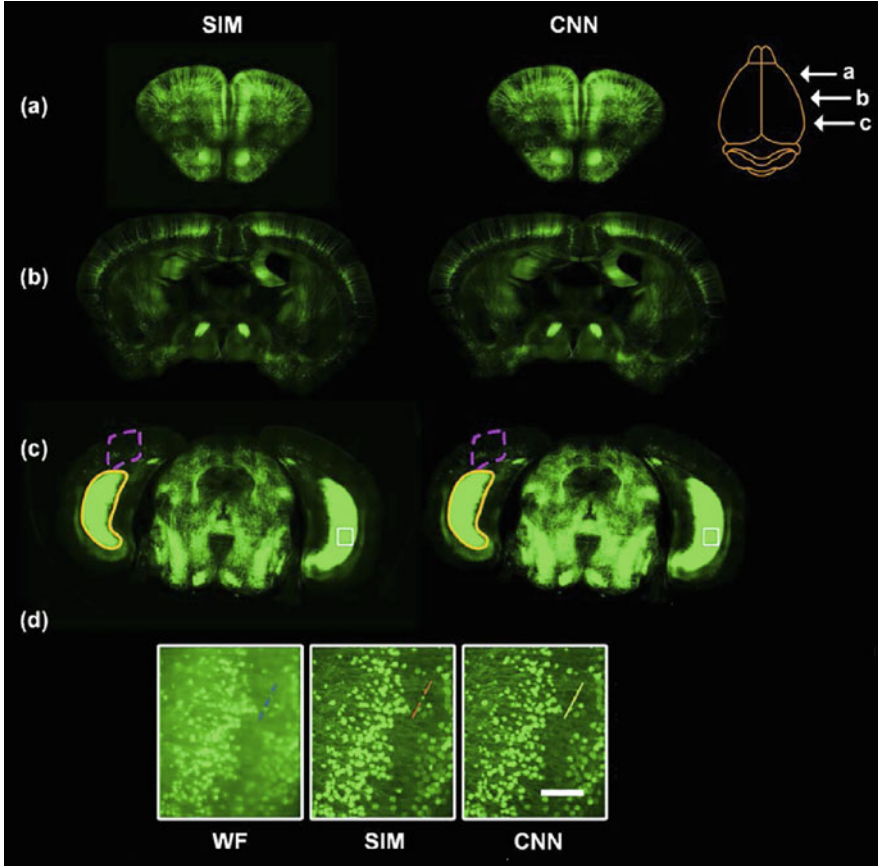


Fig. 12.5 DL-fMOST imaging of a Thy1-GFP M line mouse brain. (a–c) 200- μm -thick images of different coronal sections (2 mm interval) reconstructed by SIM and a deep-learning network prediction. Arrows at the top right corner indicate the locations of the coronal sections. (d) Enlarged views of the white rectangles in (c). The wide-field image is shown for comparison [24]

of maximum intensity projections (MIP) of mouse brain coronal sections acquired by the created method and the SIM is shown in Fig. 12.5 [24].

Optical coherence tomography is an optical method of real-time visualization of tissue structure with a spatial resolution of several micrometers. OCT was shown to differentiate tumorous and healthy brain tissues [25–27]. A machine learning technique was developed to separate brain malignant tumorous from healthy tissues [28]. The total number of the brain cancer tissue samples B-scans was 14,336. A machine learning pipeline included texture features extraction from B-scans, principal component analysis for noise and dimensionality reduction, and a support vector machine for the classification. The optimal texture parameters were computed by a grid search procedure. The example of the application of the algorithm for a threshold accuracy of 90% is shown in Fig. 12.6. Histology was used as a reference

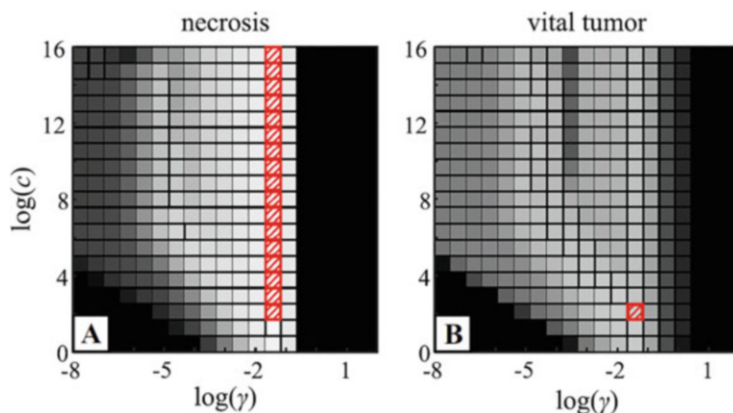


Fig. 12.6 Results of the grid search for the best SVM classification accuracy achieved for the two studied tissue types (a) necrosis, (b) vital tumor [28]

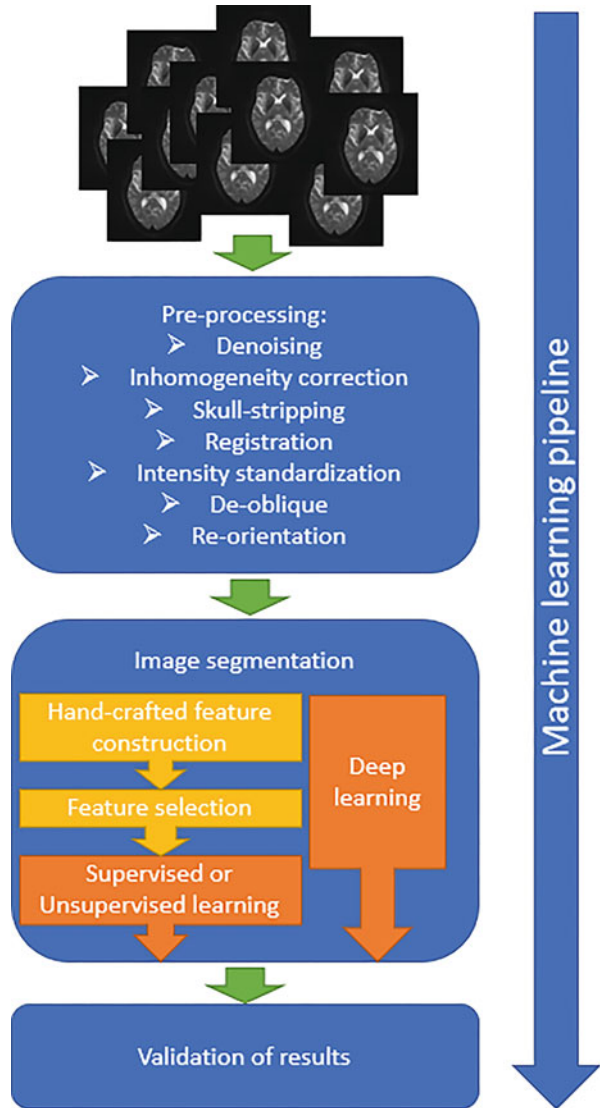
method. The authors reported the minimization of the metastases risk by using the developed approach and optimizing the tumor resection.

The ex vivo estimation of extravasation into the brain can be performed employing transcatheter perfusion. Still, its efficiency can be significantly decreased by the influence of the pathological remodeling process, particularly in tumor vasculature. This problem was solved by combining 3D imaging, machine learning, and optical clearing methods [29]. The authors created two effective machine learning algorithms, providing a measurable characteristic of both blood vessels' structure of a tumor and compound extravasation patterns. It is a new semiautomatic computer vision technique for sample analysis.

12.3 Magnetic Resonance Imaging

Magnetic Resonance Imaging (MRI) is a set of 2D intensity maps visualizing brain slices. Each map can be considered as a grayscale image, and computer vision algorithms can be applied to a region of interest estimation (segmentation). Some studies analyze the whole set of maps as 3D images, but the computation cost of processing such objects is exceptionally high, so GPU or computer clusters are needed. Computer vision algorithms allow detecting edges of brain regions, restoring damaged/noisy images, and performing segmentation of MRI. The first two tasks are auxiliary, while segmentation is the most interesting. Image segmentation is usually performed by the Machine Learning (ML) pipeline (see Fig. 12.7). The ML methods can be roughly divided into two classes, depending on how image features are generated. The “hand-crafted” features class includes methods with explicitly defined feature creation algorithms together with classification or clusterization. On the opposite side is deep learning methods, which have feature creation embedded into classification/clusterization of artificial neural networks [1].

Fig. 12.7 A standard machine learning pipeline for MRI processing



12.3.1 MRI Modalities

There are three major types of MRI, namely: structural MRI (sMRI), diffusion MRI (dMRI), and functional MRI (fMRI). sMRI includes T1-weighted (T1-w) and T2-weighted imaging (T2-w) and gives a detailed static information of brain anatomy. dMRI generates diffusion of water molecules vector for each voxel. Fractional anisotropy (FA) and mean diffusivity (MD) are the main quantitative features of dMRI, allowing to find pathologies in the subtle white matter fiber tract. fMRI

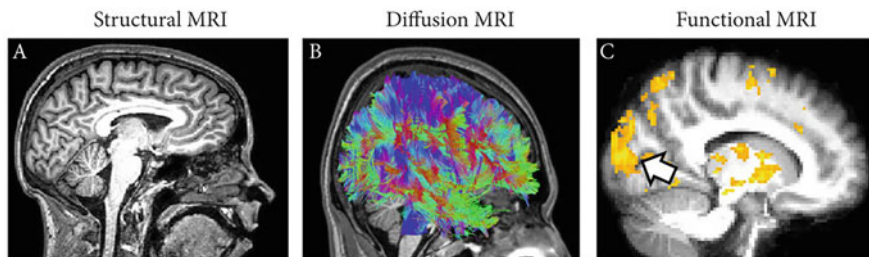


Fig. 12.8 Examples of sMRI (a), dMRI (b), and fMRI (c) images. (Taken from [31])

includes resting-state fMRI (rsfMRI) and task fMRI. These modalities can obtain dynamic physiological data because they are connected to the oxygen saturation in blood [30]. The brain's resting state is described by the metabolism, which, in turn, depends on blood oxygenation. Thus, the pathology of functional network connectivity can be revealed by fMRI. sMRI images are usually time independent. In contrast, dMRI and fMRI are time sequences. The examples of different modalities are presented in Fig. 12.8.

MRI technique computes various proton relaxation times allowing tissues differentiation [32]. Longitudinal (T1) is the time required for excited protons to return to equilibrium. It highlights the bone marrow and subcutaneous fat tissues while cerebrospinal fluid remains dark. Transverse (T2) time indicates the decaying of MR signal in the corresponding plane. It visualizes both adipose and water-based tissues. Two main parameters in the MRI study are Repetition Time (TR) and Time to Echo (TE). TR is a temporal period between pulse sequences on a single slice. TE is the time required for the RF pulse to reach the target and reflect. T1-weighted (T1-w) images correspond to short TE and TR times (approximately TR = 500 ms, TE = 14 ms), while T2-weighted (T2-w) obtained by longer TE and TR times (approximately TR = 4000 ms, TE = 90 ms). A very long TE and TR time allows to generate the so-called fluid attenuated inversion recovery (Flair) (approximately TR = 9000 ms, TE = 114 ms). The difference between them can be seen in Fig. 12.9.

12.3.2 MRI Image Preprocessing

Preprocessing the MRI data is required because image artifacts, intensity heterogeneity, etc., can lead to poor segmentation, classification quality, and misdiagnosis of the disease. The list of preprocessing methods depends on MRI modality—time-dependent dMRI and fMRI requires additional head motion compensation algorithms. Static MRI requires intensity registration, standardization, re-orientation, denoising, inhomogeneity correction, skull-stripping, and de-oblique [33]. Several automated preprocessing tools for fMRI [34, 35] and dMRI [36] were recently presented.

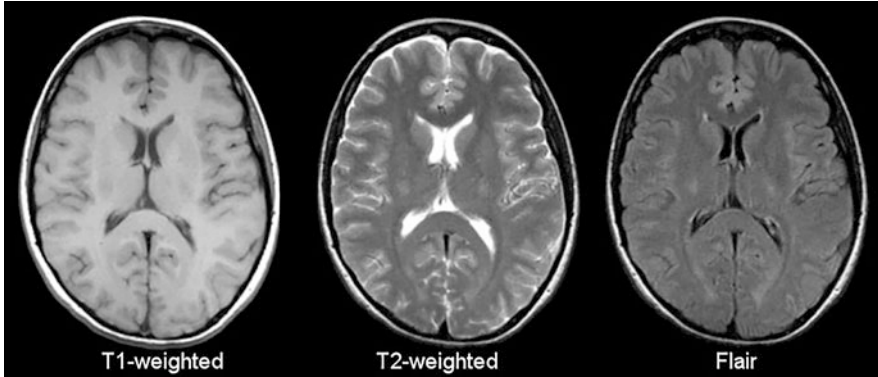


Fig. 12.9 Examples of T1-weighted, T2-weighted, and FLAIR images [32]. Cerebrospinal fluid has high intensity on T2-weighted images

12.3.2.1 Denoising

The random noise that occurs during image acquisition can be removed by various techniques. Low-pass filters can remove high-frequency noise, making edges blurry [37]. Fourier filters look more effective [38], eliminating specific noise-related components. They assume that noise has the same characteristics over the image, which is generally not valid. Wavelet filters [39] are more flexible due to localization both in frequency and time. The drawbacks of the approaches mentioned above give rise to nonlinear filters, such as anisotropic diffusion (edge-preserving property), non-local means filter (keeps the underlying anatomy), and collaborative filtering [40, 41]. Deep learning methods like DnCNN [42] also show good potency in this field [43, 44] (see Fig. 12.10).

12.3.2.2 Inhomogeneity Correction

A low-frequency variation in MRI image intensity occurs due to intensity decline (see Fig. 12.11). The correction of such inhomogeneity is performed mainly by modeling the bias of the field by an expectation-maximization algorithm and by histogram-based methods [46]. The least-squares generative adversarial neural network can rectify intensity inhomogeneity artifacts, so predicted segmentation results coincide with ground truth, and values of standard Structural Similarity Index and Peak Signal-to-Noise Ratio are higher than alternative methods [47].

12.3.2.3 Skull-Stripping

The skull-stripping procedure removes non-brain tissue from consideration, increasing the accuracy of applied supervised and unsupervised ML techniques [35, 41]. An automatic skull-stripping method SMHASS (Simplex Mesh and Histogram Analysis Skull Stripping) uses deformable models and histogram analysis [49]. The creation of the deformable model requires an optimal starting point and rough morphology-based segmentation was made. Additionally, this step was to model the image's gray level, in turn, to control simplex mesh deformation. Another automated approach

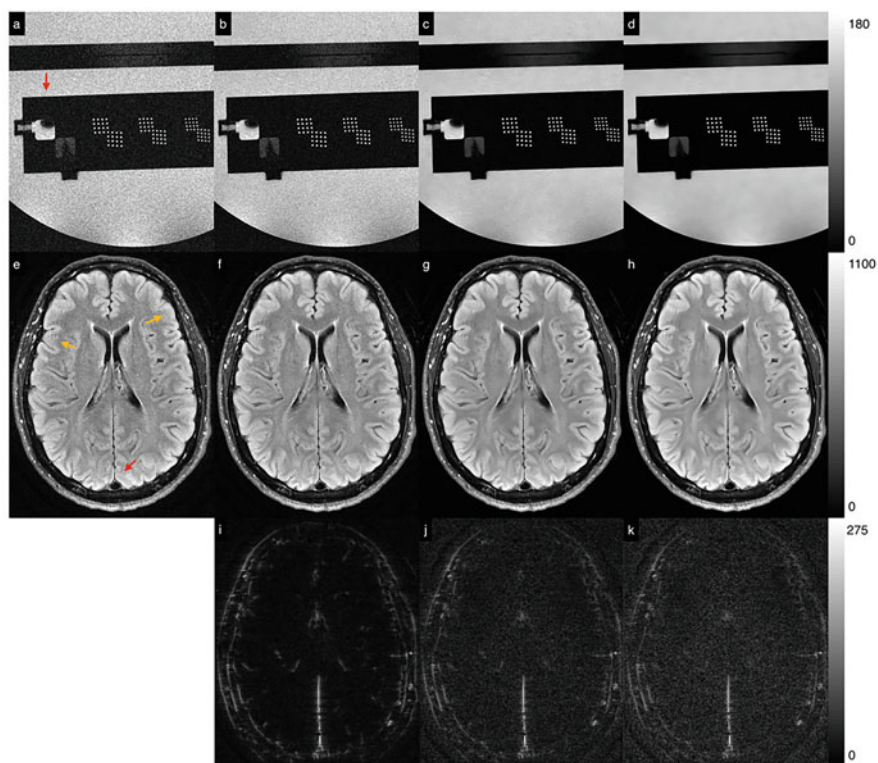


Fig. 12.10 AIR™ Recon DL performance at different denoising levels in a phantom and in vivo. Original raw images in a cropped portion of the large ACR MRI phantom (a) and in vivo (e). AIR™ Recon DL images at denoising levels of 0.30 (b, f), 0.75 (c, g), and 1.0 (d, h). Different images (i–k) between the in vivo images reconstructed with and without AIR™ Recon DL show constant ringing suppression but with the specified denoising level. Structures visible at edges in the different images represent removed truncation artifacts, not losing details. In all cases, AIR™ Recon DL removes ringing from the raw images (red arrows); motion artifacts in the in vivo image (yellow arrows) are unchanged. AIR™ Recon DL is insensitive to scaling of the source images, which differ by approximately an order of magnitude in this example. (Reprinted by permission from Marc R. Lebel [45])

called HEAD (Human Encephalon Automatic Delimiter) combines mathematical morphology and histogram analysis to achieve accurate brain segmentation [50]. These approaches suffer from two major drawbacks: morphology results depend on fixed parameters (shape and size of structural elements), and optimal values for them can be found only during experiments; the rough segmentation also requires human assistance to set a start point. A good review and classification of skull-stripping methods can be found elsewhere [51] (see Fig. 12.12). An example of a skull-stripping procedure can be seen in Fig. 12.13.

Deep learning methods can be 2D and 3D. A 2D neural network designed for segmentation, such as fully connected U-NET [52], encoder-decoder SegNet [53],

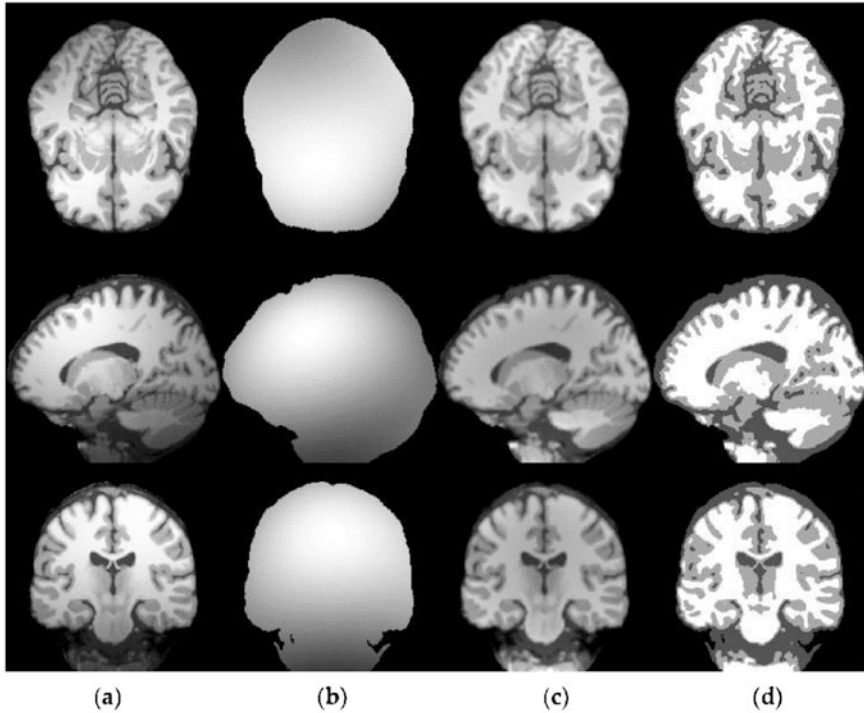


Fig. 12.11 Inhomogeneity correction examples: (a) original images; (b) estimated bias field; (c) bias field correction images; and (d) segmentation results. (Taken from [48])

and different versions of DeepLab [54], requires thousands of annotated images but, once trained, show excellent performance [51]. A 3D network can be modifications of 2D ones, like 3D U-Net [55], but they are incredibly time-consuming to train.

12.3.2.4 Registration

The registration refers to an alignment of MRI images of one brain from different sources by projecting them to a standard space like MNI or by combining several MRI modalities for further analysis [52]. A simple approach is called principal axes and assumes that the brain has an ellipsoid shape, so it has three features: center of mass and major and minor axes. An eigenvalue decomposition operation can perform aligning images using them [53]. Another approach is using correlation and Fourier Transform (FT). First, two images are projected by FT. Second, the result is projected to polar coordinates, and finally, the angle of image rotation is found by correlation. An optical flow-based method that uses differential flow estimation is fully automatic and takes into account intensity variations of the images [54]. The most complex algorithm is the public available Automated Image Registration (AIR) method. It uses all image pixels to define a single, global transformation. The AIR advantages include full automatization, applicability for various

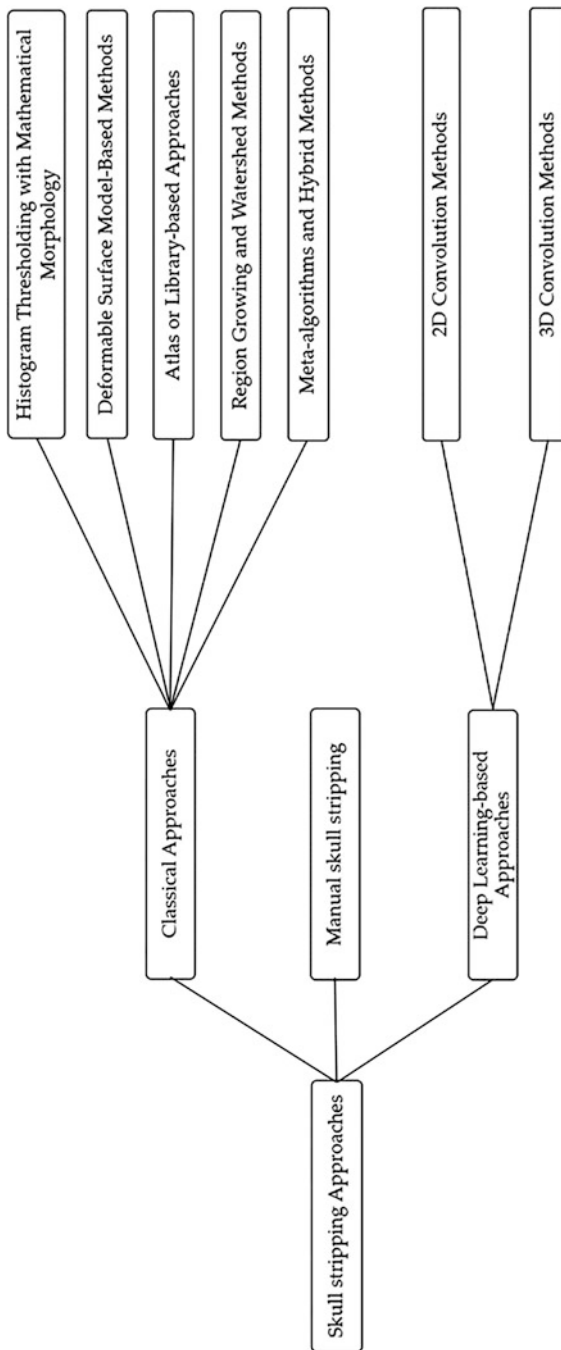


Fig. 12.12 A classification of skull-stripping methods. (Taken from [51])

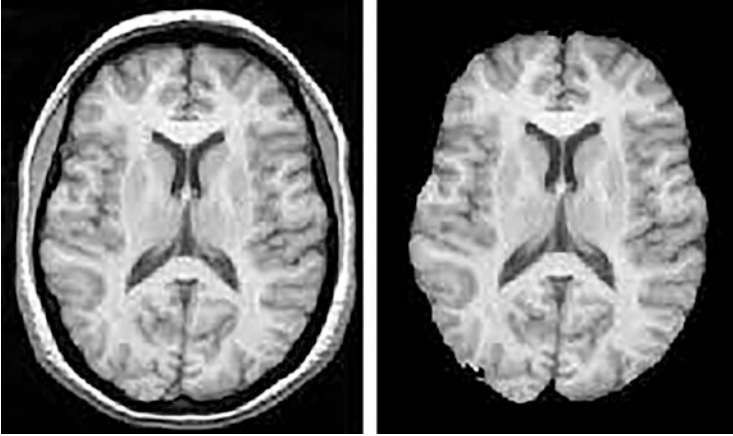


Fig. 12.13 Skull-stripping example. The skull was removed, and only the brain remains. (Taken from [51])

experimental methods, no necessary of landmark identification, and an iterativity of the algorithm [55].

12.3.2.5 Intensity Standardization

The study of images obtained from different scanners requires intensity standardization by histogram matching [56] applied before the segmentation stage. GetNet is a modification of ResNet neural network architecture [57]. It was trained on the ImageNet dataset and tested on 12,000 synthetic MRIs, created by BrainWeb and the author's random gain generator, and compared to the N4ITK algorithm [58, 59]. It uses a low-frequency gain field of size 16×16 , computed from an input image of size 256×256 . The mean absolute error, calculated for cerebrospinal fluid, GM, and WM on the original and corrected images, shows improvement up to tenth order. The example of intensity standardization can be seen in Fig. 12.14.

12.3.2.6 De-oblique

The particular type of scanning (oblique) is used to avoid humidity in the nose and eyes, which, in turn, causes visual artifacts on MRI images. The bonus of using oblique is in lower noise level compared to MRI without oblique [60]. De-oblique can be performed by a free software AFNI (Analysis of Functional NeuroImages), 3drefit function [35, 61]. The example of the de-oblique procedure can be seen in Fig. 12.15.

12.3.2.7 Re-orientation

Re-orientation of images is needed if they have different orientations and are applied before the registration stage [35]. The idea of re-orientation is shown in Fig. 12.16. It can be performed by the "3dresample" function in the AFNI package.

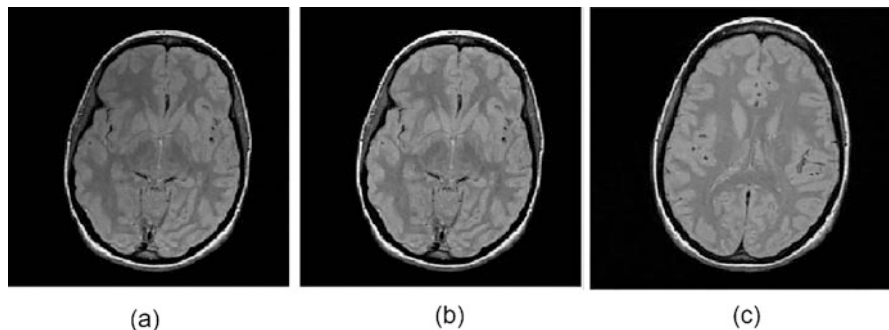


Fig. 12.14 Intensity standardization example. (a) Original MRI slice, (b) Same slice with intensity inhomogeneity correction, (c) Another slice with both intensity inhomogeneity correction and standardization [56]. (Reprinted under Elsevier license no. 5161971050868)

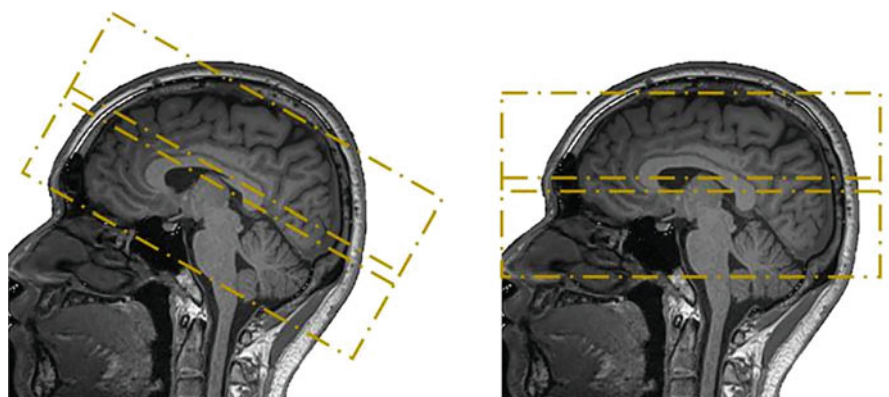


Fig. 12.15 Illustration of de-oblique procedure. (Taken from [35])

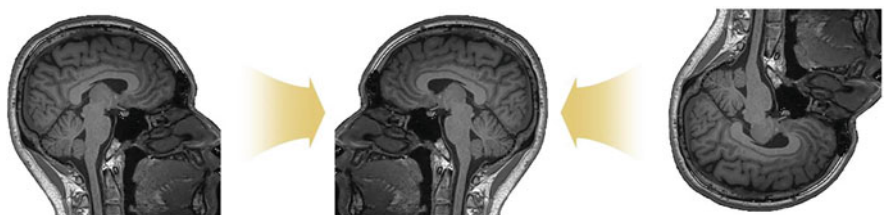


Fig. 12.16 Illustration of re-orientation process. (Taken from [35])

12.3.2.8 Motion Compensation

Various motion compensation and eddy current correction of fMRI and dMRI methods and their combinations were studied, but no perfect solution was found [62–65]. Several problems were highlighted: motion can increase the fractional anisotropy metrics for low anisotropy regions and vice versa; residual motion effects

Table 12.1 A list of widely used neuroimaging data processing tools

Package name	Modalities	Link
SPM (Statistical Parametric Mapping)	fMRI, PET, SPECT, EEG, MEG.	https://www.fil.ion.ucl.ac.uk/spm/
AFNI (Analysis of Functional NeuroImages)	sMRI, fMRI, dMRI	https://afni.nimh.nih.gov/
FSL (FMRIB Software Library)	sMRI, fMRI, dMRI	https://fsl.fmrib.ox.ac.uk/fsl/fslwiki
FreeSurfer	sMRI, fMRI, dMRI, PET	https://surfer.nmr.mgh.harvard.edu/
Workbench	Data from ConnectomeDB	https://www.humanconnectome.org/software/connectome-workbench
fMRIPrep	fMRI	https://fmriprep.org/en/stable/

affect the data despite movement correction techniques applied; the strength of connections inside the brain of different people is reduced, while the strengths of inconsistent connections are increased; the motion effects depend on the tractography algorithm applied for dMRI [62, 66]. A free tool for motion artifact removal for dMRI images is available [63, 67]. The comparison of various motion correction tools for fMRI is presented in Ref. [68].

A list of widely used neuroimaging data processing tools is presented in Table 12.1. After proper preprocessing of MRI is made, next step is to construct features and segment images. The choice of particular algorithms confides in brain pathology study and the amount of data available. Later, we will discuss brain pathologies and the application of specific ML methods.

12.4 Brain Pathologies

12.4.1 Brain Tumors

Brain tumors are solid ones with various shapes, textures, locations, and are the most frequent oncology reason for child mortality. Almost half of the brain tumors arise from the posterior fossa located between the cerebellum and foramen magnum. Such tumor location makes surgical resection possible, yet the chance of the occurrence of pathologies is very high. Successful surgery requires knowledge of tumor type and its boundaries. Depending on the location, brain tumors are classified into gliomas, central nervous system lymphomas, neuromas, pituitary tumors, and meningiomas [69].

An ML pipeline with hand-crafted features was used in [69] to classify pediatric brain tumors. 124 pediatric patients with posterior fossa tumors (55 Medulloblastomas, 36 Pilocytic Astrocytomas, 26 Ependymomas, 4 Atypical Teratoid Rhabdoid Tumors, and 3 other low-grade tumors) were scanned using dMRI across 12 different hospitals and 18 different scanners. Images were created

with $b = 0$, $b = 1000$ s/mm² parameters. The apparent diffusion coefficient (ADC) maps generated by the clinical PACS systems were used as input data to create 180 bin histograms. Specific post-processing includes computation of first and second-order statistical moments, Skew, Kurtosis, and the various quantiles used to create feature vectors. Next, principal component analysis was applied to lower the dimensionality of feature vectors and reduce noise. The results were classified by supervised learning: Naïve Bayes (NB) and Random Forest algorithms. Validation of the predictive models was performed by ten-fold cross-validation.

Another machine learning model for the diagnostic of brain tumor constructed with backpropagation ANN and trained on T2-w images was introduced in [70]. 304 T2-w scans, made up of 247 tumors and 57 healthy brain images, were collected both in Shenjing Hospital of China Medical University and Beijing Tian Tan Hospital of Capital Medical University. The data validation split was in proportion of 214/87 of training and test samples, respectively. Trained dataset includes 177 tumors and 40 normal brain images. The test dataset includes 70 tumors and 17 normal brain images. A new thresholding procedure for background removal based on low order statistics was proposed. The histogram equalization procedure intensified image contrast, and Gaussian kernel filtering was used for noise removal before it. Specifics of T2-w tumors have a higher intensity than healthy ones, so Gray Level Co-Occurrence Matrix (GLCM) was computed with the following parameters: the direction is 180°, the offset is 1. The final texture features were constructed based on various GLCM elements: homogeneity, entropy, energy, contrast, and correlation. The classification improvement was performed by applying an extended set-membership filter (ESMF). The idea of ESMF is to use the prediction-correction framework to incorporate observation data into the prediction model.

12.4.2 Disorders of Consciousness

Consciousness is described by two main components: wakefulness and awareness. Disorders of consciousness (DOC) means the severance between them. Patients with DOC can be classified into three categories: vegetative state (VS), also known as unresponsive wakefulness syndrome, minimally conscious state (MCS), and emerging from a minimally conscious state [71]. The neural mechanisms of DOC are still unclear, so such studies can help understand the organization of conscious process.

DOC was investigated by fMRI analysis in [71]. The study includes 56 patients with severe brain injuries diagnosed as DOC. Only 38 patients were selected after the inclusion criteria check. The controls group consisted of healthy subjects with mean age 41. The data was handled by the Data Processing Assistant for Resting-State fMRI (DPARSF) toolbox [72]. Also, T1-weighted images were coupled with the fMRI and divided into three classes by the Diffeomorphic Anatomical Registration Through Exponentiated Lie algebra tool: cerebrospinal fluid (CSF), white matter (WM), and gray matter (GM). A regression was used to remove noisy data from the CSF, WM, linear trends, global signal, and Friston 24-parameter model

[73]. A motion filtering procedure (scrubbing), when TRs with excessive motion or signal deviation are removed, was performed. The variance analysis of the mean framewise displacement shows that there was no significant difference among groups under study ($F(2, 76) = 10.5, P < 0.001$). In the last step, acquired data was projected to Montreal Neurological Institute (MNI) space and transformed to voxels of $3 \times 3 \times 3$ mm dimensions. The signal-to-noise ratio was enhanced by the Gaussian smoothing procedure with 6 mm kernel size. Each voxel was represented by the average square root of power in the low-frequency range of low-frequency fluctuation (ALFF) feature amplitude. The modification of ALFF by the restraining nonspecific signal components is called fALFF. The dynamic fALFF (dfALFF) features were computed by the sliding time window analysis and included the standard deviation, mean, and coefficient of variation (CV) of fALFF values. The 246 brain regions were selected according to the human Brainnetome Atlas and average dfALFF, and CV values for these regions were used as a feature vector. Together with the static fALFF features, computed and the different frequency bands, they were classified by the linear kernel SVM. The five-fold CV was used to validate models.

12.4.3 Autism Spectrum Disorder

A complex state related to brain development is an autism spectrum disorder (ASD). ASD affects the social communication, restricted interests, and repetitive behavior of a patient. Autism is highly heritable and considered a lifelong disease with different degrees of impairment in the functioning of individuals. Precise diagnostics in the early stages of ASD may drastically raise patients' quality of life. Diagnosis of ASD is difficult because of complicated pathogenesis. There is currently no unbiased ASD biomarker, and diagnosis is made according to direct behavior observations by the specialist and clinical interviews [74]. The analysis of functional connectivity of healthy and ASD subjects' differences in GM and WM volumes calculated by MRI can be a promising tool for creating a neurological ASD biomarker. This complex task with latent information is ideal for machine learning methods [75].

Accent in studies of MRI brain imaging of autism spectrum disorder moved from sMRI to fMRI [74]. The availability of open databases like the Autism Brain Imaging Data Exchange (ABIDE) [76] increased the sample size. However, a negative correlation between classification score and the sample size was found (see Fig. 12.1). The preprocessing methods are usually data-dependent and are out of the scope of the work [74]. Feature engineering must consider the unique advantages of imaging modalities, so anatomical features (GM and WM volume, cortical morphology, geometry, WM microstructure descriptors) are used in sMRI [77–82]. Functional connectivity is the main feature for fMRI [83–85], along with regional homogeneity (ReHo), ALFF, and network metrics. The spatial relations of brain regions can be described by constructing features from voxels, predefined regions of interest (ROI), and networks (interaction profiles of a set of voxels or ROI) [86, 87]. The high dimensionality of the data under study requires a feature

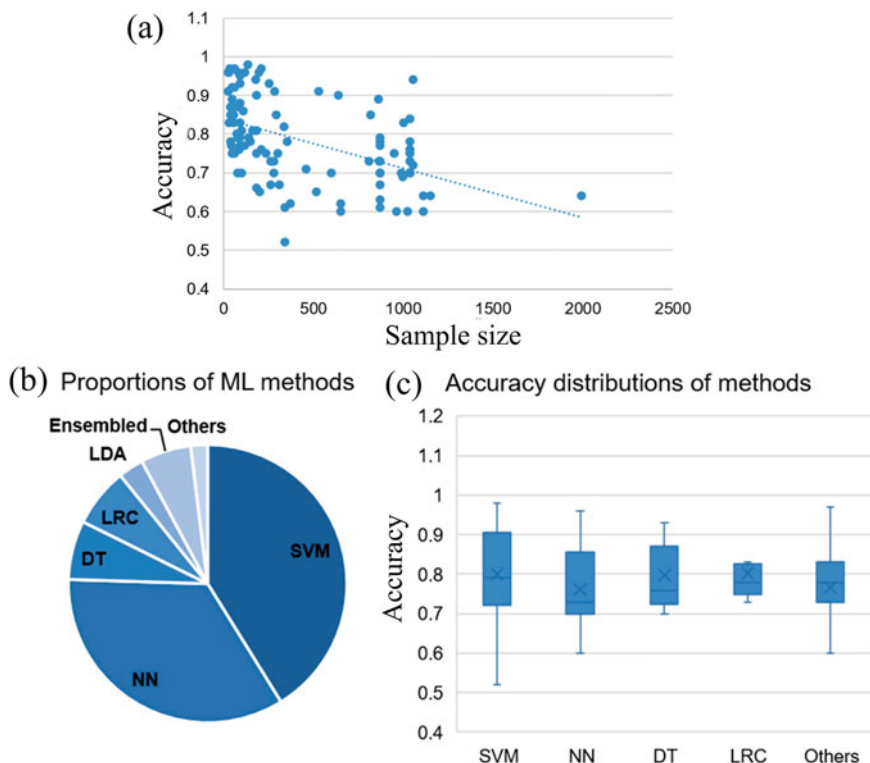


Fig. 12.17 The negative correlation of accuracy and sample size (a), proportions of ML methods (b), and accuracy distributions of corresponding methods (c) [74]. (Reprinted under Elsevier license no. 5161940506706)

selection step, so Principal and Independent component analysis, Recursive feature elimination, and LASSO are applied.

Major ML classification tools are presented in Fig. 12.17. The classification results are validated by CV methods: k-fold CV, leave-one-out CV, and stratified k-fold CV. Receiver Operator Characteristics (ROC) analysis proves that the predictive model performs better than random guessing. The confusion tables can be additionally tested by McNemar's and Friedman's tests [88]. The ML methods are susceptible to the dataset's quality, including classes intersections and bias. Future work aims to gather large-scale datasets that consider significant gender bias and comorbidity information. Another option is to analyze multi-modal data via data fusion techniques [89]. The complexity of the predictive models often comes at the cost of model transparency and interpretability [90].

12.4.4 Alzheimer's Disease

Alzheimer's Disease (AD) is a progressive brain disorder that can lead to the death of entire nerve cells, tissue loss, and fatal for the patient. It is the most common form

of dementia, with no effective drug therapy or surgery. Patients with AD first develop subtle memory loss and personality changes compared to healthy people. Also, they are particularly susceptible to depression. AD development takes decades, and early clinical stage diagnostics is complicated.

An sMRI brain imaging makes significant advances in Alzheimer’s Disease (AD) diagnostics. There are three stages of AD: early, middle, or prodromal, also called Mild Cognitive Impairment (MCI), and late. The difference between them is hard to distinguish due to the hidden development of AD. Morphological brain characteristics like hippocampal volume, cortical disease, and subcortical volume coupled with texture analysis and longitudinal biomarkers are applied to voxels to construct “hand-crafted” features [91–95]. The common problem of sMRI image analysis needs much expert knowledge [96]. An alternative approach is to use machine learning techniques to automatically create the best features for a given sMRI dataset [97–99]. A more complex approach incorporates 3D information into convolutional neural networks architecture [100–102]. Improved classification can be obtained by specifying ROI and removing irrelevant information from consideration [103–105]. The following datasets can be used for the study of AD: ADNI-1 and ADNI-2 (Alzheimer’s Disease Neuroimaging Initiative [106]); MIRIAD (Minimal Interval Resonance Imaging in Alzheimer’s Disease [107]) (see Table 12.2).

An example of the preprocessing of sMRI images for AD study can be found in [96]. It includes anterior commissure-posterior commissure correction. Intensity inhomogeneity caused by shading artifacts was removed by the N3 algorithm [108] (see Fig. 12.18). An example of N3 correction can be seen in Fig. 12.2. Regions of interest were selected by skull stripping and removing invalid areas while the brain locations remained. The intensity of images was corrected by min-max normalization. The images were resized to $90 \times 90 \times 90$ for the input of CNN.

12.4.5 Multiple Sclerosis

Multiple Sclerosis (MS) is another demyelinating disorder of the central nervous system, damaging nerve fibers and cells that produce myelin. MS has four stages, and it isn’t easy to distinguish between them [110–113]. The damage of myelin

Table 12.2 Alzheimer’s disease dataset short description

Dataset	Class	Number of subjects
ADNI-1	NC	199
	MCI	332
	AD	141
MIRIAD	NC	23
	AD	46
ADNI-2	NC	146
	MCI	114
	AD	111

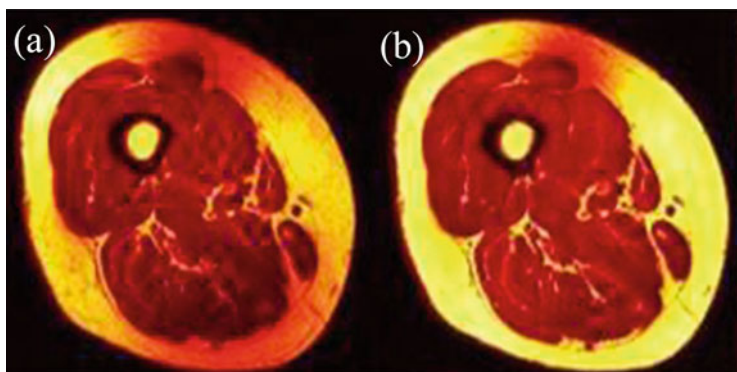


Fig. 12.18 N3 algorithm performance: (a) original image and (b) after N3 correction. (Taken from [109])

sheath decreases fat and increases water on MRI scans as an area of high intensity or lesions [33]. MRI datasets for MS lesion analysis are MICCAI 2008 [114], MICCAI 2008 [115], ISBI 2015 [116], The 2015 Longitudinal MS lesion segmentation challenge [117], simulated MRI volumes at BrainWeb [118], and eHealth Lab [119]. Following MRI modalities are used for MS lesion segmentation: 2D and 3D T1-w scans can be used to differentiate GM and WM tissues, T2-w coupled with T1-w scans to obtain T1/T2 ratio as a measure of tissue integrity T2-FLAIR and T1-w images to classify lesions. Low-level preprocessing uses a common pipeline (Fig. 12.1). The segmentation can be made by trained 2D or 3D convolutional neural networks (CNN) [120–122] with U-Net [52, 123–125] and FCN [126] architectures. Another well-suited architecture is Generative Adversarial Networks [127–131].

Another study of MS was conducted in [132]. The training set consists of 6322 patients, while the test set volume is 3068 patients. The following parameters were similar to all datasets: Expanded Disability Status Scale (EDSS), disease duration, and demographic data. 13 of 18 MRI measured features showed a significant difference. These features were processed by SuStaIn algorithm [123]. The goal was used to estimate groups depending on the quantitative characteristics of biomarkers instead of commonly used periods. It can be a prominent approach because it considers individual features of patients, which is a step towards personalized medicine. The ML pipeline used in this study is presented in Fig. 12.19.

12.4.6 Parkinson's Disease

Parkinson's disease (PD) damages neural cells in a special brain region (substantia nigra) that produce dopamine. The symptoms are different from one patient to another and develop very slowly. Though the disease is not fatal, there is no cure, only treatment with drugs and surgery. The severity of PD is usually measured by Unified Parkinson's Disease Rating Scale (UPDRS). The classification of PD is as

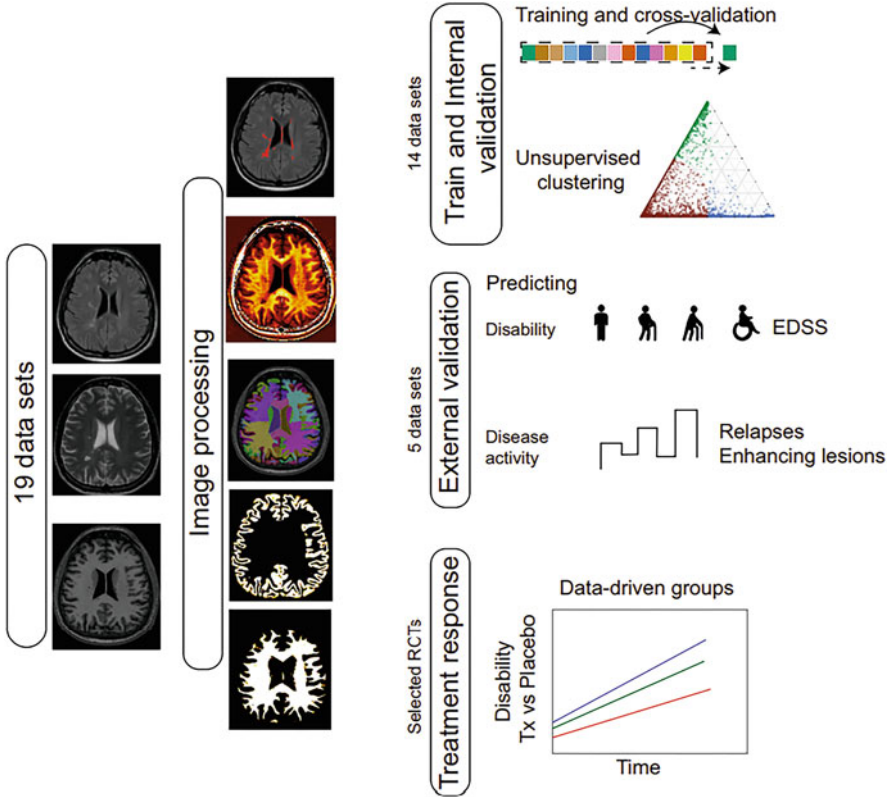


Fig. 12.19 A pipeline for the study of MS using 19 datasets. (Taken from [132])

follows: tremor-dominant (TD) and postural instability/gait difficulty (PIGD)-dominant [133].

Parkinson’s disease was studied by fMRI [133]. The dataset includes 96 PD patients: 57 were TD, and 39 were PIGD. Preprocessing steps include a temporal band-pass filter (0.01–0.08 Hz), removing noisy data, head motion correction, slice timing, transformation to the MNI space, creating isotropic $3 \times 3 \times 3$ mm sized voxels, linear detrending, and nuisance covariates regression. The following features were used: mean ReHo, voxel-mirrored homotopic connectivity (VMHC), mean ALFF, functional connectivity (FC), and degree centrality (DC). Correlation analysis and spatial smoothing create a connectivity matrix, the upper part containing 6670 values used as final features. Feature selection was performed by z -score standardization, t -test correction, and p -value thresholding, followed by LASSO regression [134]. Finally, Spearman’s rank correlation analysis (threshold was set to 0.8) was applied to eliminate multicollinearity. The most informative features were fed to the Radial-Based (RBF) kernel Support Vector Machine. The AUC analysis validated the resulting predictive model. RBF SVM does not allow us to understand each feature contributing to the prediction result. Thus, the SHAP

algorithm [135] was applied, and it was discovered that mean ReHo and FC of the frontal regions are most informative.

References

1. Davatzikos C (2019) Machine learning in neuroimaging: progress and challenges. *NeuroImage* 197:652–656. <https://doi.org/10.1016/j.neuroimage.2018.10.003>
2. Friston KJ et al (1994) Statistical parametric maps in functional imaging: a general linear approach. *Hum Brain Mapp* 2(4):189–210
3. Chapelle O, Scholkopf B, Zien A (2009) Semi-supervised learning. *IEEE Trans Neural Netw* 20(3):542–542
4. Lemm S et al (2011) Introduction to machine learning for brain imaging. *NeuroImage* 56:387–399
5. Borr E et al (2015) Data fusion methodologies for food and beverage authentication and quality assessment. A review. *Anal Chim Acta* 891:1–14
6. Bellman RE (2003) *Dynamic programming*. Princeton University Press, Princeton, NJ
7. Kistenev YV, Borisov AV, Vrazhnov DA (2021) Medical applications of laser molecular imaging and machine learning. SPIE Press, Bellingham. ISBN: 9781510645349
8. Hillman EMC (2007) Optical brain imaging in vivo: techniques and applications from animal to man. *J Biomed Opt* 12(5):051402
9. Vishniakou I, Seelig JD (2021) Differentiable model-based adaptive optics for two-photon microscopy. *Opt Express* 29(14):21418–21427
10. Moller U, Cooke DG, Tanaka K, Jepsen PU (2009) Terahertz reflection spectroscopy of Debye relaxation in polar liquids. *J Opt Soc Am B* 26(9):A113–A125
11. Smith AM, Mancini MC, Nie S (2009) Second window for in vivo imaging. *Nat Nanotechnol* 4(11):710–711. <https://doi.org/10.1038/nnano.2009.326>
12. Wang LV, Yao J (2016) A practical guide to photoacoustic tomography in the life sciences. *Nat Methods* 13(8):627–638. <https://doi.org/10.1038/nmeth.3925>
13. Zhu D, Larin KV, Luo Q, Tuchin VV (2013) Recent progress in tissue optical clearing. *Laser Photonics Rev* 7(5):732–757
14. Soekadar SR, Kohl SH, Mihara M, von Lüthmann A (2021) Optical brain imaging and its application to neurofeedback. *NeuroImage Clin* 30:102577
15. Durduran T, Yodh AG (2014) Diffuse correlation spectroscopy for noninvasive, microvascular cerebral blood flow measurement. *NeuroImage* 85(1):51–63. <https://doi.org/10.1016/j.neuroimage.2013.06.017>
16. Scholkopfmann F, Kleiser S, Metz AJ, Zimmermann R, Mata Pavia J, Wolf U, Wolf M (2014) A review on continuous wave functional near-infrared spectroscopy and imaging instrumentation and methodology. *NeuroImage* 85(1):6–27. <https://doi.org/10.1016/j.neuroimage.2013.05.004>
17. Delpy DT, Cope M, Zee PVD, Arridge S, Wray S, Wyatt JS (1988) Estimation of optical pathlength through tissue from direct time of flight measurement. *Phys Med Biol* 33(12):1433–1442
18. Shepherd GMG, Raastad M, Andersen P (2002) General and variable features of varicosity spacing along unmyelinated axons in the hippocampus and cerebellum. *Proc Natl Acad Sci U S A* 99(9):6340–6345
19. Sun Y, Nguyen AQ, Nguyen JP, Le L, Saur D, Choi J, Callaway EM, Xu X (2014) Cell-type-specific circuit connectivity of hippocampal CA1 revealed through Cre-dependent rabies tracing. *Cell Rep* 7(1):269–280
20. Seiriki K et al (2017) High-speed and scalable whole-brain imaging in rodents and primates. *Neuron* 94(6):1085–1100.e6

21. Gong H et al (2016) High-throughput dual-colour precision imaging for brain-wide connectome with cytoarchitectonic landmarks at the cellular level. *Nat Commun* 7(1):12142
22. de Haan K, Rivenson Y, Wu Y, Ozcan A (2020) Deep-learning-based image reconstruction and enhancement in optical microscopy. *Proc IEEE* 108(1):30–50
23. Yuan J, Gong H, Li A, Li X, Chen S, Zeng S, Luo Q (2015) Visible rodent brain-wide networks at single-neuron resolution. *Front Neuroanat* 9:70
24. Ning K et al (2020) Deep-learning-based whole-brain imaging at single-neuron resolution. *Biomed Opt Express* 11(7):3567–3584
25. Böhringer HJ, Boller D, Leppert J, Knopp U, Lankenau E, Reusche E, Hüttmann G, Giese A (2006) Time-domain and pectral-domain optical coherence tomography in the analysis of brain tumor tissue. *Lasers Surg Med* 38:588–597. <https://doi.org/10.1002/lsm.20353>
26. Bizheva K, Unterhuber A, Hermann B, Povazay B, Sattmann H, Fercher AF, Drexler W, Preusser M, Budka H, Stingl A, Le T (2005) Imaging ex vivo healthy and pathological human brain tissue with ultra-high-resolution optical coherence tomography. *J Biomed Opt* 10: 011006. <https://doi.org/10.1117/1.1851513>
27. Böhringer HJ, Lankenau E, Stellmacher F, Reusche E, Hüttmann G, Giese A (2009) Imaging of human brain tumor tissue by nearinfrared laser coherence tomography. *Acta Neurochir (Wien)* 151:507–517. <https://doi.org/10.1007/s00701-009-0248-y>
28. Muller J et al (2021) Applying machine learning to optical coherence tomography images for automated tissue classification in brain metastases. *Int J Comput Assist Radiol Surg* 16:1517–1526. <https://doi.org/10.1007/s11548-021-02412-2>
29. Kostrikov S et al (2021) Optical tissue clearing and machine learning can precisely characterize extravasation and blood vessel architecture in brain tumors. *Commun Biol* 4:815. <https://doi.org/10.1038/s42003-021-02275-y>
30. Ogawa S et al (1990) Brain magnetic resonance imaging with contrast dependent on blood oxygenation. *Proc Natl Acad Sci* 87(24):9868–9872
31. Hirsch GV, Bauer CM, Merabet LB (2015) Using structural and functional brain imaging to uncover how the brain adapts to blindness. *Ann Neurosci Psychol* 2:5
32. MRI basics (2021). <https://case.edu/med/neurology/NR/MRI%20Basics.htm>. Accessed 1 Oct 2021
33. Shoeibi A et al (2021) Applications of deep learning techniques for automated multiple sclerosis detection using magnetic resonance imaging: a review. Preprint at <https://arxiv.org/abs/2105.04881>
34. Cohen S, Ruppín E, Dror G (2005) Feature selection based on the shapley value. In: *Proceedings of the nineteenth international joint conference on artificial intelligence*. Edinburgh, Scotland, UK, July 30–August 5, 2005
35. Park BY, Byeon K, Park H (2019) FuNP (fusion of neuroimaging preprocessing) pipelines: a fully automated preprocessing software for functional magnetic resonance imaging. *Front Neuroinform* 13:5
36. Esteban O, Markiewicz CJ, Blair RW et al (2019) fMRIPrep: a robust preprocessing pipeline for functional MRI. *Nat Methods* 16(1):111–116
37. Rajeshwari S, Sree ST (2013) Efficient quality analysis of MRI image using preprocessing techniques. In: *2013 IEEE conference on information & communication technologies*. IEEE, Piscataway, NJ
38. Stetter E, Graumann R, Schmitt F (1985) Preprocessing steps on Fourier MRI raw data. In: *Computer assisted radiology/Computergestützte Radiologie*. Springer, Berlin
39. Pérez G et al (2014) Rician noise attenuation in the wavelet packet transformed domain for brain MRI. *Integr Comput Aided Eng* 21(2):163–175
40. Cai LY, Yang Q, Hansen CB, Nath V, Ramadass K et al (2021) PreQual: an automated pipeline for integrated preprocessing and quality assurance of diffusion weighted MRI images. *Magn Reson Med* 86(1):456–470
41. Manjón JV (2017) MRI preprocessing. In: *Imaging biomarkers*. Springer, Cham

42. Mäkinen Y, Azzari L, Foi A (2020) Collaborative filtering of correlated noise: exact transform-domain variance for improved shrinkage and patch matching. *IEEE Trans Image Process* 29:8339–8354
43. Zhang K, Zuo W, Chen Y, Meng D, Zhang L (2017) Beyond a Gaussian denoiser: residual learning of deep CNN for image denoising. *IEEE Trans Image Process* 26(7):3142–3155
44. Koonjoo N, Zhu B, Bagnall GC, Bhutto D, Rosen MS (2021) Boosting the signal-to-noise of low-field MRI with deep learning image reconstruction. *Sci Rep* 11(1):1–16
45. Lebel RM (2020) Performance characterization of a novel deep learning-based MR image reconstruction pipeline. Preprint at <https://arxiv.org/abs/2008.06559>
46. Vovk U, Pernus F, Likar B (2007) A review of methods for correction of intensity inhomogeneity in MRI. *IEEE Trans Med Imaging* 26(3):405–421
47. Venkatesh V, Sharma N, Singh M (2020) Intensity inhomogeneity correction of MRI images using InhomoNet. *Comput Med Imaging Graph* 84:101748
48. Zhang Z, Song J (2019) A robust brain MRI segmentation and bias field correction method integrating local contextual information into a clustering model. *Appl Sci* 9(7):1332
49. Galdames FJ, Jailliet F, Perez CA (2012) An accurate skull stripping method based on simplex meshes and histogram analysis for magnetic resonance images. *J Neurosci Methods* 206(2):103–119
50. Balan AG, Traina AJ, Ribeiro MX, Marques PM, Traina C Jr (2012) Smart histogram analysis applied to the skull-stripping problem in T1-weighted MRI. *Comput Biol Med* 42(5):509–522
51. Rehman HZU, Hwang H, Lee S (2020) Conventional and deep learning methods for skull stripping in brain MRI. *Appl Sci* 10(5):1773
52. Ronneberger O, Fischer P, Brox T (2015) U-net: convolutional networks for biomedical image segmentation. In: *International conference on medical image computing and computer-assisted intervention*. Springer, Cham
53. Badrinarayanan V, Kendall A, Cipolla R (2017) Segnet: a deep convolutional encoder-decoder architecture for image segmentation. *IEEE Trans Pattern Anal Mach Intell* 39(12):2481–2495
54. Chen LC, Papandreou G, Kokkinos I, Murphy K, Yuille AL (2014) Semantic image segmentation with deep convolutional nets and fully connected crfs. Preprint at <https://arxiv.org/abs/1412.7062>
55. Hwang H, Rehman HZU, Lee S (2019) 3D U-Net for skull stripping in brain MRI. *Appl Sci* 9(3):569
56. Zhuge Y, Udupa JK (2009) Intensity standardization simplifies brain MR image segmentation. *Comput Vis Image Underst* 113(10):1095–1103
57. Simkó A, Löfstedt T, Garpebring A, Nyholm T, Jonsson J (2019) A generalized network for MRI intensity normalization. Preprint at <https://arxiv.org/abs/1909.05484>
58. Woods RP, Mazziotta JC, Cherry SR (1993) MRI-PET registration with automated algorithm. *J Comput Assist Tomogr* 17(4):536–546
59. Tustison NJ, Avants BB, Cook PA, Zheng Y, Egan A, Yushkevich PA, Gee JC (2010) N4ITK: improved N3 bias correction. *IEEE Trans Med Imaging* 29(6):1310–1320
60. Sadeghi D, Shoeibi A, Ghassemi N, Moridian P, Khadem A, Alizadehsani R et al (2021) An overview on artificial intelligence techniques for diagnosis of schizophrenia based on magnetic resonance imaging modalities: methods, challenges, and future works. Preprint at <https://arxiv.org/abs/2103.03081>
61. AFNI software. <https://afni.nimh.nih.gov/>. Accessed 1 Oct 2021
62. Oldham S et al (2020) The efficacy of different preprocessing steps in reducing motion-related confounds in diffusion MRI connectomics. *NeuroImage* 222:117252
63. Andersson JLR, Stamatiou NS (2016) An integrated approach to correction for off-resonance effects and subject movement in diffusion MR imaging. *NeuroImage* 125:1063–1078
64. Ciric R et al (2017) Benchmarking of participant-level confound regression strategies for the control of motion artifact in studies of functional connectivity. *NeuroImage* 154:174–187
65. Parkes L et al (2018) An evaluation of the efficacy, reliability, and sensitivity of motion correction strategies for resting-state functional MRI. *NeuroImage* 171:415–436

66. Baum GL et al (2018) The impact of in-scanner head motion on structural connectivity derived from diffusion MRI. *NeuroImage* 173:275–286
67. Eddy software. <https://fsl.fmrib.ox.ac.uk/fsl/fslwiki/eddy>. Accessed 1 Oct 2021
68. Oakes TR et al (2005) Comparison of fMRI motion correction software tools. *NeuroImage* 28(3):529–543
69. Novak J et al (2021) Classification of paediatric brain tumours by diffusion weighted imaging and machine learning. *Sci Rep* 11(1):1–8
70. Song G et al (2021) Automatic brain tumour diagnostic method based on a back propagation neural network and an extended set-membership filter. *Comput Methods Prog Biomed* 208: 106188
71. Yu Y et al (2021) Disrupted strength and stability of regional brain activity in disorder of consciousness patients: a resting-state functional magnetic resonance imaging study. *Neuroscience* 469:59–67
72. DPABI dataset. <http://rfmri.org/DPABI>. Accessed 1 Oct 2021
73. Friston KJ, Williams S, Howard R, Frackowiak RS, Turner R (1996) Movement-related effects in fMRI time-series. *Magn Reson Med* 35:346–355
74. Xu M et al (2021) Brain imaging-based machine learning in autism spectrum disorder: methods and applications. *J Neurosci Methods* 361:109271
75. Sui J, Jiang R, Bustillo J, Calhoun V (2020) Neuroimaging-based individualized prediction of cognition and behavior for mental disorders and health: methods and promises. *Biol Psychiatry* 88(11):818–828
76. ABIDE dataset. http://fcon_1000.projects.nitrc.org/indi/abide/
77. Ecker C et al (2010) Describing the brain in autism in five dimensions—magnetic resonance imaging-assisted diagnosis of autism spectrum disorder using a multiparameter classification approach. *J Neurosci* 30(32):10612–10623
78. Ecker C et al (2010) Investigating the predictive value of whole-brain structural MR scans in autism: a pattern classification approach. *NeuroImage* 49(1):44–56
79. Jiao Y et al (2010) Predictive models of autism spectrum disorder based on brain regional cortical thickness. *NeuroImage* 50(2):589–599
80. Uddin LQ et al (2011) Multivariate searchlight classification of structural magnetic resonance imaging in children and adolescents with autism. *Biol Psychiatry* 70(9):833–841
81. Ingalhalikar M et al (2010) DTI based diagnostic prediction of a disease via pattern classification. In: *International conference on medical image computing and computer-assisted intervention*. Springer, Berlin
82. Lange N et al (2010) Atypical diffusion tensor hemispheric asymmetry in autism. *Autism Res* 3(6):350–358
83. Anderson JS et al (2011) Decreased interhemispheric functional connectivity in autism. *Cereb Cortex* 21(5):1134–1146
84. Kazeminejad A, Sotero RC (2019) Topological properties of resting-state fMRI functional networks improve machine learning-based autism classification. *Front Neurosci* 12:1018
85. Plitt M, Barnes KA, Martin A (2015) Functional connectivity classification of autism identifies highly predictive brain features but falls short of biomarker standards. *NeuroImage Clin* 7: 359–366
86. Thomas RM et al (2020) Classifying autism spectrum disorder using the temporal statistics of resting-state functional MRI data with 3D convolutional neural networks. *Front Psych* 11:440
87. Zhao F et al (2020) Diagnosis of autism spectrum disorder using central-moment features from low-and high-order dynamic resting-state functional connectivity networks. *Front Neurosci* 14:258
88. Japkowicz N, Mohak S (2015) Performance evaluation in machine learning. In: *Machine learning in radiation oncology*. Springer, Cham
89. Qi S, Morris R, Turner JA, Fu Z, Jiang R et al (2020) Common and unique multi-modal covarying patterns in autism spectrum disorder subtypes. *Mol Autism* 11(1):1–15

90. Abrol A, Fu Z, Salman M, Silva R, Du Y, Plis S, Calhoun V (2021) Deep learning encodes robust discriminative neuroimaging representations to outperform standard machine learning. *Nat Commun* 12(1):1–17
91. Guo T et al (2021) Longitudinal cognitive and biomarker measurements support a unidirectional pathway in Alzheimer's disease pathophysiology. *Biol Psychiatry* 89(8):786–794
92. Luk CC et al (2018) Alzheimer's disease: 3-dimensional MRI texture for prediction of conversion from mild cognitive impairment. *Alzheimer's Dementia Diagn Assess Dis Monit* 10:755–763
93. Fuse H et al (2018) Detection of Alzheimer's disease with shape analysis of MRI images. In: 2018 Joint 10th international conference on soft computing and intelligent systems (SCIS) and 19th international symposium on advanced intelligent systems (ISIS). IEEE, Piscataway, NJ
94. Benedet AL et al (2020) SNAP25 reflects amyloid-and tau-related synaptic damage: associations between PET, VBM and cerebrospinal fluid biomarkers of synaptic dysfunction in the Alzheimer's disease spectrum: neuroimaging: imaging the human synapse in AD. *Alzheimers Dement* 16:e046358
95. Leandrou S et al (2020) Assessment of Alzheimer's disease based on texture analysis of the entorhinal cortex. *Front Aging Neurosci* 12:176
96. Qiao H et al (2021) Early Alzheimer's disease diagnosis with the contrastive loss using paired structural MRIs. *Comput Methods Prog Biomed* 208:106282
97. Li Q et al (2021) Deep learning based neuronal soma detection and counting for Alzheimer's disease analysis. *Comput Methods Prog Biomed* 203:106023
98. Liu M et al (2020) A multi-model deep convolutional neural network for automatic hippocampus segmentation and classification in Alzheimer's disease. *NeuroImage* 208:116459
99. Lian C et al (2020) Attention-guided hybrid network for dementia diagnosis with structural MR images. *IEEE Trans Cybernet.* <https://doi.org/10.1109/TCYB.2020.3005859>
100. Liu J et al (2021) Alzheimer's disease detection using depthwise separable convolutional neural networks. *Comput Methods Prog Biomed* 203:106032
101. Wen J et al (2020) Convolutional neural networks for classification of Alzheimer's disease: overview and reproducible evaluation. *Med Image Anal* 63:101694
102. Jin D et al (2019) Attention-based 3D convolutional network for Alzheimer's disease diagnosis and biomarkers exploration. In: IEEE 16th international symposium on biomedical imaging (ISBI 2019). IEEE, Piscataway, NJ
103. Wang L et al (2020) Region-of-interest based sparse feature learning method for Alzheimer's disease identification. *Comput Methods Prog Biomed* 187:105290
104. Liu M et al (2018) Landmark-based deep multi-instance learning for brain disease diagnosis. *Med Image Anal* 43:157–168
105. Lian C et al (2018) Hierarchical fully convolutional network for joint atrophy localization and Alzheimer's disease diagnosis using structural MRI. *IEEE Trans Pattern Anal Mach Intell* 42(4):880–893
106. Alzheimer's disease neuroimaging initiative. <http://adni.loni.usc.edu>. Accessed 1 Oct 2021
107. MIRIAD dataset. <http://miriad.drc.ion.ucl.ac.uk/>. Accessed 1 Oct 2021
108. Sled JG, Zijdenbos AP, Evans AC (1998) A nonparametric method for automatic correction of intensity nonuniformity in MRI data. *IEEE Trans Med Imaging* 17(1):87–97
109. MIPAV software. https://mipav.cit.nih.gov/pubwiki/index.php/Shading_Correction:_Inhomogeneity_N3_Correction. Accessed 1 Oct 2021
110. Chung KK et al (2020) A 30-year clinical and magnetic resonance imaging observational study of multiple sclerosis and clinically isolated syndromes. *Ann Neurol* 87(1):63–74
111. Burt RK et al (2019) Effect of nonmyeloablative hematopoietic stem cell transplantation vs continued disease-modifying therapy on disease progression in patients with relapsing-remitting multiple sclerosis: a randomized clinical trial. *JAMA* 321(2):165–174
112. Rocca MA et al (2017) Long-term disability progression in primary progressive multiple sclerosis: a 15-year study. *Brain* 140(11):2814–2819

113. Kappos L et al (2018) Siponimod versus placebo in secondary progressive multiple sclerosis (EXPAND): a double-blind, randomised, phase 3 study. *Lancet* 391(10127):1263–1273
114. 2008 MICCAI MS lesion segmentation challenge. <https://www.nitrc.org/projects/msseg>. Accessed 1 Oct 2021
115. MS new lesions segmentation challenge using a data management and processing infrastructure. <https://portal.fli-iam.irisa.fr/msseg-2/data/>. Accessed 1 Oct 2021
116. Longitudinal multiple sclerosis lesion segmentation: resource and challenge. <https://smart-stats-tools.org/lesion-challenge>. Accessed 1 Oct 2021
117. 2015 Longitudinal MS lesion segmentation challenge. <http://iacl.ece.jhu.edu/index.php?title=MSChallenge/data>. Accessed 1 Oct 2021
118. BrainWeb: simulated MRI volumes for brain with multiple sclerosis lesions. https://brainweb.bic.mni.mcgill.ca/brainweb/selection_ms.html. Accessed 1 Oct 2021
119. MRI lesion segmentation in multiple sclerosis database. eHealth Lab. <http://www.medinfo.cs.ucy.ac.cy/index.php/facilities/32-software/218-datasets>. Accessed 1 Oct 2021
120. La Rosa F, Abdulkadir A, Fartaria MJ et al (2020) Multiple sclerosis cortical and WM lesion segmentation at 3T MRI: a deep learning method based on FLAIR and MP2RAGE. *NeuroImage Clin* 27:102335
121. Aslani S, Dayan M, Murino V, Sona D (2018) Deep 2D encoder-decoder convolutional neural network for multiple sclerosis lesion segmentation in brain MRI. In: International MICCAI brainlesion workshop. Springer, Cham
122. Narayana PA, Coronado I, Robinson M, Sujit SJ et al (2018) Multimodal MRI segmentation of brain tissue and T2-hyperintense white matter lesions in multiple sclerosis using deep convolutional neural networks and a large multi-center image database. In: 2018 9th Cairo international biomedical engineering conference (CIBEC). IEEE, Piscataway, NJ, pp 13–16
123. Python SuStain software. <https://github.com/ucl-pond/pySuStain>. Accessed 1 Oct 2021
124. Wei W, Poirion E, Bodini B et al (2018) Learning myelin content in multiple sclerosis from multi-modal MRI through adversarial training. In: International conference on medical image computing and computer-assisted intervention. Springer, Cham, pp 514–522
125. Salem M et al (2019) Multiple sclerosis lesion synthesis in MRI using an encoder-decoder U-NET. *IEEE Access* 7:25171–25184
126. Long J, Shelhamer E, Darrell T (2015) Fully convolutional networks for semantic segmentation. In: Proceedings of the IEEE conference on computer vision and pattern recognition. IEEE, Piscataway, NJ, pp 3431–3440
127. Finck T et al (2020) Deep-learning generated synthetic double inversion recovery images improve multiple sclerosis lesion detection. *Investig Radiol* 55(5):318–323
128. Wei W et al (2020) Predicting PET-derived myelin content from multisequence MRI for individual longitudinal analysis in multiple sclerosis. *NeuroImage* 223:117308
129. Shaul R, David I, Shitrit O, Raviv TR (2020) Subsampled brain MRI reconstruction by generative adversarial neural networks. *Med Image Anal* 65:101747
130. Zhang C et al (2018) MS-GAN: GAN-based semantic segmentation of multiple sclerosis lesions in brain magnetic resonance imaging. In: 2018 Digital image computing: techniques and applications (DICTA). IEEE, Piscataway, NJ, pp 1–8
131. Wei W, Poirion E, Bodini B, Durrleman S, Ayache N, Stankoff B, Colliot O (2019) Predicting PET-derived demyelination from multi-modal MRI using sketcher-refiner adversarial training for multiple sclerosis. *Med Image Anal* 58:101546
132. Eshaghi A et al (2021) Identifying multiple sclerosis subtypes using unsupervised machine learning and MRI data. *Nat Commun* 12(1):1–12
133. Eitel F, Albrecht JP, Paul F, Ritter K (2019) Harnessing spatial MRI normalization: patch individual filter layers for CNNs. Preprint at <https://arXiv.org/abs/1911.06278>
134. Pang H et al (2021) Use of machine learning method on automatic classification of motor subtype of Parkinson’s disease based on multilevel indices of rs-fMRI. *Parkinsonism Relat Disord* 90:65–72
135. Tibshirani R (1996) Regression shrinkage and selection via the lasso. *J R Stat Soc B Methodol* 58(1):267–288



Transgenic Brain Mapping Techniques in *Drosophila melanogaster*

13

Deepa Mugudthi Venugopal, Raifa Abdul Aziz,
and Shamprasad Varija Raghu

Abstract

Nervous system, the commanding center in our body, has an important functional role in regulating and controlling various physiological activities. However, the exact neural or cellular pathways that regulate these activities are unclear. So it is necessary to delineate neural circuits to understand their functional implications and their involvement in different neurological disorders. There are currently few techniques like fMRI, EEG, etc. employed to dissect the functional role of the nervous system but with some limitations to access the whole brain. Smaller animal models like *Drosophila* offer many genetic tools to address the functional dissection of neural circuits. It helps to understand the specific neural circuit and its regulation in different brain functions. In this chapter, we discuss two such brain mapping techniques: FLP/FRT and MARCM system. By employing these two methods, the inhibitory GABAergic and Cholinergic excitatory neurons distributed across different layers in the visual system (optic lobe) of *Drosophila* are analyzed.

Keywords

Neural circuits · *Drosophila* · GABA · Acetylcholine · FLP/FRT · MARCM · Optic lobe

D. M. Venugopal · R. A. Aziz · S. V. Raghu (✉)
Neurogenetics Lab, Department of Applied Zoology, Mangalore University, Mangaluru,
Karnataka, India

© The Author(s), under exclusive license to Springer Nature Singapore Pte Ltd. 2022
N. Mazumder et al. (eds.), *Advances in Brain Imaging Techniques*,
https://doi.org/10.1007/978-981-19-1352-5_13

231

13.1 Introduction

Nervous system in animals is considered the commanding center in our body, and it controls movements, thoughts, learning, memory, and all physiological activities, including digestions, breathing, sleep, development, etc. The nervous system consists of neurons that process and send signals to different body parts. Neurons use both electrical and chemical signals in neurotransmitters for these communications. In addition, different types of neurons perform different functions and carry different types of signals. For example, motor neurons signal muscle to move, sensory neurons receive information from various sense organs, and interneurons process the information accumulated by the sensory neurons. However, the presence of billions of neurons within the nervous system is the greatest challenge for neuroscientists to understand the functioning of the system in detail and at the neural circuit level. Moreover, a detailed understanding of the nervous system is also necessary to deal with different disorders of nervous system. Such challenges lead scientists to discover different brain imaging or mapping techniques to understand brain function [1].

Brain imaging techniques used in human studies have certain technical limitations. For example, functional magnetic resonance imaging (fMRI) technique offers spatiotemporal resolution that is far below at the single-neuron resolution. Another well-used approach, like electroencephalography (EEG), allows only partial and indirect access to the different parts in brain [1, 2]. In a vertebrate animal model like rodents, brain activity is recorded using fluorescent-mediated calcium sensor GCaMP using head-mounted microscopes while the animal moves in its experimental environment [3–6]. However, such technical advances have limitation with access restricted to a small portion of the brain. Thus, it is impossible to understand other brain regions' involvement. Therefore, neuroscientists turned into analyzing smaller animal models such as the *C. elegans*, zebrafish, and *Drosophila* for neural circuit analysis. In these smaller animals, the whole brain can be imaged at the level of a single neuron with much higher temporal and spatial resolution than the vertebrate animal model [5, 7–10].

Drosophila melanogaster is a promising genetic model system, and it promises to provide new insights into visual information and related processing steps [11, 12]. Thus, it gives neuroscientists opportunities to analyze the brain dynamics that are generated in complex neural circuits. In addition, the whole-cell recording in movement detector neurons called lobula plate tangential cells in fruit fly, *Drosophila melanogaster* [13, 14] and in other larger flies suggested a common computational processing within the visual circuitry of all dipterans compound eye [15]. *Drosophila* offers distinct genetic tools which can be used for cell-specific expression of transgenetically encoded calcium indicators [11, 12, 16, 17], temperature-sensitive neuronal inhibitors [18], and genetic actuators [19] of neural regulations make *Drosophila* a powerful genetic experimental animal for analyzing different types of neural processing [13, 20, 21].

13.2 Brain Mapping Techniques in *Drosophila*

The central nervous system (CNS) in *Drosophila* contains around 1,35,000 neurons. It is far fewer than 100 million neurons in mice or 1.3 billion neurons in macaque, or approximately 20 billion neurons in humans [22]. The CNS in *Drosophila* can be studied by analyzing a smaller set of populations using different brain mapping techniques at the single-cell resolution. *Drosophila* has many transgenic methods to map the CNS at the level of single or few cell types. This chapter discusses two such methods, FLP/FRT (Flippase Recombinase/FLP Recognition Target) and MARCM (Mosaic Analysis with Repressible Cell Marker). These two techniques are used in analyzing inhibitory [23] and excitatory [24] neurons in the *Drosophila* optic lobe.

13.3 FLP/FRT System

A flippase recombinase/FLP recognition target (FLP/FRT) technique used for mediating site-specific DNA recombination. The Gal4-UAS, in combination with FLP/FRT system, can be used for generating a cell mosaic system [11, 12, 23, 25]. In the FLP/FRT system, two Flippase Recognition Target (FRT) sites are inserted at transpositions in chromosomes that are homologous to each other. It also includes a gene that is mutated and a reporter for expression inserted next position to the two FRT sites. The late second or third instar larvae carrying heat-shock flippase inserted FRT cassette carrying GFP construct and Gal4 driver of interest are heat-shocked by keeping at 37 °C using a water bath for 45–60 min to induce the mitotic recombination. An additional 1-h heat-shock protocol can be added in the following days to increase the frequency of mitotic clones [26]. In a heterozygous parental cell, the site-specific mitotic recombination is mediated by FLP/FRT between FRT sites. The chromosomes that undergo recombination are separated into two daughter clones in cells. In that one clone carries mutant homozygous alleles. At the same time, the other clone carries double reporter alleles which are expressed in other tissues. All the remaining clones or cells will have one reporter and one mutant allele [23, 25–29] (Fig. 13.1).

In FLP/FRT system, the mitotic recombination requires cellular propagation. So such a system can be the best tool for the cell-lineage analysis and developmental defects. However, in conservative FLP/FRT genetic labeling systems, the mutant clones are invisible or negatively labeled. At the same time, the twin and the other background tissue are highlighted/labeled with the Green Fluorescent Protein (GFP) reporter [26–29].

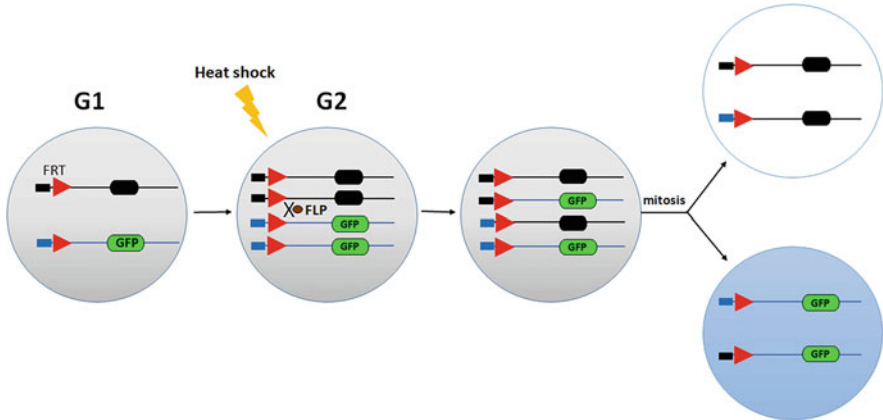


Fig. 13.1 FLP/FRT-mediated genetic labeling system consists of mutation (indicated by black box), and the reporter or GFP is placed distal position to FRT sites. The FRT site is inserted at transpositions of homologous chromosomes. Heat-shock-induced flippase (FLP) activity promotes FRT-site-specific recombination in DNA and the chromosomes that are recombined and segregated to two daughter cells. One of the cells will carry mutated homozygous alleles. The cell will have GFP-labeled neurons. The two daughter cells develop subsequently into two different cell clones followed by several rounds of cell division

13.4 Mosaic Analysis with Repressible Cell Marker (MARCM) System

MARCM is a genetic technique used for labeling single cells or multiple cells in the *Drosophila* model. In the MARCM method, a reporter gene such as GFP or other toxic molecules is placed in such a way that it will be driven by Gal4 gene. In parallel, the Gal80 gene is expressed under the control of a strong promoter like tubulin P. Functionally, Gal80 is an inhibitor of Gal4. Gal80 will suppress the expression of GFP. The tubP-GAL80 part is placed in distal position to an FRT site. A second FRT site is introduced in transposition to the GAL80 insert site. A heat-shock-induced FLP recombinase will recombine the chromosomes in cells undergoing mitosis at the two FRT sites. These cells will divide into two daughter cells that are homozygous. The daughter cell in the absence of GAL80 will be labeled with GFP expression that is driven by the Gal4 driver. All subsequent dividing daughter cells from the above progenitor cell will drive GFP expression [30–32] (Fig. 13.2).

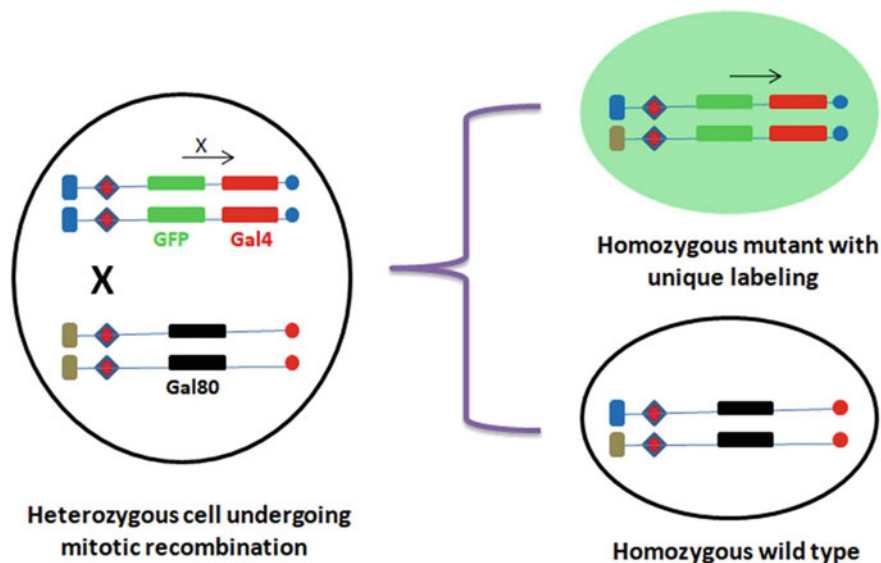


Fig. 13.2 In MARCM systems, Gal80, a suppressor gene is placed transposition to the mutated gene. Gal80 suppresses the Gal4-induced GFP expression. Upon induction of FLP through a mild heat-shock, which induces FRT-site-specific DNA recombination. In the process, a heterozygous mother cell will divide into two daughter cells. One cell will contain mutated allele that are homozygous (GFP-positive neurons). The other cell will remain invisible which carries two suppressor genes/alleles

13.5 Optic Lobe in *Drosophila melanogaster*

The compound eye in insects has a crystalline structure. The processing of different visual information and underlying computational modeling by the optic lobe in insects attracted the interest of biologists [33]. The structural organization of the insect compound eye and the optic lobe suggested that neighboring facets in the optic lobe send visual information to several optic neuropil layers that are retinotopically organized. These optic neuropils composed of longitudinal and repetitive structures are known as columns. The anatomical observation of few input fibers diverging into several interneurons in each column revealed that the signals from the visual system are processed by multiple parallel visual channels that organized in the optic lobe [34–38]. However, the precise nature and the functional connections of these different visual channels are not yet explicit. A complete anatomical description of cell types along with their distinct synaptic connection patterns helps in understanding the function of each column in the optic lobe and different visual channels.

The optic lobe in *Drosophila* is composed of around 60,000 neurons. All these neurons can be arranged into four neuropil layers: lamina, medulla, lobula, and lobula plate. Different neurons occupying these different neuropil layers are

characterized by Golgi-silver impregnation and genetic labeling techniques [23–25, 34]. The neuronal subtypes and their organization are well understood for lamina, the first layers in the optic lobe. The lamina contains individual columns called cartridges. There are about 13 anatomically distinguishable cell types in each lamina cartridge. They include five lamina monopolar cells (L1–L5), three centrifugal medulla neurons (C2, C3, and T1), amacrine cells, and three glia cells [34, 39]. The lamina layers/neurons connected to medulla layers through outer chiasm. The neural fibers in the outer chiasm switch to posterior and anterior positions while connecting the medulla.

The medulla consists of significant neuronal cell types and represents the largest portion of the optic lobe. The medulla neuropil layer consists of two distinct regions: an outer or distal and inner or proximal region. Two regions are separated by a region called serpentine layer. The serpentine layer is formed by the fusion of axonal region of large medulla tangential neurons [34]. The medulla neuropil layer is divided into ten layers. These ten layers run orthogonal to the columns. Most of the medulla neurons are columnar in nature, and all their axons are aligned parallel to the longer axis of the columns in medulla region. The structural organization of medulla interneurons are studied for two insect species in great details: *Musca domestica* (House fly) [37] and *Drosophila melanogaster* (Fruit fly) [34]. Around 120 neurons are suggested to participate in individual medulla column circuit in *Musca* [37]. A similar anatomical description of medulla interneurons has been reported in *Drosophila melanogaster* [34]. An inner chiasm is involved in connecting the medulla to the lobula and the lobula plate region.

The lobula plate and its organizations are well studied. The LPTCs residing in the lobula plate region sense and respond to large-field visual signals [13, 14, 35, 36, 40]. These cells exist and have similar functions in large fly species [41]. The lobula plate region responds to four different directions of motions and thus divided into four different functional layers. The four different layers respond to front-to-back, back-to-front, upward, and downward direction motion [42]. The fourth neuropil layer, lobula is divided into six sub-layers. These layers run in perpendicular directions to the retinotopically organized columns in the lobula [34].

13.6 Neurotransmitter System in Insects

Neurotransmitters and their functional role in processing visual signals in the insect eye have been investigated previously. These studies mainly addressed the distribution of neurotransmitters, their receptors, and different enzymes involved in their transport and synthesis. The acetylcholine [24, 43], GABA [23, 43], glutamate [25, 43], aspartate [44], taurine [45], dopamine [46], serotonin [47], and histamine [48] are the major neurotransmitters involved in different functional properties of neurons within the insect optic lobes. The histological observation does not provide a specific functional relationship between neurotransmitters and the specific neuronal types. However, a detailed description of neuronal types and detailed functional

map based on neurotransmitters released offers valuable information to understand the different cell types and their active role for the insect optic lobe [23–25, 35, 36].

13.7 GABA-Mediated Inhibitory Neurons in the Visual System

Gamma-aminobutyric acid (GABA) is one of the major and important neurotransmitters that is inhibitory in nature in the insect optic lobe [23, 43, 44, 49]. It helps in reducing neuronal excitation by inhibiting synaptic transmission through the ligand-gated chloride channel. Two types of transporter proteins are functionally involved in the recycling and storage of GABA during synaptic transmission. First, the plasma membrane GABA transporters (GATs) remove extra GABA from the synaptic cleft after it is used [43, 49]. The vesicular GABA transporter (vGAT) is required to store GABA in vesicles at the synaptic region [50, 51].

A dVGAT-Gal4 line driving expression of dVGAT in neurons is used for identifying GABAergic neurons across different layers in the optic lobe. A large number of neurons across different layers of the optic lobe are revealed to be expressing under the control of dVGAT-Gal4 transgene [49]. Here to controlled restriction of expression and identify single or few GABAergic cells in the optic lobe, dVGAT-Gal4 line is analyzed by employing the FLP-FRT-mediated recombination system [52]. The neurons are identified with their anatomical similarities to the neurons which are previously described using Golgi-staining techniques [34].

The study identified different types of GABAergic neurons distributed across different layers in the optic lobe. It includes lamina monopolar (L3 and L4), medulla intrinsic (Mi8; Mi10; Mt1; Mt7 and Mt11), bushy T (T2 and T3), transmedullary (Tm3; Tm4; Tm5; Tm9 and Tm25), transmedullary Y (TmY9; TmY10 and TmY13), Y (Y1), lobula-complex intrinsic (Lccn2), lobula columnar (Lcn5), lobula plate intrinsic (Lpi), and lobula tangential (Lt6) cell types as listed in Table 13.1 and Fig. 13.3 [23].

Table 13.1 Different types of GABAergic neurons distributed across different layers in the optic lobe [23]

Layers in the optic lobe	GABAergic neurons
Lamina	L3 and L4
Medulla	Tm3, Tm4, Tm5, Tm9, Tm25, TmY9, TmY10, TmY13, Y1, Mi8, Mi10, Mt1, Mt7, Mt11, T2, T3
Lobula	Lccn2, Lcn5, Lt6
Lobula plate	Lpi

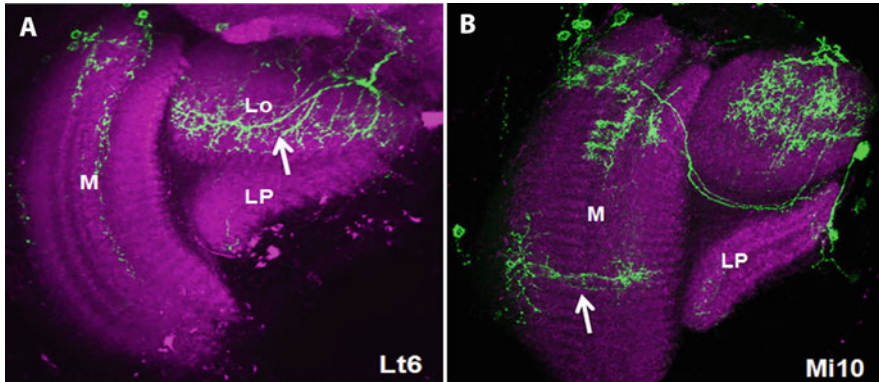


Fig. 13.3 Representative GABAergic inhibitory interneurons in the optic lobe identified by FLP/FRT analysis. (a) Lobula tangential (Lt6) and (b) medulla intrinsic (Mi10) cells distributed across Medulla (M), Lobula (Lo), and the Lobula Plate (LP) layers

13.8 Acetylcholine-Mediated Excitatory Neurons in the Visual System

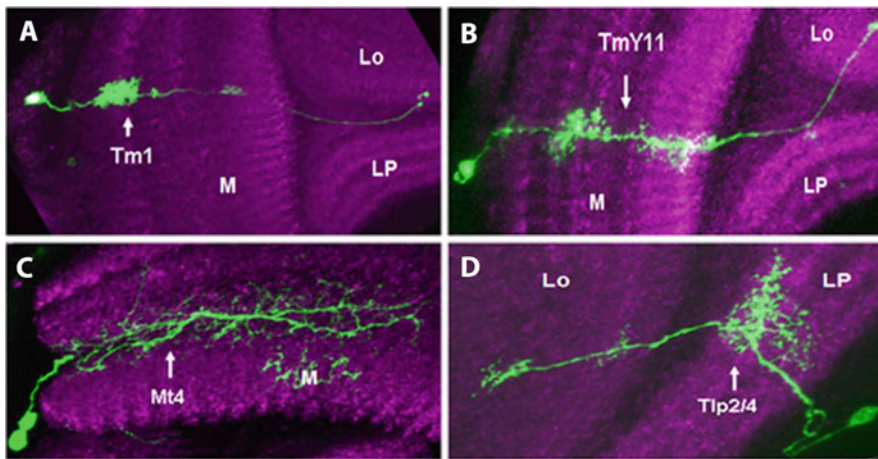
Acetylcholine (ACh) is one of the important excitatory neurotransmitters. It is distributed across different layers in the insect optic lobe. It is also an evolutionarily highly conserved signaling molecule. The cholinergic system consists of choline acetyltransferase (ChAT) enzyme involved in the synthesis of ACh, two receptors for ACh (muscarinic, mAChR and the nicotinic, nAChR), ACh-degrading esterase enzyme (AChE), and choline transporters (ChT) involved in the uptake of choline after the degradation of ACh [53, 54]. The cholinergic system and its transmission at the synaptic level have been studied intensively for the insect brain [43, 55].

MARCM with *Cha*-Gal4 driver is employed to analyze different cholinergic excitatory neurons distributed across layers in the optic lobe. In the *Cha*-Gal4 driver, the neurons are labeled by expressing the *Cha* promoter. The *Cha* regulates the expression of ChAT (choline acetyltransferase) gene and vAChT (vesicular acetylcholine transporter). ChAT is one of the important enzymes involved in the biosynthesis of acetylcholine. The vAChT is involved in enzymatic transportation of acetylcholine into the synaptic vesicles [56]. The *Cha*-Gal4 expression in different neurons was driven using membrane-tagged GFP [57]. MARCM method is used for restricting GFP expression in a single or group of cells of the *Cha*-Gal4 expression pattern in the optic lobe. The labeled neurons are further identified with their anatomical similarity to the neurons described previously using Golgi-staining techniques [34].

The study identified different types of cholinergic excitatory neurons distributed across multiple layers in the optic lobe. It includes medulla intrinsic (Mi2; Mi7; Mi11; Pm1; Pm1a; Mt4 and Mt10), bushy T (T2 and T4), transmedullary (Tm1, 2, 4, 4a, 7, 8, 11, 12, 15, 22, and 24), transmedullary Y (TmY2; TmY5; TmY9; TmY10; TmY11; and TmY12), translobula plate (Tlp2 and Tlp3), lobula columnar (Lcn1 and

Table 13.2 Different cholinergic excitatory neurons distributed across different layers in the optic lobe [24]

Layers in the optic lobe	Cholinergic neurons
Lamina	–
Medulla	Tm1, Tm2, Tm4, Tm4a, Tm7, Tm8, Tm11, Tm12, Tm15, Tm22, Tm24, TmY2, TmY5, TmY9, TmY10, TmY11, TmY12, Mi2, Mi7, Mi11, Pm1, Pm1a, Mt4, Mt10, T2, T4
Lobula	Tlp2, Tlp3, Lcn1, Lcn2, Lt6
Lobula plate	–

**Fig. 13.4** Representative cholinergic excitatory interneurons in the optic lobe as identified by MARCM analysis. (a) Transmedullary (Tm1), (b) transmedullary Y (TmY11), (c) medulla intrinsic (Mt4) and (d) translobula plate (Tlp2/4) cells distributed across Medulla (M), Lobula (Lo), and Lobula Plate (LP) layers

Lcn2), and lobula tangential (Lt6) cell types as listed in Table 13.2 and Fig. 13.4 [24].

Conflict of Interest The authors have no conflicts of interest to declare.

Acknowledgments SV Raghu gratefully acknowledges the funding received from the Department of Biotechnology, Government of India (as Ramalingaswami Fellowship).

References

1. Roalf D, Gur R (2017) Functional brain imaging in neuropsychology over the past 25 years. *Neuropsychology* 31:954–971
2. Woller A, Bandow P, Aimon S, Grunwald Kadow IC (2021) Preparing adult *Drosophila melanogaster* for whole brain imaging during behavior and stimuli responses. *J Vis Exp*. <https://doi.org/10.3791/61876>

3. Chisholm KI, Khovanov N, Lopes DM, La Russa F, McMahon SB (2018) Large scale in vivo recording of sensory neuron activity with GCaMP6. *eNeuro* 5. <https://doi.org/10.1523/NEURO.0417-17.2018>
4. Huang L, Ledochowitsch P, Knoblich U, Lecoq J, Murphy GJ, Reid RC, De Vries SEJ, Koch C, Zeng H, Buice MA, Waters J, Li L (2021) Relationship between simultaneously recorded spiking activity and fluorescence signal in GCaMP6 transgenic mice. *eLife* 10:e51675
5. Partridge JG (2015) Utilizing GCaMP transgenic mice to monitor endogenous Gq/11-coupled receptors. *Front Pharmacol* 6:42
6. Zong W, Wu R, Li M, Hu Y, Li Y, Li J, Rong H, Wu H, Xu Y, Lu Y, Jia H, Fan M, Zhou Z, Zhang Y, Wang A, Chen L, Cheng H (2017) Fast high-resolution miniature two-photon microscopy for brain imaging in freely behaving mice. *Nat Methods* 14:713–719
7. Delestro F, Scheunemann L, Pedrazzani M, Tchenio P, Preat T, Genovesio A (2020) In vivo large-scale analysis of *Drosophila* neuronal calcium traces by automated tracking of single somata. *Sci Rep* 10:7153
8. Kirk MJ, Benlian BR, Han Y, Gold A, Ravi A, Deal PE, Molina RS, Drobizhev M, Dickman D, Scott K, Miller EW (2021) Voltage imaging in *Drosophila* using a hybrid chemical-genetic rhodamine voltage reporter. *Front Neurosci* 15:754027
9. Lin H-Y, Chu L-A, Yang H, Hsu K-J, Lin Y-Y, Lin K-H, Chu S-W, Chiang A-S (2019) Imaging through the whole brain of *Drosophila* at $\lambda/20$ super-resolution. *iScience* 14:164–170
10. Sabado V, Nagoshi E (2021) Fluorescence live imaging of *Drosophila* circadian pacemaker neurons. *Methods Mol Biol* 2130:207–219
11. Brand AH, Perrimon N (1993) Targeted gene expression as a means of altering cell fates and generating dominant phenotypes. *Development* 118:401–415
12. Raghu SV, Mohammad F, Chua JY, Lam JSW, Loberas M, Sahani S, Barros CS, Claridge-Chang A (2018) A zinc-finger fusion protein refines Gal4-defined neural circuits. *Mol Brain* 11:46
13. Joesch M, Schnell B, Raghu SV, Reiff DF, Borst A (2010) ON and OFF pathways in *Drosophila* motion vision. *Nature* 468:300–304
14. Schnell B, Joesch M, Forstner F, Raghu SV, Otsuna H, Ito K, Borst A, Reiff DF (2010) Processing of horizontal optic flow in three visual interneurons of the *Drosophila* brain. *J Neurophysiol* 103:1646–1657
15. Borst A, Haag J (2002) Neural networks in the cockpit of the fly. *J Comp Physiol A Neuroethol Sens Neural Behav Physiol* 188:419–437
16. Hendel T, Mank M, Schnell B, Griesbeck O, Borst A, Reiff DF (2008) Fluorescence changes of genetic calcium indicators and OGB-1 correlated with neural activity and calcium in vivo and in vitro. *J Neurosci* 28:7399–7411
17. Mank M, Santos AF, Drenth S, Mrcsic-Flogel TD, Hofer SB, Stein V, Hendel T, Reiff DF, Levelt C, Borst A, Bonhoeffer T, Hübener M, Griesbeck O (2008) A genetically encoded calcium indicator for chronic in vivo two-photon imaging. *Nat Methods* 5:805–811
18. Kitamoto T (2001) Conditional modification of behavior in *Drosophila* by targeted expression of a temperature-sensitive shibire allele in defined neurons. *J Neurobiol* 47:81–92
19. Lima SQ, Miesenböck G (2005) Remote control of behavior through genetically targeted photostimulation of neurons. *Cell* 121:141–152
20. Borst A, Haag J, Mauss AS (2020) How fly neurons compute the direction of visual motion. *J Comp Physiol A Neuroethol Sens Neural Behav Physiol* 206:109–124
21. Mauss AS, Vlasits A, Borst A, Feller M (2017) Visual circuits for direction selectivity. *Annu Rev Neurosci* 40:211–230
22. Kaiser M (2015) Neuroanatomy: connectome connects Fly and mammalian brain networks. *Curr Biol* 25:R416–R418
23. Raghu SV, Claussen J, Borst A (2013) Neurons with GABAergic phenotype in the visual system of *Drosophila*. *J Comp Neurol* 521:252–265
24. Raghu SV, Reiff DF, Borst A (2011) Neurons with cholinergic phenotype in the visual system of *Drosophila*. *J Comp Neurol* 519:162–176

25. Raghu SV, Borst A (2011) Candidate glutamatergic neurons in the visual system of *Drosophila*. *PLoS One* 6:e19472
26. Prudêncio P, Guilgur LG (2015) FLP/FRT induction of mitotic recombination in *Drosophila* germline. *Bio-Protocol* 5:e1458
27. Lee T (2014) Generating mosaics for lineage analysis in flies. *Wiley Interdiscip Rev Dev Biol* 3: 69–81
28. Lee T, Lee A, Luo L (1999) Development of the *Drosophila* mushroom bodies: sequential generation of three distinct types of neurons from a neuroblast. *Development* 126:4065–4076
29. Theodosiou NA, Xu T (1998) Use of FLP/FRT system to study *Drosophila* development. *Methods* 14:355–365
30. Lee T, Luo L (2001) Mosaic analysis with a repressible cell marker (MARCM) for *Drosophila* neural development. *Trends Neurosci* 24:251–254
31. Marin EC, Jefferys GS, Komiyama T, Zhu H, Luo L (2002) Representation of the glomerular olfactory map in the *Drosophila* brain. *Cell* 109:243–255
32. Wu JS, Luo L (2006) A protocol for mosaic analysis with a repressible cell marker (MARCM) in *Drosophila*. *Nat Protoc* 1:2583–2589
33. Cajal SRY, Sánchez DB (1915) Contribución al conocimiento de los centros nerviosos de los insectos
34. Fischbach KF, Dittrich APM (1989) The optic lobe of *Drosophila melanogaster*. I. A Golgi analysis of wild-type structure. *Cell Tissue Res* 258:441–475
35. Raghu SV, Joesch M, Borst A, Reiff DF (2007) Synaptic organization of lobula plate tangential cells in *Drosophila*: gamma-aminobutyric acid receptors and chemical release sites. *J Comp Neurol* 502:598–610
36. Raghu SV, Joesch M, Sigrist SJ, Borst A, Reiff DF (2009) Synaptic organization of lobula plate tangential cells in *Drosophila*: $\alpha 7$ cholinergic receptors. *J Neurogenet* 23:200–209
37. Strausfeld NJ (1984) Functional neuroanatomy of the Blowfly's visual system. In: Ali MA (ed) *Photoreception and vision in invertebrates*. Springer, Boston, MA
38. Timaeus L, Geid L, Sancer G, Wernet M, Hummel T (2020) Parallel visual pathways with topographic versus nontopographic organization connect the *Drosophila* eyes to the central brain. *iScience* 23:101590
39. Meinertzhagen IA, O'Neil SD (1991) Synaptic organization of columnar elements in the lamina of the wild type in *Drosophila melanogaster*. *J Comp Neurol* 305:232–263
40. Rajashekhar KP, Shamprasad VR (2004) Golgi analysis of tangential neurons in the lobula plate of *Drosophila melanogaster*. *J Biosci* 29:93–104
41. Hengstenberg R, Hausen K, Hengstenberg B (1982) The number and structure of giant vertical cells (VS) in the lobula plate of the blowfly *Calliphora erythrocephala*. *J Comp Physiol* 149: 163–177
42. Buchner E, Buchner S, Bühlhoff I (1984) Deoxyglucose mapping of nervous activity induced in *Drosophila* brain by visual movement. *J Comp Physiol A* 155:471–483
43. Kolodziejczyk A, Sun X, Meinertzhagen IA, Nassel DR (2008) Glutamate, GABA and acetylcholine signaling components in the lamina of the *Drosophila* visual system. *PLoS One* 3:e2110
44. Sinakevitch I, Strausfeld NJ (2004) Chemical neuroanatomy of the fly's movement detection pathway. *J Comp Neurol* 468:6–23
45. Schafer S, Bicker G, Ottersen OP, Storm-Mathisen J (1988) Taurine-like immunoreactivity in the brain of the honeybee. *J Comp Neurol* 268:60–70
46. Schürmann FW, Elekes K, Geffard M (1989) Dopamine-like immunoreactivity in the bee brain. *Cell Tissue Res* 256:399–410
47. Homberg U, Hildebrand JG (1989) Serotonin-immunoreactive neurons in the median protocerebrum and suboesophageal ganglion of the sphinx moth *Manduca sexta*. *Cell Tissue Res* 258:1–24
48. Stuart AE, Borycz J, Meinertzhagen IA (2007) The dynamics of signaling at the histaminergic photoreceptor synapse of arthropods. *Prog Neurobiol* 82:202–227

49. Fei H, Chow DM, Chen A, Romero-Calderon R, Ong WS, Ackerson LC, Maidment NT, Simpson JH, Frye MA, Krantz DE (2010) Mutation of the *Drosophila* vesicular GABA transporter disrupts visual figure detection. *J Exp Biol* 213:1717–1730
50. Wojcik SM, Katsurabayashi S, Guillemain I, Friauf E, Rosenmund C, Brose N, Rhee JS (2006) A shared vesicular carrier allows synaptic corelease of GABA and glycine. *Neuron*. 50(4):575–587. <https://doi.org/10.1016/j.neuron.2006.04.016>
51. Gasnier B (2004) The SLC32 transporter, a key protein for the synaptic release of inhibitory amino acids. *Pflugers Arch*. 447(5):756–759. <https://doi.org/10.1007/s00424-003-1091-2>
52. Wong AM, Wang JW, Axel R (2002) Spatial representation of the glomerular map in the *Drosophila* protocerebrum. *Cell* 109:229–241
53. Wessler I, Kirkpatrick CJ (2008) Acetylcholine beyond neurons: the non-neuronal cholinergic system in humans. *Br J Pharmacol* 154:1558–1571
54. Wessler IK, Kirkpatrick CJ (2017) Non-neuronal acetylcholine involved in reproduction in mammals and honeybees. *J Neurochem* 142(Suppl 2):144–150
55. Goldberg F, Grunewald B, Rosenboom H, Menzel R (1999) Nicotinic acetylcholine currents of cultured Kenyon cells from the mushroom bodies of the honey bee *Apis mellifera*. *J Physiol* 514(Pt 3):759–768
56. Kitamoto T, Wang W, Salvaterra PM (1998) Structure and organization of the *Drosophila* cholinergic locus. *J Biol Chem* 273:2706–2713
57. Salvaterra PM, Kitamoto T (2001) *Drosophila* cholinergic neurons and processes visualized with Gal4/UAS-GFP. *Brain Res Gene Expr Patterns* 1:73–82



Behavioural Phenotyping to Study Cognitive and Non-cognitive Symptoms in the Rodent Model of Alzheimer's Disease

14

Apoorva Bettagere Shivakumar, Sonam Fathima Mehak, Sparsha Kumari, Vikyath Saraf, and Gireesh Gangadharan

Abstract

Alzheimer's disease (AD) is a progressive and irreversible neurological disorder that gradually erodes memory and reasoning skills, as well as the ability to perform even simple tasks. Although AD is generally considered a memory disorder, patients with AD shows a range of behavioural and psychological symptoms of dementia (BPSDs) including anxiety, aggression, depression, agitation, apathy, and social dysfunctions. Due to its early impact on the hippocampus and entorhinal cortex, critical brain regions for the memory processing, non-cognitive symptoms associated with AD pathology are frequently overlooked. Animal models are indispensable tools for AD research and have been extensively used to represent the cognitive deficits caused by AD pathology. We are discussing here the most commonly used behavioural tests to detect cognitive and non-cognitive symptoms of AD in rodent models.

Keywords

Neurodegenerative disorders · Alzheimer's disease · Rodent model · Cognition · Behavioural assays

A. B. Shivakumar · S. F. Mehak · S. Kumari · V. Saraf · G. Gangadharan (✉)
Department of Cell and Molecular Biology, Manipal School of Life Sciences, Manipal Academy of Higher Education, Manipal, Karnataka, India
e-mail: gireesh.g@manipal.edu

14.1 Introduction

Neurodegenerative disorders (NDs) are a group of diseases marked by progressive loss of neuronal function and structural deterioration. This could be the result of genetic and ageing factors, congenital defects, or a combination of these factors [1, 2]. NDs are prevalent, largely incurable, and cause a major health and social cost around the world [3]. Alzheimer's disease (AD) is a severe, progressive NDs marked by a loss in cognitive function that begins with memory problems and progresses to include numerous behavioural, neuropsychological, and cognitive domains. AD is a complex, heterogeneous disorder with a varying age of disease onset, degree of progression, and advancement of pathology. The high incidence rate of AD has emerged as the most serious threat to human health and the third most common cause of mortality and disability among the elderly [4–8]. AD is defined by histological markers such as extracellular amyloid beta deposits, intracellular neurofibrillary tangles as well as hyperphosphorylated tau protein along with massive neuronal cell and synapse loss at specific sites in the brain tissue [9–11]. Based on pathological changes in the hippocampus and cortex, the clinical phases of Alzheimer's disease are characterised as pre-symptomatic, early, moderate, and late stage [12, 13].

Behavioural abnormalities become more prevalent as the disease progresses. In addition to memory impairments, AD patients show a variety of non-cognitive symptoms which is often referred as BPSDs, these include anxiety, aggression, depression, agitation, apathy, and reduced sociability. However, the major attention is focused on memory because of early and significant impact of AD on memory centres [14, 15]. Understanding the neurobiological basis of behavioural and neuropsychiatric symptoms is still limited [16]. The study of behaviour is undoubtedly one of the most difficult aspects of neurodegenerative research [3]. The knowledge gathered about AD behavioural changes could be useful in understanding and treating the diseases. Uncovering the neurobiology of AD and creating treatments for its behavioural and psychological manifestations could lead to better treatment [16]. Since the process of neurodegeneration is complex and multifaceted, there are currently no proper therapies available to “cure” AD. Despite this, extensive research is undertaken to better understand the pathogenic pathways to generate novel therapies and tactics [17].

Despite the multiple possibilities available, animal models are one of the most popular approaches to examine human illnesses [18]. They form an important experimental, pre-clinical step in learning more about neurodegeneration and creating and testing treatments. The models are designed to mimic a certain condition in an animal, allowing researchers to learn more about the disease's pathogenesis and obtain access to answers that were previously unavailable in human patients [17]. These models have proven to be a valuable tool in the exploration of the many genetic, environmental, and pharmacological factors that might create symptoms that are comparable to those of people who have a particular condition [18]. The behavioural outcomes in rodent models are influenced by factors like

genetic background of the experimental animal, sex, age, other factors such as dosage and timing of injections, genetic manipulation.

Some common behavioural tests for cognitive and non-cognitive AD symptoms in rodent models are discussed here.

14.2 Spatial Memory Tasks

Spatial memory is an essential part of cognitive function. To assess this aspect of memory in rodents, a number of behavioural experiments have been devised. However, in most of the tests, positive or negative reinforcers are used, like water immersion in a water maze test or food in a radial maze test. Animals must learn a rule in these tasks, with reinforcers guiding the learning process. Because human cognitive abilities are rarely evaluated with powerful reinforcers under conditions like extreme hunger, the outcomes of animal research that use such typical reinforcers may not be properly transferred to the human population. Therefore, cognitive tests without traditional reinforcers may be more appropriate for investigating neural function [19].

14.2.1 Morris Water Maze

The Morris water maze (MWM) is a commonly employed and sensitive test for assessing learning and memory deficits in rodents. In this experiment, animals are placed in a water-filled circular tank, which is utilised to persuade the animal to swim and learn to discover a platform buried in the water and escape the water. This test normally takes 6 days to complete, with the main benefit of distinguishing between spatial and non-spatial circumstances. Distance swam, swim speed, and latency to reach the platform are the common measures of this test. Spatial learning is evaluated across repeated trials and when the platform is absent, preference for the platform region is used to determine reference memory. The use of reversal and shift trials can help detect spatial deficits [20–23].

14.2.2 Radial Arm Maze

The radial arm maze (RAM) is one of the most extensively used mazes for testing spatial working memory and reference memory in rodents. A typical setup consists of four to eight evenly spaced arms extending from a central platform, each arm of the maze can be reward-baited with food pellets or water, and rodents must navigate to reach a reward hidden in one of the arms. The animals use spatial cues to navigate themselves across the room in this activity, with the goal of entering each arm just once to get the most rewards in the minimum amount of time and effort. This test entails the application of working and reference memory. Here, the animal must recall the arms baited and arms entered (working memory), also avoid the arms

without bait across trials (reference memory) all of which is accomplished by successful spatial information encoding. Re-entries into a previously visited radial arm is considered as working memory error, whereas entering an unbaited arm is regarded as reference memory error [24–26].

14.2.3 Y-Maze

The Y-maze spontaneous alternation paradigm test is based on rodents' natural tendency to shift arms when investigating a novel environment. The equipment comprises of three identical arms positioned at a 120° angle around a central equilateral triangular platform. In this experiment, animals are placed in a Y-shaped maze for certain time and the total arms entered, the order of entries into arms, are recorded and a score (frequency of arm entries without repetitions) is analysed to determine alternation rate. A rodent with intact working memory recalls the arms it has previously visited and exhibits a high rate of alternation [27, 28].

14.2.4 T-Maze

The spontaneous alternation T-maze is well-known test for assessing spatial working memory. This maze is a T-shaped apparatus with two opposing arms to choose from. The procedure is based on rodents' innate preference for a novel arm over a familiar one, which prompts them to switch goal arms. If two trials are given in quick series, unexplored arm is chosen in the second trial. During the third trial, the arm that has been examined the longest is favoured. Alteration has been classified as spontaneous since it does not require pre-training and depends solely on rodents' innate preference for novelty. Another theory for the alternation is that rodents have an inbuilt predisposition to shift. Going to a place with a food reward, for example, results in a win-shift behaviour, but visiting a location without food results in a loose-shift behaviour. In novelty seeking and innate shifting behaviour, an animal must recall which arm was visited in the earlier trial to appropriately switch selections across trials, making the spontaneous alternation T-maze an ideal paradigm for spatial working memory [29].

14.2.5 Object Recognition Test

The object recognition test (ORT) was designed to evaluate non-spatial memory in rodents in the absence of typical reinforcers [30]. The test is based on rodents' natural proclivity to investigate new stimuli. The experimental procedure depends on habituation, training, and test session. The training session involves investigating two identical objects, whereas the test session requires the substitution of one of the earlier investigated objects with a new one. Since rodents have a natural affinity for

novelty, they will spend more time investigating the novel object over familiar one [19, 31–33].

14.2.6 Object Location Test

The object location test (OLT), which uses a similar methodology to the ORT, was developed in rodents as a method for spatial memory evaluation. In an experimental setup, animals are first exposed to two similar objects, after which they are exposed to the same objects but one of the objects will be displaced. Animals that recall their earlier encounter spend more time investigating the displaced object over stationary one [19, 31].

Because ORT is less stressful and takes substantially less time than other regularly used memory tests like Morris water maze, Radial maze, and Barnes maze, which can take up to a week or longer to complete. Also, the conditions employed in ORT resembles the test employed in studying human cognition, enhancing the test's ecological validity over many other rodent memory tests [32]. The choice to explore novel object in (ORT) and displaced object in (OLT) demonstrates the utilisation of learning and recognition memory processes. The application of spatial and non-spatial memory tests, with similar emotional stimulation levels and procedures is optimal to examine particular cognitive component [19].

14.3 Anxiety

14.3.1 Open Field Test

The open field test is basically employed to assess motor function by measuring spontaneous activity of rodent in an open field apparatus. The process entails exposing a rodent to an unknown environment from which it is unable to escape due to surrounding walls. The test offers a distinctive opportunity to evaluate general locomotor activity, novel environment exploration, and an early screen for anxiety-related behaviour. Furthermore, repeated exposure or a longer session length allows for the assessment of habituation to the increasingly familiar chamber environment. The stress induced by novel environment which is highly illuminated is one the element thought to influence anxiety-like behaviour in the open field [34].

14.3.2 Light/Dark (LD) Test

The LD test is a frequently used exploration test in rodents to detect anxiety-like behaviour. This test is based on an approach-avoidance conflict between rodents' intrinsic aversion to bright open spaces and novel environments exploration. This model facilitates rodents to freely explore two interconnected compartments that differ in illumination (bright:dim), colour (white:black) and size (2:1). As a result,

control rodent placed in the highly lighted region will quickly migrate to the dark area [18].

14.3.3 Elevated Plus Maze (EPM)

The EPM is often used test for measuring of anxiety-like behaviour based on the conflict between rodent's innate aversion for open spaces and the desire to explore a novel environment. The maze is in the form of cross-shaped platform with equal-sized arms and a central intersection that allows rodents to freely move through each zone. The apparatus is raised from the ground so that the open arms combine elements of elevation, openness, and unfamiliarity. The total open arm entries and the time spent on open are used to assess anxiety [18, 35].

14.4 Social Behaviour

Social cognitive neuroscience is the study of the neurobiological systems underlying effective social behaviour. Social interactions are an adaptive and vital part of the biology of various species. The structure and stability of the networks and interactions that characterise societies are dependent on social recognition. Identification of social cognitive defects in Alzheimer's disease and their neural basis is becoming more apparent, which may lead to a better understanding of the disease. Understanding social cognitive shortcomings in Alzheimer's disease may aid in explaining and possibly predicting social psychopathologies [36, 37].

14.4.1 Three Chamber Test

Three chamber paradigm tests have been effectively used in rodent model to examine social attachment and memory. The primary principle of this experiment is centred on the rodent's free decision to spend time in any of the three compartments of the box throughout the trials consisting of indirect interaction with one or two stranger animals. The major challenges in quantifying the experimental rodents' social inclinations are to measure, the preference for a novel conspecific and time spent with a novel animal over a familiar animal. As a result, the setup for this test allows the assessment of important but distinct components of social behaviour: social motivation, social novelty, and social memory. This experiment provides a reliable result, but they must be thoroughly studied, understood, and supported by other confirmatory tests. Also, this test can be used as part of a rodent's general behavioural assessment, in addition to particular applications [38, 39].

14.4.2 Social Recognition Test

The social recognition test is a potent paradigm that is well-known for its suitability for studying rodents' social memory. In this test, a decrease in spontaneous exploratory behaviours observed in a rodent re-exposed to a familiar conspecific is used to measure social recognition memory. In rodents, social recognition can be tested by putting a juvenile in the same cage as an adult. The adult animal spontaneously explores the younger animal, and the duration of this investigation will reflect the two animals' familiarity. When the same juvenile is exposed repeatedly, the investigation time decreases. As a result, the time difference between the first and second exposures can be employed as a social memory index [40].

14.4.3 Five Trial Social Memory Assay

The 5-trial social memory assay is a more stringent test for social memory confirmation. A stimulus animal will be introduced to a subject animal for four trials in this test. A new stimulus animal will be added on the fifth trial. Here, a marked habituation, i.e., reduced exploration during trials 1–4 and a striking dishabituation, i.e., increased exploration following introduction of an unfamiliar animal on the fifth trial is employed to evaluate social memory [41].

14.5 Apathy

14.5.1 Burrowing Test

Burrowing is regarded as a motivation-dependent behaviour representing rodents' ability to carry out day-to-day activities [42]. Burrowing test exploits a rodent natural behaviour. The test determines how much an animal burrows, or how much burrowing material (e.g., gravel, food pellets, or other substances) is removed from a full container during a set period. Kicks and coordinated hind- and forelimb movements are used by rodents to remove the material. The amount of burrowing material in the container at the start of the experiment against the amount left over after the experiment is used to quantify this burrowing behaviour [43].

14.5.2 Nest Building Test

Nest construction is said to demonstrate the ability to execute day-to-day activities in rodents, which is an inherent behaviour. The nest building test can be used to determine the quality of rodent's nests by simply giving nesting material overnight and grading the nest quality the next day. In addition, the weight of shredded nesting material can be utilised to estimate nest complexity in a semi-independent manner [44, 45].

14.6 Aggression

14.6.1 Resident-Intruder Test

The resident-intruder test is regarded as the standard experiment for evaluating aggressive behaviour in rodents. The paradigm allows for the natural and spontaneous expression of both defensive and offensive aggression behaviour in laboratory rodents. A thorough quantitative picture of offensive and defensive aggression behaviour by resident and intruder rodents can be obtained by documenting the durations, latencies, frequencies, and temporal and sequential patterns of all observed behavioural acts and postures in the animals during these confrontations [46, 47].

14.7 Depression

14.7.1 Forced Swim Test

The forced swimming test (FST) is a method used for evaluating depressive-like behaviour in rodents. The test is based on the observation that animals in an inescapable cylinder filled with water adopt an immobile posture. When an animal is forced to swim without the ability to escape, it learns that there is nothing it can do to escape and, as a result, it spends less time in performing conventional escape behaviours such as climbing and swimming and only makes the movements required to maintain its head above water. The total period of immobilisation in the animal model of depression is higher than in the control condition [48–50].

14.7.2 Tail Suspension Test

The forced swim test and the tail suspension test are basically identical. The test is based on the assumption that animals that are suspended by their tail for a short interval of time develop an immobile posture. Similar to the FST, the TST is predicted to use a passive reaction in a stressful circumstance. The stress situation in TST is the haemodynamic stress of being hung by their tail in an unpredictable manner. The animal stops struggling after a given amount of time and becomes immobile; extended periods of immobility are a symptom of depressive behaviour [50–52].

14.7.3 Sucrose Preference Test

A basic sucrose preference test can be used to determine sensitivity to reward, in which animals are given access to water with and without different doses of sugar, and the preference rate is then studied. In rodents, the sucrose preference test (SPT)

is the most often used method for evaluating anhedonia, a primary symptom of depression. Depressive behaviour is characterised by a loss of interest in the reward [50, 53].

14.8 Conclusion

It has long been believed that AD is a memory disorder, as it affects the brain areas related to memory early in the progression of the disease. There is also recent evidence that non-cognitive symptoms of the disease play a critical role. The nature of these symptoms questions whether they are caused by the spread of neurodegeneration in the brain regions, or if it was early pathogenic events that led to the development of AD. It is evident that a better understanding of AD requires a more in-depth understanding of the behavioural and psychological symptoms of dementia (BPSDs). Here we have discussed some of the behavioural tests to study cognitive and non-cognitive symptoms in the context of AD. Several transgenic animal models of AD are available (as shown in Table 14.1) to explore behavioural and cognitive abnormalities associated with amyloid and tau pathologies. Continued study of BPSD-like behaviours in these animal models may help in opening up new possibilities for investigation for therapeutic interventions. Based on the available literatures, there are a few essential considerations to improve the translation from animal models to the clinic. Firstly, selecting a model, carefully designing the experiment, and understanding its constraints are crucial. Following a set of clear, consistent steps will result in better pre-clinical outcomes, which will aid in better clinical translation.

Conflict of Interest The authors declare no conflict of interest.

Authors' Contributions All authors contributed to the literature search, writing and editing of the manuscript. All authors read and approved this manuscript.

Acknowledgements This work was supported by Science and Engineering Research Board (SERB), Government of India (No. CRG/2020/004205) and Ramalingaswami Re-entry Fellowship, Department of Biotechnology, Government of India (No. BT/RLF/Re-entry/49/2018) to GG. ABS was supported by Innovation in Science Pursuit for Inspired Research (INSPIRE) fellowship, Department of Science and Technology, Government of India (IF190783). SFM was supported by Dr. TMA Pai Ph.D. scholarship, Manipal Academy of Higher Education, Manipal, India. The authors thank Manipal School of Life Sciences, Manipal Academy of Higher Education (MAHE), Manipal for the infrastructure and support.

Table 14.1 Alzheimer's disease: rodent models

Transgenic line	Mutation	Neuropathology	References
PDAPP	APPV717F (Indiana)	<ul style="list-style-type: none"> • Aβ deposition at 3 months • Mature plaques from 5 months in hippocampus, cerebral cortex • Decreased synaptic and dendritic density in the hippocampus 	[54]
Tg2576	APP KM670/671NL (Swedish)	<ul style="list-style-type: none"> • Plaque formation in 11–13 months in cortex, hippocampus • Plaque-associated astrogliosis and microgliosis from 12 months • No tangles or neuronal loss 	[55, 56]
APP23	APP KM670/671NL (Swedish)	<ul style="list-style-type: none"> • Aβ deposits at 6 months • Plaque formation in thalamus, hippocampus, and amygdala at 12 months • Neurodegradation in CA1 from 14 to 18 months • Fibrillar plaque-associated astro- and microgliosis 	[57–59]
TgCRND8	APP KM670/671NL (Swedish), APP V717F (Indiana)	<ul style="list-style-type: none"> • Parenchymal amyloid deposition at 3 months • Dense-core plaques and neuritic pathology from 5 months • Plaque-associated microglia and astrocytes • Dystrophic neurites at 5 months 	[60, 61]
J20	APP KM670/671NL (Swedish), APP V717F (Indiana)	<ul style="list-style-type: none"> • Diffuse plaques in hippocampus from 5 months • Neurodegradation in CA1 at 3 months • General astrogliosis in hippocampus from 3 months • Microgliosis in hippocampus from 6 months 	[62, 63]
APP/PS1	APP KM670/671NL (Swedish), PSEN1L166P	<ul style="list-style-type: none"> • Amyloid plaque deposition begins at 1.5 months in cortex and 3–4 months in hippocampus • CAA development in 8 months • Plaque-associated astro- and microgliosis 	[64]
5 \times FAD	APP KM670/671NL (Swedish), MAPT P301L, PSEN1 M146V, PSEN1 L286V	<ul style="list-style-type: none"> • Early Aβ accumulation at 6 weeks • Plaque formation at 2 months in subiculum and cortex • Gliosis and synapse degradation • Neuron loss in cortical layer 4 and subiculum • No neurofibrillary tangles 	[65–67]

(continued)

Table 14.1 (continued)

Transgenic line	Mutation	Neuropathology	References
3xTg	APP KM670/671NL (Swedish), MAPT P301L, PSEN1 M146V	<ul style="list-style-type: none"> • Age-related, progressive plaques and tangles • Plaque development at 6 months in the cortex and hippocampus • NFTs at 12 months, initially in CA1 and then in the cortex • Synaptic impairment and cognitive deficits from 6 months 	[68]
APP E693Δ-Tg (Osaka)	APP E693del	<ul style="list-style-type: none"> • Age-dependent accumulation of Aβ oligomers within hippocampal and cortical neurons, but negligible deposits of extracellular amyloid • Abnormal tau phosphorylation, but no tangle pathology • Synaptic loss and gliosis in hippocampus and cerebral cortex • Late neuronal loss in the CA3 region of the hippocampus 	[69, 70]
APP ^{swe} /PS1 ^{dE9}	APP KM670/671NL (Swedish), PSEN: deltaE9	<ul style="list-style-type: none"> • Plaque formation at 4 months in hippocampus and cortex • Neurodegradation at 24 months • Leptomeninges formation in 6 months • General and plaque-associated astro- and microgliosis at 12–14 months • Amyloid angiopathy in retina 	[71]
P301L tau	MAPT P301L	<ul style="list-style-type: none"> • NFT identified in brain and spinal cord at 7 months • Motor neurons reduced two-fold in spinal cord • Age-dependent increase in total tau 	[72]
hTau-AT	MAPT A152T	<ul style="list-style-type: none"> • Hyperphosphorylated tau at 2 months • Dense NFTs in hippocampus, cortex, cerebellum, and spinal cord at 3 months • Astrocytosis, microgliosis, and neuroinflammation at 10 months • Neuronal loss in hippocampus and cortex at 12 months 	[73, 74]

References

1. Agrawal M, Biswas A (2015) Molecular diagnostics of neurodegenerative disorders. *Front Mol Biosci* 2:54
2. Burns A, Lewis G, Jacoby R, Levy R (1991) Factors affecting survival in Alzheimer's disease. *Psychol Med* 21(2):363–370
3. Fisher EMC, Bannerman DM (2019) Mouse models of neurodegeneration: know your question, know your mouse. *Sci Transl Med* 11(493):eaaq1818
4. Du X, Wang X, Geng M (2018) Alzheimer's disease hypothesis and related therapies. *Transl Neurodegener* 7:2
5. Gao F, Gao K, He C, Liu M, Wan H, Wang P (2019) Multi-site dynamic recording for A β oligomers-induced Alzheimer's disease in vitro based on neuronal network chip. *Biosens Bioelectron* 133:183–191
6. Prince M, Ali G-C, Guerchet M, Prina AM, Albanese E, Wu Y-T (2016) Recent global trends in the prevalence and incidence of dementia, and survival with dementia. *Alzheimers Res Ther* 8: 23
7. Webster SJ, Bachstetter AD, Nelson PT, Schmitt FA, Van Eldik LJ (2014) Using mice to model Alzheimer's dementia: an overview of the clinical disease and the preclinical behavioral changes in 10 mouse models. *Front Genet* 5:88
8. Wu X, Li J, Zhou W, Tam K (2015) Animal models for Alzheimer's disease: a focused review of transgenic rodent models and behavioral assessment methods. *ADMET DMPK* 3(3): 242–253
9. Götz J, Ittner LM (2008) Animal models of Alzheimer's disease and frontotemporal dementia. *Nat Rev Neurosci* 9(7):532–544
10. Jellinger KA (2020) Neuropathological assessment of the Alzheimer spectrum. *J Neural Transm* 127(9):1229–1256
11. Salari S, Bagheri M (2016) A review of animal models of Alzheimer's disease: a brief insight into pharmacologic and genetic models. *J Physiol Pharmacol* 20(1):5–11
12. Apostolova LG (2016) Alzheimer disease. *Continuum (Minneapolis Minn)* 22(2 Dementia):419–434
13. Samaey C, Schreurs A, Stroobants S, Balschun D (2019) Early cognitive and behavioral deficits in mouse models for tauopathy and Alzheimer's disease. *Front Aging Neurosci* 11:335
14. Selles MC, Oliveira MM, Ferreira ST (2018) Brain inflammation connects cognitive and non-cognitive symptoms in Alzheimer's disease. *J Alzheimers Dis* 64(S1):S313–S327
15. Zhao Q-F, Tan L, Wang H-F, Jiang T, Tan M-S, Tan L et al (2016) The prevalence of neuropsychiatric symptoms in Alzheimer's disease: systematic review and meta-analysis. *J Affect Disord* 190:264–271
16. Cummings JL, Zhong K (2006) Treatments for behavioural disorders in neurodegenerative diseases: drug development strategies. *Nat Rev Drug Discov* 5(1):64–74
17. Commins S, Kirby BP (2019) The complexities of behavioural assessment in neurodegenerative disorders: a focus on Alzheimer's disease. *Pharmacol Res* 147:104363
18. Bourin M, Petit-Demoulière B, Nic Dhonnchadha B, Hascöet M (2007) Animal models of anxiety in mice. *Fundam Clin Pharmacol* 21(6):567–574
19. Murai T, Okuda S, Tanaka T, Ohta H (2007) Characteristics of object location memory in mice: behavioral and pharmacological studies. *Physiol Behav* 90(1):116–124
20. Bromley-Brits K, Deng Y, Song W (2011) Morris water maze test for learning and memory deficits in Alzheimer's disease model mice. *J Vis Exp* 53:2920
21. Morris R (1984) Developments of a water-maze procedure for studying spatial learning in the rat. *J Neurosci Methods* 11(1):47–60
22. Tian H, Ding N, Guo M, Wang S, Wang Z, Liu H et al (2019) Analysis of learning and memory ability in an Alzheimer's disease mouse model using the Morris water maze. *J Vis Exp* 152: 60055

23. Vorhees CV, Williams MT (2006) Morris water maze: procedures for assessing spatial and related forms of learning and memory. *Nat Protoc* 1(2):848–858
24. Ikegami S (1994) Behavioral impairment in radial-arm maze learning and acetylcholine content of the hippocampus and cerebral cortex in aged mice. *Behav Brain Res* 65(1):103–111
25. Mei J, Kohler J, Winter Y, Spies C, Endres M, Banneke S et al (2020) Automated radial 8-arm maze: a voluntary and stress-free behavior test to assess spatial learning and memory in mice. *Behav Brain Res* 381:112352
26. Olton DS, Collison C, Werz MA (1977) Spatial memory and radial arm maze performance of rats. *Learn Motiv* 8(3):289–314
27. Höltner SM, Garrett L, Einicke J, Sperling B, Dirscherl P, Zimprich A et al (2015) Assessing cognition in mice. *Curr Protocols Mouse Biol* 5(4):331–358
28. Kraeuter A-K, Guest PC, Sarnyai Z (2019) The Y-maze for assessment of spatial working and reference memory in mice. In: *Pre-clinical models*. Humana Press, New York, pp 105–111
29. d’Isa R, Comi G, Leocani L (2021) Apparatus design and behavioural testing protocol for the evaluation of spatial working memory in mice through the spontaneous alternation T-maze. *Sci Rep* 11(1):21177
30. Ennaceur A, Delacour J (1988) A new one-trial test for neurobiological studies of memory in rats. 1: behavioral data. *Behav Brain Res* 31(1):47–59
31. Chen G, Chen KS, Knox J, Inglis J, Bernard A, Martin SJ et al (2000) A learning deficit related to age and b-amyloid plaques in a mouse model of Alzheimer’s disease. *Nature* 408(6815):695–699
32. Lueptow LM (2017) Novel object recognition test for the investigation of learning and memory in mice. *J Vis Exp* 126:55718
33. Vaucher E, Fluit P, Chishti MA, Westaway D, Mount HTJ, Kar S (2002) Object recognition memory and cholinergic parameters in mice expressing human presenilin 1 transgenes. *Exp Neurol* 175(2):398–406
34. Prut L, Belzung C (2003) The open field as a paradigm to measure the effects of drugs on anxiety-like behaviors: a review. *Eur J Pharmacol* 463(1–3):3–33
35. Eltokhi A, Kurpiers B, Pitzer C (2020) Behavioral tests assessing neuropsychiatric phenotypes in adolescent mice reveal strain- and sex-specific effects. *Sci Rep* 10(1):11263
36. Elamin M, Pender N, Hardiman O, Abrahams S (2012) Social cognition in neurodegenerative disorders: a systematic review. *J Neurol Neurosurg Psychiatry* 83(11):1071–1079
37. Kosel F, Munoz PT, Yang JR, Wong AA, Franklin TB (2019) Age-related changes in social behaviours in the 5xFAD mouse model of Alzheimer’s disease. *Behav Brain Res* 362:160–172
38. Crawley JN, Chen T, Puri A, Washburn R, Sullivan TL, Hill JM et al (2007) Social approach behaviors in oxytocin knockout mice: comparison of two independent lines tested in different laboratory environments. *Neuropeptides* 41(3):145–163
39. Kaidanovich-Beilin O, Lipina T, Vukobradovic I, Roder J, Woodgett JR (2011) Assessment of social interaction behaviors. *J Vis Exp* 48:2473
40. Kogan JH, Frankland PW, Silva AJ (2000) Long-term memory underlying hippocampus-dependent social recognition in mice. *Hippocampus* 10(1):47–56
41. Hitti FL, Siegelbaum SA (2014) The hippocampal CA2 region is essential for social memory. *Nature* 508(7494):88–92
42. Sherwin CM, Haug E, Terkelsen N, Vadgama M (2004) Studies on the motivation for burrowing by laboratory mice. *Appl Anim Behav Sci* 88(3–4):343–358
43. Deacon RMJ (2006) Burrowing in rodents: a sensitive method for detecting behavioral dysfunction. *Nat Protoc* 1(1):118–121
44. Baumann A, Moreira CG, Morawska MM, Masneuf S, Baumann CR, Noain D (2016) Preliminary evidence of apathetic-like behavior in aged vesicular monoamine transporter 2 deficient mice. *Front Hum Neurosci* 10:587
45. Deacon RM (2006) Assessing nest building in mice. *Nat Protoc* 1(3):1117–1119

46. Koolhaas JM, Coppens CM, de Boer SF, Buwalda B, Meerlo P, Timmermans PJA (2013) The resident-intruder paradigm: a standardized test for aggression, violence and social stress. *J Vis Exp* 77:4367
47. Lumley LA, Charles RF, Charles RC, Hebert MA, Morton DM, Meyerhoff JL (2000) Effects of social defeat and of diazepam on behavior in a resident-intruder test in male DBA/2 mice. *Pharmacol Biochem Behav* 67(3):433–447
48. Álvarez-Suárez P, Banqueri M, Vilella M, Méndez M, Arias JL (2015) The effect of recording interval length on behavioral assessment using the forced swimming test. *Revista Iberoamericana de Psicología y Salud* 6(2):90–95
49. Aydin E, Hritcu L, Dogan G, Hayta S, Bagci E (2016) The effects of inhaled *Pimpinella peregrina* essential oil on scopolamine-induced memory impairment, anxiety, and depression in laboratory rats. *Mol Neurobiol* 53(9):6557–6567
50. Belovicova K, Bogi E, Csatlósova K, Dubovický M (2017) Animal tests for anxiety-like and depression-like behavior in rats. *Interdiscip Toxicol* 10(1):40–43
51. Cryan JF, Mombereau C, Vassout A (2005) The tail suspension test as a model for assessing antidepressant activity: review of pharmacological and genetic studies in mice. *Neurosci Biobehav Rev* 29(4–5):571–625
52. Duman CH (2010) Models of depression. *Vit Hormones* 82:1–21
53. Wu C, Yang L, Li Y, Dong Y, Yang B, Tucker LD et al (2020) Effects of exercise training on anxious-depressive-like behavior in Alzheimer rat. *Med Sci Sports Exerc* 52(7):1456–1469
54. Games D, Adams D, Alessandrini R, Barbour R, Berthelette P, Blackwell C et al (1995) Alzheimer-type neuropathology in transgenic mice overexpressing V717F beta-amyloid precursor protein. *Nature* 373(6514):523–527
55. Irizarry MC, McNamara M, Fedorchak K, Hsiao K, Hyman BT (1997) APPSw transgenic mice develop age-related A beta deposits and neuropil abnormalities, but no neuronal loss in CA1. *J Neuropathol Exp Neurol* 56(9):965–973
56. Lanz TA, Carter DB, Merchant KM (2003) Dendritic spine loss in the hippocampus of young PDAPP and Tg2576 mice and its prevention by the ApoE2 genotype. *Neurobiol Dis* 13(3):246–253
57. Calhoun ME, Wiederhold KH, Abramowski D, Phinney AL, Probst A, Sturchler-Pierrat C et al (1998) Neuron loss in APP transgenic mice. *Nature* 395(6704):755–756
58. Stalder M, Phinney A, Probst A, Sommer B, Staufenbiel M, Jucker M (1999) Association of microglia with amyloid plaques in brains of APP23 transgenic mice. *Am J Pathol* 154(6):1673–1684
59. Sturchler-Pierrat C, Abramowski D, Duke M, Wiederhold KH, Mistl C, Rothacher S et al (1997) Two amyloid precursor protein transgenic mouse models with Alzheimer disease-like pathology. *Proc Natl Acad Sci U S A* 94(24):13287–13292
60. Chishti MA, Yang DS, Janus C, Phinney AL, Horne P, Pearson J et al (2001) Early-onset amyloid deposition and cognitive deficits in transgenic mice expressing a double mutant form of amyloid precursor protein 695. *J Biol Chem* 276(24):21562–21570
61. Dudal S, Krzywkowski P, Paquette J, Morissette C, Lacombe D, Tremblay P et al (2004) Inflammation occurs early during the A beta deposition process in TgCRND8 mice. *Neurobiol Aging* 25(7):861–871
62. Mucke L, Masliah E, Yu GQ, Mallory M, Rockenstein EM, Tatsuno G et al (2000) High-level neuronal expression of A beta(1-42) in wild-type human amyloid protein precursor transgenic mice: synaptotoxicity without plaque formation. *J Neurosci* 20(11):4050–4058
63. Wright AL, Zinn R, Hohensinn B, Konen LM, Beynon SB, Tan RP et al (2013) Neuroinflammation and neuronal loss precede A beta plaque deposition in the hAPP-J20 mouse model of Alzheimer's disease. *PLoS One* 8(4):e59586
64. Radde R, Bolmont T, Kaeser SA, Coomaraswamy J, Lindau D, Stoltze L et al (2006) Abeta42-driven cerebral amyloidosis in transgenic mice reveals early and robust pathology. *EMBO Rep* 7(9):940–946

65. Buskila Y, Crowe SE, Ellis-Davies GCR (2013) Synaptic deficits in layer 5 neurons precede overt structural decay in 5xFAD mice. *Neuroscience* 254:152–159
66. Jawhar S, Trawicka A, Jenneckens C, Bayer T, Wirths O (2012) Motor deficits, neuron loss, and reduced anxiety coinciding with axonal degeneration and intraneuronal A β aggregation in the 5XFAD mouse model of Alzheimer's disease. *Neurobiol Aging* 33(1):196.e29
67. Richard B, Anastasiia K, Sandra B, Bayer T, Weggen S, Wirths O (2015) Gene dosage dependent aggravation of the neurological phenotype in the 5XFAD mouse model of Alzheimer's disease. *J Alzheimers Dis* 45(4):1223–1236
68. Oddo S, Caccamo A, Shepherd JD, Murphy MP, Golde TE, Kaye R et al (2003) Triple-transgenic model of Alzheimer's disease with plaques and tangles: intracellular A β and synaptic dysfunction. *Neuron* 39(3):409–421
69. Tomiyama T, Matsuyama S, Iso H, Umeda T, Takuma H, Ohnishi K et al (2010) A mouse model of amyloid beta oligomers: their contribution to synaptic alteration, abnormal tau phosphorylation, glial activation, and neuronal loss in vivo. *J Neurosci* 30(14):4845–4856
70. Umeda T, Maekawa S, Kimura T, Takashima A, Tomiyama T, Mori H (2014) Neurofibrillary tangle formation by introducing wild-type human tau into APP transgenic mice. *Acta Neuropathol* 127(5):685–698
71. Borchelt DR, Ratovitski T, van Lare J, Lee MK, Gonzales V, Jenkins NA et al (1997) Accelerated amyloid deposition in the brains of transgenic mice coexpressing mutant presenilin 1 and amyloid precursor proteins. *Neuron* 19(4):939–945
72. Terwel D, Lasrado R, Snauwaert J, Vandeweert E, Van Haesendonck C, Borghgraef P et al (2005) Changed conformation of mutant Tau-P301L underlies the moribund tauopathy, absent in progressive, nonlethal axonopathy of Tau-4R/2N transgenic mice. *J Biol Chem* 280(5):3963–3973
73. Decker JM, Krüger L, Sydow A, Dennissen FJ, Siskova Z, Mandelkow E et al (2016) The Tau/A152T mutation, a risk factor for frontotemporal-spectrum disorders, leads to NR2B receptor-mediated excitotoxicity. *EMBO Rep* 17(4):552–569
74. Sydow A, Hochgräfe K, Könen S, Cadinu D, Matenia D, Petrova O et al (2016) Age-dependent neuroinflammation and cognitive decline in a novel Ala152Thr-Tau transgenic mouse model of PSP and AD. *Acta Neuropathol Commun* 4:17